Quantum Monte Carlo study of extended Bose-Hubbard models with short- and infinite-range interactions

Dissertation

zur Erlangung des Grades
des Doktors der Naturwissenschaften
der Naturwissenschaftlich-Technischen Fakultät
der Universität des Saarlandes

von

Benjamin Bogner

Saarbrücken

2020

Eidesstattliche Versicherung

Hiermit versichere ich an Eides statt, dass ich die vorliegende Arbeit selbstständig und ohne Benutzung anderer als der angegebenen Hilfsmittel angefertigt habe. Die aus anderen Quellen oder indirekt übernommenen Daten und Konzepte sind unter Angabe der Quelle gekennzeichnet. Die Arbeit wurde bisher weder im In- noch im Ausland in gleicher oder ähnlicher Form in einem Verfahren zur Erlangung eines akademischen Grades vorgelegt.

Ort, Datum

_____

Unterschrift

_____

Benjamin Bogner

Tag des Kolloquiums:	12.11.2020
Dekan:	Prof. Dr. Jörn E. Walter
Berichterstatter:	Prof. Dr. Dr. h.c. Heiko Rieger Prof. Dr. Ludger Santen
Vorsitzender:	Prof. Dr. Romanus Dyczij-Edlinger
Akad. Mitarbeiter:	Dr. Christian Spengler

Zusammenfassung

Ultrakalte Atome in optischen Gittern sind eine der wenigen experimentellen Realisierungen von Quantensystemen. Sie können mit Hilfe von Bose-Hubbard-Modellen beschrieben werden. In den letzten Jahrzehnten wurden die experimentellen Konfigurationen immer fortschrittlicher, sodass auch längerreichweitige Wechselwirkungen zwischen den kalten Atomen eingeführt werden konnten.
Diese Dissertation befasst sich mit der Untersuchung von Phasen und Phasenübergängen in erweiterten Bose-Hubbard-Modellen, welche die Versuchssysteme mit längerreichweitigen Wechselwirkungen beschreiben. Da die zugrundeliegenden Schrödingergleichungen nicht analytisch lösbar sind, werden zwei approximative Verfahren verwendet, um ihre Eigenschaften zu simulieren. Bei der ersten Methode handelt es sich um ein Variations-Monte-Carlo-Verfahren, das auf Wellenfunktionsoptimierung basiert und sich zur Betrachtung von Systemen im kanonischen Ensemble in einer und zwei Dimensionen eignet. Darüber hinaus wird ein nicht-exakter Weltlinien-Quanten-Monte-Carlo-Algorithmus eingesetzt, um eindimensionale Systeme in kanonischen und großkanonischen Ensembles zu untersuchen.
Es zeigt sich, dass beide angewendeten Verfahren zur Simulation der Eigenschaften bosonischer Systeme mit kurz- und langreichweitigen Wechselwirkungen geeignet sind und die korrekte Universalitätsklasse für die meisten Phasenübergänge vorhersagen.
Zusätzlich wird die selten auftretende Haldane-Isolator-Phase mit beiden Methoden untersucht. Bei ihr handelt es sich um eine isolierende Phase, deren Existenz für eindimensionale fermionische und bosonische Modelle mit kurzreichweitigen Wechselwirkungen nachgewiesen wurde.

Abstract

Ultracold atoms in optical lattices are one of the few experimental realizations of quantum systems. They can be described by Bose-Hubbard models. In the last decades experimental setups became more sophisticated so that off-site interactions between the cold atoms could be introduced, too.
In this thesis, phases and phase transitions in extended Bose-Hubbard models are studied, which describe the experimental setups with long-range interactions. As the underlying Schrödinger equations are not analytically solvable, two approximative methods are used to simulate their properties. The first technique is a variational Monte Carlo method based on wave function optimization, which is suitable to describe systems in the canonical ensemble in one or two dimensions. In addition, a non-exact world-line quantum Monte Carlo algorithm is applied to simulate one-dimensional systems within canonical and grand-canonical ensembles.
Comparing the results to those of exact algorithms shows that both techniques are suitable to simulate the properties of bosonic systems with short- and long-range interactions and to predict the correct universality classes for most of the transitions.
Additionally, the rare Haldane insulator phase is studied with either methods. This phase is a gapped insulating phase whose existence has been proven for fermionic and bosonic one-dimensional models with short-range interactions.

Publications

Results of this thesis are published in the following peer-reviewed journal:

[1] B. Bogner, C. De Daniloff and H. Rieger.
Variational Monte-Carlo study of the extended Bose-Hubbard model with short- and infinite-range interactions.
Eur. Phys. J. B, *2019*, 92, 111

Contents

List of Figures v

List of Tables vii

1 Introduction 1

2 Critical phenomena 5
2.1 Phase transitions . . . 5
2.2 Quantum phase transitions . . . 6
2.3 Classification . . . 7
2.4 Critical exponents . . . 8
2.5 Scaling relations . . . 9
2.6 Universality classes . . . 10
2.7 Finite-size scaling . . . 11

3 Ultracold atoms 13
3.1 Cooling atoms . . . 14
3.2 Optical lattices . . . 15
3.3 Control of parameters . . . 17
3.4 Experimental realizations . . . 18
3.4.1 Superfluid to Mott insulator transition . . . 18
3.4.2 Nearest-neighbour interactions . . . 20
3.4.3 Long-range interactions . . . 21

4 The Bose-Hubbard model 23
4.1 Standard Bose-Hubbard model . . . 24
4.2 Bose-Hubbard model with nearest-neighbour interactions . . . 28
4.3 Bose-Hubbard model with long-range interactions . . . 31
4.4 Bose-Hubbard model with long-range and nearest-neighbour interactions . . . 33
4.5 Parameters . . . 34
4.6 Phases . . . 34
4.6.1 Mott insulator . . . 34
4.6.2 Superfluid . . . 36
4.6.3 Density wave . . . 37
4.6.4 Supersolid . . . 39
4.6.5 Phase separation . . . 40
4.6.6 Symmetry-breaking and phase transitions . . . 40
4.7 Order parameters . . . 41
4.7.1 Phase coherence correlation function and condensate fraction . . . 42
4.7.2 Density-density correlation function and structure factor . . . 43
4.7.3 Superfluid density . . . 44
4.7.4 Occupation imbalance . . . 45
4.7.5 Further observables . . . 46

5 Haldane insulator phase 49
5.1 Haldane insulator in the antiferromagnet spinchain . . . 50

5.2 Haldane Bose insulator . . . 50
5.3 Order parameters . . . 51
5.3.1 String order . . . 52
5.3.2 Parity order . . . 53
5.3.3 Evaluation . . . 53
5.4 Motivation . . . 55

6 Quantum Monte Carlo 57
6.1 Monte Carlo methods . . . 57
6.1.1 Monte Carlo integration . . . 58
6.1.2 Random number generators . . . 59
6.1.3 Partition function and Boltzmann weights . . . 59
6.1.4 Random walks and Markov chains . . . 61
6.1.5 Ergodicity . . . 61
6.1.6 Detailed Balance . . . 61
6.1.7 Acceptance ratios . . . 62
6.1.8 Metropolis algorithm . . . 63
6.1.9 Computational aspects and quality control . . . 64
6.2 From classical to quantum problems . . . 65
6.2.1 Partition function of a quantum system . . . 65
6.3 Quantum Monte Carlo state of the art . . . 67

7 Variational Monte Carlo 69
7.1 The variational method . . . 70
7.2 Trial wave function . . . 71
7.2.1 Jastrow factor . . . 72
7.2.2 Many-body interaction term . . . 73
7.2.3 Number of parameters to be optimized . . . 73
7.3 Optimization algorithm . . . 74
7.3.1 Monte Carlo sampling . . . 74
7.3.2 Wave function optimization . . . 75
7.4 Error estimation . . . 77
7.5 Limitations and caveats . . . 77

8 Discrete time world-line quantum Monte Carlo 81
8.1 Path integral representation of the quantum problem . . . 82
8.2 The Monte Carlo process . . . 85
8.2.1 Local updates . . . 85
8.2.2 Global updates . . . 87
8.3 Nearest-neighbour interactions . . . 88
8.4 Cavity-induced long-range interactions . . . 88
8.5 Error estimation . . . 89
8.6 Measurement of observables . . . 90
8.6.1 Superfluid density . . . 90

9 One-dimensional phase analysis of the Bose-Hubbard models 93
9.1 Standard Bose-Hubbard model . . . 94
9.2 Bose-Hubbard model with nearest-neighbour interactions . . . 99
9.2.1 Haldane insulator phase . . . 105
9.3 Bose-Hubbard model with long-range interactions . . . 108
9.4 Comparison of the $\rho = 1$ phase diagrams . . . 111
9.5 Bose-Hubbard model with both nearest-neighbour and long-range interactions . . . 113

10 Two-dimensional phase analysis of the Bose-Hubbard models **115**
10.1 Standard Bose-Hubbard model 115
10.2 Bose-Hubbard model with nearest-neighbour interactions 117
10.3 Bose-Hubbard model with long-range interactions 121
10.4 Bose-Hubbard model with nearest-neighbour and long-range interactions 125
10.4.1 Nearest-neighbour and long-range interactions equally strong 125
10.4.2 Nearest-neighbour interactions with fixed long-range interactions 127
10.4.3 Long-range interactions with fixed nearest-neighbour interactions 128
10.5 Comparison of the resuls of the different models 129

11 Conclusion **131**

Bibliography **I**

Acknowledgments **IX**

List of Figures

2.1 Phases of water . . . 5
2.2 Quantum critical region . . . 6
2.3 First and second order quantum phase transtions . . . 7
2.4 Finite-size scaling . . . 12

3.1 Phase diagram reprint . . . 14
3.2 Atoms in an optical potential . . . 16
3.3 Scheme of the transition from superfluid to Mott insulator phase . . . 18
3.4 Absorption images . . . 19
3.5 Dipole interactions . . . 20
3.6 Experimental scheme of cavity-induced interactions between bosons . . . 21
3.7 Photon scattering inside a cavity . . . 22

4.1 Interactions of the standard Bose Hubbard model . . . 25
4.2 Nearest-neighbour interactions between bosons . . . 28
4.3 Long-range interactions between bosons . . . 31
4.4 Scheme of the Mott insulator phase in 2D . . . 36
4.5 Scheme of the superfluid phase in 2D . . . 37
4.6 Scheme of the density wave phase in 2D . . . 38
4.7 Comparison of density wave configurations in 2D . . . 39
4.8 Scheme of the supersolid phase in 2D . . . 39
4.9 Phase coherence correlation function . . . 42
4.10 Condensate fraction . . . 43
4.11 Structure factor . . . 44
4.12 Density and occupation imbalance . . . 45
4.13 Comparison of ground state energies . . . 46

5.1 String order . . . 52
5.2 Parity order . . . 53
5.3 Order parameters in the Haldane phase . . . 54

6.1 Integration by Monte Carlo sampling . . . 58

7.1 Thermodynamic limit extrapolation . . . 78

8.1 Single slice of imaginary time . . . 83
8.2 World-line representation of bosons . . . 84
8.3 Local world-line update . . . 86
8.4 Configurations of individual plaquettes . . . 86
8.5 Global world-line update . . . 88
8.6 Extrapolation of the superfluid denstiy . . . 91

9.1 Grand-canonical phase diagram of the standard BHM in 1D (world-line QMC) . . . 94
9.2 Density profiles in the standard BHM (world-line QMC) . . . 95
9.3 Finite-size scaling of the critical point of the MI-SF transition in the standard BHM (world-line QMC) . . . 96

9.4 Parity order parameter during the MI-SF transition for various L in the standard BHM (world-line QMC) . . . 96
9.5 Finite-size scaling of the parity order parameter at the MI-SF transition in the standard BHM (world-line QMC) . . . 97
9.6 Ground state energy during the SF to MI transition in the standard BHM (VMC) 97
9.7 Correlationfunction $G(L/2)$ during the SF to MI transition for various L (VMC) . 98
9.8 Grand-canonical phase diagram of the BHM with NN interactions in 1D at $U_{nn} = 0.4$ (world-line QMC) . . . 99
9.9 Density profiles of the BHM with NN interactions in 1D at $U_{nn} = 0.4$ (world-line QMC) . . . 100
9.10 Grand-canonical phase diagram of the BHM with NN interactions in 1D at $U_{nn} = 0.75$ (world-line QMC) . . . 101
9.11 Phase diagram of the BHM with NN interactions in 1D at $\rho = 1$ (world-line QMC) 101
9.12 Order parameters in the BHM with NN interactions in 1D at $\rho = 1$ (world-line QMC) . . . 102
9.13 Phase diagram of the BHM with NN interactions in 1D at $\rho = 1$ (VMC) . . . 103
9.14 Order parameters in the BHM with NN interactions in 1D at $\rho = 1$ (VMC) . . . 104
9.15 Order parameters during phase transitions from DW to HI to SF at $\rho = 1$ (world-line QMC) . . . 105
9.16 Finite-size effects of order parameters at the HI (world-line QMC) . . . 106
9.17 Order parameters during expected phase transitions from DW to HI to SF (VMC) 107
9.18 Phase coherence correlation function at various t (VMC) . . . 107
9.19 Grand-canonical phase diagram of the BHM with LR interactions in 1D at $U_l = 0.3$ (world-line QMC) . . . 108
9.20 Phase diagram of the BHM with LR interactions in 1D (world-line QMC) . . . 109
9.21 Phase diagram of the BHM with LR interactions in 1D at $\rho = 1$ (VMC) . . . 109
9.22 Comparison of the $\rho = 1$ phase diagrams in one dimension . . . 111
9.23 Order parameters along the HI in a BHM with NN interactions at $U_{nn} = 0.75$ and $U_l = 0$ (World-line quantum Monte Carlo) . . . 113
9.24 Suppression of the HI phase through LR interactions . . . 114

10.1 Finite-size scaling of the MI-SF transition in the standard BHM at $\rho = 1$ . . . 116
10.2 Ground state phase diagram of the BHM with NN interactions at $\rho = 1$ . . . 117
10.3 Phase diagrams of the BHM with NN interactions at various densities ρ . . . 118
10.4 Finite-size scaling of the SF-MI transition in the BHM with NN interactions at $\rho = 1$ . . . 119
10.5 Finite-size scaling of the SS-DW transition in the BHM with NN interactions . . . 120
10.6 Finite-size scaling of the SF-SS transition in the BHM with NN interactions . . . 120
10.7 Phase diagram of BHM with LR interactions at $\rho = 1$ . . . 121
10.8 Experimentally obtained phase diagram of a system with cavity-induced long-range interactions . . . 122
10.9 Phase diagrams of the BHM with LR interactions at various densities ρ . . . 123
10.10 Finite-size scaling of the SF-MI transition in the BHM with LR interactions at $\rho = 1$ . . . 124
10.11 Finite-size scaling of the SF-SS transition in the BHM with LR interactions at $\rho = 1$ 124
10.12 Phase diagram of the BHM with NN and LR interactions at $\rho = 1$ . . . 125
10.13 Phase diagrams of the BHM with NN and LR interactions at various ρ . . . 126
10.14 Phase diagrams of the BHM with NN interactions at $\rho = 1$ and constant LR interactions . . . 127
10.15 Phase diagrams of the BHM with LR interactions at $\rho = 1.5$ and constant NN interactions . . . 128
10.16 Comparison of the phase diagrams of the different models at $\rho = 1$ . . . 129

List of Tables

2.1 Critical exponents 9
2.2 Critical exponents of universality classes 10

4.1 Symmetries and universality classes 41
4.2 Phases and order parameters 47

5.1 String and parity order parameters 54

8.1 World-line updates 87

Chapter 1

Introduction

Strongly correlated systems and their nontrivial phase diagrams are an intensely studied topic in condensed matter physics and material sciences. Predicting or even understanding the behaviour of these systems is a compelling task for both experimentalists and theoretical scientists. Competing interactions between particles make their collective states difficult to comprehend and lead to complex phases of matter. Especially when quantum effects are involved, the studies of many-body systems with high correlations are a demanding challenge.
For this reason ultracold atoms in optical lattices are of extraordinary significance for modern physics. Within an appropriate setup, cold atoms constitute a strongly correlated yet highly controllable system. The individual particles arrange according to the confinements of the optical lattice and collectively depict an ultracold bosonic gas on a lattice, thereby mimicking the behaviour of a bosonic quantum system. Hence ultracold atoms in optical lattices have been in the focus of quantum physics for the last decades and continue to be one of the most vital fields in physics in general. Unique possibilities regarding the investigation of strongly correlated quantum many-body phases are given by these experimental setups.
The development of cooling techniques for atoms, later decorated with the Nobel prize [2–4], laid the foundation for a large field of research. With the combined efforts of quantum optics and atomic physics, experimentalists are capable of implementing setups which are almost perfect realizations of quantum systems. The quantum phase transition from a superfluid (SF) to Mott insulator (MI) regime was experimentally observed for the first time in 2002 by Greiner et al. A gas of ^{57}Rb-atoms was exposed to a laser-generated lattice-potential. This makes the bosonic particles in the gas localize, the overall state changes from a superfluid to Mott insulating [5]. The possibility to tune between insulating and conducting phases by controlling external parameters immediately evokes the analogy to classical electronic systems [6, 7]. The fact that quantum fluctuations can be observed in such systems makes them a possible basis for quantum computers. This leads to the proposal to use cold atoms in optical traps as experimental realizations of the Bose-Hubbard model [8], which is synonymous to use them as the basis of a quantum computer. In recent years, it has become possible to introduce higher correlations between particles by constructing experimental setups comprising inter-particle interactions that go beyond on-site range [9–11]. These experiments offer the possibility to emulate even more advanced quantum systems. This drives the urge to look into the underlying quantum mechanical models with theoretical methods, which is the topic of this thesis. To properly motivate the theoretical examination, a brief historical introduction follows.
Quantum mechanics is essential in the investigation of natural processes on an atomic or subatomic level, as the existence and the behaviour of atoms cannot be explained by classical physics. Consequently, quantum mechanics provides the basis of the modern understanding of nature [12]. Furthermore, quantum mechanics took a major part in consolidating the concepts of physics at the beginning of the 20th century. Prior to this, it was necessary to fundamentally distinguish between matter, described by the laws of Newton [13], and radiation, characterized by the wave equation and Maxwell's equations. Maxwell's equations represented the pillars of the theory of electromagnetism, unifying the description of electricity, magnetism, and optics [14]. The Lorentz force interlinked the branches of matter and radiation by describing the interaction between par-

ticles and waves. However, experimental observations like black-body radiation, the photoelectric effect, and the Compton effect could only be explained by theories not reconciling with classical physics [15]. In a groundbreaking proposal, Planck assumed the energy to be quantized by a natural constant h. Motivated by the photoelectric effect, Einstein later generalized this hypothesis, considering the light of frequency ν as a stream of photons with the identical energy $h\nu$ [12]. Nevertheless, phenomena like interference and deflection prohibit a description solely based on the particle qualities. This implies that objects on a microscopic scale exhibit characteristics of both particles and waves and that there is a limit to the precision at which quantities can be measured because of the finite size of the Planck constant h. The newly arising theory leaped forward when Schrödinger formulated the wave interpretation of quantum mechanics in 1926 [16]:

$$\imath\hbar\frac{\partial}{\partial t}\psi(\mathbf{r},t) = \left(-\frac{\hbar^2}{2m}\nabla^2 + V(\mathbf{r},t)\right)\psi(\mathbf{r},t), \tag{1.1}$$

This relation is known as the Schrödinger equation and characterizes the particle wave function $\psi(\mathbf{r},t)$ in the presence of an external potential $V(\mathbf{r},t)$. Another landmark in the same year was Born's proposal to interpret $\psi(\mathbf{r},t)$ as a probability amplitude and $|\psi(\mathbf{r},t)|^2$ as a probability density [17]. Heisenberg and Bohr used this interpretation to deduce the basics of the uncertainty principle [18], stating that there is a fundamental limit to the precision for the measurement of a pair of complementary variables (e.g. momentum and location) of a quantum particle.
Furthermore, the wave nature of the particles makes them indistinguishable, or identical. Consequently, the many-body wave function describing multiple particles is either symmetric or antisymmetric under particle permutation. Accordingly, two types of particles exist in nature, specifiable by the statistics they follow: fermions and bosons. While fermions obey the Pauli exclusion principle, stating that two or more identical fermions can not occupy the same quantum state in the system simultaneously, bosons are not subject to this restriction [12]. A requirement for appropriate statistics to describe how a collection of indistinguishable non-interacting particles will occupy a set of available discrete energy states is furthermore that the permutation of two particles does not create a new state. Fermions on the other hand, following antisymmetric statistics under permutation because of the Pauli exclusion principle, will distribute according to the Fermi-Dirac statistics [19, 20]. Bosons, on the other hand, follow the Bose-Einstein statistics [21] and are allowed to occupy the very same state.
As a consequence of the wave-particle duality, effects like superconductivity, superfluidity or the Bose condensation arise, which can not be described by classical physics. Therefore, quantum mechanics plays a major role in the exploration of macroscopic systems. Naturally, macroscopic systems are composed of a tremendous number of quantum particles, which complicates an analytical treatment. If relativistic effects can be neglected, a physical system is entirely described by the many-body Schrödinger equation (see Eq. 1.1). Solving this equation allows the prediction of the behaviour of the corresponding system. However, the Hilbert space, in which the SEQ and its solving wave function operate, typically scales exponentially with the number of particles. This makes an exact analytical solution impossible in most cases.
For this reason, quantum Monte Carlo methods are used to study complex quantum many-body problems. Based on Monte Carlo methods, computational algorithms that are intended to obtain numerical results by random sampling, quantum Monte Carlo methods mostly rely on Markov chains [22]. Yet, in contrast to classical systems, quantum problems are usually more difficult to treat as the distributions to be sampled are frequently unknown [23]. Effects like entanglement make the state space of a quantum system far more complex. Hence, drawing a quantitative conclusion requires the knowledge of the state space distributions and the ability to sample them efficiently [24]. Modern advanced methods yield numerically exact results for certain bosonic systems but go along with a high computational effort. To this date, the interest in developing and improving statistical methods to investigate quantum systems is not declining.
Taking a different approach, Feynman proposed to rather simulate the behaviour of quantum

systems instead of using numerical or analytical methods [25]. His idea was to establish a controllable quantum system which is used to simulate other quantum systems. He suggested that a *quantum computer* should be able to simulate any local quantum system. This conjecture was later shown to be correct [26, 27]. When considering quantum simulators, a differentiation between analog and digital simulators should be made, depending on the method of simulation [28]. Only the digital quantum simulator, also named universal quantum simulator, should be able to simulate any finite-dimensional quantum system based on a local Hamiltonian. It is more commonly referred to as a quantum computer and currently great efforts are invested in its implementation [29]. Very recently a breakthrough on this field was reached, when the creation of a processor with a set of 53 programmable superconducting qubits succeeded [30]. The resulting 2^{53}-dimensional computational state-space allows for very fast computations on the processor.
An analog quantum simulator is also known as a quantum emulator. It is a highly controllable and well measurable physical system in such a way that it can be driven to mimic a quantum system of interest. Ultracold atoms have proven to be a very good basis for the construction of experimental quantum emulators. Modern laser cooling methods have made the necessary ultracold temperatures accessible. An important advantage is that individual atoms can be well isolated from their environment and their properties can be widely tuned with electromagnetic fields and lasers. Furthermore, with the knowledge of atomic physics and condensed matter physics, theoretical predictions about their behaviour can be derived. In the last decades, significant progress has been achieved concerning many-body physics with ultracold gases [31, 32]. As mentioned above, the first breakthrough was the observation of a superfluid to Mott insulator quantum phase transition within an atomic gas [5]. Subsequent experiments amended dipolar repulsion between the particles to the experiment [9, 10], which can be approximated as nearest-neighbour repulsions. However, the added interactions were too small to enrich the phase diagram.
In recent years, theoretical considerations proposed that long-range interactions between particles could be introduced by photon scattering inside a cavity [33, 34]. This idea is based on Bragg spectroscopy of cold atoms [35, 36]. Further theoretical investigation predicted new quantum phases caused by these interactions [37, 38]. After first attempts [39], an impactful paper about an experiment with cavity-mediated long-range interactions was published in 2016 [11]. The interactions between atoms are transferred via photon scattering. The scattered photons build standing waves inside the cavity. If the wavelength of the driving laser supplying the photons is chosen to be twice the wavelength of the lattice potential and shifted by a quarter of that wavelength, then the interactions build a dynamic quasi-potential, preferring every other site on the lattice and punishing the other half. A ground phase diagram with four stable phases was acquired.
Motivated by these developments in experimental physics, the interest in the theoretical study of the describing models increased even more. This is justified because only a few quantum models can be observed in experiments. As the underlying Hamiltonians operate in a Hilbert space which is too large, an analytical treatment is impossible. However statistical methods based on random-number-generation can be used. Although quasi-exact methods are available, it might still be appealing to work with non-exact, but faster, approximative approaches. This dissertation examines the Bose-Hubbard model with nearest-neighbour interactions as well as with long-range interactions with two of these numerical approaches belonging to the quantum Monte Carlo methods. A discrete-time world-line quantum Monte Carlo algorithm, which can sample the canonical ensemble with a fixed particle number and the grand-canonical ensemble with varying particle number, is used to investigate problems in one dimension. The variational quantum Monte Carlo, restricted to fixed particle numbers, works in one and two spatial dimensions.
The standard Bose-Hubbard model, the Bose-Hubbard model with nearest-neighbour interactions and the Bose-Hubbard model with long-range interactions are thoroughly analyzed with the two algorithms. The performance and exactness of both methods are compared to each other and to acknowledged references.

Overview

The main focus of this dissertation is the investigation of critical phenomena in various quantum models with different methods. These phenomena are introduced in chapter 2. Elaborating phase transitions and quantum phase transitions, the matter of phase separation is also addressed. The symmetries of the models are presented because every breaking of symmetry is associated with a phase transition. Qualitative differences between continuous and discontinuous phase transitions are explained. The order parameters, with which these transitions are investigated, are illustrated. The interlinks between the topics universality classes, critical exponents, scaling relations and finite-size scaling are explained.
The experimental background of the theoretical studies in this thesis is discussed in chapter 3. Ultracold atoms and their applications are introduced. A short overview of how atoms can be cooled down to the necessary temperatures is provided as well as a section about the creation and modification of optical lattices in which cold atoms can be confined. The management of the parameters is also elaborated. After these basics, possible experimental realizations of the models treated in this thesis are presented.
Chapter 4 deals with Bose-Hubbard models. The Hamiltonians considered in this work are introduced and the individual interaction terms are derived from the experimental properties. Limiting cases, and thereby the possible phases, are examined.
The rare Haldane insulator phase is presented in Chapter 5. This quantum phase is dealt with in a separate chapter due to its rarity and complexity. After an introduction to the origins of the Haldane phase in the antiferromagnetic spin chain the mapping to the Bose-Hubbard model is elaborated. The significance of the Haldane phase in bosonic systems is discussed. Appropriate order parameters are introduced and reference measurements from former publications are presented.
Two different quantum Monte Carlo methods were used within the scope of this thesis. Before explaining these methods in detail, Chapter 6 gives an introduction to quantum Monte Carlo methods in general. After a brief historical overview, the idea behind random-number based computations is explained. The process of random-number generation is presented, as well as possible sampling methods. Requirements and ground rules for a proper simulation are explained. Also, caveats and limitations are mentioned.
Chapter 7 presents the variational Monte Carlo method. After a short introduction of the variational idea and an overview of early approaches in this field, the correlated wave function formalism is introduced, as it is the basis of the method. Consequently, the Jastrow wave function is presented, with its main components, the Jastrow factor and the many-body term. The minimization algorithm and the calculation of the observables are explained. After elaborating on the limitations of the method, some implementation details are given. The second method, the discrete-time world-line quantum Monte Carlo algorithm is discussed in chapter 8. For this purpose, the quantum-classical mapping and the Suzuki-Trotter decomposition are executed. With these presets, the path-integral formalism can be treated, together with the density matrix description of the system. The effects of the long-range and nearest-neighbour interactions on the calculations are considered and an overview of how the observables are calculated is given.
The results section is split into multiple chapters in order to provide a better accessibility and to avoid confusion. The outcomes of simulations in one and two spatial dimensions are presented in separate chapters, Chap. 9 for 1D and Chap. 10 for 2D. The majority of the results presented in Chap. 10 have been published in [1]. These chapters present phase diagrams and finite-size scaling analysis of the phase transitions. The final chapter of the results section provides a detailed analysis and comparison between results of the three different models.
Chapter 11 concludes the thesis with a summary of the results and an outlook on possible future research on the topic.

Chapter 2

Critical phenomena

2.1 Phase transitions

Thermodynamic systems inhabit states which are called phases. The external variables which characterize the macroscopic state that the system occupies are called phase variables. The best-known example to understand the concept behind classical thermodynamic phases is water. Depending on the combination of the parameters temperature and pressure, water arranges in the form of a solid, a liquid or a gas. Variation of one of the external parameters (or both) can be utilized to "drive" the water from one state into another. Raising the temperature to a certain extent may cause a phase transition from the solid ice phase to the liquid phase. Such a change in the macroscopic appearance of a substance is called a *phase transition*. During a phase transition, the microscopic properties of the system change in such a way that the macroscopic behaviour of the system is significantly altered. A schematic phase diagram of water can be seen in Fig. 2.1. Changing the temperature T or the pressure p to a certain extent changes the state or aggregation, or in other words, drives the system through a transition to another phase.

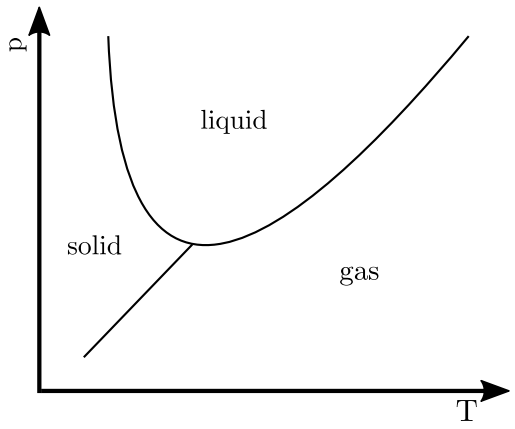

Figure 2.1: Schematic phase diagram of water depending on the temperature T and the pressure p. The phases are solid, liquid and gas. Direct transitions between all phases are possible. There is a tricritical point where all phases meet.

These drastic changes in the macroscopic behaviour of materials are caused by thermal fluctuations. Changing external parameters affects the degree of the fluctuations and new phases emerge as the system aims to minimize its energy and simultaneously to maximize its entropy. The properties that change during phase transitions are often associated with symmetries.
This can be easily seen in the example of water. The molecules in solid water are arranged to crystalline structures with a discrete translational and rotational symmetry. Hexagonal crystal systems are most common, but the explicit structure of ice varies with pressure and temperature. During the transition to the liquid state, the symmetries are broken. In liquid water, continuous translational and rotational degrees of freedom exist.

Ultimately, classical phase transitions are a result of the interplay between the attempt of a system to minimize its energy and to maximize the entropy of its thermal fluctuations. The thermal fluctuations are entirely cancelled out at zero temperature by definition. Consequently, a classical system does not exhibit entropy at $T = 0$.

2.2 Quantum phase transitions

Phase transition at zero temperature are ruled out by classical physics due to the lack of thermal fluctuations. Quantum mechanics, however, predicts quantum fluctuations associated with Heisenberg's uncertainty principle [18]. They become relevant in the ground state at $T = 0$, when thermal fluctuations are cancelled out. The characteristics of quantum phase transitions can also be observed at finite temperatures, near the quantum critical point [40]. Even at temperatures this low, thermal fluctuations of the energy scale $k_B T$ exist. These fluctuations compete with the quantum fluctuation of the energy scale $\hbar\omega$, where ω is the characteristic frequency of the quantum oscillation. The small segment of the parameter space in which quantum fluctuations dominate the system, with

$$\hbar\omega > k_B T\,, \tag{2.1}$$

is referred to as the quantum critical region.

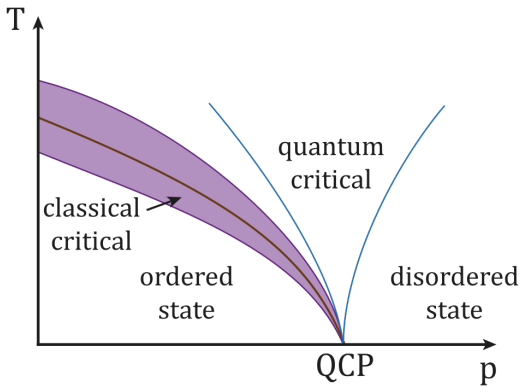

Figure 2.2: Diagram of temperature (T) and pressure (p) showing the quantum critical point (QCP) and quantum phase transitions.
Reprinted figure, taken from https://en.wikipedia.org/wiki/Quantum_phase_transition.

A phase diagram in the T-p-plane is shown in Fig. 2.2. A *quantum phase transition* describes a change in the ground state of a many-body system, which is caused by the quantum fluctuations. Such a transition can be induced by varying a physical parameter and thereby altering the quantum fluctuations. At a quantum critical point, the quantum fluctuations driving the transition become scale invariant and the quantum phase transition takes place [41]. This particular characteristic of quantum fluctuations will be useful in the investigation of quantum phase transitions, as the scaling behaviour can give insight into the quality of the transition.
One of the most important concepts in the examination of phase transitions are *order parameters* [15]. As the name suggest, the order parameter measures the "order" that is destroyed or established during a phase transition. Consequently, it is defined in a way that it equals zero in the disordered phase and is non-zero in the ordered phase. Finding an appropriate order parameter is essential to study a quantum phase transition. Often the choice of an order parameter is obvious, e.g. the total magnetization for a transition from a non-magnetic to a magnetic phase. Yet in some cases it proves cumbersome to find a suitable order parameter. Order parameters generally measure an internal symmetry of the system, as phase transitions are in most cases

associated with the breaking of a symmetry. Ref. [42] provides a thorough and wide introduction to quantum phase transitions.

2.3 Classification

Similar to classical phase transitions, quantum phase transtions can be classified as first or second order transitions. The distinction is based on the behaviour of the order parameter during the phase transition. If the order parameter changes instantaneously, the phase transition is a discontinuous or *first order phase transition*. The latter name originates from the discontinuity in the first order derivative of the thermodynamic free energy of the system.
If the change in order parameter happens smoothly, the phase transition is referred to as a continuous or *second order phase transition* [43]. Hereby the ordered phase is destroyed by transversal logarithmic fluctuations, which diverge with the system-size. In this case, the second order derivative of the free energy shows a discontinuity. This classification goes back to Ehrenfest and is also known as Ehrenfest-classification of phase transitions [44].
The transition point of a continuous phase transition is called the *critical point*. The behaviour of the order parameters in different second order phase transitions can vary. Second order phase transitions can therefore be classified according to their behaviour at the critical point. To do this, order parameters are described as functions of the distance to the critical point, powered with critical exponents. In classical systems, the temperature is usually the parameter which drives a system through a phase transition, when the Ehrenfest-classification is applied. The phase transition takes place at a critical temperature T_C [41]. Quantum phase transitions happen at $T = 0$. The system is therefore driven through the quantum phase transition by varying some other parameter p. In most cases, p is one of the defining parameters of the system given by the Hamiltonian or a ratio of such parameters. Section 4.5 presents the parameters of the models considered in this work. The dimensionless distance t_{rt}, which will be defined in Eq. 2.3, to the critical point p_c of the quantum phase transition can be seen as an analogy to the temperature in classical systems in the sense of Ehrenfest's classifications. It is sometimes called the "reduced temperature".

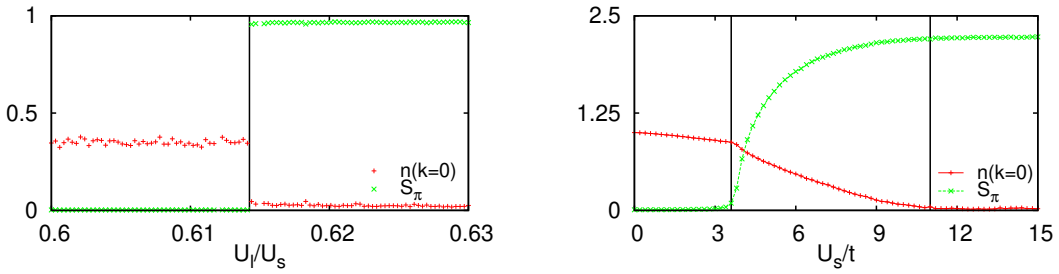

(a) (b)

Figure 2.3: Quantum phase transitions in an extended Bose-Hubbard model with long-range interactions. The Hamiltonian of this model is given in Eq. 4.37. The data was acquired with a variational Monte Carlo simulation with system size $L^2 = 196$. Fig. 2.3a shows a first order quantum phase transition for $\rho = 1$ and $U_s/t = 15$. The order parameters change instantaneously at the transition point. Fig. 2.3b shows the progression of order parameters during a second order phase transition at $\rho = 3/2$ and $U_l/U_s = 0.8$. These figures were also published in Ref. [1]. Reprinted with permission.

Examples for the behaviour of order parameters during quantum phase transitons are displayed in Fig. 2.3. The order parameters change instantaneously at the first order quantum phase transition shown in Fig. 2.3a. In contrast this, the same order parameters change continuously during the second order phase transtion in Fig. 2.3b.
There are, however, exceptions from the Ehrenfest-classification. Some quantum phase transitions cannot be assigned to the group of first or second order transitions. One of these exceptions, which will be important in the course of this work, is the Kosterlitz-Thouless transition [43]. This type of phase transition is also continuous, but does not follow the behaviour of the second order type. The fluctuations which destroy the ordered phase diverge exponentially in a *Kosterlitz-Thouless transition*. It is a phase transition of infinite order.

2.4 Critical exponents

The behaviour of systems near the critical point is the key to retrace the universality class of phase transitions. It is therefore necessary to take a closer look at the order parameter in this region. Starting in the disordered phase, the thermodynamic average of the order parameter is zero. However, it is subject to quantum fluctuations. As described in Sec. 2.2, the spatial correlations of the fluctuations in the order parameter become long-ranged near the critical point. Their typical length scale is denoted the *correlation length* ξ and diverges with the distance t_{rt} from the critical point as

$$\xi \propto |t_{rt}|^{-\nu} . \tag{2.2}$$

ν is the critical exponent associated with the correlation length. t_{rt} is a dimensionless measure of the distance from the critical point. It can be associated with whatever parameter p which is used to drive the system through the phase transition at the critical point p_c, and is usually defined in the form [45]

$$t_{rt} = \frac{|p - p_c|}{p_c} . \tag{2.3}$$

In the case of a Kosterlitz-Thouless transition [43], as mentioned above, the correlation length diverges exponentially

$$\xi \propto \exp\left(k \cdot t_{rt}^{-\frac{1}{2}}\right) , \tag{2.4}$$

where k is a constant.
Apart from the long-range spatial correlations, the order parameter is also subject to long-range correlations in time. The decay of the fluctuations is characterized by the *correlation (or equilibration) time* τ_c. The correlation time diverges as

$$\tau_c \propto \xi^z \propto |t_{rt}|^{-\nu z} \tag{2.5}$$

when approaching the critical point [42]. z is called the dynamic exponent. The correlation length ξ and the correlation time τ_c are the only characteristic length scales in space and time near the critical point.
The divergences in Eqs. 2.2 and 2.5 lead to infinite correlation length and correlation time at the phase transition point. The system is denoted *scale invariant* at this point and there are fluctuations throughout all length and time scales. In this crucial region, all observables depend via power laws on the external parameters [42]. The exponents defining these power laws characterize the critical behaviour of the system near the particular phase transition and are therefore called *critical exponents*.
The scaling of an observable m is generally dependent on two external parameters: the distance t_{rt} to the critical point, defined by the parameter p (Eq. 2.3) used to drive the system through the phase transition, and an external field O_f, conjugate to the specific order parameter. To offer a simple example, in a classical ferromagnet, an obvious order parameter would be the

Physical quantity	Exponent	Behaviour	Condition
Specific heat	α	$C \propto \lvert t_{rt}\rvert^{-\alpha}$	$t_{rt} \to 0$, $O_f = 0$
Order parameter	β	$m \propto \lvert t_{rt}\rvert^{\beta}$	$t_{rt} \to 0$, $O_f = 0$
Order parameter	δ	$m \propto O_f^{1/\delta}$	$t_{rt} = 0$, $O_f \to 0$
Susceptibility	γ	$\chi \propto \lvert t_{rt}\rvert^{-\gamma}$	$t_{rt} \to 0$, $O_f = 0$
Correlation length	ν	$\xi \propto \lvert t_{rt}\rvert^{-\nu}$	$t_{rt} \to 0$, $O_f = 0$
Correlation function	η	$G(r) \propto \lvert r\rvert^{-d+2-\eta}$	$t_{rt} = 0$, $O_f = 0$
Dynamics	z	$\tau_c \propto \xi^z$	$t_{rt} \to 0$, $O_f = 0$

Table 2.1: Critical exponents for the order parameter o and its conjugate field O_f.

magnetization with the conjugate field being a magnetic field B and the reduced temperature $t_{rt} = |T - T_c|/T_c$.
As the correlation length is the only relevant length scale at the critical point, physical properties should be invariant to rescaling all lengths in the system by a common factor and simultaneously adjusting the external parameter to conserve the initial value of the correlation length. Considering this, a homogeneity relation for the free energy density f can be derived with renormalization group theory [46, 47]:

$$f(t_{rt}, O_f) = b^{-d} f(t_{rt} b^{1/\nu}, O_f b^{d\delta/(1+\delta)}) \tag{2.6}$$

The scale factor b is a positve number, d denotes the dimension of the system. Based on this, homogeneity relations for further thermodynamic quantities can be derived by differentiating from the free energy density [42]. There are various critical exponents to describe the behaviour of the order parameter m and its correlations depending on the distance t_{rt} from the critical point and the conjugate external field O_f. Table 2.1 presents definitions of the common critical exponents.

2.5 Scaling relations

Critical exponents are not independent of each other, but connected through scaling relations. The fact that the exponents α, β, γ and δ are interlinked in some way is evident, as they can be all obtained from the free energy (Eq. 2.6). These thermodynamic exponents obey the scaling relations [48]

$$\alpha + 2\beta + \gamma = 2 \tag{2.7}$$

and

$$\alpha + \beta(1 + \delta) = 2\,. \tag{2.8}$$

The critical exponents associated with the correlation length and correlation function, ν and η, are linked with the thermodynamic exponents through the hyperscaling realtions:

$$\alpha = 2 - \nu d\,, \tag{2.9}$$

$$\gamma = \nu(2 - \eta)\,. \tag{2.10}$$

The first of the hyperscaling relations explicitly includes the dimensionality d of the system. The dynamic exponent z is independet of all other exponents. While the scaling relations described by Eq. 2.7 and Eq. 2.8 always apply, the hyperscaling relation from Eq. 2.9 can be violated when mean-field theories are considered, as the critical behaviour becomes independet of the dimension in that case.

Universality class	α	β	γ	δ	ν	η
Mean-field	0	1/2	1	3	1/2	0
2D Ising	0	1/8	7/4	15	1	1/4
3D Ising	0.11007(7)	0.32653(10)	1.2373(2)	4.7893(8)	0.63012(16)	0.03639(15)
3D XY	0.0146(8)	0.3485(2)	1.3177(5)	4.780(2)	0.67155(27)	0.0380(4)

Table 2.2: Critical exponents for various universality classes.

2.6 Universality classes

Different models often share a single scale invariant limit. Although their behaviour differs significantly at finite scales, it becomes increasingly similar in the vicinity of the critical point. This universality of phase transitions is an important concept in statistical physics and the theoretical description of critical phenomena. Models with the same scale behaviour during a phase transition are summarized as a universality class. The explanation for this interesting phenomenon lies in the fluctuations which occur during a phase transition [40]. At the critical point, these take place at all length scales, inducing correlation effects. These correlation effects on all length scales dominate the properties of the system, overriding the microscopic features of the individual model. The system averages over large spatial distances near the critical point. In other words, the correlations at large distances are independent of the details of the interactions on the scale of the lattice constant [41].
Second order phase transitions can thus be assigned to universality classes with regards to the critical exponents characterizing their behaviour at the critical point. The universality class of a phase transition is determined only by the spatial dimension of the system and the symmetries of the particular order parameter [15]. In theory, it is possible to determine the critical exponents and thereby gain insight into the critical behaviour of any system by studying a simpler system of the same dimension and symmetries. Tab. 2.2 shows the critical exponents for various universality classes. The universality class to which a phase transition belongs even depends on the density of the system. There is no comparable categorization for first order phase transitions.

2.7 Finite-size scaling

The direct measurement of critical exponents proves to be difficult for several reasons. One possibility would be to measure the thermodynamic quantities for different distances t_{rt} to the critical point and then fit the data. Only points within the critical region should be considered for this fit. However, it is difficult to estimate where the critical region ends and the imprecision in the exponents depends on what points are incorporated in the fit. Unfortunately, with the direct measurement method it is required to know the critical value of the parameter that is used to drive the system through the transition, which is not known in general. Furthermore, large system sizes and highly precise algorithms are necessary to obtain exact data.
To overcome the apparent issues and caveats of the direct measurement, the finite-size scaling method was developed [49–51]. It provides a way to extract the values of critical exponents by analyzing how measured quantities scale with the size L^d at which they are obtained. The finite size scaling even returns the critical value of the distance t_{rt} to the critical point, which is equivalent to the reduced temperature in a classical system.
To motivate the finite-size scaling method, it is necessary to anticipate the computational methods which will be used to simulate the models. Monte Carlo simulations are obviously limited to finite system sizes with L^d lattice sites. In these finite systems, the correlation length ξ is cut off as it reaches the size of the system. The fluctuations cannot diverge in the thermodynamic limit. This also holds for the other thermodynamic observables as well.
The derivation of the finite size scaling is now performed for an order parameter m, which can, for example, be a magnetization, as argued in Sec. 4.6.6. As mentioned, the critical value p_c of the driving parameter is not known in general. Consequently, t_{rt} should be eliminated from the representation of m. Using Tab. 2.1, it is possible to express the order parameter m in terms of the correlation length. Eliminating $|t_{rt}|$ from the equations for m and ξ leads to the relation

$$m \propto \xi^{-\beta/\nu} \tag{2.11}$$

close to the phase transition. If ξ is assumed to be the actual correlation length in an infinte system at distance t_{rt}, then it would be cut off if $\xi > L$ in the simulated system. m could therefore not diverge. However, if $\xi \ll L$ the value of m is the same as it would be in an infinite system. The true value of the order parameter m can thus be expressed through a function $m_0(x)$:

$$m = \xi^{-\beta/\nu} m_0(L/\xi)\,. \tag{2.12}$$

The function m_0 is in fact measured in the Monte Carlo simulations. With the correlation length cut-off, it is constant for $x \gg 1$ and obeys

$$m_0(x) \sim x^{-\beta/\nu} \tag{2.13}$$

for $x \to 0$. In order to eliminate the unknown correlation length from Eq. 2.12 a new function $\tilde{m}$ is introduced:

$$\tilde{m}(x) = x^{\beta} m_0(x^{\nu})\,. \tag{2.14}$$

Using this relation for m_0 and the identity $\xi \approx |t_{rt}|^{-\nu}$ allows to express Eq. 2.12 as

$$m = L^{-\beta/\nu} \tilde{m}(L^{1/\nu} t_{rt})\,, \tag{2.15}$$

if negative distances t_{rt} to the critical point are allowed. This equation defines the finite size behaviour of the order parameter m by giving information on how it varies close to the critical temperature with system size L. So far, the function $\tilde{m}$ is not specified. The definitions in Eq. 2.14 and Eq. 2.12 however give information about the behaviour at $x \to 0$:

$$\tilde{m} \to x^{\beta} (x^{\nu})^{-\beta/\nu} = \text{const}\,. \tag{2.16}$$

This shows that it is finite in the region of interest. The unknown function $\tilde{m}$ can be measured by performing Monte Carlo simulations. It is called the *scaling function*. The idea is to measure the order parameter $m_L(t_{rt})$ for different system sizes L^d and various distances t_{rt} to the critical point. Rearranging Eq. 2.15 to [51]

$$\tilde{m}(L^{1/\nu} t_{rt}) = L^{\beta/\nu} m_L(t_{rt}) \tag{2.17}$$

delivers an estimation for the scaling function for various combinations of L and $t_{rt} = (p - p_c)/p_c$. As the scaling function should be independent of the system length, the curves depending on the distance t_{rt} from the critical point should all coincide. However, a perfect data-collapse is only possible if the correct values for the exponents β, ν and the critical temperature p_c are used. If simulation data for different system sizes exists, the critical exponents can be "measured" by variation until the curves coincide. The finite size scaling can also be performed with other quantities, in order to obtain a full set of critical exponents.

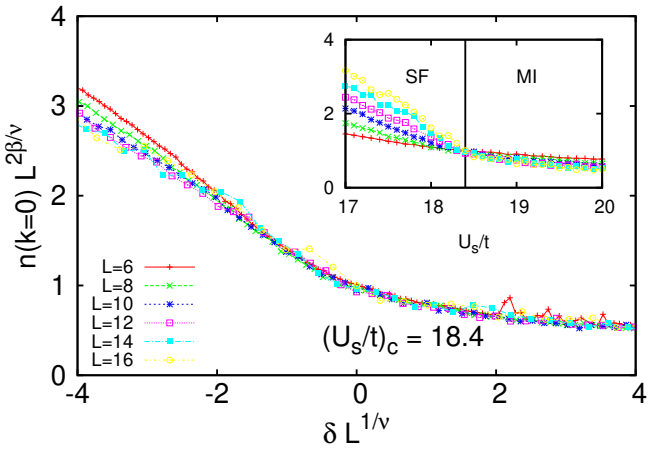

Figure 2.4: Finite-size scaling of the superfluid to Mott insulator transition in the standard Bose-Hubbard model in 2D at $\rho = 1$. This figure was also published in Ref. [1]. Reprinted with permission.

An example of finite-size scaling can be seen in Fig. 2.4. The model in this case was the standard Bose-Hubbard model in 2D at density $\rho = 1$ (Eq. 4.2). The inline picture shows the behaviour of the condensate fraction during the superfluid to Mott insulator transition for different system sizes. While it can be clearly seen that the consendsate fraction, and thereby the superfluidity, is continuously decreasing until it reaches zero, no sharp phase transition is present. The underlying reason for this are the finite system sizes. The main plot shows a data-collapse, obtained by rescaling the values for the individual system sizes as given by Eq. 2.17. The very good collapse of the data confirms the correct determination of the phase transition point and the choice of the correct universality class. The factor 2 in the exponent of the rescaling factor in the y-axis in Fig. 2.4 is necessary, as the order parameter $n(k)$ is the Fourier-transform of a two-dimensional order parameter.

Chapter 3

Ultracold atoms

Theoretical works have dealt with quantum critical phenomena for a long time now. In the last decades the technological progress has made them accessible to experimentalists, too. Performing controlled quantum phase transitions is however not only interesting as theoretical predictions can be contradicted or confirmed. Driving a system through such a transition basically creates a quantum variable, which is the foundation of an entirely new way of computation. The most commonly used and well-known example of experimental setups to simulate quantum systems are ultracold atoms in optical lattices [31].
Atoms cooled down to the realm of μK are called ultracold, as their temperature is fairly close to absolute zero. At these temperatures, almost all thermal fluctuations are frozen out. Quantum fluctuations, driven by the Heisenberg uncertainty principle [18], become relevant and prevail. The thermal de Broglie wavelength of ultracold atoms with mass m is given by $\lambda = \hbar/\sqrt{2mk_BT}$ [52], which is comparable to the inter-atomic distance. The atoms are therefore in the regime of quantum degeneracy. The microscopic quantum fluctuations can even change the macroscopic phase behaviour of the ground state of a many-body system. When the ratio between two competing energy contributions to the system is altered accross a certain measure, the critical value, the system will undergo a quantum phase transition.
Especially if the purpose of the setup is the use as a quantum simulator [26, 28], a very good control over all relevant system parameters is required. The number of degrees of freedom must ideally be reduced to the ones under investigation. To make quantum fluctuations in a system or single particles significant and properly observable, thermal fluctuations have to be eliminated to the greatest possible extent.
For several years now, ultracold atomic gases in optical lattices play a major role in condensed matter physics [53]. They allow the simulation and observation of real quantum systems in controllable environments and thereby give insight into concepts which were formerly only theoretically accessible. As mentioned in the introduction, the demand for a highly controllable many-body quantum system is closely associated with the newly spawned interest in understanding the connection between quantum information and many-body systems.
Formerly, quantum mechanical effects were mainly studied with only limited control over the properties. For example, adsorbing a ^{4}He-film to plane graphite would suppress disorder in the Helium, because of the periodic structure of the graphite on atomic length scales [54]. Starting in a fluid phase, the atoms would arrange according to the geometric properties of the graphite and adopt an insulating state. These setups were among the first realizations of the then recently introduced Bose-Hubbard model [55] and also subject to theoretical investigations [56]. However, the means of varying the characteristics of the experiments were restricted. The geometry of the graphite-lattice is predetermined and the density of the ^{4}He continuously variable.
In contrast to the earlier experiments, ultracold atoms in optical lattices offer versatile opportunities to change the relative strength of the competing energy terms of the system. After the original idea to use ultracold atomic gases in optical lattices for quantum computing [8], proposals followed on how to create the necessary entangled states [57]. Only a short time later, the first connections between entanglement and quantum phase transitions were discussed [58, 59]. In the very same year, for the first time, it was possible to experimentally induce and observe a quan-

tum phase transition in an atomic gas [5]. These developments ignited the desire to understand quantum phase transitions in real systems. Also, the use of realizable many body systems as a viable basis for quantum computing became seizable. The high controllability of the system is fundamental for these purposes. Fig. 3.1 is a reprint of the phase diagram presented in Ref. [11]. It shows that even rich phase diagrams can be depicted experimentally with sharp transitions between phases.

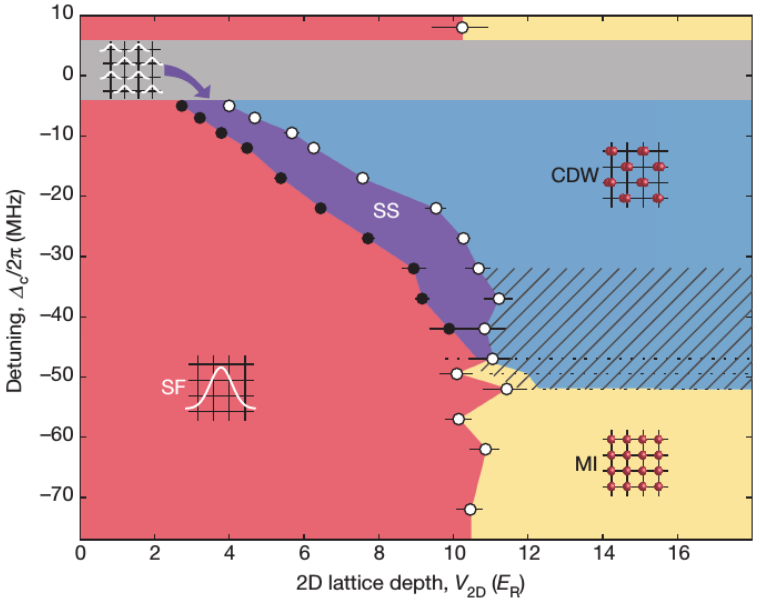

Figure 3.1: Reprint of an experimentally obtained phase diagram for a system with long-range interactions between bosons. It comprises four different stable phases, which are superfluid (SF), Mott insulator (MI), density wave (CDW) and supersolid (SS). Originally published in [11], reprinted with permission.

Consequently, the advances in the cooling, trapping and controlling atoms via optical lattices sparked interest among theoretical condensed matter physicists. More elaborate models, with better control over the parameters, could be experimentally realized. Hence this branch of physics plays now a major role in analyzing the role of strong correlations in real materials. In 2007, Lewenstein et al. published an extensive review on the then state of the art of ultra-cold atomic gases in optical lattices [53].

3.1 Cooling atoms

Modern laser cooling and trapping methods made ultracold atoms in optical lattices an attractive candidate for the construction of a highly tunable quantum emulator. By reaching the regime of very low temperatures, even down to a few nK, thermal fluctuations can virtually be suspended. Also, the trapping of particles on an atomic scale reached very high precision, thereby providing accurate management over the properties of the system. The efforts on this domain were awarded the Nobel Prize in 1997 [2–4]. A good early overview of the progress in controlling the motion of neutral atoms was published in 1988 [60].
The thermal motion of particles has always been a major obstacle in atomic physics. It usually limits the precision of atomic spectroscopy, as frequencies associated with transitions between atomic energy levels are shifted and spread by Doppler effects. Collision studies are affected similarly, as random thermal motion hinders a precise determination of the velocities. Most

importantly, the quantum effects that are the topic of this thesis only occur at very low temperatures, when the quantum nature of the particles becomes predominant.
The naive approach to cool down an atom would be to place it inside of a refrigerated box. This will ultimately fail, as at a temperature low enough, the atom would condense at the walls instead of just transferring thermal energy. The solution is to replace the box with an electromagnetic trap, where no condensation on walls is possible, and start the cooling process from there [60].
The cooling techniques used today rely on multiple physical effects to cool atoms as effectively as possible. Almost all of these depend on laser techniques. One way to achieve the deceleration of particles is Doppler cooling [61]. A moving atom hereby absorbs photons of a counter-propagating laser beam. It is slowed down by absorbing the momentum of the photons. To take advantage of the Doppler effect, the laser beam is chosen to be slightly off-resonant, so the absorption rate is highest for atoms moving rapidly towards the photon source. Atoms moving slowly or in the direction away from the laser beam absorb only a few photons. To achieve this, the laser frequency is tuned below the frequency for resonant absorption. Thus, on average, the kinetic energy of the atoms is reduced by the laser. This results in the atoms cooling down evenly.
The cooling works best with counter-propagating laser beams, to avoid an acceleration of the atoms into the direction opposed to the photon source. However, a single photon source is sufficient if the atoms are inside of an electromagnetic trap that restricts their movement [4].
Laser cooling as described above was first demonstrated on trapped ions. Because of their inherent charge, they can be trapped in deep potential wells. This allows for long interaction time with photons from the laser beam and therefore permits an effective cooling process.
The cooling of neutral atoms is more ambitious [2, 4]. Neutral traps are not deep enough to hold atoms with typical thermal energies. Consequently, neutral atoms have to be cooled down before they can be trapped. This is accomplished by colliding an atomic beam with a counter-propagating laser beam. The individual atoms collide with photons and absorb them. Each absorption reduces the velocity. The excited atoms radiate photons by stimulated and spontaneous emission. Every emission goes along with a velocity kick in the opposite direction of the emitted photon. If the atoms are driven into the excited states by a plane laser beam, the stimulated emission is aimed towards the incoming laser. These photons cancel out the momentum transferred by the absorbed ones. But not all photon-emissions are stimulated. The spontaneously emitted photons have no preferred direction. As they go off in a random direction, the momentum transfer by them is zero on average. Therefore the net momentum transfer of a process in which a photon is absorbed and spontaneously emitted is the momentum transfer of the absorption. Because this method of deceleration relies on spontaneous emission, it is limited by the rate of spontaneous emissions.
If the density of the atoms is high enough, the system can be cooled down further by evaporative cooling. This relies on elastic collisions between atoms of similar energy. Both involved atoms will scatter into different vibrational states. The hotter one will then escape the system and the other one will re-thermalize. This results in the remaining atoms being colder than before.

3.2 Optical lattices

The confinement of atoms utilizing electromagnetic fields, or trapping, is an important aspect of atomic physics. It allows for long observation times of atoms and a relatively precise determination of their location. As mentioned above, it is sometimes crucial for the cooling process. Furthermore, it is an important part of the examination of interactions between particles in many-body problems. Optical lattices are fundamental in mimicking condensed matter physics with quantum gases. Using periodic potentials of light to store ultracold quantum gases opened manifold possibilities of control and manipulation of the ensemble of atoms. This makes such a setup the perfect basis for a quantum simulator, as it constitutes a controllable quantum system that can be used to simulate the dynamical behaviour of another complex quantum system [25, 31]. In

particular, it is possible to simulate the Bose-Hubbard model [8], the main focus of this work. It incorporates a kinetic nearest-neighbour tunneling and a local repulsion potential between bosons on the same location.
A competent and comprehensive overview of ultracold quantum gases in optical lattices was given by Bloch [31] following the seminal experiment by Greiner et al [5].
Charged particles can be trapped with a magneto-optical trap. This method utilizes the magnetic charge of atoms to keep them in place. Neutral atoms are usually stored using optical dipole traps. The oscillating electric light field from a laser hereby induces an oscillating dipole moment in the atoms. At the same time, the electric field also interacts with the dipole moments $\mathbf{d}$ of the atoms. This creates a trapping potential for the atom [62]. The trapping potential $V_{dip}(\mathbf{r})$ at position $\mathbf{r}$ is characterized by the electric field amplitude $\mathbf{E}(\mathbf{r})$:

$$V_{dip}(\mathbf{r}) = -\mathbf{d} \cdot \mathbf{E}(\mathbf{r}) \propto \alpha(\omega_L)|\mathbf{E}(\mathbf{r})|^2 \tag{3.1}$$

The intensity of the laser light field $I(\mathbf{r})$ at location $\mathbf{r}$ is proportional to the squared absolute value of the electric field amplitude $I(\mathbf{r}) \propto |\mathbf{E}(\mathbf{r})|^2$. The polarizability of an atom depends on the frequency ω_L of the laser light and is denoted $\alpha(\omega_L)$. To avoid resonant excitation of the atoms, the laser light frequency ω_L is tuned to be far away from the atomic resonance frequency ω_a. This also avoids spontaneous emission and the resulting dipole potential is conservative.
Optical lattices are created via interferences of counter-propagating laser beams. The overlapping of the laser beams results in the creation of a periodic potential in the form of a standing wave with period $\lambda_L/2$. Atoms can be trapped in the potential depths and consequently inside this lattice. Using two laser beams leads to a single standing wave interference pattern. Although the individual potential depths are two-dimensional traps, the overall lattice can be considered to be one-dimensional, because movements from one trap in the array to another trap are confined to one dimension. Constructing a setup of three orthogonal standing waves results in a 3D array of potential depths, in which atoms are trapped. Each of these traps has the function of a tightly confining harmonic oscillator potential. The whole system with its geometry corresponds to a simple cubic crystal and is therefore well suited to investigate solid-state physics. Changing the angles between the standing waves results in a different lattice geometry. A large variety of lattice geometries can be realized this way. The depth of the potential can be tuned by altering the intensity of the laser, offering the possibility to drive the system through phase transitions by increasing or decreasing the laser intensity. This allows the investigation of the dynamics of phase transitions.
Each pair of counter-propagating laser beams results in a standing wave, which forms a periodic potential

$$V(x) = V_0 \sin^2(k_L x)\,. \tag{3.2}$$

The wave vector of the laser light is $k_L = 2\pi/\lambda_L$. The lattice potential depth V_0 is proportional to the intensity of the light. The natural energy scale for atoms with mass m in periodic light fields is the recoil energy $E_R = \hbar^2 k_L^2/2m$. A picture of multiple atoms arranged in an optical

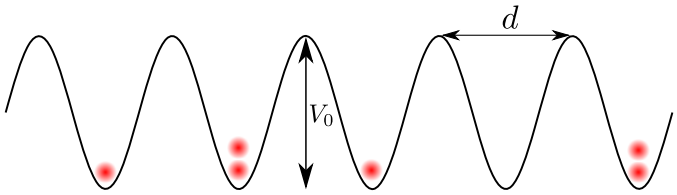

Figure 3.2: Scheme of atoms trapped in an optical potential. The distance d between minima and the lattice depth V_0 can be experimentally adjusted. Bosonic movement is increasingly supressed with growing V_0.

lattice can be seen in Fig. 3.2. In a 3D setup without anisotropy, the overall potential can be

written as:

$$V(\mathbf{r}) = V_0 \left(\sin^2(k_L x) + \sin^2(k_L y) + \sin^2(k_L z)\right) . \tag{3.3}$$

The dipole potential $V_{dip}(\mathbf{r})$ can be expressed in dependency of the local laser intensity $V(\mathbf{r})$ and the detuning $\Gamma = \omega_L - \omega_a$ of the laser frequency from the atomic resonance frequency [62]:

$$V_{dip}(\mathbf{r}) \sim \frac{V(\mathbf{r})}{\Gamma} . \tag{3.4}$$

The trapping force on the atoms can thus be written as

$$\mathbf{F}_{dip} = -\nabla V_{dip}(\mathbf{r}) . \tag{3.5}$$

Considering this, it is straightforward to see that the positioning of the atoms in the light field depends on the detuning Γ. If the laser light is tuned below the resonance frequency, the trapping force $\mathbf{F}_{dip}$ is overall positive and the atoms are pulled towards higher field intensity. In this case, they rest at the potential-maxima of the standing waves. Tuning ω_L below ω_a causes the atoms to rest in the potential depths.
Recent experiments succeeded in studying strongly correlated bosons on a dynamical lattice [63]. In contrast to setups with a static optical lattice to store the ultracold gas, a system with dynamical lattices include more degrees of freedom, resulting in the description of a more elaborate Hamiltonian.

3.3 Control of parameters

The most fascinating and attractive feature of the physics of ultracold atoms is the high controllability of the experiments. As pointed out above, quantum optics and atomic physics offer unique methods of quantum engineering. This section is not meant to be comprehensive but rather focusses on the tuning of parameters that are relevant for the models treated in this thesis. Numerous other techniques to modify the experimental setup exist.
The Bose-Hubbard models that are the subject of this work comprise nearest-neighbour tunneling, on-site repulsion, and off-site interactions up to infinite range.
The optical potentials introduced in Sec. 3.2 are an incredibly powerful tool. The composition of the laser beams that generate the light field allows to produce almost any lattice geometry. It is possible to change the dimensionality, and even periodic boundary conditions may be realized [64]. Also, the creation of superlattices as heat-baths is possible. This is helpful to emulate grand-canonical systems.
The tunneling rate t of particles between lattice-sites can be tuned by altering the intensity of the optical lattices. The tunneling rate is inverse proportional to the laser intensity. For large laser intensities, the atoms are tightly confined to their lattice sites. At low laser intensities, the potential wells are lower and the atoms are more likely to overcome them and change their location by tunneling. There is also the possibility of laser-assisted tunneling, where atoms are coherently stimulated to increase the probability of hopping.
The on-site interactions between atoms are initially restricted to s-wave collisions, assuming the temperature is low enough. The scattering length can be altered with a magnetic field, utilizing Feshbach resonances [65]. The scattering length a, and with it the inter-particle interaction U_s at the same site, can be changed close to a Feshbach resonance. With this, the relative position of two atoms on the same site can be altered with an external magnetic field B. The bound state of the upper potential is shifted relative to the dissociation energy of the lower potential. If the two levels of the atoms are in resonance at a magnetic field B_0, the scattering length a diverges. Around the Feshbach resonance, it follows the relation:

$$a = a_0 \left(1 - \frac{\Delta_B}{B - B_0}\right) . \tag{3.6}$$

The width of the resonance is described by Δ_B and the scattering length far from resonance is denoted with a_0. With $U_s \propto a$, attractive and repulsive inter-particle interactions can be realized close to the Feshbach resonance.
The main focus of this work is to study extended Bose-Hubbard models. In contrast to the standard Bose-Hubbard model, these enclose off-site interactions. An obvious approach to generate off-site interactions between particles would be to use magnetic instead of neutral atoms. The first experiments using atoms with dipolar interactions were performed in 2002 [66].

3.4 Experimental realizations

This section describes experimental techniques appropriate to treat the models presented in this thesis, based on the methods and setups introduced above. This includes driving the particles from a delocalized to a localized state as well as the implementation of off-site interactions between the atoms.

3.4.1 Superfluid to Mott insulator transition

The simplest model considered in this thesis is the ordered standard Bose-Hubbard model. It features tunneling of particles to nearest-neighbour lattice sites and on-site repulsion between lattice sites. The phase diagram of a lattice system of spinless bosons incorporating these parameters comprises two phases. In the Mott insulating phase, the particles are localized, while the superfluid phase consists of entirely delocalized bosons. Altering the ratio of the parameters results in a phase transition. This transition is illustrated in Fig. 3.3.

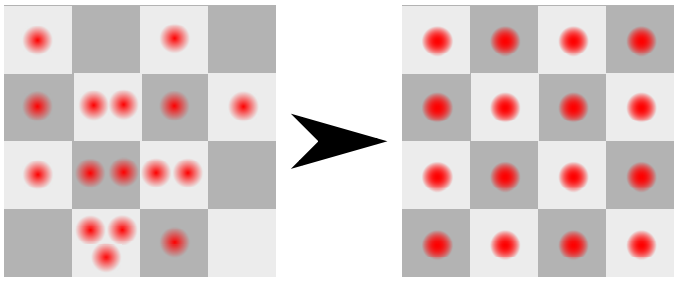

Figure 3.3: Transition from the superfluid to the Mott insulator state. Note that this is just a "snapshot" of the system, with the purpose to illustrate the highly fluctating particle number on each site in the superfluid phase.

Early considerations proposed liquid helium to investigate the transition from a superfluid to an insulator. As mentioned at the beginning of this chapter, Ref. [8] suggested the possibility of driving ultracold atoms through a quantum phase transition by applying an optical lattice.
In 2002, an experiment by Greiner et al. successfully realized this [5]. In the setup, ^{87}Rb atoms in the superfluid state are exposed to a three-dimensional lattice potential. The number of particles in this condensate is of order 10^5. The optical lattice is generated by lasers, as described in Sec. 3.2, and the atoms consequently feel a cubic potential seen in Eq. 3.3. Increasing the lattice potential will result in a decreasing tunneling rate t and an increasing on-site potential U_s. The system is driven through a quantum phase transition, when a critical ratio U_s/t is passed and long-range phase coherence is lost. The average number of particles per site in this experiment varies around $\bar{n}_i = 1$ to $\bar{n}_i = 3$, which makes it a good basis to investigate the Bose-Hubbard model at low densities.
The ^{87}Rb atoms are laser-cooled and confined to a magnetic trapping potential in advance to the actual experiment. Quantum fluctuations prevail, as thermal movement is canceled out beyond

measurable effects. The wavelength of the atoms is of the same order as the interatomic distance and there is long-range phase coherence in the many-body ground state. This condensate is then exposed to the optical lattice potential. In order not to lose phase coherence, the intensity of the lattice potential is gently increased. This way, the atoms will distribute over the sites of the optical lattice, without leaving their many-body ground state. In the beginning, when the lattice potential is low, all atoms are delocalized over lattice sites. The relative phases between different lattice sites are equal. The system is in the superfluid phase and remains in this regime as long as the atom-atom interactions are small compared to the tunnel coupling among lattice sites. Increasing the lattice potential depth V_0 leads to a shifted ratio of U_s/t, simultaneously increasing the atom-atom interactions and lowering the spatial hopping. The atoms in the system tend to localize. Reduced fluctuations in atom number on each site ultimately lead to increased fluctuations in the phase. When the critical ratio $(U_s/t)_c$ is passed, the phase coherence is completely lost and the atoms are entirely localized. The system is now in another quantum phase, the Mott insulator phase.
To test the phase coherence, the optical lattice is suddenly turned off. This allows the atomic wave functions to expand freely and interfere with each other. After a short expansion time ($t \approx 15ms$) interference patterns are measured by obtaining absorption images along two orthogonal directions. When the atoms are delocalized, in the superfluid phase, a high-contrast interference pattern is to be expected and was observed. The resulting picture is depicted in Fig. 3.4. Changing the lattice potential alters the interference pattern significantly. Initially,

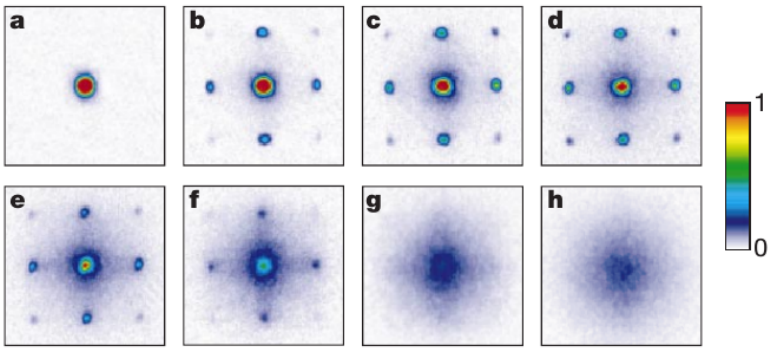

Figure 3.4: Experimentally obtained absorption images of matter wave interference patterns. The lattice depth V_0 was gradually increased from 0 in picture **a** to its maximal value in **h**. The patterns indicate a superfluid phase in **a** that successively looses coherence, until the Mott insulator state is reached in **h**, where the interference pattern has disappeared. Originally published in Ref. [5], reprinted with permission.

higher-order maxima become sharper when V_0 is increased. This can be explained by a tighter localization of the atomic wave functions to the lattice sites. However, increasing the depth results in an increasingly diffused pattern. Ultimately, no phase coherence is visible any more. The incoherent part of the atomic wave functions is predominant here, atoms are localized at individual lattice sites. Subsequent experiments confirmed these observations [67].
Measuring the phase coherence by taking absorption images is suited to observe global fluctuations and still presents a valuable tool. It is however even more intriguing to be able to measure individual quantum fluctuations. In a quantum system, the fluctuations and their underlying distribution characterize the properties of the system entirely. Therefore, measurements of the statistical ensemble might not reveal all information about the system.
A solution to this problem is the single-atom sensitive detection of atoms by fluorescence imaging. References [68] and [69] report the first successful applications of these experimental techniques in strongly correlated quantum systems. Fluorescence images with single-atom and single-site

resolutions were obtained, principally allowing to track all quantum fluctuations in the system. The phase transition described in this section is purely driven by the balance between the kinetic energy, or zero-point motion, of the particles and on-site collisional interactions. Exposing the system to off-site interactions between particles however is predicted to alter the quantum behaviour of the entire system, changing transitions between states and inducing more complex many-body quantum phases. Ref. [70] provides an extensive overview of the experimental realization of non-standard Hubbard models.
This work also treats systems with nearest-neighbour and long-range interactions. The following sections elaborate on possible experimental realizations of these interactions.

3.4.2 Nearest-neighbour interactions

The implementation of nearest-neighbour interactions between the particles has been realized recently with strongly magnetic atoms [10]. An ultracold gas of such atoms is confined to a three-dimensional optical lattice, much alike the experiment by Greiner et al [5]. However, the atoms used in this case are fully spin-polarized and comprise a magnetic moment. A polarizing magnetic field is applied to control the dipole orientation. Two dipoles oriented in parallel will repel each other, while anti-parallel placement will result in attraction. If the dipole-direction is orthogonal to the plane on which the atoms are confined to, long-range interactions between all the particles on the lattice will form. Usually, the interactions decay with spatial distance r between the dipoles. The intensity of the interactions can, however, be controlled by changing the orientation of the dipoles concerning the interaction-direction. This is drafted in Fig. 3.5. The

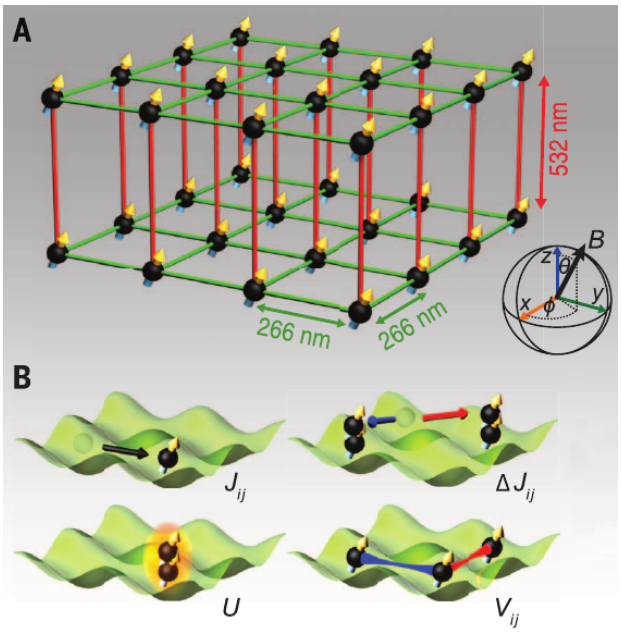

Figure 3.5: **A** Scheme of a lattice consisting of dipoles. The dipoles arrange according to the magnetic field B, their orientation is given by the polar angles θ and ϕ. **B** Visualization of the interaction terms in clockwise order: tunneling (J_{ij},ΔJ_{ij}), on-site repulsion (U) and nearest-neighbour repulsion (V_{ij}). Originally published in Ref. [10], reprinted with permission.

magnetic field is thereby utilized to change the angle between dipole orientation and the atomic plane. If tuned correctly, the long-range interactions can approximately be reduced to nearest-neighbour distance. Even next-nearest interactions have been established with this method [71]. The results presented in Ref. [10] are based on experiments with ^{168}Er atoms and exhibited

a shifted transition from a superfluid to Mott insulator phase, compared to the standard Bose-Hubbard model. However, it was proposed to employ Feshbach molecules of magnetic lanthanides in future experiments. Realizing strong nearest-neighbour interactions would be possible with these molecules, because of their very large dipole moments [72]. This should make it easier to realize the theoretically predicted density wave and supersolid phases.

3.4.3 Long-range interactions

Utilizing dipolar repulsion between particles to realize off-site interactions in the systems is appropriate if nearest-neighbour repulsion, next-nearest interactions or distance-decaying interactions shall be simulated. Additionally, changing the strength of dipolar interactions usually also alters the tunneling-strength and the on-site repulsion. If non-decaying long- and short-range interactions shall be realized in the same system and be tunable independently, more elaborate setups are necessary.
Based on Bragg spectroscopy [35] and advances realizing phase-transitions of ultracold atoms inside optical resonators [34, 39, 73, 74], it was proposed to use photons to transport interactions between particles [33, 36]. A comprehensive overview of cold atoms in cavity-generated optical potentials is given in Ref. [75]. Theoretical studies picked up the proposed interactions and predicted rich phase diagrams for the corresponding extended Bose-Hubbard models. Complex phases like density-wave, Bose-glass and supersolid were predicted [37, 38, 76].

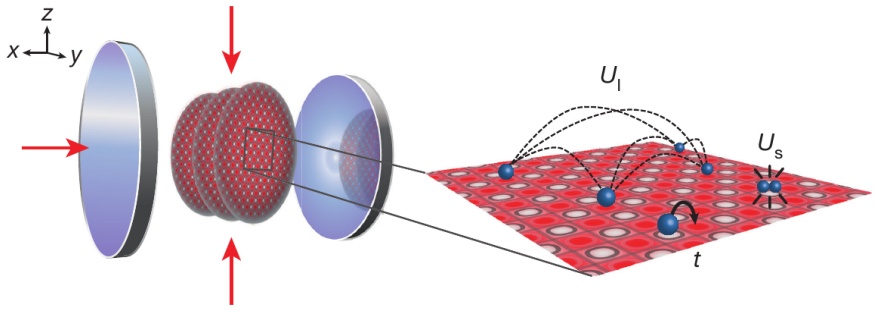

Figure 3.6: Scheme of an experiment that allows the realization of long-range interactions between bosons on a lattice. A stack of two-dimensional systems is placed inside of a cavity, which induces infinite range interactions between bosons. The energy scales are t (tunneling), U_s (on-site repulsion) and U_l (cavity-induced interactions). Originally published in Ref. [11], reprinted with permission.

The first successful experimental implementation of this proposal was presented in Ref. [11]. Like in the experiment by Greiner et al. described above, a condensate of ^{87}Rb atoms is exposed to a three-dimensional optical lattice. One lattice direction splits the system into a stack of weakly-coupled virtually two-dimensional layers. In each layer, the atoms arrange according to a square lattice. In contrast to the other experiments above, the setup is placed inside an optical cavity. For convenience, it shall be assumed that the atoms are confined to the x-y-plane and the cavity is placed along the x-axis. The optical lattice confining the atoms is then created by an intracavity standing wave in x-direction and two counter-propagating lasers in z-direction. Both are chosen in a way that a square lattice of periodicity $\lambda/2$ emerges. A schematic depiction of such a setup is shown in Fig. 3.6
Depending on the detuning $\Delta_c = \omega_z - \omega_c$ between the laser frequency ω_z and the cavity resonance frequency ω_c, photons from the standing lattice wave in z-direction will scatter off the atoms on the lattice and delocalize within the cavity mode. This way, standing waves of scattered photons emerge, creating a lattice of density-density correlations with periodicity λ.

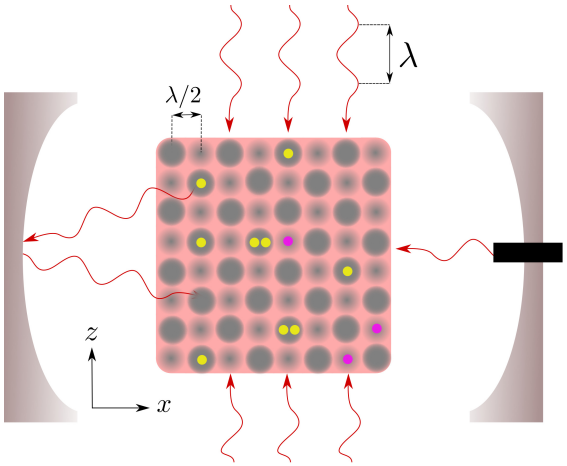

Figure 3.7: Portrayal of the photon scattering inside an optical cavity. Scattered photons lead to the formation of standing waves, whose strength depends on the filling of the original lattice. This figure was created by Clément De Daniloff.

These interactions between the atoms on the lattice, transported via the scattered photons, have infinite range and can be considered as an effective self-consistent potential with alternating strength on neighbouring lattice positions. Also, photons from the cavity mode are scattered into the z-direction, arranging a two-dimensional long-range interaction. The relative strength of these cavity-mediated interactions can be controlled by altering the detuning Δ_c. A bosonic lattice with tunneling, on-site repulsion and photon-induced interactions between bosons is shown in Fig. 3.7.
Ref. [11] provides a comprehensive phase diagram for the system with cavity-mediated long-range interactions, on-site repulsion, and boson-tunneling. It comprises the insulating Mott and density wave phases, as well as supersolid and superfluid regions. Bosons are localized in the Mott and density wave phases and delocalized in superfluid and supersolid phases. Density wave and supersolid states show imbalance between the average boson densities on even and odd sites, while Mott insulator and superfluid states do not.

Chapter 4

The Bose-Hubbard model

In an early attempt to describe the movement of electrons in crystalline solids, or energetically speaking in narrow conductive bands, the original Hubbard model was created [77]. A bosonic version was proposed various times, mainly motivated by the desire to characterize the behaviour of ^4He [78, 79]. The Bose-Hubbard model was finally introduced in 1989 [55]. In the standard version, it describes the physics of spinless bosons on a lattice at zero temperature $T = 0$. Bosonic movement is restricted to nearest-neighbour tunneling, particles occupying the same site interact repulsively. The phase diagram comprises superfluid and Mott insulator phases, showing a zero temperature phase transition between both phases. Since the phase transition is only driven by quantum fluctuations and not thermal fluctuations, it is a prime example of a quantum phase transition. Thereby the Bose-Hubbard model provides one of the simplest realizations of d-dimensional quantum phase transitions that cannot be mapped to a known $d + 1$-dimensional classical phase transition [41]. Consequently, the Bose-Hubbard model has been a research focus since its introduction. Motivated by the effort to construct quantum computers, it was pointed out that ultracold bosonic atoms in periodic optical lattices are perfectly theoretically described by the Bose-Hubbard model, making them an attractive realization of the theoretical model [8]. These particles serve as a quantum system ideal for comparing theoretical and experimental results. The phase transition from a superfluid to a Mott insulator in a gas of ultracold atoms in an optical lattice was experimentally observed for the first time in 2002 [5].
In recent years several non-standard Bose-Hubbard models were treated with ultracold quantum gases in optical lattices [70]. Of particular interest is the realization of the extended Bose-Hubbard models with dipolar ultracold magnetic atoms [10]. The respective Hamiltonian features repulsive interaction between bosons on neighbouring sites, aside from the hopping and on-site repulsion terms. To be entirely correct, these dipolar atoms exhibit two-body non-local repulsive interactions, typically decaying as $1/r^3$ with local distance r [80]. By reducing these originally long-range interactions to short-range nearest-neighbour repulsion the effects are changed quantitatively, but not qualitatively [81]. The presence of this additional interaction enriches the phase diagram of the Bose-Hubbard model by introducing new phases. The new density-wave phase is, as the Mott insulator phase, an insulator. However, induced by the nearest-neighbour repulsion, there exists a spatial modulation in a way that not all sites are occupied by the same number of particles, but the occupation number alternates between even and odd sites on the lattice. The supersolid (SS) phase also exhibits this charge-ordering effect, but also long-range phase coherence, and is therefore non-insulating. However, another rare insulating phase is stabilized by the r^{-3}-decaying long-range interactions, named the bosonic Haldane insulator (HI). This phase is also stable when the interactions are reduced to nearest-neighbour repulsion.
Moreover, an even more elaborate experimental setup allowed the introduction long-range interactions between bosons [11]. The energy exchange is realized by standing waves of scattered photons. Aside from being of virtually infinite range, these interactions do not decay with spatial distance.
In the course of this work the standard Bose-Hubbard model, the extended Bose-Hubbard model with nearest-neighbour interactions and the extended Bose-Hubbard model with cavity-induced long-range interactions are investigated. Simulations are performed in one and two dimensions,

in the canonical as well as in a grand-canonical ensemble. Disorder is not considered in any of the simulations.
The models describe bosonic particles on a lattice and arranging into various configurations. Lattice sites can either be empty or contain one or more particles. As mentioned in the introduction, these are quantum systems and consequently can be described by a wave function $\psi(\mathbf{r}, t)$ which satisfies the Schrödinger equation:

$$\imath\hbar\frac{\partial}{\partial t}\psi(\mathbf{r},t) = \left(-\frac{\hbar^2}{2m}\nabla^2 + V(\mathbf{r},t)\right)\psi(\mathbf{r},t), \tag{4.1}$$

This representation implies an important aspect of quantum theory. The system is not necessarily engaged in a specific configuration of particles on sites, but more generally in a linear superposition of various configurations. The probability of each configuration can be derived from the wave function.
The dimension of the Hilbert space of the system depends on the number of possible different configurations, or states, the system can arrange to.

4.1 Standard Bose-Hubbard model

The standard Bose-Hubbard Hamiltonian is defined as [55]

$$\hat{\mathcal{H}}_{BH} = -t\sum_{\langle \mathbf{r},\mathbf{r}'\rangle}\left(\hat{b}^\dagger_{\mathbf{r}}\hat{b}_{\mathbf{r}'} + \hat{b}^\dagger_{\mathbf{r}'}\hat{b}_{\mathbf{r}}\right) + \frac{U_s}{2}\sum_{\mathbf{r}}\hat{n}_{\mathbf{r}}(\hat{n}_{\mathbf{r}}-1) - \mu\sum_{\mathbf{r}}\hat{n}_{\mathbf{r}} \tag{4.2}$$

where $\langle ...\rangle$ indicates the summation over all nearest-neighbours pairs on the lattice. To avoid double countings, the order is irrelevant. The second-quantized operators $\hat{b}_{\mathbf{r}}$ and $\hat{b}^\dagger_{\mathbf{r}}$ annihilate or create a boson which is strongly localized at site $\mathbf{r}$, while

$$\hat{n}_{\mathbf{r}} = \hat{b}^\dagger_{\mathbf{r}}\hat{b}_{\mathbf{r}} \tag{4.3}$$

is the boson number operator for site $\mathbf{r}$. The creation and annihilation operators obey the following commutation relations [78]:

$$\left[\hat{b}_{\mathbf{r}}, \hat{b}^\dagger_{\mathbf{r}'}\right] = \delta_{r,r'} \text{ and } \left[\hat{b}^\dagger_{\mathbf{r}}, \hat{b}^\dagger_{\mathbf{r}'}\right] = \left[\hat{b}_{\mathbf{r}}, \hat{b}_{\mathbf{r}'}\right] = 0 \ , \forall \mathbf{r}, \mathbf{r}' \tag{4.4}$$

Multiple bosons are allowed to occupy the same site $\mathbf{r}$, making this a soft-core Bose-Hubbard model. The operators act on the eigenbasis of the single-site boson occupation number operator as

$$\begin{aligned}
\hat{b}_{\mathbf{r}}\,|\hat{n}_{\mathbf{r}}\rangle &= \sqrt{n_{\mathbf{r}}}\,|\hat{n}_{\mathbf{r}}-1\rangle \ , \\
\hat{b}^\dagger_{\mathbf{r}}\,|\hat{n}_{\mathbf{r}}\rangle &= \sqrt{n_{\mathbf{r}}+1}\,|\hat{n}_{\mathbf{r}}+1\rangle \ , \\
\hat{n}_{\mathbf{r}}\,|\hat{n}_{\mathbf{r}}\rangle &= n_{\mathbf{r}}\,|\hat{n}_{\mathbf{r}}\rangle \ ,
\end{aligned} \tag{4.5}$$

where $n_{\mathbf{r}}$ is always a non-negative integer. The kinetic energy contribution is proportional to the tunneling strength $t > 0$. $U_s > 0$ is the strength of the local on-site repulsive interaction. $\mu \in \mathbb{R}$ is the global chemical potential, a measure of the energy that can be absorbed or released due to a change of the particle number. Essentially it sets the total number of particles. This last term only appears when the grand-canonical ensemble is considered. The grand-canonical ensemble is the statistical ensemble in which neither the total energy nor the total particle number of the system are fixed. Possible states of the system may vary in these quantities. In the canonical ensemble the particle number is fixed, thus the term is absent as no energy can be gained or lost by adding or removing particles. The total energy however is not fixed in the canonical ensemble. Only the ordered Bose-Hubbard model is considered in this thesis, hence t, U_s and μ have the

same value on each site $\mathbf{r}$.
The first term in the Hamiltonian describes particle-hopping between nearest neighbouring sites. The hopping rate is given by $t/\hbar$. With positive tunneling strengths t, the overall negative term favours delocalization of the bosons. A visualization is seen in Fig. 4.1a. The second term describes the repulsive interactions between bosons on the same lattice site. Particles sitting on the same location increase the energy of the system by U_s. This is illustrated in 4.1b. The last term, tuned by μ, describes an offset in the energy of each individual site depending on the local number of bosons. This term, depicted in 4.1c, has a negative sign and therefore favours higher occupancy.

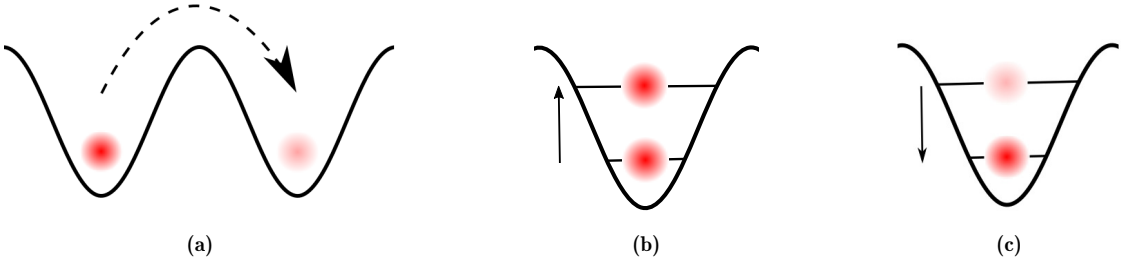

Figure 4.1: Interactions in the standard Bose-Hubbard model **(a)** nearest-neighbour tunneling, **(b)** on-site repulsion, **(c)** chemical potential

The competition between these terms results in a quantum phase-transition between superfluid and Mott insulator phase. A quantum phase transition occurs at zero temperature and is basically a change in the ground state of a system due to an alteration of the parameters of the Hamiltonian.

Derivation

A widespread overview on realizations of various models in the frame of ultracold atoms in optical lattices, including the derivation of the Hamiltonians by means of the experimental properties, is given in Ref. [70].
The Bose-Hubbard model can be derived directly from the experiments described in Chapter 3. The most efficient approach is to start with a single particle. As mentioned in Section 3.2, the optical lattices, in which the particles are placed, are basically arrays of traps. A particle in such a trap can be considered as a standard „particle in a box"-problem.
To start the derivation, a free particle in a periodic potential with lattice constant $\mathbf{l}$, such that $V(\mathbf{r}) = V(\mathbf{r}+\mathbf{l})$, shall be considered. The Hamiltonian can be expressed as

$$\hat{\mathcal{H}}_0(\mathbf{r}) = -\frac{\hbar^2}{2m}\nabla^2 + V(\mathbf{r})\,. \tag{4.6}$$

The potential $V(\mathbf{r})$ is the one introduced in Eq. 3.3. If the maximal values of $V(\mathbf{r})$ are low, the kinetic term dominates and the particle tends to delocalize over the lattice. In this case, the eigenstates of the system are Bloch states. This ansatz is chosen in analogy of the treatment of electrons in perfect crystals [82]. Bloch states are plain waves with wave-vector $\mathbf{k}$ in a periodic lattice with

$$e^{\imath\mathbf{k}(\mathbf{r}+\mathbf{l})} = e^{\imath\mathbf{k}\mathbf{r}}\,. \tag{4.7}$$

The amplitude of the waves is characterized by a function with the same periodicity:

$$u_{n,\mathbf{k}}(\mathbf{r}+\mathbf{l}) = u_{n,\mathbf{k}}(\mathbf{r})\,. \tag{4.8}$$

Thus the Bloch states for the possible energetic states n in $\mathbf{k}$-space are given by:

$$\Psi_{n,\mathbf{k}}(\mathbf{r}) = u_{n,\mathbf{k}}(\mathbf{r})e^{\imath\mathbf{k}\mathbf{r}}\,. \tag{4.9}$$

In the opposite limit, if the maximal values of $V(\mathbf{r})$ are large, the particles are strongly localized at the potential minima, i.e. the lattice sites. For a better description of this case, the more local Wannier functions are chosen as basis states. These construct a complete set of localized states from the lattice-periodic Bloch states, thereby describing the tight-binding limit. The Wannier functions for the energetic states n and lattice constant $\mathbf{l}$ can be expressed as [83]

$$\omega_{n,\mathbf{l}}(\mathbf{r}) = \mathcal{N} \sum_{\mathbf{k}} e^{-\imath \mathbf{k}\mathbf{l}} \Psi_{n,\mathbf{k}}(\mathbf{r}) = \mathcal{N} \sum_{\mathbf{k}} e^{\imath \mathbf{k}(\mathbf{r}-\mathbf{l})} u_{n,\mathbf{k}}(\mathbf{r}) \,, \tag{4.10}$$

where $\mathcal{N}$ is a normalization factor. These functions form a complete basis set of orthogonal states

$$\int d\mathbf{r} (\omega_{n,\mathbf{l}}(\mathbf{r}))^* \omega_{n',\mathbf{l}'}(\mathbf{r}) = \delta_{n,n'} \delta_{\mathbf{l},\mathbf{l}'} \tag{4.11}$$

and are localized around the potential minima as

$$\lim_{|\mathbf{r}-\mathbf{l}| \to \infty} \omega_{n,\mathbf{l}}(\mathbf{r}) = 0 \,. \tag{4.12}$$

Moving to second quantization representation and using that the Wannier functions form a complete basis, field operators $\hat{\Psi}^\dagger(\mathbf{r})$ and $\hat{\Psi}(\mathbf{r})$ can be introduced to create and annihilate bosons at position $\mathbf{r}$ in continuous space. The bosonic creation operator has the form

$$\hat{\Psi}^\dagger(\mathbf{r}) = \sum_{n,\mathbf{l}} \omega_{n,\mathbf{l}}(\mathbf{r})^* \hat{b}_{\mathbf{l}}^\dagger \tag{4.13}$$

and the corresponding annihilation operator can be expanded as

$$\hat{\Psi}(\mathbf{r}) = \sum_{n,\mathbf{l}} \omega_{n,\mathbf{l}}(\mathbf{r}) \hat{b}_{\mathbf{l}} \,. \tag{4.14}$$

With these field operators, and assuming two-body interactions between the bosons, the full many-body Hamiltonian can be rewritten in second quantization as:

$$\hat{\mathcal{H}} = \hat{\mathcal{H}}_{mb,0} + \hat{\mathcal{H}}_{mb,1} \tag{4.15}$$

$$\hat{\mathcal{H}}_{mb,0} = \int d\mathbf{r} \hat{\Psi}^\dagger(\mathbf{r}) \hat{\mathcal{H}}_0(\mathbf{r}) \hat{\Psi}(\mathbf{r}) \tag{4.16}$$

$$\hat{\mathcal{H}}_{mb,1} = \frac{1}{2} \int d\mathbf{r} \int d\mathbf{r}' \hat{\Psi}^\dagger(\mathbf{r}) \hat{\Psi}^\dagger(\mathbf{r}') v(\mathbf{r},\mathbf{r}') \hat{\Psi}(\mathbf{r}) \hat{\Psi}(\mathbf{r}') \,. \tag{4.17}$$

The interaction amplitude v between the two interacting particles at positions $\mathbf{r}$ and $\mathbf{r}'$ depends on the distance between them:

$$v(\mathbf{r},\mathbf{r}') = v(|\mathbf{r}-\mathbf{r}'|) \tag{4.18}$$

For simplification, only the lowest energy state $n = 0$ shall be considered and the potential minima as discrete lattice sites $\mathbf{l}_i \equiv i$. Considering this and inserting the operators from Eq. 4.13 and Eq. 4.14 into the Hamiltonian from Eq. 4.15 leads to an effective lattice Hamiltonian:

$$\hat{\mathcal{H}} = \sum_{i,j} t_{i,j} \hat{b}_i^\dagger \hat{b}_j + \frac{1}{2} \sum_{i,j,k,l} U_{i,j,k,l} \hat{b}_i^\dagger \hat{b}_j^\dagger \hat{b}_k \hat{b}_l \,. \tag{4.19}$$

The kinetic and interaction terms are simplified here. Written in explicit form, the kinetic term reads as

$$t_{i,j} = \int d\mathbf{r} (\omega_i(\mathbf{r}))^* \hat{H}_0(\mathbf{r}) \omega_j(\mathbf{r}) \tag{4.20}$$

with the interaction term

$$U_{i,j,k,l} = \int d\mathbf{r} d\mathbf{r}' \left(\omega_i(\mathbf{r})\omega_j(\mathbf{r}')\right)^* v(\mathbf{r},\mathbf{r}')\omega_k(\mathbf{r})\omega_l(\mathbf{r}')\,. \tag{4.21}$$

The effective lattice model with the Hamiltonian written in Eq. 4.19 can be used to derive the standard Bose-Hubbard model with only few assumptions. Presuming the Wannier functions (Eq. 4.10) are strongly localized, the kinetic term from Eq. 4.20 reduces to

$$t_{i,j} = \begin{cases} -\mu & \text{if } |i-j| = 0 \\ -t & \text{if } |i-j| = \mathbf{1} \\ 0 & \text{else.} \end{cases} \tag{4.22}$$

This means that there is only a contribution to the kinetic energy if the indices i and j denote either the same site or on nearest-neighbouring sites. If $i = j$, a particle exists at that site and contributes the chemical potential $-\mu$ to the entire system energy. If i and j denote nearest-neighbouring sites, a particles changes its position be hopping and contributes the kinetic energy $-t$.
Similarly, the localization of the atoms leads the integral in the interaction-term Eq. 4.21 to be only non-zero, contributing the contact interaction U, if the term describes particles on the same site:

$$U_{i,j,k,l} = \begin{cases} U_s & \text{if } i = j = k = l \\ 0 & \text{else.} \end{cases} \tag{4.23}$$

In summary, the assumption of particles strongly localized at the lattice sites leads to the Hamiltonian:

$$\hat{\mathcal{H}} = -t \sum_{\langle i,j \rangle} \left(\hat{b}_i^\dagger \hat{b}_j + \hat{b}_j^\dagger \hat{b}_i \right) + \frac{U_s}{2} \sum_i \hat{b}_i^\dagger \hat{b}_i^\dagger \hat{b}_i \hat{b}_i - \mu \sum_i \hat{b}_i^\dagger \hat{b}_i \,. \tag{4.24}$$

Applying the commutation relations from Eq. 4.4, using the particle-number operator from Eq. 4.3, and summarizing over the spatial positions $\mathbf{r}$ instead of lattice indices, the common representation of the Bose-Hubbard Hamiltonian can be achieved:

$$\hat{\mathcal{H}}_{BH} = -t \sum_{\langle \mathbf{r},\mathbf{r}' \rangle} \left(\hat{b}_\mathbf{r}^\dagger \hat{b}_{\mathbf{r}'} + \hat{b}_{\mathbf{r}'}^\dagger \hat{b}_\mathbf{r} \right) + \frac{U_s}{2} \sum_\mathbf{r} \hat{n}_\mathbf{r}(\hat{n}_\mathbf{r} - 1) - \mu \sum_\mathbf{r} \hat{n}_\mathbf{r} \tag{4.25}$$

4.2 Bose-Hubbard model with nearest-neighbour interactions

The Hamiltonian of the extended Bose-Hubbard model is given by [84]:

$$\hat{\mathcal{H}}_{NN} = -t \sum_{\langle \mathbf{r},\mathbf{r}' \rangle} \left(\hat{b}^\dagger_{\mathbf{r}} \hat{b}_{\mathbf{r}'} + \hat{b}^\dagger_{\mathbf{r}'} \hat{b}_{\mathbf{r}} \right) + \frac{U_s}{2} \sum_{\mathbf{r}} \hat{n}_{\mathbf{r}} (\hat{n}_{\mathbf{r}} - 1) - \mu \sum_{\mathbf{r}} \hat{n}_{\mathbf{r}} + U_{nn} \sum_{\langle \mathbf{r},\mathbf{r}' \rangle} \hat{n}_{\mathbf{r}} \hat{n}_{\mathbf{r}'}. \tag{4.26}$$

Aside from the nearest-neighbour interaction term, which is tuned by the parameter U_{nn}, it is identical to the Hamiltonian from the standard Bose-Hubbard model in Eq. 4.2. The nearest-neighbour interaction is depicted in Fig. 4.2.The sign indicates that the additional interaction between particles on direct neighbour sites is repulsive for positive U_{nn}. Consequently, there is a competition between two short-range repulsive terms and a kinetic term in this Hamiltonian. While the kinetic term favours movement of the particles and thereby delocalization, the interaction terms favour localization of the bosons. However, the contact-interaction promotes a uniform distribution of the particles, minimizing the average deviation of the number of particles per site from the density. The nearest-neighbour repulsion stimulates an imbalance in the occupation of adjacent sites, as it favours multiple particles on the same site over particles on neighbouring locations. Compared to the standard Bose-Hubbard model, this results in more complex phase behaviour and an expanded phase diagram. The phase diagram of the standard Bose-Hubbard model at zero temperature comprises a superfluid phase and a Mott insulating phase. Both these phases exhibit a uniform distribution of the particles over the lattice. The nearest-neighbour interaction in the extended Bose-Hubbard model, however, favours a spatial modulation in the average number of bosons per site. This leads to two additional phases, a supersolid phase with delocalized particles and a density-wave phase with localized particles. In the latter phase, the nearest-neighbour interaction is the dominant part of the Hamiltonian. The supersolid is a special case, as the tunneling term delocalizes the particles. The nearest-neighbour interaction affects the particles by altering the particle-wave, thereby introducing a spatial modulation in the occupation probability. These overall four phases form depending on the ratio of the three kinetic and interaction terms.

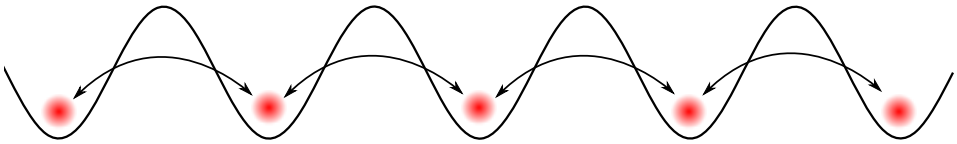

Figure 4.2: Nearest-neighbour interaction between bosons.

Derivation of the nearest-neighbour repulsion

As mentioned in Sec. 3.4.2, nearest-neighbour repulsions between bosons are usually realized with dipole-dipole interactions. Although these may have magnetic origin, experiements generally use electric dipole interactions. This shall be the basis of the derivation, which is generally analogue to the derivation executed in Sec. 4.1. The matter is discussed in greater detail in Ref. [70].
If a system of dipoles is considered, which all point in the same direction, the interactions consist of contact interactions U_c for particles on the same site, and dipole-dipole interactions U_{dd} between particles on different sites.

$$U(\mathbf{r} - \mathbf{r}') = U_c + U_{dd} = g\delta(\mathbf{r} - \mathbf{r}') + \frac{d^2}{4\pi\epsilon_0} \frac{1 - 3\cos^2\theta}{|\mathbf{r} - \mathbf{r}'|^3} \tag{4.27}$$

θ is the angle between the relative position vector $\mathbf{r} - \mathbf{r}'$ and the polarization direction of the dipoles. The amplitude of the contact interaction is g and d is the electric dipole moment. The lattice potential $V(\mathbf{r})$ introduced in Eq. 3.3 is still present. Similar to Sec. 4.1, the expansion of the field operators in the basis of Wannier functions is used. Only the lowest energy state (Bloch band) is considered. Taking the effective lattice Hamiltonian from Eq. 4.19 as a starting point again, the only difference to the derivation of the standard Bose-Hubbard model is the interaction term (compare Eq. 4.21):

$$\hat{\mathcal{H}} = \sum_{i,j} t_{i,j} \hat{b}_i^\dagger \hat{b}_j + \frac{1}{2} \sum_{i,j,k,l} U_{i,j,k,l} \hat{b}_i^\dagger \hat{b}_j^\dagger \hat{b}_k \hat{b}_l \,. \tag{4.28}$$

It is again assumed that the potential $V(\mathbf{r})$ induced by the optical lattice is large enough, so that the Wannier functions $\omega_i(\mathbf{r})$ are only significantly non-vanishing for $\mathbf{r} \approx \mathbf{l}_i$. Presuming this strong localization, the kinetic contribution takes the same form as seen in Eq. 4.22. The tunneling and chemical potential terms are identical to the former model and are not affected by the dipolar interactions.
The tensor elements U_{ijkl} in the basis of Wannier functions are again given by

$$U_{ijkl} = \int d\mathbf{r} d\mathbf{r}' (\omega_i(\mathbf{r}) \omega_j(\mathbf{r}'))^* U(\mathbf{r} - \mathbf{r}') \omega_k(\mathbf{r}) \omega_l(\mathbf{r}') \tag{4.29}$$

Because of the localization of the particles close to the lattice centers, this integral has only significantly non-zero contributions for $i = k$ and $j = l$.
The on-site interaction consists of two contributions, as seen in Eq. 4.27. A contact-interaction with the amplitude g and a dipolar interaction. The latter comes into play if the particles are on the same lattice site, but still have a distance between them smaller than the lattice spacing. Considering this spatial distribution at the lattice site, the term

$$U_{iiii} = \int d\mathbf{r}_1 d\mathbf{r}_2 n(\mathbf{r}_1) U(\mathbf{l}_1 - \mathbf{l}_2) n(\mathbf{r}_2) \tag{4.30}$$

with $n(\mathbf{r}) = |\omega(\mathbf{r})|^2$ is best solved via Fourier transformation:

$$U_d = U_{iiii} = \frac{1}{(2\pi)^3} \int d\mathbf{k} \tilde{U}_d(\mathbf{k}) \tilde{n}^2(\mathbf{k}) \,. \tag{4.31}$$

Together with the contact-interaction, the full on-site interaction U_s is given by

$$U_s = g \int d\mathbf{r} |\omega(\mathbf{r})|^4 + \frac{1}{(2\pi)^3} \int d\mathbf{k} \tilde{U}_d(\mathbf{k}) \tilde{n}^2(\mathbf{k}) \,. \tag{4.32}$$

With Eq. 4.28 and the commutation relations from Eq. 4.4, the on-site interaction term has the same form as in the standard Bose-Hubbard model. However, in this case U_s also depends on the dipolar interaction:

$$\hat{\mathcal{H}}_{\text{on-site}} = \frac{U_s}{2} \sum_{\mathbf{r}} \hat{n}_{\mathbf{r}} (\hat{n}_{\mathbf{r}} - 1) \tag{4.33}$$

Moving on to the off-site interactions, the case $i = k \neq j = l$ has to be considered. The contact interaction obviously vanishes. The dipolar potential $U_{dd}(\mathbf{r}_1 - \mathbf{r}_2)$ can be approximated by the constant values for fixed distances $U_{dd}(\mathbf{l}_i - \mathbf{l}_j)$. This simplifies the integration to:

$$U_{ijij} \approx U_{dd}(\mathbf{l}_i - \mathbf{l}_j) \int d\mathbf{r}_1 |\omega_i(\mathbf{r}_1)|^2 \int d\mathbf{r}_2 |\omega_j(\mathbf{r}_2)|^2 \,. \tag{4.34}$$

Inserting into Eq. 4.28 and using the number operator leads to the off-site interaction part of the Hamiltonian:

$$\hat{\mathcal{H}}_{\text{off-site}} = \frac{1}{2} \sum_{i \neq j} \frac{U_{nn}}{|i - j|^3} \hat{n}_i \hat{n}_j \tag{4.35}$$

with $U_{nn} = U_{ijij}$ and the sum running over all sites of the lattice. Assuming the strength of the dipolar interactions drops rapidly with spatial distance, the summation can be reduced to nearest-neighbouring pairs only. Combining all the terms, the Hamiltonian of the Bose-Hubbard model with nearest-neighbour interactions (Eq. 4.26) is obtained:

$$\begin{aligned}\hat{\mathcal{H}}_{NN} = &- t \sum_{\langle \mathbf{r},\mathbf{r'} \rangle} \left(\hat{b}^{\dagger}_{\mathbf{r}} \hat{b}_{\mathbf{r'}} + \hat{b}^{\dagger}_{\mathbf{r'}} \hat{b}_{\mathbf{r}} \right) + \frac{U_s}{2} \sum_{\mathbf{r}} \hat{n}_{\mathbf{r}} (\hat{n}_{\mathbf{r}} - 1) - \mu \sum_{\mathbf{r}} \hat{n}_{\mathbf{r}} \\ &+ U_{nn} \sum_{\langle \mathbf{r},\mathbf{r'} \rangle} \hat{n}_{\mathbf{r}} \hat{n}_{\mathbf{r'}}. \end{aligned} \tag{4.36}$$

4.3 Bose-Hubbard model with long-range interactions

Section 3.4.3 described how modern experimental techniques allow the realization of global-range interactions between particles in bosonic lattice systems by photon scattering. An impactful experiment realized this and introduced the corresponding Hamiltonian [11]:

$$\begin{aligned}\hat{\mathcal{H}}_{LR} = &- t \sum_{\langle \mathbf{r},\mathbf{r}' \rangle} \left(\hat{b}^\dagger_{\mathbf{r}} \hat{b}_{\mathbf{r}'} + \hat{b}^\dagger_{\mathbf{r}'} \hat{b}_{\mathbf{r}} \right) + \frac{U_s}{2} \sum_{\mathbf{r}} \hat{n}_{\mathbf{r}} (\hat{n}_{\mathbf{r}} - 1) - \mu \sum_{\mathbf{r}} \hat{n}_{\mathbf{r}} \\ &- \frac{U_l}{L^d} \left(\sum_{\mathbf{r} \in e} \hat{n}_{\mathbf{r}} - \sum_{\mathbf{r} \in o} \hat{n}_{\mathbf{r}} \right)^2 . \end{aligned} \tag{4.37}$$

The summation indices $\mathbf{r} \in e$, $\mathbf{r} \in o$ extend over even and odd lattice-sites respectively. The lattice-sites are numbered by simply summing the coordinates in the spatial directions. This way, every "even" site is surrounded by "odd" sites and vice versa. The strength of the off-site interactions is scaled by U_l. Drawing a comparison to the former case, the short-range interactions stimulate the formation of local imbalances, ultimately resulting in the development of a global pattern of imbalance. The long-range interactions, however, promote imbalance on a global scale, because all particles on the lattice interact with each other and the strength of this interaction does not depend on their distance [1]. This is illustrated in Fig. 4.3. It should be noted that the interactions described by the last term in Eq. 4.37 are not depending on spatial distance. This is in contrast to most other long-range interactions, for example the dipolar interaction introduced in Eq. 4.27. In fact, these are global-range interactions for any system size.
As the long-range interaction term clearly favours the occupation of even lattice sites, it also promotes the spatial modulated supersolid and density-wave phases. However, depending on the parameter configuration, the phase diagram also comprises Mott insulator (on-site repulsion dominant) and superfluid (hopping term dominant) phases.
The description above relates to the case of commensurate ratios of the cavity and external lattice wavelengths. Only this case is treated in this thesis. Incommensurate ratios lead to a different phase behaviour [85].

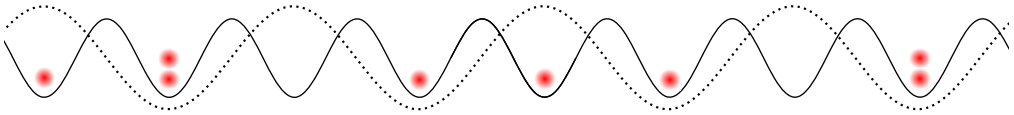

Figure 4.3: Long-range interaction between bosons according to the last term in Eq. 4.37. The dotted line visualizes the interactions in form of a potential. The depth of the energetic reward on the even sites and the penalty on odd sites depends on the total number of bosons on even and odd lattice sites respectively.

Derivation of the cavity-induced interactions

The Hamiltonian with long-range interactions presented in Eq. 4.37 can be derived directly from the experimental properties, similar to the derivations in Sec. 4.1 and 4.2. It was introduced for the first time in Ref. [86] and [11]. In this publication the first experimental realization of the cavity-induced interactions was reported. Yet the long-range interaction term was already mentioned in theoretical publications before [34, 38].
Similar to the derivation of the standard and nearest-neighbour Hamiltonians, it is best to start the description with a single-particle Hamiltonian $\hat{\mathcal{H}}_{sp}$. For convenience, only the x-z-plane is considered. The optical lattice confines the atoms, and interactions between them, to this plane. The single particle Hamiltonian is given by

$$\hat{\mathcal{H}}_{sp} = \hat{\mathcal{H}}_0 + V_{trap}(x,z) + \hbar\eta(\hat{a}^\dagger + \hat{a}) \cos(kx) \cos(kz) - \hbar(\Delta_c - U_0 \cos^2(kx)) \hat{a}^\dagger \hat{a} \,. \tag{4.38}$$

The kinetic energy of the free particle and the lattice-potential (see Eq. 3.3) are merged in $\hat{\mathcal{H}}_0$, as introduced in Eq. 4.6. Reduced to the x-z-plane, it reads:

$$\hat{\mathcal{H}}_0 = \frac{\hat{p}_x^2}{2m} + \frac{\hat{p}_z^2}{2m} + V_{2D}(\cos^2(kx) + \cos^2(kz)) \,. \tag{4.39}$$

As it does not affect the derivation, $V_{trap}(x,z)$ does not need to be specified, it is the potential which confines the atoms to the x-z-plane.
The third term represents a checkerboard lattice that the atoms feel. It is caused by photons which are scattered into the cavity mode at a two-photon Rabi frequency η. The operators $\hat{a}^\dagger$ and $\hat{a}$ create and annihilate photons in the cavity mode. In the course of this derivation, it becomes clear that the occupation of the cavity field mode is determined self-consistently by the atomic distribution and motion in the lattice. Basically, it represents infinite-range interactions between the atoms.
The last term in Eq. 4.38 is the cavity field in the rotating frame with $\Delta_c = \omega_z - \omega_c$. U_0 represents the maximum light shift per atom. This is limited by the dispersive shift of the cavity resonance frequency.
The many-body description is accomplished as seen in Sec. 4.1, by using the bosonic field operators:

$$\hat{\mathcal{H}}^{MB} = \int d\mathbf{r} \hat{\Psi}^\dagger(\mathbf{r}) \left(\hat{\mathcal{H}}_{sp} + g\hat{\Psi}^\dagger(\mathbf{r})\hat{\Psi}(\mathbf{r}) - \mu \right) \hat{\Psi}(\mathbf{r}) \,. \tag{4.40}$$

Using the bosonic field operators introduced in Eq. 4.13 and Eq. 4.14 and considering what is known from Sec. 4.1, the Hamiltonian can be rewritten:

$$\begin{aligned} \hat{\mathcal{H}}_{LR} = & -t \sum_{\langle \mathbf{r},\mathbf{r}' \rangle} \left(\hat{b}_\mathbf{r}^\dagger \hat{b}_{\mathbf{r}'} + \hat{b}_{\mathbf{r}'}^\dagger \hat{b}_\mathbf{r} \right) + \frac{U_s}{2} \sum_\mathbf{r} \hat{n}_\mathbf{r}(\hat{n}_\mathbf{r} - 1) - \mu \sum_\mathbf{r} \hat{n}_\mathbf{r} \\ & + \hbar\eta M_0 (\hat{a}^\dagger + \hat{a}) \left(\sum_{\mathbf{r}\in e} \hat{n}_\mathbf{r} - \sum_{\mathbf{r}\in o} \hat{n}_\mathbf{r} \right) \\ & - \hbar(\Delta_c - \delta)\hat{a}^\dagger \hat{a} \,. \end{aligned} \tag{4.41}$$

The tunneling amplitude t, chemical potential μ, and contact interaction U_s are known from Eqs. 4.20- 4.23. Altough the self-consistent cavity lattice should affect the tunneling along the x-direction, this effect is small enough to be neglected. The dispersive shift δ of the cavity is described by

$$\delta = U_0 M_1 N \,, \tag{4.42}$$

where N is the total number of atoms in the lattice. M_0 and M_1 are overlap integrals over Wannier functions on the x-z-plane:

$$M_0 = \int d\mathbf{r} \omega_i^*(\mathbf{r}) \cos(kx) \cos(kz) \omega_i(\mathbf{r}) \tag{4.43}$$

$$M_1 = \int d\mathbf{r} \omega_i^*(\mathbf{r}) \cos^2(kx) \omega_i(\mathbf{r}) \,. \tag{4.44}$$

The creation and annihilation operators of the cavity field are directly proportional to the two-photon Rabi frequency η and the imbalance of the number of atoms on the even and odd lattice sites. Both operators are inversely proportional to the cavity decay rate κ, the dispersive shift δ and the detuning of the cavity mode [86]. Altogether, the annihilation operator is defined as

$$\hat{a} = \frac{\eta M_0}{\Delta_c - \delta + \imath\kappa} \left(\sum_{\mathbf{r}\in e} \hat{n}_\mathbf{r} - \sum_{\mathbf{r}\in o} \hat{n}_\mathbf{r} \right) \,. \tag{4.45}$$

Inserting the photonic annihilation and creation operators given by Eq. 4.45 into Eq. 4.41 leads to the Hamiltonian with cavity-induced long-range interactions 4.37:

$$\begin{aligned}\hat{\mathcal{H}}_{LR} = &- t \sum_{\langle \mathbf{r},\mathbf{r}' \rangle} \left(\hat{b}^\dagger_{\mathbf{r}} \hat{b}_{\mathbf{r}'} + \hat{b}^\dagger_{\mathbf{r}'} \hat{b}_{\mathbf{r}} \right) + \frac{U_s}{2} \sum_{\mathbf{r}} \hat{n}_{\mathbf{r}} (\hat{n}_{\mathbf{r}} - 1) - \mu \sum_{\mathbf{r}} \hat{n}_{\mathbf{r}} \\ &- \frac{U_l}{L^d} \left(\sum_{\mathbf{r} \in e} \hat{n}_{\mathbf{r}} - \sum_{\mathbf{r} \in o} \hat{n}_{\mathbf{r}} \right)^2 . \end{aligned} \tag{4.46}$$

The interaction strength U_l is directly proportional to the strength of the lattice and inversely proportional to the cavity detuning:

$$U_l = -K\hbar |\eta M_0|^2 \frac{\Delta_c - \delta}{(\Delta_c - \delta)^2 + \kappa^2} \propto \frac{V_{2D}}{\Delta_c} . \tag{4.47}$$

This allows for a high controlability of the long-range interaction in experimental realizations.

4.4 Bose-Hubbard model with long-range and nearest-neighbour interactions

It is also interesting to consider a system with nearest-neighbour interactions and cavity-mediated long-range interactions between the particles. The Hamiltonian of such a model is given by:

$$\begin{aligned}\hat{\mathcal{H}}_{\mathrm{BOTH}} = &- t \sum_{\langle \mathbf{r},\mathbf{r}' \rangle} \left(\hat{b}^\dagger_{\mathbf{r}} \hat{b}_{\mathbf{r}'} + \hat{b}^\dagger_{\mathbf{r}'} \hat{b}_{\mathbf{r}} \right) + \frac{U_s}{2} \sum_{\mathbf{r}} \hat{n}_{\mathbf{r}} (\hat{n}_{\mathbf{r}} - 1) - \mu \sum_{\mathbf{r}} \hat{n}_{\mathbf{r}} \\ &+ U_{nn} \sum_{\langle \mathbf{r},\mathbf{r}' \rangle} \hat{n}_{\mathbf{r}} \hat{n}_{\mathbf{r}'} - \frac{U_l}{L^d} \left(\sum_{\mathbf{r} \in e} \hat{n}_{\mathbf{r}} - \sum_{\mathbf{r} \in o} \hat{n}_{\mathbf{r}} \right)^2 . \end{aligned} \tag{4.48}$$

There has been no experimental realization of such a system up to now. It should however be possible by using dipolar particles inside a cavity. The magnetic field which controls the orientation of the dipoles is not affected by the photonic cavity-field and vice versa. At first glance, the potential gain of knowledge does not appear to be too great. Both interactions promote a spatial modulation of the average occupancy of bosons per site. However, the topology of the local nearest-neighbour interactions and the cavity-mediated global range interactions is different. Fluctuations for example are much more likely to appear with nearest-neighbour interactions. A boson changing position only affects its direct neighbourhood with nearest-neighbour interactions, while such a move affects all other bosons with the long-range interactions. Therefore it might be interesting to look into this combined Hamiltonian.

4.5 Parameters

This section gives a summary of the interactions in the Hamiltonian and the parameters controlling their strength.
The hopping term tuned by t represents the kinetic energy in the system. It originates from the quantum fluctuations of the particles, as thermal fluctuations are ruled out. The quantum fluctuations happen in the form of boson tunneling to nearest-neighbouring sites. The term favours the delocalization of the particles.
The on-site interaction is a repulsive interaction between particles on the same lattice site of the strength U_s. It represents contact interaction (scattering) for neutral atoms. In the case of dipolar atoms, it also represents the dipolar repulsion between the particles. Multiple particles on the same lattice site are energetically punished. This is an extremely local interaction, which favours localization of the particles and an even distribution of the particles over the lattice sites.
The chemical potential μ controls the particle number of a system in the grand-canonical ensemble. It lowers or increases the energy of the system if a particle is added or removed. This term does not influence the localization or delocalization of particles. If systems in the canonical ensemble are regarded and the particle number is conserved, the chemical potential is reduced to a simple constant shift in the energy. It is therefore set to zero in the Hamiltonian. The chemical potential can, however, be evaluated from the ground-state energy E_0, using the relation

$$\mu(N_b) = E_0(N_b + 1) - E_0(N_b) \tag{4.49}$$

with the number of bosons N_b in the system. This is helpful to create grand-canonical phase diagrams from simulations with fixed particle number and to calculate quantities depending on μ.
The nearest-neighbour interaction term represents an interaction between particles located on neighbouring lattice sites. The interaction only applies to bosons between sites which are direct neighbours and the strength is given by U_{nn}. This interaction term competes with the on-site repulsion. While the latter favours localized particles evenly distributed over the lattice, the nearest-neighbour interaction favours a spatial modulation in the occupation of lattice sites. When it is the dominant term, the energy is minimized if sites with zero occupation alternate with occupied sites.
The long-range interaction, tuned by the parameter U_l, is a global-range term. In the other energetic contributions above, a single fluctuation of a particle only affects the energetic properties of the direct vicinity of the involved lattice sites. In a model including the cavity-mediated long-range interactions however, a single move of a boson has an energetic effect on all particles in the system. This term also favours localization. Like the nearest-neighbour interaction, a spatial imbalance between even and odd sites is energetically preferable.

4.6 Phases

The competition and interplay of the various energetic contributions described above results in the development of different quantum phases. Depending on the Hamiltonian parameters, the system arranges in different ground states. This section describes the physical aspects of the quantum phases. The order parameters used to define the phases are treated in Sec. 4.7.
Phase diagrams which incorporate the phases presented in this section are shown in Chap. 9 for one-dimensional systems and in Chap. 10 for two-dimensional systems.

4.6.1 Mott insulator

Considering the standard Bose-Hubbard model in the atomic limit is the simplest approach to understand the Mott insulator phase [87]. The atomic limit is the limit of zero tunneling, i.e.

$t/U_s = 0$. In this case, interactions between the particles dominate the Hamiltonian, while fluctuations in the atom number are energetically punished. Consequently, the ground state of the system consists of localized individual atomic wave functions with a fixed integer number of atoms per site, minimizing the interaction energy. The many-body ground state of the Mott insulating phase cannot be described by a macroscopic wave function, but as a product of local Fock states for each lattice site. There is no phase coherence in this state, but correlations in the atom number between lattice sites prevail.
Neglecting the hopping term, the remaining Hamiltonian is diagonal and the occupancy number basis $\{|n_1, ..., n_{L^d}\rangle\}$ is a basis of eigenvectors for a system with L^d lattice sites. All associated eigenvalues are positive. Using the bosonic density $\rho = N/L^d$, the ground state of the many-body system in the zero tunneling limit is given by

$$|\Psi_{\mathbf{MI}}\rangle_{t=0} = \prod_{\mathbf{r}} \frac{1}{\sqrt{\rho!}} (\hat{b}_{\mathbf{r}}^{\dagger})^{\rho} |0\rangle \propto \prod_{\mathbf{r}} |n_{\mathbf{r}}\rangle \ . \tag{4.50}$$

Thus the ground state is a tensor product of on-site Fock states $|n_{\mathbf{r}}\rangle$, defined as eigenstates of the on-site boson number operator $\hat{n}_{\mathbf{r}}$ (see Eq. 4.3) with the on-site integer occupation numbers $n_{\mathbf{r}}$ as its eigenvalues. The variance of this on-site occupation number, defined as

$$\sigma_{\mathbf{r}} = \langle (\hat{n}_{\mathbf{r}} - \langle \hat{n}_{\mathbf{r}} \rangle)^2 \rangle^{1/2} , \tag{4.51}$$

vanishes in the $t = 0$-limit. This however only holds if the ground state is given by Eq. 4.50. However, the Mott insulator state exists also for $t \neq 0$ and has a more complicated ground state in general. Quantum correlated particle-hole pairs emerge already at small tunneling rates t. This leads to correlated number-fluctuation in the systems and thereby non-vanishing on-site fluctuations $\sigma_{\mathbf{r}} > 0$, altough the system is still in the Mott insulating regime. Hence a vanishing on-site fluctuation is not a suitable defining property of the Mott insulator phase.
To find an appropriate characteristic to define the Mott-insulating state, it is necessary to consider the interplay between the chemical potential μ and the occupation number $n_{\mathbf{r}}$. The Bose-Hubbard Hamiltonian can be written as the sum of local on-site terms $\hat{\mathcal{H}}_{\mathbf{r}}$ in the atomic limit ($t/U_s = 0$):

$$\hat{\mathcal{H}}_{BH} \approx \sum_{\mathbf{r}} \hat{\mathcal{H}}_{\mathbf{r}} = \sum_{\mathbf{r}} \left[\frac{U_s}{2} \hat{n}_{\mathbf{r}} (\hat{n}_{\mathbf{r}} - 1) - \mu \hat{n}_{\mathbf{r}} \right] , \tag{4.52}$$

where the state of the system is defined by the relation of chemical potential and on-site interaction. As mentioned above in Eq. 4.50, the eigentstates of the system in this limit are products of Fock-states $|n_{\mathbf{r}}\rangle$ with a well defined occupation number $n_{\mathbf{i}}$. Defining the on-site eigenenergy $E(\mathbf{r})$ by

$$\hat{\mathcal{H}}_{\mathbf{r}} |n_{\mathbf{r}}\rangle = E(\mathbf{r}) |n_{\mathbf{r}}\rangle \ , \tag{4.53}$$

Eq. 4.52 and Eq. 4.50 give the relation

$$E(n_{\mathbf{r}}) = \frac{U_s}{2} n_{\mathbf{r}} (n_{\mathbf{r}} - 1) - \mu n_{\mathbf{r}} \, , \tag{4.54}$$

with the total eigenenery $E = \sum_{\mathbf{r}} E(n_{\mathbf{r}})$. In order to reach the ground state, the energy E has to be minimized. For a given chemical potential μ, the energy is minimzed by

$$n_{\mathbf{r}} = \lceil \mu/U_s \rceil \tag{4.55}$$

where $\lceil \ \rceil$ denotes the ceiling. Thus the groundstate occupation number depends on the chemical potential in the form of a staircase function. $n_{\mathbf{r}}$ increases by one at integer values of μ/U_s and stays constant otherwise. For non-integer values of μ/U_s, the system is incompressible:

$$\frac{\partial \langle \hat{n}_{\mathbf{r}} \rangle}{\partial \mu} = 0 \tag{4.56}$$

The incompressibility is the defining property of the Mott insulator phase.
Consequently, the Mott insulator exists in general only at integer filling, where the particles can distribute to average non-zero integer on-site occupation $\langle n_{\mathbf{r}} \rangle$. Additional particles in the system cannot be described by localized atomic wave functions. Due to degeneracy, they would move freely over the Mott insulating background and form a condensate state [55]. As all bosons in the system are indistinguishable, the whole system becomes superfluid. The same effect comes into play if particles are removed from the Mott insulating state, resulting in a condensate of holes. Deviations from integer filling immediately cause a superfluid state. Fig. 4.4 shows the configuration of a two-dimensional system in the Mott insulator phase.

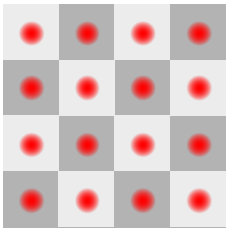

Figure 4.4: Visualization of the Mott insulator phase in a two-dimensional model at density $\rho = 1$. The bosons are higly localized and evenly distributed. Note that a real quantum system is always subject to fluctations.

The removal or addition of every single particle from or to a Mott insulator state goes along with a finite change in energy. This energy gap is non-zero for all combinations of t/U_s and μ inside of a Mott lobe and vanishes at the boundaries of the lobes [88]. Within a particular lobe, the ground state has always the same total number of atoms, independent of μ. The Mott state is incompressible (Eq. 4.56), as the average number of bosons per site $\langle n_{\mathbf{r}} \rangle$ is also independent of μ. This originates in the translational invariance of the system. The incompressibility is, therefore, a consequence of the finite excitation gap of the Mott insulator phase. The excitation gap for adding or removing a particle is given by the width of the Mott lobe in t/U_s-direction for a given parameter configuration μ, t, U_s [55].
Excited states at constant particle number correspond to the formation of particle-hole pairs in the lattice. The excitation gap, in this case, is given by the width of the Mott lobe in μ-direction [89].
The properties discussed in this section also hold for the extended Bose-Hubbard models if the off-site interactions are small compared to the on-site repulsion.

4.6.2 Superfluid

The standard Bose-Hubbard model is also considered to illustrate the superfluid phase. Neglecting the interparticle interactions results in a Hamiltonian dominated by the tunneling term. The ground state energy is minimized if the N particles in the systems are completely delocalized over the L^d lattice sites. In other words, the single-particle wave functions are distributed over the entire lattice. All atoms occupy the same Bloch state with the lowest energy $\mathbf{k} = 0$. The ground state in the limit U_s/J is given by

$$|\Psi_{\mathbf{SF}}\rangle_{U_s=0} = \frac{1}{\sqrt{N!}} \left(\sum_{\mathbf{r}} \frac{1}{\sqrt{L^d}} \hat{b}_{\mathbf{r}}^{\dagger} \right)^N |0\rangle \ . \tag{4.57}$$

The probability to observe a certain on-site occupation number $n_{\mathbf{r}}$ for a single site $\mathbf{r}$ follows a Poisson distribution. This results in large on-site number fluctuations $\sigma_{\mathbf{r}}^2 = \langle \hat{n}_{\mathbf{r}} \rangle$. In contrast to the Mott insulator state, the superfluid phase is not limited to integer fillings.

The superfluid ground state written in Eq. 4.57 becomes indistinguishable from a coherent state in the thermodynamic limit, for sufficiently large N and L^d, at fixed density $\rho = N/L^d$ [32]:

$$\exp\left(\sqrt{N}\,\hat{b}^\dagger_{\mathbf{k}=0}\right)|0\rangle = \prod_{\mathbf{r}}\left(\exp\left(\sqrt{\rho}\,\hat{b}^\dagger_{\mathbf{r}}\right)|0\rangle_{\mathbf{r}}\right) \propto \prod_{\mathbf{r}}|\alpha_{\mathbf{r}}\rangle\ . \tag{4.58}$$

$|\alpha_{\mathbf{r}}\rangle$ denotes an on-site coherent state with complex eigenvalue $\alpha_{\mathbf{r}}$. The occurrence of phase coherence distinguishes the superfluid state from insulating states.
The superfluid state is a compressible phase, in contrast to the Mott insulator. This means that Eq. 4.56 does not hold for the superfluid phase. A visualization of the superfluid phase is provided in Fig. 4.5.

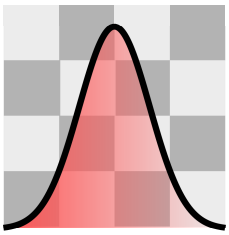

Figure 4.5: Sketch of the distribution of particles in the superfluid phase. The particles are completely delocalized and can be described by a single, coherent wave function.

Simplified, this means that every atom wants to be at all lattice sites with equal amplitude, in order to achieve energy minimization. This leads to off-diagonal long-range order, which is also clear from Eq. 4.58. This long-range order is defined as the infinite-distance limit of the single-particle density matrix $G^{(1)}(\mathbf{r},\mathbf{r}')$ [32]:

$$\lim_{|\mathbf{r}-\mathbf{r}'|\to\infty} G^{(1)}(\mathbf{r},\mathbf{r}') = \lim_{|\mathbf{r}-\mathbf{r}'|\to\infty}\langle\hat{b}^\dagger_{\mathbf{r}}\hat{b}_{\mathbf{r}'}\rangle \neq 0\,. \tag{4.59}$$

In experiments, $G^{(1)}(\mathbf{r},\mathbf{r}')$ is observable with time-of-flight imaging (Sec. 3.4.1), making it a valuable tool to detect the superfluid-Mott-insulator transition for large systems [5, 55].
The superfluid phase however does not only occurr in the $U_s = 0$-limit, but also for finite on-site interactions. The inter-atomic repulsion reduces the number-fluctuations $\sigma^2_{\mathbf{r}}$. Consequently, the ground state is more complicated than specified in Eq. 4.57 for the no-interaction limit. Instead of checking the system for long-range phase correlations with the limit defined in Eq. 4.59, it is preferable to look for an algebraic decay of $G^{(1)}(\mathbf{r},\mathbf{r}')$. This can be interpreted as quasi long-range order and holds especially for smaller systems and lower dimensional models.
The superfluid phase is gapless, unlike the Mott insulator phase [5].

4.6.3 Density wave

The standard Bose-Hubbard model only comprises the Mott insulator and the superfluid phase at $T = 0$. Extending the model to off-site interactions gives rise to additional phases. The density wave phase is an insulating phase with localized particles. The spatial arrangement of the bosons on the lattice is however different from the Mott insulator phase. In a perfectly unperturbed Mott insulating state, all lattice sites are occupied with the same integer number of bosons. Thus a system can only form a Mott insulator at integer fillings, e.g. at boson densities $\rho = 1, 2, 3, \ldots$ [90].
The density wave phase shows a modulation in the occupation between alternating sites. All even sites are, on average, occupied with the same integer number of bosons and odd sites are occupied with a different integer number of bosons. As a result, the density wave phase does not

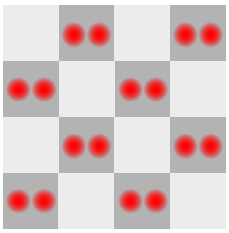

Figure 4.6: Boson configuration of a system with density $\rho = 1$ in the density wave phase.

only form at integer but also half-integer densities $\rho = 0.5, 1, 1.5, 2 \ldots$. An example of a system with $\rho = 1$ in the density wave phase is given in Fig. 4.6.
Concerning the models discussed in this thesis, the density wave phase is induced by the off-site interactions in the extended Bose-Hubbard models. If the nearest-neighbour interactions (Eq. 4.26) or the cavity-mediated long-range interactions (Eq. 4.37) dominate the respective Hamiltonians, the system tries to minimize the energy by taking on the density wave state.
Although both interactions promote the same phase, their effect is fundamentally different. To explain this, the atomic limit ($t = 0$) is considered once again. The on-site interaction is assumed to be low in comparison to the respective off-site interactions ($U_s \ll U_{nn}, U_l$).
The nearest-neighbour repulsion tuned by U_{nn} is a local interaction between bosons on direct neighbour sites. In other words, a boson at position $\mathbf{r}$ suppresses the occupation of the nearest-neighbour sites. At dilute fillings, the spatial distance r between individual bosons is insignificant, as long as $r > 1$, due to on-site and nearest-neighbour interactions. At integer or half-integer fillings, the ground state corresponds to a structure where sites occupied by 2ρ bosons alternate with empty lattice sites. Technically, the ground state is two-fold degenerate at finite system sites, because there is no preference if the even or odd sites are either the occupied or the empty sites. Finite systems become however translationally invariant if periodic boundary conditions are considered, overriding the degeneracy.
The behaviour of the system with long-range interactions is similar. At integer or half-integer densities $\rho = 0.5, 1, 1.5, 2 \ldots$, the ground state has the same form as in the model with nearest-neighbour interactions. However, the cavity-mediated interactions are of infinite range. All bosons interact with each other, in a way that bosons on even lattice sites energetically favour other bosons on even lattice sites and punish bosons on odd sites, and vice versa. This leads to restricted fluctuations, compared to the short-ranged nearest-neighbour interactions. It also affects the matter of dilute fillings. There are also multiple configurations with identic ground state energy, but the condition for these is that all bosons are either on even or odd lattice sites.
If the on-site interactions U_s are of the same magnitude as the off-site interactions, phases with a more complex structure may form at half-integer densities greater than $\rho = 1$. The occupation structure where sites with zero bosons alternate with sites occupied by 2ρ bosons can be unfavourable because the energy-punishment induced by the on-site repulsion might be too high. Instead, depending on the ratio U_s/U_l, the occupancy of neighbouring sites will alternate between two distinct, integer fractions of ρ. For example, at $\rho = 2.5$, there are three possible density wave phases, depending on the ratio of the terms in the Hamiltonian:

....5050505050...
....4141414141...
....3232323232...

Density wave phases with different shapes can usually be identified with the common order parameters (see Chap. 2). Fig 4.7 shows the two possible shapes of the density wave phase at $\rho = 3/2$.
Note that the limit $U_s = 0$ at $t = 0$ would not result in a single stable state, but in a superposition

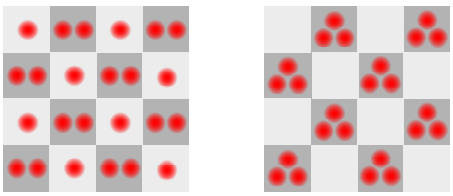

Figure 4.7: Possible density wave configurations of a system with desnity $\rho = 3/2$.

of numerous energetically equivalent states, as there is no punishment if the bosons accumulate at the same site or at multiple sites. It should be mentioned that the sets of these states are different for the model with nearest-neighbour interactions and the model with long-range interactions. The only constraint for the former is that bosons do not occupy nearest-neighbour sites, while all bosons will arrange on even sites or all on odd sites to minimize the energy in the system with cavity-mediated interactions.
Defining properties of the density wave phase are vanishing phase coherence correlations, incompressibility (Eq. 4.56) and non-vanishing density-density fluctuations. To identify the spatial modulation of the density wave phase, the structure factor can be used. As an alternative, it is possible to just consider the imbalance in the occupation between even and odd lattice sites. This allows to distinguish between density wave and Mott insulator phases and also between different shapes of the density wave.
The interplay between $t \neq 0$ and the on- and off-site interactions may also affect the shape of the density wave phase.

4.6.4 Supersolid

The supersolid phase is a phase with non-vanishing phase coherence correlations and a non-zero structure factor. The particle-wave functions in this phase extend over the entire system, but the probability of presence alternates between nearest-neighbouring sites. Thus the supersolid state shows characteristics of both superfluid and density wave phases. It does not appear in the phase diagram of the standard Bose-Hubbard model, as it results from the interplay between particle tunneling and the off-site interactions between bosons. While the particles are largely delocalized, their interactions among each other result in a spatially modulated particle-wave amplitude [91]. The amplitude is, however, non-zero for all lattice sites. This is illustrated in Fig. 4.8.

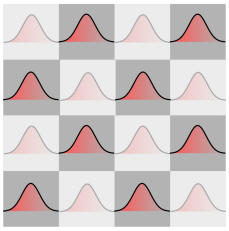

Figure 4.8: Draft of the supersolid phase in a 2D system. The particles are delocalized, but the occupancy probabilities on even and odd lattice sites differ.

The phase diagram of the Bose-Hubbard model with nearest-neighbour interactions (Eq. 4.26) and the model with long-range interactions (Eq. 4.37) both comprise the supersolid state. It is a compressible phase, such that Eq. 4.56 does not hold. The supersolid phase does not necessarily require integer or half-integer fillings. However, it does not exist at arbitrary densities for all dimensions [92].
The supersolid phase shows simultaneous diagonal and off-diagonal long-range order. Conse-

quently, two order parameters are necessary to identify this state. A parameter to check the phase coherence, e.g. Eq. 4.59, and a parameter to monitor the imbalance between the occupancy of even and odd lattice sites, e.g the structure factor.

4.6.5 Phase separation

This thesis is concerned only with ground state properties of the models discussed above. Given the rather complex density wave and supersolid phases, it has to be ensured that the true ground state is always reached.
The density wave phase at high densities for example is susceptible to the formation of metastable states. The competition between long-range attractive forces, caused by the cavity-mediated interactions, and strong on-site repulsion might destabilize the system in some parameter regions. An analysis of the total energy of the system at different states is a way to determine the ground state in uncertain parameter areas.
However, even if the system is prepared in its ground state, there is still the possibility that it is not in a stable phase, even if the order parameters might suggest it. This condition is called phase separation. A stability check is required to distinguish the supersolid phase from a phase separation [93]. The supersolid phase is especially frail to this, as it exhibits diagonal and off-diagonal long-range order. So far, no stable supersolid phase was found in one-dimensional extended Bose-Hubbard models at $\rho = 0.5$. In this case, there exists a phase separation however [92, 94, 95].
To test the stability of a phase at a certain density, the particle number can be varied in order to compute the chemical potential as described in Eq. 4.49. The density can then be evaluated as a function of the chemical potential. An area is unstable if the density ρ shrinks for growing μ.

4.6.6 Symmetry-breaking and phase transitions

Two symmetries are important for the investigation of transitions between the phases presented in this section, the continous $U(1)$ phase symmetry and the discrete $\mathbb{Z}_2$ translation symmetry. Neglecting fluctuations and thereby assuming phases in perfect ground state, the Mott insulator and density wave phases are invariant under $U(1)$ phase transitions, while the Mott insulator and superfluid phases are symmetric with regard to discrete $\mathbb{Z}_2$ translations.
A global $U(1)$ transformation would shift the entire system by a continous phase ϕ:

$$\hat{b}_{\mathbf{r}} \to \hat{b}_{\mathbf{r}} e^{\imath\phi} \, , \, \hat{b}^{\dagger}_{\mathbf{r}} \to \hat{b}^{\dagger}_{\mathbf{r}} e^{-\imath\phi} \tag{4.60}$$

for all operators at all sites $\mathbf{r}$. As seen in Eq. 4.50 from Sec. 4.6, the Mott insulator phase (and similarly the density wave phase) is described by the particle operators

$$\hat{n}_{\mathbf{r}} = \hat{b}^{\dagger}_{\mathbf{r}} e^{-\imath\phi} \hat{b}_{\mathbf{r}} e^{\imath\phi} = \hat{b}^{\dagger}_{\mathbf{r}} \hat{b}_{\mathbf{r}} \tag{4.61}$$

which are invariant to phase transitions. The superfluid state (and the supersolid state, too) however depends solely on the particle creation operator (cf. Eq. 4.57) and is therefore not invariant to $U(1)$ translations. Consequently, $U(1)$ phase symmetry shows that the system is in an insulating state. It should be noted that this symmetry is also associated with the particle number conservation, which is also expressed by the fact that the superfluid phase can be approximatively regarded as a coherent state in the thermodynamic limit, as argued in Sec. 4.6.2.
The $\mathbb{Z}_2$ translational symmetry refers to discrete spatial translations on the lattice:

$$\hat{b}_{\mathbf{r}} \to \hat{b}_{\mathbf{r}+\mathbf{t}} \, , \, \hat{b}^{\dagger}_{\mathbf{r}} \to \hat{b}^{\dagger}_{\mathbf{r}+\mathbf{t}} \, , \, \hat{n}_{\mathbf{r}} \to \hat{n}_{\mathbf{r}+\mathbf{t}} \tag{4.62}$$

where all spatial components of $\mathbf{t}$ are integer. Obviously, the Mott insulator and superfluid phases are invariant under these translations, as there is the same expactation value for the number of

Phase transition	Symmetry	Type	Universality class
MI-SF	$U(1)$	second order	XY
DW-SS	$U(1)$	second order	XY
MI-DW	$\mathbb{Z}_2$	second order	Ising
SF-SS	$\mathbb{Z}_2$	first order	-
DW-SF	$U(1)$,$\mathbb{Z}_2$	first order	-
DW-DW	-	first order	-

Table 4.1: Symmetries and universality classes associated to the quantum phase transitions.

bosons on every site. This translational symmetry is partially broken in the density wave and supersolid phases. The expectation value for the number of bosons is alternating in these phases for nearest-neighbouring sites. With this modulation, the system is only invariant under translations with $|\mathbf{t}| \mod 2 = 0$.
The breaking of the $U(1)$ symmetry through the formation of a condensate of particles in the ground state corresponds to the emergence of magnetization in the 3D XY-model [96]. A phase transition at which this symmetry breaks should therefore behave according to the 3D XY universality class [1]. The spatial modulation that appears in the density wave and supersolid phases, and which breaks the $\mathbb{Z}_2$ symmetry, corresponds to an Ising magnetization. Consequently, if the $\mathbb{Z}_2$ symmetry is broken during a phase transition in a 1D or 2D Bose-Hubbard model, this transition is associated with the 2D or 3D Ising universality class. The mapping from a Bose-Hubbard to an Ising model results in a change in dimension.
The quantum phase transitions relevant to this work along with the associated symmetry breaks and expected universality classes are specified in Tab. 4.1. If the simulations accomplish to describe the properties of the systems adequately, a finite-size scaling analysis should confirm the correct universality class for every phase transition.
Note that the last entry in Tab. 4.1 denotes a phase transition from one density wave phase to another, while the occupation number modulation is different in both phases. This transition does not break any obvious symmetry, but is identfied by a spontaneous change in the value of the order parameter.

4.7 Order parameters

Order parameters are an essential tool in the investigation of phase transitions and critical phenomena. With the help of appropriate order parameters, phase transitions can be identified, classified and the exact transition point can be determined. This section discusses observables which are helpful in the evaluation of the Bose-Hubbard models either in the form of order parameters or as thermodynamic quantities that give further insight to the physics of the system.
The choice of suitable order parameters is crucial in the investigation of the phase behaviour of a system. An order parameter is defined in such a way that it is zero in the "disordered" phase and non-zero in the "ordered" phase. Often phase transition can be associated with the breaking of at least one symmetry. Order parameters can then be defined with regard to these symmetries.
The set of observables should provide a full set of order parameters to identify the phase transitons listed in Tab. 4.1 for both methods discussed in Chap. 6 and should also give information about the stability of the particular phases and if the system has reached its true ground state.
Whether an observable is an appropriate and convenient order parameter or not depends not only on the properties of the system, but also on the methods and algorithms used for its simulation.
The following list provides definitions and explanations for the order parameters and observables

[1] This is holds for the 2D-BHM, as the condensate fraction is not defined in 1D (see Sec. 4.7).

used in the course of this thesis. The results chapters provide detailed information on which parameters were used for which purpose.

4.7.1 Phase coherence correlation function and condensate fraction

A possibility to distinguish phases with localized and phases with delocalized particles is the phase coherence correlation function or Green's function. It evaluates correlators between field operators and measures if the single-particle density matrix shows long-range order. This is a property of superfluid states, as introduced in Eq. 4.59. The phase coherence correlation function is defined as:

$$G(\boldsymbol{R}) = \frac{1}{2L^2} \sum_{\boldsymbol{r}} \langle \hat{b}^\dagger_{\boldsymbol{r}} \hat{b}_{\boldsymbol{r}+\boldsymbol{R}} + \text{H.c.} \rangle, \tag{4.63}$$

where $\boldsymbol{R}$ is the distance between two sites and the brackets $\langle ... \rangle = \langle \Psi | ... | \Psi \rangle$ denote the mean value of an observable in the system state $|\Psi\rangle$. If the $G(\boldsymbol{R})$ is non-zero for all R up to $R > L$, there exist phase coherence between all lattice sites. The wave function of the particles extends over the entire system, particles can „move freely" and are in a superfluid state. Examples for the phase coherence function in different phases in a system with long-range interactions are provided in Fig. 4.9. It should be noted that the shape of $G(r)$ also gives information about spatial modulation in the system. This offers the possibility to not only distinguish insulating from conducting phases, but also to discriminate the supersolid from the superfluid phase. The

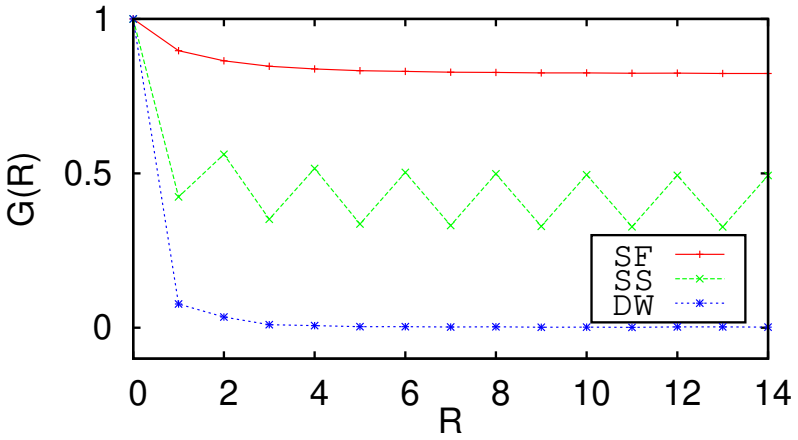

Figure 4.9: Phase coherence correlation function in different phases of a system with with long-range interactions, $L^2 = 196$ sites and $\rho = 1$ at a fixed ratio $U_l/U_s = 0.7$. The superfluid phase was measured at $U_s/t = 5$, supersolid at $U_s/t = 8$ and denisity wave at $U_s/t = 15$. This figure was also published in Ref. [1]. Reprinted with permission.

number of particles of the system with a wave vector $\boldsymbol{k}$ is given by the Fourier transform $n(\boldsymbol{k})$ of the phase coherence correlation function,

$$n(\boldsymbol{k}) = \frac{1}{L^2} \sum_{\boldsymbol{R}} e^{i\boldsymbol{k}\cdot\boldsymbol{R}} G(\boldsymbol{R}), \tag{4.64}$$

whose value for $\boldsymbol{k} = \boldsymbol{0}$ is the condensate fraction, i. e. the fraction of bosons occupying the superfluid ground state. The condensate fraction is a suitable order parameter for the two-dimensional models. It is zero in the phases with localized bosons and non-zero for delocalized bosons. Examples for the condensate fraction are provided in Fig. 4.10.

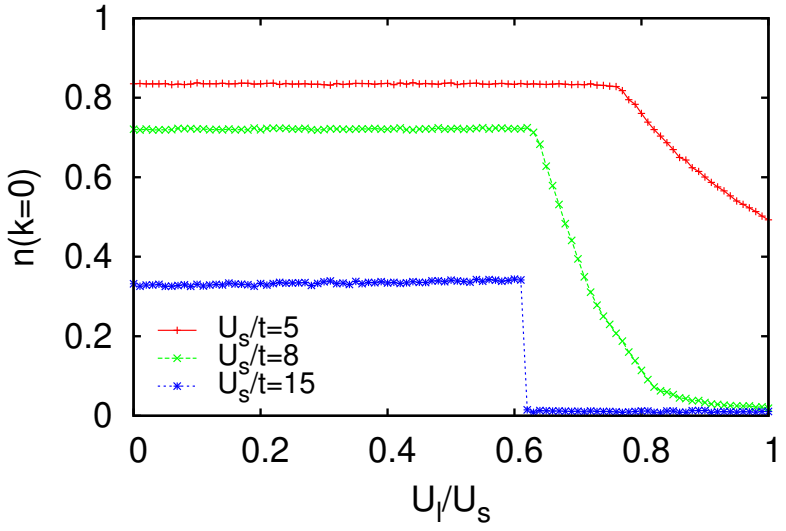

Figure 4.10: Condensate fraction as a function of the ratio U_l/U_s for three different values of U_s/t in a system with long-range interactions, $L^2 = 196$ sites and $\rho = 1$.

In one dimension, the situation is different. The condensate fraction is always zero in the thermodynamic limit. However, there is a Kosterlitz-Thouless transition as the behaviour of the decay of the phase coherence correlation function changes during the process. In the low temperature limit, $G(\boldsymbol{R})$ decays algebraically at first, leading to a quasi-long range order, but then decays exponentially.

4.7.2 Density-density correlation function and structure factor

It was stated in Secs. 4.6.3 and 4.6.4 that spatial modulation in the boson occupancy is a property of the density-wave and supersolid phases. This can be observed with the density-density correlation function $C_d(\boldsymbol{R})$, which is defined as:

$$C_d(\boldsymbol{R}) = \frac{1}{L^2} \sum_{\boldsymbol{r}} \langle \hat{n}_{\boldsymbol{r}} \hat{n}_{\boldsymbol{r}+\boldsymbol{R}} \rangle \,. \tag{4.65}$$

The brackets $\langle .. \rangle = \langle \Psi | \, ... \, | \Psi \rangle$ denote the mean of the value of an observable is in the ground state $|\Psi\rangle$. Thus for every distance $\boldsymbol{R}$, the mean over all the pairwise combinations of sites with distance $\boldsymbol{R}$ is calculated. The function C_d thus delivers the average density-density correlations between lattice sites, depending on their spatial distance.
The Fourier transformation of $C_d(\boldsymbol{R})$ is called the structure factor $S(\boldsymbol{k})$:

$$S(\boldsymbol{k}) = \frac{1}{L^2} \sum_{\boldsymbol{R}} e^{i\boldsymbol{k}\cdot\boldsymbol{R}} C_d(\boldsymbol{R}). \tag{4.66}$$

For the purpose of this work, when the occupancy-imbalance between nearest-neighbouring sites is of interest, the value $\boldsymbol{k} = \boldsymbol{\pi}$ is considererd. $S(\boldsymbol{\pi}) = S_\pi$ is particularly useful, because the exponential in the Fourier transform takes the value 1 when two sites of distance $\boldsymbol{R}$ have equal parity and -1 when the sites have different parity. With this, S_π is zero in the Mott insulator and superfluid phases, and non-zero in the density-wave and supersolid phases. The structure factor is thereby an appropriate order parameter. As with the imbalance Φ, the actual value of

S_π is necessary to evaluate the quality of the density wave phase at higher densities as different imbalances between even and odd sites might be possible. Fig. 4.11 presents examples of the structure factor.

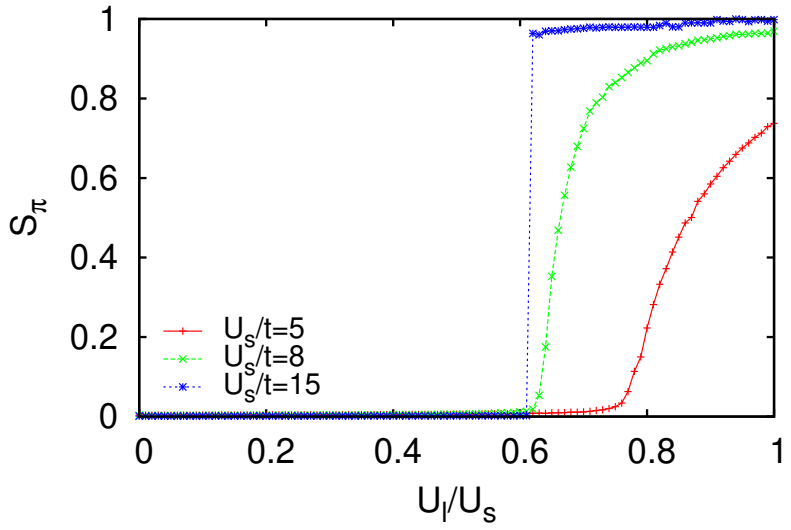

Figure 4.11: Structure factor as a function of the ratio U_l/U_s for three different values of U_s/t in a system with long-range interactions, $L^2 = 196$ sites and $\rho = 1$.

4.7.3 Superfluid density

The phase coherence correlation function defined in Eq. 4.63 is the most straightforward way to identify superfluidity in a system. It is defined to directly measure delocalization of particles, which is a defining property of the superfluid and supersolid phases. This function is easy to measure when the variational Monte Carlo method is used, which will be introduced in Chap. 7. The necessary information is readily available in this methiod, as it is part of the updating process. The phase coherence correlation function can however be cumbersome to evaluate in other methods. One of these methods is the discrete-time world-line quantum Monte Carlo method that is presented in Chap. 8. Therefore, an alternative, more economic way to differ insulating and superfluid states is introduced.
The superfluid density ρ_s is the most efficient way to differ states with localized and delocalized particles if a world-line quantum Monte Carlo algorithm is used:

$$\rho_s \propto \frac{\langle W^2 \rangle}{L^{d-2}} \,. \tag{4.67}$$

A detailed derivation is provided in Ref. [97]. The superfluid density in this form is an observable which is closely related to the world-line Monte Carlo method. The winding number W states if world-lines have wound around the whole spatial direction of the system, thereby overcoming the periodic boundary conditions. Consequently, the winding number provides information if the wave functions of particles extend over the entire system.
Apart from parameters of the simulation, the superfluid density is proportional to the average mean-squared winding number $\langle W^2 \rangle$. The winding number indicates if particles "move" over the entire extent of the system. It is zero in the localized phase and non-zero in the delocalized phase. The world-line Monte Carlo method and the calculation of W in the course of this dissertation

are elaborated in Sec. 8.
When determining the winding number in this way, it should be remembered that it is really only an interpolation. Especially in simulations with smaller system, fluctuations and statistical effects can lead to falsified measurements. It is best to double-check parameter areas in question with the parity order parameter, which will be introduced in Sec. 5.3.2.

4.7.4 Occupation imbalance

The density-density correlation function from Eq. 4.65 is a byproduct of the variational Monte Carlo method and therefore directly accessible, but complicated to evaluate when the world-line quantum Monte Carlo algorithm is used.
For this method, it is more efficent to directly consider the imbalance Φ in the occupation of even and odd lattice sites. The occupation numbers on all even sites and all odd sites are added respectively and the difference between both values is calculated. This observable is defined as:

$$\Phi = \sum_{\mathbf{r}\in e} \hat{n}_{\mathbf{r}} - \sum_{\mathbf{r}\in o} \hat{n}_{\mathbf{r}} \tag{4.68}$$

The Hamiltonian of the Bose-Hubbard model with long-range interactions (Eq. 4.37) contains Φ in quadratic form, as the contribution of the long-range term depends on this imbalance.
When the N bosons in the system are, in mean, equally distributed over all L^d lattice sites, Φ returns the value zero, while it is nonzero if there is a structured imbalance, or modulation, in the occupation number of even and odd lattice sites. Thus Φ is a suitable and convenient order parameter to distinguish the Mott insulator and superfluid phases from the density wave and supersolid phases, in which the $\mathbb{Z}_2$-symmetry is broken.
The sign of Φ shows if there is a higher occupation on the even or the odd sites of the lattice. However, in a lattice with L^d sites with even L, there is no site-preference in the Hamiltonians Eq. 4.26 and Eq. 4.37. Therefore, in Monte Carlo simulations this will happen randomly. Consequently, the absolute value of Φ should be used when averaging over multiple realizations.
The imbalance Φ is also able to differ the various shapes of the density wave phase. Fig. 4.12

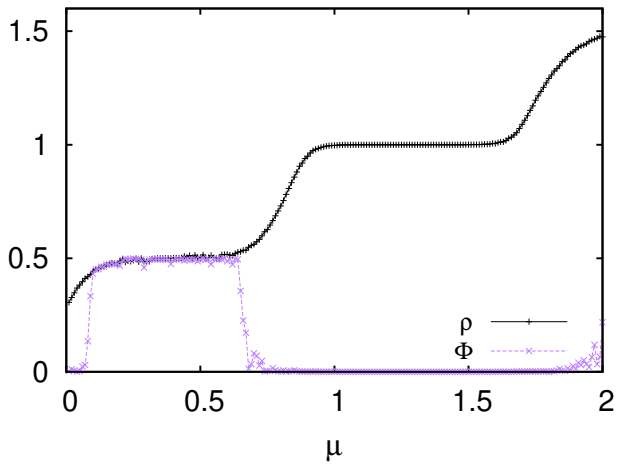

Figure 4.12: Density ρ and occupation imbalance Φ as a function of the chemical potential μ. The plateaus of constant density indicate incompressible phases. The non-zero value of Φ in the first area indicates a spatial modulation, while the vanishing Φ in the second plateau indicates equal distribution. Cross checking with the superfluid density shows that these are in fact density wave and Mott insulator phases.

presents the boson density and Φ as a function of the chemical potential in a grand-canonical simulation. It should be stressed that the superfluid density ρ_s and the occupation imbalance Φ in principle deliver the same information as the more "natural" correlation functions $G(\boldsymbol{R})$ and $C_d(\boldsymbol{R})$ that were specifically defined to satisfy the defining properties of the phases. The corresponding order parameters are therefore interchangeable.

4.7.5 Further observables

Apart from the order parameters, there are other helpful observables when phase transitions are considered. However, it may depend of the kind of simulation if they are useful.
In all cases, the ground state energy E_0 should be evaluated, which is useful for several reasons. For one part, knowing the energy of a system allows to check if the system is in a true ground state or in an excited, metastable state. An example for the comparison of ground state energies is shown in Fig. 4.13. The energies of different ground states can be very close to each other,

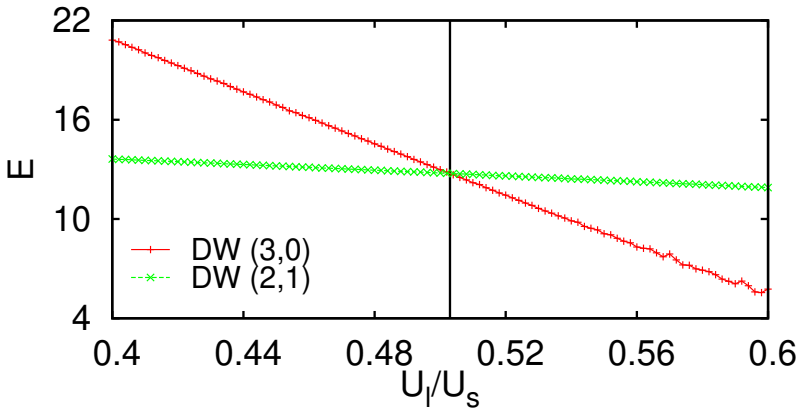

Figure 4.13: Ground state energies of two different density-wave phases in a LR interacting system with $L^2 = 196$ sites and $\rho = 1$ at a fixed tunneling $t = 1$. The lines cross at $U_l/U_s = 0.5$, where the ground state changes. This figure was also published in Ref. [1]. Reprinted with permission.

especially in the vicinity of phase transitions. In simulations, the system might get stuck in a state that is not the ground state. Therefore the comparison of state energies is a valuable tool, when it is uncertain whether the simulation has properly equilibrated and the system is in its true ground state.
The ground state energy is also helpful in the calculation of the chemical potential. If canonical simulations at fixed densities are performed, the chemical potential $\mu(N)$ is not a parameter. It can however be calculated from the ground state energy, as the chemical potential of a system with N bosons is the difference in the ground state energy which occurrs if a boson is added to the system [98]:

$$\mu(N) = E_0(N+1) - E_0(N)\,. \tag{4.69}$$

With this method, grand-canonical phase diagrams can be produced with simulations that conserve the particle number.
The matter of phase separation was discussed in Sec. 4.6.5 and as mentioned the chemical potential is helpful to test the stability of a phase. It is advised to keep track of the particle number, when the data is obtained with simulations in the grand-canonical ensemble. This gives further insight to the thermodynamic behaviour of the system, e.g. if the density is truly constant within the insulating lobes.

Phase	Φ	S_π	$n(\boldsymbol{k}=\mathbf{0})$	ρ_s
MI	0	0	0	0
SF	0	0	>0	>0
DW	$\neq 0$	>0	0	0
SS	$\neq 0$	>0	>0	>0

Table 4.2: Phases and the corresponding values of the order parameters. Note that the condensate fraction is only valid at $d > 1$.

The behaviour of the order parameters in the different phases is summarized in Tab. 4.2. It is possible to distinguish the four phases with these order parameters. The additional observables give further indication whether the system is in a particular state.

Chapter 5

Haldane insulator phase

The quantum phases introduced and discussed in Sec. 4.6 are very common and well understood. The spatial structure and the correlations between particles in theses phases are very simple, as they follow non-complex periodicities. If minor quantum fluctuations are neglected, the phases can be considered as translationally invariant. This fact will come into play in the computational part of this thesis, when the algorithms used to simulate the models are presented.
The Mott insulator and superfluid phases are present in the standard Bose-Hubbard model, where only particle hopping and on-site repulsion compete. The off-site interactions in the extended models give rise to new phases in the ground state phase diagram. In the density wave and supersolid phase, not all sites are equivalent, but two different types of sites emerge. The system however follows a strong periodicity with length two. The question is whether the nearest-neighbour and long-range interactions stabilize any other phases in the ground state, maybe even with non-trivial structures.
In fact, it was shown that the rare Haldane insulator is stable in the ground state of the Bose-Hubbard with long-range interactions that decay with growing distance [99]. This gapped phase appears only at density $\rho = 1$ in one dimensional systems, on a small parameter area in the ground state, right between the Mott insulator and the density wave phases. The Haldane phase is characterized by a subtle order and non-local order parameters are necessary to identify it.
Since the Haldane-Bose isolator is a non-trivial phase, a short pictorial explanation follows before the phase is described in detail in the following sections. To understand the Haldane phase, it is best to first comprehend the nature of the Mott insulator phase. While most of the sites in a one-dimensional system in the Mott phase are occupied by exactly one boson, there area some particle-hole pairs, due to quantum fluctuations. These pairs are tightly bound and can usually not move away too far from another. The formation of the particle-hole pairs happens randomly and does not follow a particular pattern. In the Haldane insulator phase however, the off-site interactions between the bosons induce correlations between such fluctuations, thus every "defect" in form of an excess particle is followed by a hole in the chain and vice versa. Most sites are still occupied by exactly one boson and the system stays insulating. The only order is the alternating occurrence of the defects, there is no periodicity in the distance.
Apparently, off-site interactions between bosons are necessary to stabilize the Haldane Bose insulator phase, yet it was only observed for long-range interaction that weaken with inter-particle distance. For infinte-range interactions, like the cavity-induced interactions investigated in this thesis, there are no results so far which confirm or rule out the existence of the Haldane phase in the ground state.
Because of its special properties and the fact that the stable Haldane phase in the ground state of Bose-Hubbard models was discovered only recently, it is elaborated in this separate chapter. After a short historical overview on the Haldane insulator in spin-1 chains and bosonic systems, the phase is explained in greater details and the common order parameters are presented. Finally, important results from former publications are presented to provide a motivation for further investigations.

5.1 Haldane insulator in the antiferromagnet spinchain

The Haldane Bose insulator is a rare insulating phase with hidden, non-local order, which causes a gap in the energy spectrum of the respective system at density $\rho = 1$. It was originally discovered for 1D spin systems, when the continuum dynamics of the 1D Heisenberg antiferromagnet [100] were considered. This led to numerous approaches to investigate this phase in Heisenberg chains, like semiclassical field theory on Heisenberg antiferromagnets [101], mean-field theoretical treatments of quantum Heisenberg chains at various densities [102], exact diagonalization and Lanczos algorithm applied on the spin-1 Heisenberg chain [103]. The gap in the energy spectrum of the Heisenberg antiferromagnet was also examined with Monte Carlo methods [104] and exact calculations for small systems [105]. While this gap was the only indicator of the Haldane phase at first, Ref. [106] introduced the long-range string order parameter to verify the existence of the non-local interactions which characterize this phase. It was also shown that the Haldane insulator comes with a full break of the $Z_2 \times Z_2$-symmetry of the spin chain [107].

5.2 Haldane Bose insulator

When setups with ultracold atoms in optical traps made experiments on bosonic systems possible [5, 8], even with long-range interactions [32, 108], the interest in Bose-Hubbard models with off-site interactions was boosted. It is especially interesting to investigate if the interplay of the different terms in the models can lead to more complex phases than those presented in Sec. 4.6. Since it is possible to map spin-1 fermionic systems to bosonic systems at density $\rho = 1$, and limited to a maximal occupation of two Bosons per site, a Haldane insulator-like phase was assumed to appear in the 1D extended Bose-Hubbard model. It was discovered in the ground state phase diagrams of the Bose-Hubbard model with polarized dipolar interactions [99] and nearest-neighbour interactions [81, 98, 109, 110] with density matrix renormalization group methods. The order parameters introduced for the fermionic chains [106] are also applicable to bosonic systems. Furthermore, the entanglement properties [111] and dynamics [112] of the Haldane Bose phase have been subject to research, as well as its behaviour in the presence of local disorder [113]. The analogy to spin-chains is crucial to understand the physics behind the Haldane Bose insulator. It is named after the Haldane gapped phase, which appears in quantum spin-1 chains. In such a chain, a spin at site i can have three different states $S_i^z = 0, \pm 1$ in a spin-1 system. The Haldane phase is only relevant for one-dimensional systems, therefore the notation in this chapter is kept simple. Lattice sites are referred to with indicies, which determine the position in the chain.
The existence of the Haldane Bose insulator was first proposed in Ref. [99] for an extended Bose-Hubbard model with distance dependant ($1/r_{ij}^3$) interactions between bosons. It was argued that a new insulating phase exists aside from the above mentioned phases, containing a subtle order which is only identifiable by nonlocal string correlation functions. Similar order exists in the Haldane phase [100] in fermionic systems, so that the phase in the bosonic case was named Haldane Bose insulator [99]. To make the analogy more apparent, the Bose system at density $\rho = 1$ can be mapped to a spin-1 chain. In order to perform a proper mapping, the maximum boson occupation per site is limited to $n = 2$ (for example by choosing the U_s large enought that higher occupations are negligible). Each site in the system is then arranged in one of the occupation states $n = 0, 1, 2$ with the average filling $\bar{n} = 1$. Ref. [99] then defines "an effective spin-1 model" with the boson fillings at site i being pseudospins with states $S_i^z = n_i - \bar{n}$. Every site i can then be assigned a "spin"-value $S_i^z = \delta n_i = n_i - \bar{n}$ when $\bar{n} = 1$ is the average occupation per site. Then:

$$S_i^z = 0 - \bar{n} = -1 \tag{5.1}$$

$$S_i^z = 1 - \bar{n} = 0 \tag{5.2}$$

$$S_i^z = 2 - \bar{n} = 1 \tag{5.3}$$

While the S_i^z alternate in the density wave phase between ± 1, the state $S^z = 0$ prevails in the Mott insulator phase. However, because of quantum fluctuations, tightly bound particle-hole pairs will appear. Off-site interactions between bosons can now introduce correlations between the "defects" in the chain, in a way that each excess particle is followed by a hole and vice versa. This leads to the formation of a Haldane insulator phase in the bosonic system.
The Haldane insulator phase is characterized by long-range correlations between these fluctuations. Every "positive" deviation from the average state value is followed by a "negative" one and vice versa, while the distance between them can be of long-range and in general does not follow a simple periodicity. This new phase is separated to the Mott insulator and density wave phases by second order transitions. For long-range and nearest-neighbour extended Bose-Hubbard models, the Haldane Bose phase was found between Mott insulator and density wave phases by density matrix renormalization group methods [99] and for the nearest-neighbour Bose-Hubbard model between Mott insulator and density wave and between density wave and superfluid phases [81, 98, 109, 110]. Particularly the Mott to Haldane to density wave transition is interesting, as the transition between Mott insulator and density wave was detected to be a first order transition [114–116], when the long-range correlations within the Haldane insulator are not considered.
The Bose-Hubbard model with nearest-neighbour repulsion between bosons is known to show the Haldane phase in its ground state phase diagram. It serves as a good example to understand the energetic properties. The hopping term favors maximum delocalization of the particles and holes, while the contributions by the nearest-neighbour interactions are minimal if particles and holes are direct neighbours. Energetically, the Haldane phase is a compromise between both effects.

5.3 Order parameters

The order parameters of the conventional Mott insulator, superfluid, density wave and supersolid phases have been discussed in Sec. 4.7. It is helpful to consider the behaviour of those order parameters in the Haldane phase, before additional parameters are introduced.
The structure factor (Sec.4.7.2) and the occupation imbalance (Sec. 4.7.4) behave in the Haldane phase the same way as in the Mott insulator phase. The phase is in fact very similar to the Mott insulator phase, with the difference that the particle-hole pairs, which originally arise due to quantum fluctuations are correlated. This correlation does however not feature a peridicity in the distance between particles and holes, such that these will ultimately average out for large enough systems. Occupation imbalance and structure factor should consequently be zero in the Haldane phase.
The superfluid density (Sec. 4.7.3), which is used to measure superfluid behaviour of the bosons in the world-line algorithm shows a rather interesting behaviour. In parameter regions near the Haldane insulator phase, the superfluid density rises to a non-zero value, indicating superfluidity. However, this is just a mere measurement error, which is increased by the approximation that is used to determine the superfluid density. The measurement of the superfluid density will be described in Sec. 8.6.1. At this point, a short description will be sufficient to understand and classify the effect. In the superfluid phase, the wave functions of the bosons extend over the entire lattice and have a non-zero amplitude at all sites. This is impossible to measure in the non-exact world-line algorithm, as the algorithm does not take such states into account. Consequently, the superfluid density has to be approximated. Basically, an correlation function is defined, which tracks the movement of bosons on the lattice. If there is a lot of movement, especially with a tendency towards a particular side, superfluid behaviour can be extrapolated from this, even though the winding number is restricted to zero (compare Sec. 4.7.3 and Sec. 8.6.1). During the phase transition between the Mott and the Haldane insulator phases, intensified boson movement occurs because neither phase is stable. Consequently, the interpolation method may measure non-zero superfluid density.

It is therefore important to double check on the order parameters if possible and to always keep in mind the physical effects on the one side and the limitations of the algorithms on the other side. The fact that the superfluid order parameter becomes inreliable near the phase transition might not entirely break the identification of the phases. Yet the best solution is to introduce an additional order parameter to doubtlessly distinguish the phases from one another. Consequently, two additional order parameters should be introduced.

5.3.1 String order

As stated above, the Haldane Bose insulator is characterized by a non-local string correlation function [99]. These non-local correlations should not be confused with long-range order in local order parameters. To differentiate the Haldane insulator from other phases, a non-local string order parameter $\mathcal{O}_s$ is necessary. Using the analogy to the $S = 1$ spin chain, the deviation from the average value $\bar{n}$ directly gives the spin-orientation:

$$S_i^z = \delta n_i = n_i - \bar{n} \tag{5.4}$$

Utilizing this, string and parity order parameters for one dimensional systems are defined as:

$$\mathcal{O}_s\left(|i-j|\right) = \langle \delta n_i \exp\left(\imath\pi \sum_{k=i}^{j} \delta n_k\right) \delta n_j \rangle \,. \tag{5.5}$$

The braces $\langle , \rangle$ refer to averaging over the possible subsystems with length $|i - j|$.
To speak in terms of bosons, the Haldane phase consists of configurations in which most of the sites of the lattice have the average occupation $\bar{n}$ but there are also particle-hole fluctuations. In the Haldane phase, these fluctuations are not locally bound. However, if all sites with occupation $\bar{n}$ were removed from the system, the remaining sites would have density wave order. This is exactly what the string order parameter measures [109]. It performs a renormalization of the chain, which removes the sites with average occupation and calculates the structure factor of the remaining sites. In the Mott insulator phase, the non-local order described by $\mathcal{O}_s$ is not present. Therefore the string order parameter is suited to identify a phase transition, as it vanishes in the Mott phase and has a non-zero value in the Haldane phase.
From a physical point of view, the string correlations in the Haldane phase are a result of the interplay between the kinetic and off-site interaction terms in the Hamiltonian. The hopping term, which is tuned by the parameter t favors delocalization of particles and holes. The contribution of the nearest-neighbour interaction term, tuned by U_{nn}, is minimal if excess particles and holes are direct neighbours. Consequently, the Haldane insulator phase is stable for intermediate t/U_{nn} [109].

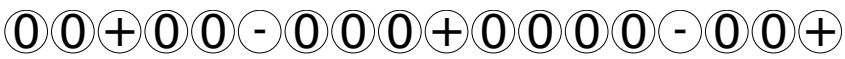

Figure 5.1: Example for a configuration in the Haldane insulator phase. The signs represent the bosonic occupation according to Eq. 5.4. 0 represents an occupation that is identical to the average number of particles per site $\bar{n}$, while + and − represent a boson more or less compared to $\bar{n}$. Each excess boson is followed by a boson deficiency, but there is no particular distance between them [109].

However, especially in grand-canonical systems, it has proven undependable to rely exclusively on the string order parameter, as the parameter regime in which the Haldane insulator exists is very narrow and it is easily confused with phase separation or phase coexistence of adjacent phases [98,117]. Therefore, calculations and simulations are generally executed within the canonical ensemble. The maximum allowed number of particles per site has proven to be a valuable

parameter in this context. Recently, grand-canonical results have been obtained with stochastic-series expansion [118]. A typical configuration of a one-dimensional system in the Haldane phase is depicted in Fig. 5.1.

5.3.2 Parity order

The Mott insulator is characterized by a vanishing structure factor and a vanishing superfluid density. Similar to the Haldane insulator, the Mott insulator does not inherit long-range order in any local order parameter. However, as argued above, having an additional order parameter would be an advantage. The Mott insulator phase is characterized by a non-local correlation function, which is, in one dimension, evaluated through the parity order parameter:

$$\mathcal{O}_p\left(|i-j|\right) = \langle \exp\left(\imath\pi \sum_{k=i}^{j} \delta n_k\right)\rangle\,. \tag{5.6}$$

This order parameter is very similar to the string order parameter from Eq. 5.5. $\mathcal{O}_s$ is a long-range correlation function which evaluates if succeeding deviations from the average occupation alternate between positive and negative values. The parity order $\mathcal{O}_p$ measures if the fluctations in the occupation are closely bound particle-hole pairs. This means that particles and holes are either direct neighbours or fluctuate only in the vicinity of each other. Like the string order $\mathcal{O}_s$, this definition of $\mathcal{O}_p$ relies on the assumption that the Hilbert space can be reduced to states with only the three lowest occupation numbers $n_i = 0, \pm 1$. The mapping from Eq. 5.1 only holds in this case. An example of a system in the Mott insulator phase is shown in Fig. 5.2. The major part of the sites is occupied with exactly one boson, and the particle-hole fluctations are all closely bound. The parity order parameter is zero in the superfluid phase and non-zero in the

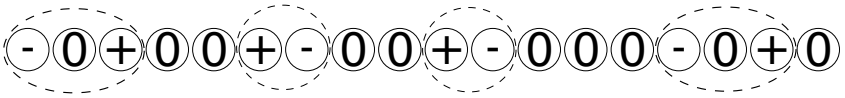

Figure 5.2: Example for a configuration of a system in the Mott insulator phase. Defects appear as closely bound particle-hole pairs. There are however no significant correlations between multiple particle-hole pairs [109].

Mott insulator phase. It is therefore able to identify the transition between these phases. This is especially useful when the system is subject to large fluctuations due to the finite size. This was also mentioned in Sec. 5.3.

5.3.3 Evaluation

Ideally, the order parameters described above would be evaluated in the limit $|i-j| \to \infty$, in practice the maximum distance L_{max} is constrained by the size of the chain with periodic boundary conditions, therefore $\mathcal{O}_s$ and $\mathcal{O}_p$ are obtained for $L_{max} = L/2$. The value is calculated for all sites with this distance and then averaged to obtain the most accurate result. Of course, all other averages inherent in the respective algorithm are also carried out.
The behaviour of the new order parameters $\mathcal{O}_s$ and $\mathcal{O}_p$ in the other phases should also be considered. The string order parameter disappears in the superfluid phase. This makes sense because the bosons are delocalized in this phase and on average there is the same number of particles on all sites. There are no interactions between defects, as in the Mott phase. $\mathcal{O}_p$ is also zero in the superfluid phase. The formation of locally bound particle-hole pairs is impossible, because of the delocalization of the bosons.
In the density wave and supersolid phase, $\mathcal{O}_s$ and $\mathcal{O}_p$ are different from 0. This is because when calculating the string order parameter, a transformation is performed that eliminates the lattice

locations whose occupancy corresponds to the total density. In the spatially modulated phases, these lattice locations represent the "defects". The rest of the sites consists of succeeding positive and negative deviations from $\bar{n}$. The parity operator is non-vanishing for the same reason.
Together with the previously introduced order parameters, which observe delocalization and spatial modulation, all phases can be distinguished. The behaviour of all order parameters in the various phases is summarized in Tab. 5.1. The parity order parameter is seemingly redundant, but helps during emerging fluctuations near phase transitions. An example for the course of

Phase	ρ_S	$S(\pi)$	$\mathcal{O}_p(L/2)$	$\mathcal{O}_s(L/2)$
MI	0	0	$\neq 0$	$= 0$
DW	0	$\neq 0$	$\neq 0$	$\neq 0$
SF	$\neq 0$	0	0	0
SS	$\neq 0$	$\neq 0$	$\neq 0$	$\neq 0$
HI	0	0	0	$\neq 0$

Table 5.1: Behaviour of the order parameters in the different phases.

all four order parameter during two phase transitions, with the Haldane insulator being the intermediate phase, can be seen in Fig. 5.3.

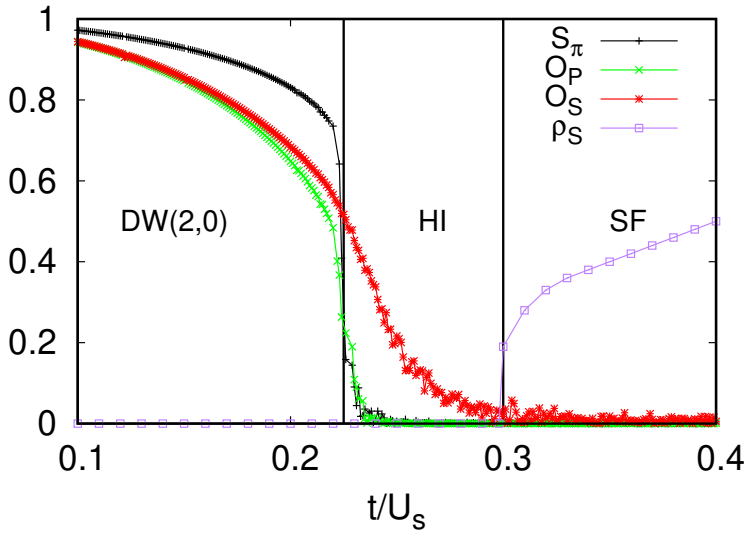

Figure 5.3: Order parameters in dependency of the ratio t/U_s in a system with nearest-neighbour interactions of strength $U_{nn}/U_s = 0.75$. The data was obtained with a world-line algorithm for a system with $L = 256$ sites and $\rho = 1$. The vertical black lines indicate phase transitions.

5.4 Motivation

There are multiple reasons to emphasize the Haldane insulator phase in this work. First and foremost, the phase must be considered if the ground state phase diagram of the Bose Hubbard model is to be accurately reproduced. Former results already showed the existence of the Haldane insulator in that particular model [98, 110, 117]. Furthermore, it is interesting to see whether the Haldane insulator phase will be destabilized by the cavity-induced interactions. So far, the Haldane phase seems to be stable only for models in which the interactions between particles become weaker with increasing distance [99]. However, this is not the case for cavity-induced interactions. In addition, it is interesting to check whether the algorithms used are capable of correctly simulating the Haldane phase. Both the world-line algorithm and the variational Monte Carlo approach are only approximations.

Chapter 6

Quantum Monte Carlo

The Bose-Hubbard models introduced in Chap. 4 have been one of the most vital fields of research in theoretical physics in the last decades. This is hardly surprising, as these models give insight into complex quantum phenomena while maintaining a relatively simple way of describing intricate systems. The fact that these theoretically constructed models can be realized and investigated in experiments, as elaborated in Chap. 3, makes them even more attractive.
For common purposes, it is necessary to consider sufficiently large systems in theoretical studies. This counteracts boundary issues and thereby helps to avoid finite-size effects. Finite-size scaling methods can cushion these problems to a good amount (see Sec. 2.7), yet demand for simulations at a reasonable size to deliver reliable results. Additionally, the Schrödinger equation might provide a theoretical description of the behaviour of any quantum system, yet it is still challenging to describe the evolution of many-body systems or to even solve the many-body problem. The dimension D of the Hilbert space of Bose-Hubbard models grows quickly with increasing system size and the number of bosons [119, 120]. It is associated with the number of possibilities to distribute N indistinguishable bosons onto L^d distinguishable lattice sites:

$$D = \frac{(N + L^d - 1)!}{N!(L^d - 1)!} \tag{6.1}$$

The way the Hilbert space scales with the system size and the number of particles indicates that an analytical treatment of systems with a reasonable size is impossible on current machines. However, there have been significant advances in solving the problem approximatively. The idea behind most of these methods is to sample the values of occurring integrals instead of solving them explicitly. As this approach is based on random numbers, algorithms based on it are consolidated under the name Monte Carlo methods. Two different quantum Monte Carlo approaches were utilized in the course of this dissertation.
The concept of Monte Carlo methods is introduced in this chapter and the matters of sampling and random number generation are addressed. A short overview of the state of the art regarding the theoretical research of the Bose-Hubbard models considered in this dissertation is provided.
After these preliminary considerations, detailed introductions to the variational Monte Carlo algorithm and the discrete-time world-line Monte Carlo algorithm are provided in the following chapters.
Excellent and comprehensive introductions to the vast topic of Monte Carlo methods are provided by Refs. [119], [121] and [122], which were the main sources in the creation of this chapter.

6.1 Monte Carlo methods

Before the quantum Monte Carlo method is considered, it is wise to explain the basics of classical Monte Carlo methods first. The Monte Carlo technique is a general approach to solve problems in physics by statistical analysis and is the most important numerical method in statistical physics. Before going into the more specific details of the particular methods relevant for this work, it makes sense to first understand the general idea behind Monte Carlo sampling and where it pays of, or is even possible, to resort to this procedure.

6.1.1 Monte Carlo integration

A major obstacle in theoretical physics is the evaluation of integrals, very often high-dimensional partition functions. The exact calculation is often a tedious and time-consuming task, if even possible at all. Consequently, there is a high demand for ways to solve integrals efficiently. Monte Carlo methods deliver a solution to this problem. The Monte Carlo procedure uses uniformly distributed random numbers to compute integrals. A simple example of a Monte Carlo integration will clarify the process of Monte Carlo sampling.
If the integral

$$I = \int_a^b f(x)dx \tag{6.2}$$

over a steady function $f(x)$ on the interval $[a, b]$ is considered, then the integration can be carried out via the Monte Carlo method in three steps. For the sake of simplicity, $f(x)$ is assumed to be non-negative and real-valued in the interval $[a, b]$. See also Fig. 6.1 in this context.

- First, a value $F \geq f_{max}$ has to be chosen, where f_{max} is the largest value of $f(x)$ in the interval $[a, b]$.
- In the second step, a pair of random numbers (x, y) is generated, with $x \in [a, b]$ and $y \in [0, F]$. The random numbers have to be uniformly distributed in the case of arbitrary $f(x)$ [123]. If $f(x) \leq y$, the pair counts as a hit. This second step is executed N times, where the number of hits N_{hit} is counted.
- The integration value of $f(x)$ is given by

$$I \approx \mathcal{I} = \frac{N_{hit}}{N}(b - a)F\,. \tag{6.3}$$

This procedure can be generalized in a way that basically every integration over arbitrary intervals may be estimated by generating random numbers between zero and one. Naturally, the value of I is more precise for a higher number of samples. The estimate tends to the true value of the integral for $N \to \infty$. Obviously, this way of sampling to evaluate the integral is neither limited to one dimension, nor to finite integration intervals. As mentioned in the introduction,

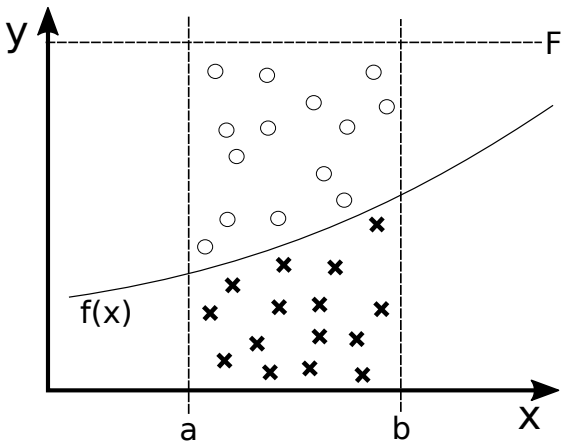

Figure 6.1: Scheme for the integration of $f(x)$ through sampling within the interval $x \in [a; b]$. The crosses represent hits and the circles rejects.

this procedure is not restricted to classical problems, but can be applied to quantum systems in which the number of basis states is extremely large. The individual algorithms for simulations

of different quantum systems are highly dependend on the underlying Hamiltonian. Although the structure of different Hamiltonians appear very similar, the associated Monte Carlo quantum algorithms can be different.

6.1.2 Random number generators

Monte Carlo methods, named after the famous casino location, are hugely depended on random numbers. Therefore, the generation of these numbers is of great importance for the reliability of the entire algorithm. If the numbers used for the sampling are not random, they will not adequately represent the distributions that they are picked from. This leads to a bias in the procedure, which affects the outcome of the method. An example can be seen in Fig. 6.1, where an even distribution of numbers between $[a, b]$ and between $[0, F]$ is demanded. If the random numbers are biased in a way that too many pairs below $f(x)$ are picked, the ratio $\frac{N_{hit}}{N}$ is shifted, as too many hits are generated. The integrate of $f(x)$ will be over-estimated (or vice-versa under-estimated) if the random numbers are biased to be too high. Random numbers are a fundamental component of the Monte Carlo method, so special attention should be given to their generators. In general, classical computers are not able to generate sequences of true random numbers by pure coding. Instead, conventional random number generators rather provide sequences of pseudo-random numbers. The generator is fed with a seed, which it uses to calulate the first number. Subsequent numbers are computed with the help of sophisticated algorithms. While the numbers might have no obvious dependencies between each other (at least to human eyes and brains), such a method can clearly not result in a string of truly random numbers. Hence a generator that is based on this principle is said to produce "pseudo random numbers". This constraint has its origin in the fundamental architecture of classical computers, where each Bit has a specific value of 0 or 1.
There are several workarounds for this problem, which are all based on the inclusion of external sensors. Measuring natural observables that are subject to fluctuations will provide random number generators with new seeds for each number in the sequence. The observables currently used are for example radioactive decay, atmospheric fluctuations or changes in magnetic fields. This proves however impractical for common purposes. Quantum computing, as sketched in Chap. 1, would solve this problem. It should be noted, however, that pseudo random numbers also have advantages in certain situations. This comes into play mainly during testing, porting or bugfixing, where replicability may be desired. The simulations performed in the course of this thesis used the Mersenne twister [124].

6.1.3 Partition function and Boltzmann weights

The role of Monte Carlo methods in statistical physics is not reduced to the evaluation of integrals over plain functions. To understand the application on many-body models, it is necessary to introduce statistical descriptions of the physical quantities first.
The thermodynamic properties of any system are defined by its various states and the probabilities to form them under different conditions. Consequently, the starting point for the Monte Carlo method is the partition function. The partition function of a canonical, discrete ensemble, which is described by the Hamiltonian $\mathcal{H}$, at temperature T is given by [125]:

$$Z = \sum_n e^{-\beta E_n} \,. \tag{6.4}$$

It is the trace over the exponential of the product of the Hamiltonian $\mathcal{H}$ and the inverse temperature $\beta = 1/(k_B T)$, where k_B is the Boltzmann constant. While it may seem like a mere normalizing constant in the following sections, it is a powerful tool in the mathematical description of statistical mechanics. The partition function contains all possible configurations n of the system. Thus the average value of any physical quantity can be derived from it. All information

about the macroscopic behaviour of a system described by the Hamiltonian $\mathcal{H}$ is contained in the variation of Z with temperature, volume or any other parameter that affects the system. The average of a physical observable A is computed as the average over the possible configurations n with energy E_n, weighted by their probability

$$p_n = \frac{1}{Z} e^{-\beta E_n} \tag{6.5}$$

which is given by the Boltzmann weight $e^{-\beta E_n}$. Statistically, the system spends more "time" in states with a high Boltzmann weight, thus those configurations contribute more to $\langle A \rangle$. Configurations with smaller Boltzman weights contribute less. With Eq. 6.4 and Eq. 6.5, the average of an observable A can be written as [121]

$$\langle A \rangle = \sum_n A_n p_n = \frac{1}{Z} \sum_n A_n e^{-\beta E_n} = \frac{\sum_n A_n e^{-\beta E_n}}{\sum_n e^{-\beta E_n}} \,. \tag{6.6}$$

This means that $\langle A \rangle$ can, ideally, be computed by calculating the explicit value A_n of the observable for every state, weighing each with its Boltzmann probability. This is only a valid option for a small system, with small numbers of possible states. For larger systems, the best option is to average over a subset of states. Consequently, this is a prime example of the Monte Carlo principle sketched in Sec. 6.1 for the calculation of integrals. Here, it works by randomly choosing a subset of states from a probability distribution p_n which has to be specified. If M different states $\{n_1 \dots n_M\}$ are sampled, the best estimate of the observable A is given by

$$A_M = \frac{\sum_{i=1}^{M} A_{n_i} p_{n_i}^{-1} e^{-\beta E_{n_i}}}{\sum_{j=1}^{M} p_{n_j}^{-1} e^{-\beta E_{n_j}}} \,. \tag{6.7}$$

This estimate becomes more accurate if the number of states sampled is increased. For a very large number of samples $M \to \infty$ this process delivers an almost accurate average $A_M = \langle A \rangle$. However, as seen in Eq. 6.1, the Hilbert space of the many-body problems treated in this dissertation grows very fast, and it is therefore only possible to sample a small fraction of all the states. If the goal is to reliably sample the expectation value of observables, an efficient Monte Carlo algorithm has to be implemented. Efficient in this framework means that the algorithm preferentially generates states with a high Boltzmann weight and only occasionally states with low Boltzmann weight, to produce an accurate average. Consequently, instead of picking the states with equal probability, it is better to pick the states in a way that the probability to choose any state n is just its Boltzmann weight. Then the estimator from Eq. 6.7 becomes [121]

$$A_M = \frac{1}{M} \sum_{i=1}^{M} A_{n_i} \,. \tag{6.8}$$

This way of sampling the states is called importance sampling. It has the advantage that the frequency with which the states are picked corresponds directly to the probability to rest in this state. In theory, this seems like a very elegant solution. But the difficulty is now how to choose the states so that each one is picked with its Boltzmann probability. For this reason, the majority of Monte Carlo algorithms, and hence the majority of quantum Monte Carlo algorithms, are based on random walks.

6.1.4 Random walks and Markov chains

Mathematically, these random walks are known as Markov chains [126], which is a stochastic model that describes a series of events. The peculiarity is that the probability of the next event depends only on the current state and not on the preceeding one. This property of memorylessness is the defining feature of a Markov process. Knowing the full history of the process does not provide a gain in information about the future of the process, in comparison to only being aware of the current state.
In other words, if a system is in a state μ, the Markov process generates a new state ν. To ensure a true Markov process probability to generate a new state from a given one is only depending on these very states, and it should not vary over time. The transition probability from state μ to ν is denoted $P(\mu \to \nu)$. Since a state ν has to be generated by the Markov process when fed with a state μ, the sum of the transition probabilities has to be 1:

$$\sum_{\nu} P(\mu \to \nu) = 1\,. \tag{6.9}$$

When the Markov process is used repeatedly within the Monte Carlo simulation, a Markov chain of states is produced. It should be noted that $P(\mu \to \mu)$ is not necessarily zero. While the state of the system may be the same as before in this case, it still marks a new element in the Markov chain of states. Even if many consecutive events in the Markov process result in the very same state, each counts as an individual statistical event. This fact is of great significance for the statistics of the simulation and will be addressed again later.
The Markov process has to be executed long enough to ensure that the states appear with probabilities that correspond to their Boltzmann weight. For this reason, further conditions have to be introduced.

6.1.5 Ergodicity

One of these conditions is that the process needs to be ergodic. This means that the Markov process has to be able to reach any state ν in a finite number of steps when starting in some state μ. This is due to the fact that every state ν appears with a non-zero probability p_ν in the Boltzmann distribution of states. If the probability of finding ν in the chains when starting in μ is zero, the correct Boltzmann probability p_ν is not reflected by the Markov process [119, 121]. This does by no means forbid to set some transition probabilities to zero. In fact, in a competent Monte Carlo algorithm, most of the direct transition probabilities between states have to be set to zero, to simulate the system efficiently. But the condition of ergodicity dictates that there must at least be one path of non-zero transition probabilities between each pair of states.

6.1.6 Detailed Balance

The fact that a Markov process needs to be ergodic is quite obvious, as the consequences of impossible transitions between pairs of states violate the fact that the states obey a Boltzmann distribution. The condition of detailed balance, however, requires some explanation. While its derivation is not mathematically difficult, it needs some thought. The detailed balance ensures that after the system has equilibrated, the generated distribution of states is in fact a Boltzmann distribution.
The term equilibrium is crucial here and should thus be elaborated. If a system is in equilibrium, changes in its configurations are just random fluctuations without statistical significance, instead of alterations that drive the system towards a different characteristics. Transferring this to terms of the Monte Carlo simulation, it means that the rate at which transitions into and out of any state μ occur must be equal:

$$\sum_{\nu} p_\mu P(\mu \to \nu) = \sum_{\nu} p_\nu P(\nu \to \mu) \quad \forall \mu\,. \tag{6.10}$$

With Eq. 6.9, this can be reduced to the probability condition

$$p_\mu = \sum_\nu p_\nu P(\nu \to \mu)\,, \tag{6.11}$$

which is an equilibrium distribution of the Markov process. However, this condition alone does not ensure that the probability distribution will tend towards p_μ from any state of the system when running the Monte Carlo simulation. To solve this, the condition of detailed balance has to be defined more restrictively [119]:

$$p_\mu P(\mu \to \nu) = p_\nu P(\nu \to \mu)\,. \tag{6.12}$$

Each set of probabilites satisfying this condition also clearly satisfy Eq. 6.10. It also eliminates the possibility that the Monte Carlo simulation gets "locked" in a small set of states in which it cycles, with little probabilty to reach other states, as the detailed balance demands that the rates of the system from reaching ν starting from μ and of reaching μ starting from ν are equal. Going from state ν to state μ is therefore as likely (or unlikely) as the other way round. If the system could be trapped in a small set of states, this condition would be violated.
This means that by choosing the transition probabilites according to Eq. 6.12, the Markov process can converge to any stationary probability distribution of states that is desired. As argued in Sec. 6.1.3, the equilibrium distribution should be the Boltzmann distribution, so the probabilites p_μ should be the Boltzmann probabilites from Eq. 6.5. Together with the detailed balance, this leads to the condition:

$$\frac{P(\mu \to \nu)}{P(\nu \to \mu)} = \frac{p_\nu}{p_\mu} = e^{-\beta(E_\nu - E_\mu)} \tag{6.13}$$

The most obvious choice would be

$$P(\mu \to \nu) \propto e^{-\frac{1}{2}\beta(E_\mu - E_\nu)}\,, \tag{6.14}$$

which is however not an efficient foundation for fast sampling. A better alternative is presented in Sec. 6.1.8.

6.1.7 Acceptance ratios

The previous paragraphs lead to the plain fact that an appropriate set of transition probabilites is crucial for the successful generation of a Boltzmann distribution. As the established conditions are not exactly strict, there is great freedom in the choice of the individual transition probabilities between each pair of states, yet the sum of all probabilities needs to be one, as stated in Eq. 6.9. This condition may not be violated. Consequently, when altering any $P(\mu \to \nu)$, at least one further transition probability needs to be changed to preserve the integrety of the system.
This is however not that crucial as it seems at first. In the initial considerations about random walks (Sec. 6.1.4), it was already noted that the transition probability $P(\mu \to \mu)$ is not necessarily zero. The fact that the new state of the system can be identical to the current state is a useful tool when tuning the acceptance ratios. If a transition probability $P(\mu \to \nu)$ needs to be adjusted, the necessary correction in order to satisfy Eq. 6.9 can simply be applied to $P(\mu \to \mu)$. The only constraint is that $0 \leq P(\mu \to \mu) \leq 1$ for all possible states μ. Also, an adjustment of $P(\mu \to \nu)$ might be accompanied by a concurrent adjustment of $P(\nu \to \mu)$, in order to keep the ratio expressed in Eq. 6.13 unchanged.
With these rather theoretical concepts in mind, computational aspects may not be disregarded, as an efficient and reliable algorithm for the simulation of the many-body problems is the ultimate goal of all these considerations. As stated above, sampling the entire Hilbert space without concept will result in very long running times, until a Boltzmann distribution of states is reached. Proposing updates that are rejected too often is equivalently bad for the efficiency.

It can be useful to regard the transition probabilites of the form $P(\mu \to \mu)$ as "rejections" in the sense of the simulations. If a transition $\mu \to \nu$ is not accepted by the Monte Carlo algorithm, the system stays in its current configuration. Or, formulated in a different way, a transition to the same state has occurred.
With regards to the actual sampling process during the simulation, it is useful to split each transition probabilitiy into two factors

$$P(\mu \to \nu) = g(\mu \to \nu)A(\mu \to \nu)\,. \tag{6.15}$$

where $g(\mu \to \nu)$ is the selection probability to propose a transition from state μ to state ν and $A(\mu \to \nu)$ is the probability to accept and execute this transition. This procedure contains two random processes instead of one and allows for more fine-tuning within the sampling process. The ratio between the transition probability from state μ to state ν and the reverse case is given by [121]

$$\frac{P(\mu \to \nu)}{P(\nu \to \mu)} = \frac{g(\mu \to \nu)A(\mu \to \nu)}{g(\nu \to \mu)A(\nu \to \mu)}\,. \tag{6.16}$$

The splitting up of the transition probability makes it possible to mirror the physical conditions of the system within the acceptance ratio. This way an arbitrary selection probability can be provided, but the physics of the many body systems is reflected in the acceptance ratio.
Speaking in terms of the simulation, the algorithm generates a random state ν from the current state μ with probability $g(\mu \to \nu)$, which is then accepted or rejected with the acceptance ratio $A(\nu \to \mu)$. While there is great freedom in the choice of these probabilites, Eq. 6.16 has to be satisfied. This is the basis to create a string of states which each appear with their Boltzmann probability, once the algorithm has reached equilibrium. In practice, the acceptance ratios may take any value between 0 and 1, but with regard to an efficient simulation, it should be as close to 1 as possible. Then only a small portion of updates is rejected. As Eq. 6.16 implies only the ratio between two acceptance ratios $A(\nu \to \mu)$ and the reverse $A(\mu \to \nu)$, one of the two can be set to 1 and the other is chosen in a way that the equation is satisfied.

6.1.8 Metropolis algorithm

The common choice for selection probabilities and acceptance ratios are those proposed by the Metropolis algorithm. It was originally introduced with simulations on hard-sphere gases in mind [22], but the concept can be generalized. The Metropolis algorithm takes into account the actual system to be simulated and represents its physical properties in the selection and acceptance probabilities. The starting point is the fact that a system in equilibrium will experience fluctuations, but these will not significantly alter its total energy. Instantaneous dramatic changes of the energy are very unlikely and are therefore omitted in the simulation and only small updates, which correspond to the actual physical fluctations, are proposed. As fluctations are a random, undirected process, the Metropolis algorithm assumes the selection probabilites for all these updates to be equal. The selection probabilities to all other states are however set to zero. This means that if a system is currently in the state μ and N subsequent configurations ν are possible, then the selection probability for each transition $\mu \to \nu$ is given by

$$g(\mu \to \nu) = \frac{1}{N}\,. \tag{6.17}$$

Note that this includes also the case $\nu = \mu$. States ξ which are not reachable via a single "fluctuation-update" have the selection probability $g(\mu \to \xi) = 0$. Knowing that the states follow a Boltzmann distribution, the detailed balance in the Metropolis algorithm can then be expressed solely through the energies of the states E_μ, E_ν and the inverse temperature β:

$$\frac{P(\mu \to \nu)}{P(\nu \to \mu)} = \frac{g(\mu \to \nu)A(\mu \to \nu)}{g(\nu \to \mu)A(\nu \to \mu)} = \frac{A(\mu \to \nu)}{A(\nu \to \mu)} = e^{-\beta(E_\nu - E_\mu)} \tag{6.18}$$

With this, a possible choice for the acceptance ratio would be the symmetric function

$$A(\mu \to \nu) = A_0 e^{-\frac{1}{2}\beta(E_\nu - E_\mu)} \tag{6.19}$$

where A_0 is a constant. The Metropolis algorithm takes a different approach, which tries to embed the behaviour of the real physical system more closely. The goal is to equilibrate the system. However, it has to be considered that a Monte Carlo method is a stochastical approach which can and will not operate like an iterative, analytical method, where the equilibration progresses in each step. The Metropolis algorithm reflects both these facts [22], by choosing the acceptance ratio as

$$A(\mu \to \nu) = \begin{cases} e^{-\beta(E_\nu - E_\mu)} & \text{if } E_\nu - E_\mu > 0 \\ 1 & \text{otherwise.} \end{cases} \tag{6.20}$$

This means that an update is accepted every time if it is beneficial with regard to the energy of the system. In other words, if the energy of the new state is lower than the one of the current state, the system will undergo a transition. Yet, the update will also be accepted with a probability of $e^{-\beta(E_\nu - E_\mu)}$ if the energy of the new state is higher than the energy of the current state. This prevents the system from being locked in local minima. Also, fluctuations are reflected by this.
The Metropolis algorithm is the most important Monte Carlo algorithm, and its basic idea of choosing the selection and acceptance probabilities has been highly influential on statistical physics and its methods. However, while the ansatz of the Metropolis algorithm to update the system in the same way as fluctuations occur in the real physical system, there are some disadvantages of this method. In many cases a long equilibration time is necessary, as the individual updates only provide minor changes within the overall systems [22, 119]. For larger system, a huge number of updates might be needed to equilibrate the system, if the initial state is poorly chosen. Also, the algorithm tends to perform badly in critical regions, as the acceptance rate for energetically infavourable states is still very high if the energy-difference between states is small. This fact might even result in the formation of metastable states.
Other algorithms, like cluster- and loop-algorithms have persued and evolved the idea of the Metropolis algorithm, to provide a more efficient basis for simulations.

6.1.9 Computational aspects and quality control

Modern Monte Carlo and quantum Monte Carlo algorithms are capable of delivering excellent statistical results, when used well. One important aspect is that there is no algorithm which perfectly suits every problem. Choosing an appropriate algorithm is essential.
The quality of the random number generator can also effect the outcome of a simulation. As elaborated in the section before, basically all generators used in practice only produce pseudo-random numbers out of an underlying algorithm. In the statistical analysis of a physical system, a badly performing random number generator might result in artificats in the form of pseudo-correlations, a shifted or wrong statistical representation of the properties of the system or even prevent the system from properly equilibrating.
The selection of the initial condition can affect the running time of the algorithm. While the starting configuration of the system is a priori not important, the simulation might take significantly longer to equilibrate, if the initial state is chosen far from equilibrium. In any way, it is necessary to check if the system has properly equilibrated before starting the measurements. An easy way to accomplish this is to repeatedly measure the total energy of the system after a fixed interval of Monte Carlo updates. Once the fluctations in energy ceased to decrease and stay within a narrow range, the system is either equilibrated or trapped in a local minimum. If the latter cannot be excluded with certainty, the simulation should be restarted with a distinctly different inital configuration. Provided that the system equilibrates to the same energy as before, the ground state might in fact be reached. When multiple simulations with a similar set

of parameters are performed, it is usual to take the closing state of the previous simulation as initial conditions. This saves some computation time, as the equilibration phase will take much less effort, in comparison to a random starting configuration
Aside from the equilibration, the measurements themselves should be performed often enough and each measurement should take place after an appropriate number of Monte Carlo updates. This supports the aim to get an exact statistical representation of the system.
Regarding all these variables that can influence the outcome of the simulation, the quality of the algorithm should be tested. An obvious way of quality control is, for small systems at least, the comparison to the results of an analytic method. Obviously, the Monte Carlo methods were invented to work where exact methods fail, but if a simulation produces reliable outcomes for small systems, which are often plagued with finite-size effects and non-vanishing correlations, then there is a high chance that the simulation will also deliver good results for larger system sizes. Exact diagonalization is an excellent solution for this purpose, as it is easy to understand and straightforward to implement for bosonic problems [127].
Countless works have dealt with improving the efficiency of Monte Carlo methods. Some approaches are of general nature and applicable to all different forms of the Monte Carlo method, for example the optimization of the estimator [128] or alternative ways of sampling [129]. Other publications aim at an improvement of specific methods, for example wave function optimization in the variational Monte Carlo method [130–132]. Generally speaking, there is no universally perfect Monte Carlo method. For each problem, the advantages and disadvantages of the different methods have to be weighted up, and possibilities for custom optimizations have to be considered.

6.2 From classical to quantum problems

Instead of a Hamilton function, quantum systems are described by Hamilton operators. Therefore, providing a reliable solution for many-body quantum problems is a challenging task, as the Hilbert space grows quickly with the number of degrees of freedom. The properties of quantum systems are governed by the Schrödinger equation. Solving the stationary Schrödinger equation provides insight into the physics of the specific system at hand. However, the stationary Schrödinger equation can only be analytically solved in some exceptional cases. Exact solutions can be found for the harmonic oscillator, a free particle or even the hydrogen atom. But quantum many-body systems have to be treated approximately. Also, simulations are currently (for the most part) restricted to classical computers. Quantum computers would be ideal to perform simulations, but are not widely available yet.

6.2.1 Partition function of a quantum system

The partition function of a quantum system described by the Hamiltonian $\hat{\mathcal{H}}$ looks similar to the classical counterpart from Sec. 6.1.3. For a canonical ensemble that is quantum mechanical and contains a discrete number of states, the partition function is defined as the trace over the state space:

$$Z = \operatorname{Tr} e^{-\beta\hat{\mathcal{H}}} \,. \tag{6.21}$$

The dimension of the Boltzmann factor $e^{\beta\hat{\mathcal{H}}}$ corresponds exactly to the number of eigenstates of the system. This representation may seem unintuitive at first. The exponential of an operator can be defined using the exponential power series. Clearly, the trace over the exponential of an operator is much more complicated to evaluate than a classical partition function, which is just the sum over exponentials of the eigenenergies of the Hamilton-function.
The two methods presented in Chaps. 7 and 8 use different approaches to treat quantum problems with Monte Carlo methods. The basic idea however is somewhat similar. Imprecisely formulated,

the quantum mechanical states are considered a superpositions of classical systems. The idea is to map the quantum problem to a classical problem and to use Monte Carlo methods to simulate the latter.
The variational Monte Carlo is known as a quantum Monte Carlo method, yet it lies right on the seperating line between classical and quantum Monte Carlo methods [133]. However its application of the Markov-Chain and Metropolis sampling is very plausible. The ground state quantum fluctuations of a system are simulated with a Metropolis algorithm. During the Markov-chain procedure, the system is treated like a classical system. However the different states and their statistical representation during the simulation are used to form the variational parameters of a trial wave function. This many-body wave function provides an approximate description of the quantum system.
For the world-line quantum Monte Carlo method, a quantum-classical mapping is performed. The d-dimensional quantum system with temperature $T = 0$ is mapped to a $d + 1$-dimensional classical system with temperature $T > 0$. It is considered a true quantum Monte Carlo method. Both methods are extensively elaborated in the respective chapters.

6.3 Quantum Monte Carlo state of the art

Since the introduction of the Bose-Hubbard model [55], many techniques have been established to investigate it in its standard and extended forms at multiple dimensions. Approximative methods like mean-field theory [55], renormalization group theory [134], density-matrix renormalization group [135], Gutzwiller wave function optimization [136, 137] or strong coupling expansion [137] have delivered reliable results for the standard Bose-Hubbard model and are used to this date.
Approaches to treat the standard Bose-Hubbard model by means of quantum Monte Carlo have resulted in elaborate methods, like world-line quantum Monte Carlo [138, 139] or path-integral Monte Carlo [140–142]. Advanced methods, like worm algorithms [143–148] and the related stochastic Greensfunction algorithm in one [149, 150] and higher dimension [67, 151–156] provide exact results by covering the entire Hilbert space.
The interest in models with nearest-neighbour, next-nearest-neighbour, dipolar or long-range interactions between bosons increased when experiments on boson-like systems, e.g. ultracold atoms trapped in optical lattices [5, 8, 32, 75], became more elaborate and off-site interactions between particles [10, 70] were implemented, as described in Chap. 3. The off-site interactions in the extended models do not complicate the calculations too much, but the phase diagrams are richer, with additional density wave and supersolid phases [157, 158], which both feature long-range spatial ordering. Extended models were investigated by density matrix renormalization group theory [81, 84, 112, 114, 118], Gutzwiller ansatz [66, 159, 160] and quantum Monte Carlo [71, 95, 110, 161, 162].
Concerning the Bose-Hubbard model with nearest-neighbour interactions in particular, theoretical works in 2D [154, 157, 163] and 3D [164, 165] were able to show the existence of the additional density wave and supersolid phases. However, early publications on 1D models were not able to confirm the existence of the supersolid phase for this dimension [84, 114] yet, as there is an issue with phase separation in lower dimensional systems [92, 95, 166]. However, following approaches, which used Gutzwiller ansatz [115] and QMC [161], indicated the existence of a supersolid region in the ground state phase diagram of the 1D model. Since then, the BHM with NN interactions is a common subject to further investigation [95, 154, 160, 166].
When experimental realizations of the Bose-Hubbard model with cavitiy-mediated long-range interactions were proposed [33, 36], early simulations for the 1D and 2D system were performed [37] and the existence of a supersolid phase was proposed [76]. Ground state phase diagrams of the corresponding model were computed with the help of mean-field approaches in 1D [167, 168], 2D [76, 85, 169] and 3D [170], with Gutzwiller ansatz [93, 171], DMRG [81] and QMC methods [37, 93, 169]. Also, the dynamics of the model was investigated using dynamical mean-field methods [172] and quench dynamics for the hard-core Boson limit [173–175]. Futhermore, the quantum Monte Carlo method was also influential on the field of molecular physics and chemistry [176].
The simulations performed for this thesis are based on Monte Carlo techniques. More specifically, the data was created using the discrete-time world-line Monte Carlo method and a wave function variational Monte Carlo technique. A comprehensive overview on the modern application of quantum Monte Carlo simlations in the field of cold gases was published in Ref. [177]

Chapter 7

Variational Monte Carlo

The first specific quantum Monte Carlo scheme to be discussed in this thesis is the variational Monte Carlo approach. It is a very transparent application of the Monte Carlo idea. While the world-line Monte Carlo method is a full-on quantum Monte Carlo method, the variational Monte Carlo approach lies in a grey area between classical Monte Carlo and quantum Monte Carlo. While this method has been a frequently used tool to treat fermionic system for a long time, it has also been used to treat bosonic systems in the last decades and the Bose-Hubbard model in particular in recent years.
The variational Monte Carlo method [79, 178] is a zero-temperature method, which aims at computing the ground state wave function of the system. Thermal fluctuations are not taken into account, only quantum fluctuations. Generally speaking, variational Monte Carlo is a form of quantum Monte Carlo, in which the ground state of a quantum system is approximated by means of variational methods. The quantum Monte Carlo part is embedded into an iterative method of wave function optimization. For this purpose, a trial wave function, depending on a set of optimization parameters, is defined. The values of these parameters are iteratively improved through the minimization of the total energy of the system. The integrals that occur during the energy minimization are evaluated statistically with quantum Monte Carlo. Once a further minimization of the energy of the system through alteration of the parameters is not possible any more, the wave function has its final, optimized form.
There are different approaches for the ansatz of the trial wave function. Which ansatz is best depends on the kind of quantum particles in the system to be simulated and on their interaction. The most well-known forms might be the Gutzwiller wave function and the Jastrow wave function. This work uses the Jastrow ansatz. While this ansatz is not frequently used when treating bosonic system, variational Monte Carlo already delivered very good results for the standard Bose-Hubbard model [179, 180]. Moreover, it is even appropriate for the simulation of systems with long-range interactions [181].
Obviously, the trial wave function cannot provide an exact description of a quantum system, because of the large Hilbert space (compare Eq. 6.1). There has to be some form of approximation in order to reduce the number of degrees of freedom that are reflected in the trial wave function, otherwise an inappropriately large number of samples would be required. This will lead to a certain inaccuracy in the description of the system. But depending on the Hamiltonian and the problem under consideration, one or another of the different wave function approaches might provide satisfying results. For the Bose-Hubbard models, the Jastrow wave function is an appropriate choice. The approximation when using the Jastrow wave function lies in the fact that the system is assumed to be translational invariant. The optimization parameters in the Jastrow wave function reflect the correlations between sites with fixed distances, so the number of parameters depends on the number of independent distances in the systems. It is assumed that the correlations between pairs of sites with a distance R behave in the same way for the entire system. This seems like a rather large restriction for the degrees of freedom, and in fact it is. States and phases which obey nonlocal order parameters cannot be represented with such a wave function. This is the case for the Haldane insulator phase, which does not contain a simple spatial symmetry. This is the case for the Haldane insulator phase, presented in Chap. 5. It does

not contain a simple spatial symmetry.
However, the Jastrow wave function provides a very good description of the Bose-Hubbard model for the largest part of the phase space treated in this work. The quantum phases introduced in Sec. 4.6 all have a periodic spatial structure and follow system wide symmetries. While the Jastrow wave function already presents a good description of these phases, the accuracy can even be improved by introducing an additional parameter that characterizes the quantum fluctuations in the system. This is the many-body term, which will be described in Sec. 7.2.2.
It should be stressed that the Jastrow wave function might be limited by its reduced set of parameters, but these constraints do not influence the underlying quantum Monte Carlo simulation. In this, the whole Hilbertspace is sampled with a Metropolis algorithm. This improves the accuracy of the method, especially in cases where a transition takes place between two phases, which both can be described by the Jastrow wave function. In short, the quantum system is simulated with the algorithm and the parameters of the wave function are changed iteratively in such a way that the physical conditions represented by the simulation are reflected in it. The parameters are optimised with the aim of reducing the expected energy value.
Because of the translational invariant form of the wave function, the quantum Monte Carlo simulations need to be performed with periodic boundary conditions. Also, as the number of bosons N has to be fixed, simulations are performed in the canonical ensemble. For reasons of symmetry, especially concerning the spatially imbalanced phases (Sec. 4.6.3 and 4.6.4), only systems with even edge lengths are considered.

7.1 The variational method

As the name suggests, the variational Monte Carlo method is a form of quantum Monte Carlo which utilizes the variational method. This is a popular method in computational physics to approximate the ground state, or even excited states, of a quantum system. The results finally allow to create an approximated wave function. An upper bound to the ground state energy of the system is found when the parameters of the trial wave function are fixed such that the expectation value of the energy is the lowest possible. The basis for this approach is the variational theorem. Aside from the variational quantum Monte Carlo method used in this work, the variational method is also applied in the Ritz method [182], the density matrix renormalization group [135] and the Hartree-Fock method [183].

The variational theorem

The variational theorem is the basis for the application of the variational Monte Carlo method. It states that the true ground-state energy E_0 of a Hamiltonian $\hat{\mathcal{H}}$ is always smaller or equal to the expectation value E_T of this Hamiltonian when calculated with a trial wave function $|\Psi_T\rangle$. This means that an approximation of the ground-state wave function, and thereby also the ground-state energy, can be obtained by varying $|\Psi_T\rangle$ until the expectation value of $\hat{\mathcal{H}}$ is minimized [184].
The normalized wave function Ψ_T is a non-specific trial solution of the Schrödinger equation, which is a composition of various Ψ_n. The Ψ_n are true eigenstates of the Hamiltonian with the eigenenergies E_n:

$$\hat{\mathcal{H}}|\psi_n\rangle = E_n|\psi_n\rangle\,, \tag{7.1}$$

where the eigenstates are orthonormal

$$\langle\psi_n|\psi_m\rangle = \delta_{nm} \tag{7.2}$$

and the eigenvalues obey the inequality

$$E_0 < E_1 < E_2 < \dots \tag{7.3}$$

The trial wave function can then be expressed through the eigenstates of the Hamiltonian:

$$|\Psi_T\rangle = \sum_n c_n \psi_n \tag{7.4}$$

with the normalization constants

$$\sum_n |c_n|^2 = 1\,. \tag{7.5}$$

The expectation value of $\hat{\mathcal{H}}$ with respect to the trial wave function using the eigenstate representation from Eq. 7.4 and the eigenvalue-equations Eq. 7.1 can be expressed as a sum of the eigenenergies:

$$\begin{aligned}
\langle\Psi_T|\hat{\mathcal{H}}|\Psi_T\rangle &= \langle\sum_n c_n\psi_n|\hat{\mathcal{H}}|\sum_m c_m\psi_m\rangle && (7.6)\\
&= \sum_{n,m} c_n^* c_m \langle\psi_n|\hat{\mathcal{H}}|\psi_m\rangle && (7.7)\\
&= \sum_{n,m} c_n^* c_m E_m \langle\psi_n|\psi_m\rangle && (7.8)\\
&= \sum_n E_n |c_n|^2\,. && (7.9)
\end{aligned}$$

All off-diagonal matrix elements are zero, as the eigenstates are orthonormal (Eq. 7.2). Since the goal is to show that the ground state energy E_0 is a lower bound to the expectation value E_T, the sum is partially pulled apart:

$$\langle\Psi_T|\hat{\mathcal{H}}|\Psi_T\rangle = |c_0|^2 E_0 + \sum_{n>0} |c_n|^2 E_n\,. \tag{7.10}$$

In a similar step, the normalization constants introduced in Eq. 7.5 are also split up:

$$|c_0|^2 = 1 - \sum_{n>0} |c_n|^2\,. \tag{7.11}$$

Inserting Eq. 7.11 into Eq. 7.10 leads to the relation

$$\langle\Psi_T|\hat{\mathcal{H}}|\Psi_T\rangle = E_0 + \sum_{n>0} |c_n|^2 (E_n - E_0)\,, \tag{7.12}$$

which implies, with Eq. 7.3 in mind, that the expectation value of $\hat{\mathcal{H}}$ cannot be smaller than E_0. The second term in Eq. 7.12 is positive definite, because $E_n - E_0 > 0$ for all n, therefore the inequality

$$\langle\Psi_T|\hat{\mathcal{H}}|\Psi_T\rangle \geq E_0 \tag{7.13}$$

holds and the variational theorem is proven.

7.2 Trial wave function

As mentioned before, the choice of a suitable trial wave function is very important for the success of the method when applied to the respective system. The systems are treated using wave functions with fixed particle number. The individual sites are however described by Fock spaces, as the particles can move. The relations from Eq. 4.5 and the commutation relations from Eq. 4.4 are crucial for the following description.
As introduced in Sec. 4.1, the wave functions are expressed in the occupation number basis. The

general state vector of the whole system with $\sum_{\mathbf{r}} n_{\mathbf{r}} = N$ bosons in this basis is represented by a tensor product of single site states:

$$|n_1, n_2, n_3, ..\rangle = |n_1\rangle_1 \otimes |n_2\rangle_2 \otimes |n_3\rangle_3 \otimes ... \,, \tag{7.14}$$

where $|n_i\rangle_i$ corresponds to the state in which the site labelled by $\mathbf{r}$ contains $n_{\mathbf{r}}$ particles.
The trial wave function used for the simulations in this work is the Jastrow wave function with an additional many-body term [179]:

$$|\Psi_T\rangle = \exp\left(\frac{1}{2}\sum_{\mathbf{r},\mathbf{r}'} v_{\mathbf{r},\mathbf{r}'}\hat{n}_{\mathbf{r}}\hat{n}_{\mathbf{r}'} + g_{MB}\sum_{\mathbf{r}}\hat{\xi}_{h-d,\mathbf{r}}\right)|\Psi_0\rangle\,. \tag{7.15}$$

The basis is $|\Psi_0\rangle$, a wave function of non-interacting bosons, similar to the superfluid ground state from Eq. 4.57:

$$|\Psi_0\rangle = \left(\sum_{\mathbf{r}}\hat{b}^\dagger_{\mathbf{r}}\right)^N |0\rangle\,. \tag{7.16}$$

It is the ground-state of a system of N non-interacting ($U_s = U_l = U_{nn} = 0$) bosons. This is a good choice, because if the approach is chosen that way, all interactions between the bosons will be determined by optimization parameters. The Parameters $v_{\mathbf{r},\mathbf{r}'}$ and g_{MB} are to be optimized.

7.2.1 Jastrow factor

The Jastrow factor [185]

$$\exp\left(\frac{1}{2}\sum_{\mathbf{r},\mathbf{r}'} v_{\mathbf{r},\mathbf{r}'}\hat{n}_{\mathbf{r}}\hat{n}_{\mathbf{r}'}\right) \tag{7.17}$$

in the trial wave function (Eq. 7.15) allows to control density-density correlations between sites. The scalars $v_{\mathbf{r},\mathbf{r}'}$ are the Jastrow parameters and account for particle-particle correlations. In order to keep the number of parameters reasonable, the Hamiltonian is assumed to be translational invariant and periodic boundary conditions are applied. This way, the Jastrow parameters $v_{\mathbf{r},\mathbf{r}'} = v(|\mathbf{r}-\mathbf{r}'|)$ only depend on the distance between positions $\mathbf{r}$ and $\mathbf{r}'$, and not on the particular sites themselves. In the wave function, the Jastrow parameters represent the strength of density-density correlations between sites with distance $|\mathbf{r}-\mathbf{r}'|$, as they are prefactors to the product of operators $\hat{n}_{\mathbf{r}}\hat{n}_{\mathbf{r}'}$. In other words, the Jastrow factor reflects interactions between bosons in the wave function, which started as a wave function of uncorrelated bosons in the superfluid ground state.
Other works showed that $|\Psi_T\rangle$ is a decent trial state for the standard Bose-Hubbard Hamiltonian [179], which contains only on-site interactions, and it also has been discussed that the Jastrow factor is able to describe long-range interactions [181]. Consequently, it is suitable to simulate the model with short- as well as long-range interactions. Since even and odd sites play equivalent roles in the system, the assumption $v_{\mathbf{r},\mathbf{r}'} = v(|\mathbf{r}-\mathbf{r}'|)$ still holds, and thus strongly reduces the number of parameters. As we will see in the following section, the order parameters we use behave in the same way for pairs of sites $\mathbf{r}_1, \mathbf{r}_1'$ and $\mathbf{r}_2, \mathbf{r}_2'$ with $R = |\mathbf{r}_1 - \mathbf{r}_1'| = |\mathbf{r}_2 - \mathbf{r}_2'|$. Therefore, the $v_{\mathbf{r},\mathbf{r}'}$ are well suited to reproduce the symmetries in the Hamiltonians, including the long-range interaction [1].
The Jastrow wave function is not only a valuable tool for bosonic systems. It was already used to examine various physical effects, like the quantum Hall effect [186] or the excitation scheme of ethene [187].

7.2.2 Many-body interaction term

Bose-Hubbard models are subject to quantum fluctuations. The results for the trial wave function can be improved by adding the many-body term

$$\exp\left(g_{MB}\sum_{\mathbf{r}}\hat{\xi}_{h-d,\mathbf{r}}\right) \tag{7.18}$$

which reflects spatial fluctuations of bosons. g_{MB} is the many-body parameter, which is optimized depending on the formation of particle-hole pairs in the system. For this purpose, the sum

$$\sum_{\mathbf{r}}\hat{\xi}_{h-d,\mathbf{r}} \tag{7.19}$$

counts the number of isolated holons h and doublons d in the system. In this context, "holon" denotes an empty site, while "doublon" denotes a site occupied by two bosons. The operator $\hat{\xi}_{h-d,\mathbf{r}}$ controls if spontaneously forming holon-doublon pairs can unbind, such that h and d propagate freely in the system:

$$\hat{\xi}_{h-d,\mathbf{r}} = \hat{h}_{\mathbf{r}}\prod_{\boldsymbol{\delta}}(1-\hat{d}_{\mathbf{r}+\boldsymbol{\delta}}) + \hat{d}_{\mathbf{r}}\prod_{\boldsymbol{\delta}}(1-\hat{h}_{\mathbf{r}+\boldsymbol{\delta}})\,. \tag{7.20}$$

The summation over $\boldsymbol{\delta}$ connects the site at position $\mathbf{r}$ with its nearest neighbours, $\hat{h}_{\mathbf{r}}$ is 1 if the site is empty and 0 otherwise, $\hat{d}_{\mathbf{r}}$ is 1 if the site is doubly occupied and 0 otherwise. The many-body operator controls short-range interactions [188]. The resulting parameter g_{MB} has proven to increase the accuracy for bosonic systems in 2D and 3D [179].
Of course, this improvement is only effective at density $\rho = 1$ and there only in the Mott insulator phase. At higher densities, it has to be modified. For example at density $\rho = 2$, the holon-doublon interaction described in (7.20) was changed to a singlon-triplon interaction by replacing $\hat{\xi}_{h-d,\mathbf{r}}$ with $\hat{\xi}_{s-t,\mathbf{r}}$:

$$\hat{\xi}_{s-t,\mathbf{r}} = \hat{s}_i\prod_{\boldsymbol{\delta}}(1-\hat{t}_{\mathbf{r}+\boldsymbol{\delta}}) + \hat{t}_i\prod_{\boldsymbol{\delta}}(1-\hat{s}_{\mathbf{r}+\boldsymbol{\delta}})\,. \tag{7.21}$$

The summation over $\boldsymbol{\delta}$ still connects site $\mathbf{r}$ with its nearest neighbours, but this time $\hat{s}_{\mathbf{r}}$ is 1 if the site contains a single boson (i.e. a singlon) and 0 otherwise, $\hat{t}_{\mathbf{r}}$ is 1 if the site is triply occupied (i.e. a triplon) and 0 otherwise. This interaction is more suited to the $\rho = 2$, as it describes the deviation from the average occupation. Starting from the most symmetrical case where all sites contain exactly ρ, singlon-triplon pairs are created by a boson hoping to one of its nearest neighbours. Analogously, holon-doublon pairs are created by fluctuations in the $\rho = 1$ system.

7.2.3 Number of parameters to be optimized

To close the section about the trial wave function, the number of optimization parameters is discussed. The many-body parameter g_{MB} from Sec. 7.2.2 represents one of the parameters, independet of the dimension of the problem. The Jastrow parameters $v_{\mathbf{r},\mathbf{r}'}$ from Sec. 7.2.1 make up the rest. There is one Jastrow parameter for each independent distance between lattice sites. Of course the distance $v_{\mathbf{r},\mathbf{r}} = 0$ is not included.
The number of independent distances in one dimensional systems with periodic boundaries is straightforward. The longest possible distance in a system of L lattice sites is just $d_{max} = L/2$, given that the distance between neigboring sites is set to one. The total number of parameters $N_{p(1d)}$ is then given by:

$$N_{p(1d)} = \left(\frac{L}{2}+1\right)\,. \tag{7.22}$$

In two dimensional systems, the number of parameters $N_{p(2d)}$ is not so obvious, as the number of independent distances is not a linear function. However, the upper bound can easily be estimated:

$$N_{p(2d)} \leq \frac{1}{2}\left(\frac{L}{2}+1\right)\left(\frac{L}{2}+2\right) \tag{7.23}$$

Here, L denotes the edge length of the two dimensional lattice, the total number of sites is $N_{2d} = L^2$ and the lattice obeys the Eucledian metric. The distance between sites can be computed with the help of the Pythagorean theorem. The exact number of parameters is obtained by grouping together double occurring distances. For example, a lattice with an edge length of $L = 14$ has 33 different distances, so there is a total of 34 optimization parameters.
To guarantee an efficient simulation, the number of optimization parameters is computed beforehand for each individual value the pairs of sites that have exactly this distance are stored in an array.

7.3 Optimization algorithm

If the number of optimization parameters is known, the actual algorithm can be executed. The variational Monte Carlo method, as shown in the Variation Theorem section, allows iteratively approximated wave functions to be constructed for the energetic states of the system. When the ground state wave function is found, the wave function of the first excited state can be determined and so on. In the context of this work, however, only the ground state is to be considered. Therefore, it is the goal to optimize $|\Psi_T\rangle$ in a way that its corresponding energy E_T is as close to the true ground-state energy of $\hat{\mathcal{H}}$ as possible.
The basis for the optimization of the variational parameters is the occupation number representation. Then the system undergoes the Monte Carlo algorithm, in which the dynamics of the Hamiltonian are stochastically calculated via Metropolis-like sampling. Particles are randomly proposed to change their site and the proposal is accepted or rejected depending on the change in energetic properties, as described in Sec. 6.1.8. This evaluates the local energy with respect to the Hamiltonian. The variational parameters are then altered to reflect these properties of the system.
The trial wave function has the same form as Eq. 7.15. In the further description, the Jastrow factors $v_{i,j}$ and the many-body term g_{MB} are for simplicity summarized to a set $\boldsymbol{\alpha}$. The set consists of α_k with $k = 1, ..., p$, which are the different variational parameters. The explicit form

$$|\Psi_T(\boldsymbol{\alpha})\rangle \tag{7.24}$$

is imposed, such that whenever parameters α_k are specified all components of the trial wave function in number basis $\{|n_1, n_2, ...\rangle\}$ are known.

7.3.1 Monte Carlo sampling

As soon as the trial wave function with the corresponding set of optimization parameters α_k is defined, the actual minimization algorithm can begin. The goal is to change the α_k iteratively until the expectation value $E_T(\boldsymbol{\alpha})$ of the wave function is minimal. The eigenenergy is evaluated with quantum Monte Carlo methods, more specifically with the Metropolis algorithm for bosonic systems. This method was presented in Sec. 6.1.8. The basis for this procedure is the variational theorem from Sec. 7.1. It states that the true ground-state energy E_0 of a system described by the Hamiltonian $\hat{\mathcal{H}}$ is always lower than or equal to the normalized expectation-value $E_T(\boldsymbol{\alpha})$ of the trial wave function [184]:

$$E_0 \leq E_T(\boldsymbol{\alpha}) = \frac{\langle\Psi_T(\boldsymbol{\alpha})|\hat{\mathcal{H}}|\Psi_T(\boldsymbol{\alpha})\rangle}{\langle\Psi_T(\boldsymbol{\alpha})|\Psi_T(\boldsymbol{\alpha})\rangle} \tag{7.25}$$

This means that the approximation $E_T(\boldsymbol{\alpha})$ will only approach E_0 but not undercut it by optimizing $|\Psi_T(\boldsymbol{\alpha})\rangle$. The energy can be rewritten by inserting completeness relations $\sum_n |n\rangle \langle n|$ over the possible configurations $|n\rangle$ of the systems. This will make the application of the Monte Carlo method more straightforward. The expectation value of the trial wave function can then be expressed as [189]:

$$E_T(\boldsymbol{\alpha}) = \frac{\sum_n |\langle n|\Psi_T(\boldsymbol{\alpha})\rangle|^2 E_L(n,\boldsymbol{\alpha})}{\sum_n |\langle n|\Psi_T(\boldsymbol{\alpha})\rangle|^2}\,, \tag{7.26}$$

with the local energy

$$E_L(n,\boldsymbol{\alpha}) = \frac{\langle n|\hat{\mathcal{H}}|\Psi_T(\boldsymbol{\alpha})\rangle}{\langle n|\Psi_T(\boldsymbol{\alpha})\rangle}\,. \tag{7.27}$$

This local energy $E_L(n,\boldsymbol{\alpha})$ corresponds to the energy of a specific configuration $|n\rangle$ with regards to the trial wave function $|\Psi_T(\boldsymbol{\alpha})\rangle$ with the parameter set $\boldsymbol{\alpha}$. Now the Monte Carlo method can be applied to get an estimate for the energy of the trial wave function. Random vectors $|n\rangle$ are picked from the number basis, distributed according to the probability distribution

$$\rho(n) = \frac{|\langle n|\Psi_T(\boldsymbol{\alpha})\rangle|^2}{\sum_{n'} |\langle n'|\Psi_T(\boldsymbol{\alpha})\rangle|^2}\,. \tag{7.28}$$

An estimate of $E_T(\boldsymbol{\alpha})$ is then obtained by averaging $E_L(n,\boldsymbol{\alpha})$ over M stochastically generated configurations $|n\rangle$:

$$E_T(\boldsymbol{\alpha}) = \frac{1}{M}\sum_{i=1}^{M} E_L(n_i,\boldsymbol{\alpha}) \tag{7.29}$$

The sampling works in form of a Markov chain, based on the Metropolis algorithm. New states are produced out of the current state by proposing random moves of bosons.The energy difference to the current state is calculated and the update is then accepted or rejected according to the Boltzmann probability. This very simple sampling algorithm delivers a good estimate for the energy of the trial wave function with the set of parameters $\boldsymbol{\alpha}$. A big advantage of this procedure is the fact that it can be handled solely with ratios between wave functions. This means that the normalization of the wave function does not need to be known.

7.3.2 Wave function optimization

The most important part of the variational Monte Carlo method lies in the variation and thereby optimization of the parameters α_k. In order to optimize the wave function by finding a better set of parameters

$$\boldsymbol{\alpha}' = \boldsymbol{\alpha} + \boldsymbol{\gamma}\,, \tag{7.30}$$

the parameters are iteratively altered, until the difference $\boldsymbol{\gamma}$ becomes negligible. The optimization scheme, which is used in the course of the simulations performed for this thesis, is rapidly converging and uses statistical evaluation of first and second order energy derivatives. It was first derived and described in Ref. [132].
In this optimization method, an operator $\hat{\mathcal{O}}_k$ for each variational parameter α_k is defined at each iteration. It is diagonal in the configuration basis and has the diagonal elements

$$\hat{\mathcal{O}}_k(n) = \frac{\partial_{\alpha_k}\Psi_T(\alpha,n)}{\Psi_T(\alpha,n)}\,. \tag{7.31}$$

For the sake of simplicity, it is preferrable if the derivation is easy to compute. In this sense, it is assumed that the variational parameters and the operators $\hat{\mathcal{O}}_k(n)$ appear in the wave function in an exponential form:

$$|\Psi_T(\alpha)\rangle \propto \exp\left[\sum_k \alpha_k \left(\hat{\mathcal{O}}_k - \langle\hat{\mathcal{O}}_k\rangle\right)\right] \tag{7.32}$$

This choice is advantageous, but not arbitrary. Looking at the trial wave function 7.15, it is clear that it has exactly that form. The variational parameters are prefactors and the operators $\hat{\mathcal{O}}_k$ just correspond to the density-density correlations. $\langle\hat{\mathcal{O}}_k\rangle$ is the average value of $\hat{\mathcal{O}}_k$ and can be subtracted from each term, as it is just an irrelevant prefactor.
This representation can also be used to express the updated wave function $|\Psi_T(\boldsymbol{\alpha}+\boldsymbol{\gamma})\rangle$ with the new set of parameters $\boldsymbol{\alpha}' = \boldsymbol{\alpha}+\boldsymbol{\gamma}$. The new wave function then corresponds to the old function, with a pre-factor that is of linear order in gamma:

$$|\Psi_T(\alpha+\gamma)\rangle \propto \exp\left[\sum_k \gamma_k \left(\hat{\mathcal{O}}_k - \langle\hat{\mathcal{O}}_k\rangle\right)\right] |\Psi_T(\alpha)\rangle \ . \tag{7.33}$$

A simple second order Taylor approximation eliminates the exponential and the new wave function can be expressed through the operators $\hat{\mathcal{O}}_k$:

$$\begin{aligned} |\Psi_T(\boldsymbol{\alpha}+\boldsymbol{\gamma})\rangle \approx \Bigg[1 + \sum_k \gamma_k(\hat{\mathcal{O}}_k - \langle\hat{\mathcal{O}}_k\rangle) \\ + \frac{\beta}{2}\sum_{k,k'} \gamma_k\gamma_{k'}(\hat{\mathcal{O}}_k - \langle\hat{\mathcal{O}}_k\rangle)(\hat{\mathcal{O}}_{k'} - \langle\hat{\mathcal{O}}_{k'}\rangle)\Bigg] |\Psi_T(\boldsymbol{\alpha})\rangle \ . \end{aligned} \tag{7.34}$$

In the standard Taylor-expansion the prefactor β takes the value 1. In the course of this algorithm, it is not fixed to this, but can be used as a parameter to optimize the iteration scheme [132].
To check if the new set of parameters is an improvement, the change in the mean value of the energy between $|\Psi_T(\boldsymbol{\alpha})\rangle$ and $|\Psi_T(\boldsymbol{\alpha}+\boldsymbol{\gamma})\rangle$ has to be considered. Inserting the explicit form from Eq. 7.34 into Eq. 7.25 and expanding the equation in powers of γ_k delivers an advantageous representation of the difference in energy:

$$\Delta E = -\sum_k \gamma_k f_k + \frac{1}{2}\sum_{k,k'} \gamma_k\gamma_{k'}[S_h^{k,k'} + (1+\beta)G^{k,k'}] \, . \tag{7.35}$$

For a wave function with p different optimization parameters, the vector $\mathbf{f}$ has p components and the matrices S^h and G have the dimension $p \times p$. The individual entries are defined as

$$\begin{aligned} f_k &= -\partial_{\alpha_k} E_T(\boldsymbol{\alpha}) = -2\langle(\hat{H} - E_T)\hat{\mathcal{O}}_k\rangle \, , \\ S_h^{k,k'} &= \langle[\hat{\mathcal{O}}_k, [\hat{H}, \hat{\mathcal{O}}_{k'}]]\rangle \, , \\ G^{k,k'} &= 2\langle(\hat{H} - E_T)(\hat{\mathcal{O}}_k - \langle\hat{\mathcal{O}}_k\rangle)(\hat{\mathcal{O}}_{k'} - \langle\hat{\mathcal{O}}_{k'}\rangle)\rangle \, . \end{aligned} \tag{7.36}$$

This form is very helpful, as S^h, G and f can be computed entirely through the derivation of the wave functions according to the variational parameters (Eq. 7.31) and the energy of the trial wave function (Eq. 7.26). Furthermore, with regards to the left hand side of Eq. 7.35, the matrix

$$B = S_h + (1+\beta)G \, , \tag{7.37}$$

is defined. The left hand side of Eq. 7.35 is then minimized by

$$\boldsymbol{\gamma} = B^{-1}\mathbf{f} \, . \tag{7.38}$$

So the set of correctional parameters $\boldsymbol{\gamma}$ for the next iteration of the wave function can be derived by measuring S^h, G, f, calculating B and taking its inverse. All quantities can be calculated with the help of the local energy $E_L(n, \boldsymbol{\alpha})$ (Eq. 7.27) from the Monte Carlo sampling:

$$\begin{aligned} f_k &= -\partial_{\alpha_k} E_T(\boldsymbol{\alpha}) = -2\left(\langle E_L\hat{\mathcal{O}}_k\rangle - \langle E_L\rangle\langle\hat{\mathcal{O}}_k\rangle\right) , \\ S_h^{k,k'} &= \langle[\hat{\mathcal{O}}_k, [\hat{H}, \hat{\mathcal{O}}_{k'}]]\rangle \\ &= \langle\partial_{\alpha_k} E_L\hat{\mathcal{O}}_{k'}\rangle - \langle\partial_{\alpha_k} E_L\rangle\langle\hat{\mathcal{O}}_{k'}\rangle, \\ &\quad + \langle\partial_{\alpha_{k'}} E_L\hat{\mathcal{O}}_k\rangle - \langle\partial_{\alpha_{k'}} E_L\rangle\langle\hat{\mathcal{O}}_k\rangle, \\ G^{k,k'} &= 2\langle\langle E_L\rangle(\hat{\mathcal{O}}_k - \langle\hat{\mathcal{O}}_k\rangle)(\hat{\mathcal{O}}_{k'} - \langle\hat{\mathcal{O}}_{k'}\rangle)\rangle. \end{aligned} \tag{7.39}$$

This is how the parameters are optimized. Clearly, the minimum energy is obtained for $\boldsymbol{\gamma} = B^{-1}\boldsymbol{f}$ with $B = S_h + (1+\beta)G$. This procedure is iteratively repeated until the changes in ΔE or $\boldsymbol{\gamma}$ become negligible.

7.4 Error estimation

The variational theorem was derived in Sec. 7.1. It states that the variational energy is an upper bound for the true ground state energy. This means that the ground state energy cannot be underestimated. That being said, it does not mean that the algorithm can approach the true ground state energy arbitrarily close. It is a flawed method and not exact.
There are two types of errors that affect the outcome of variational Monte Carlo methods. The first type is a systematic error which arises because approximative wave functions are used. This work uses a Jastrow-Ansatz (Sec. 7.2.1) with an additional many-body interaction (Sec. 7.2.2) term to improve the results. The approximation is that only translational invariant states contribute to the wave function. This restriction is known as the Jastrow-Ansatz and it keeps the number of optimization parameters reasonable. The many-body term is added to the wave function to better reflect fluctuations. The exact extent of the systematic error is usually unknown. In order to determine it, the exact solution must be at hand. However, there is reason to suspect that the error may be of different magnitude in different regions of the phase diagram. Phases like the Mott insulator (Sec. 4.6.1), that are largely composed of translational-invariant states, should be reflected better by the variational Monte Carlo approach than phases with a more complex order, like the Haldane insulator (Chap. 5). This will be elaborated in the following section.
Aside from the systematic error, there is of course the statistical uncertainty of sampling a system of finite size with an algorithm based on pseudo random numbers. As mentioned in Sec. 6.1.9, there have to be enough Monte Carlo steps between two measurements in order to ensure statistically independent samples. In the simulations performed in the course of this work, measurements were carried out after $2 \cdot N_B$ Monte Carlo updates. The statistical uncertainty decreases as $1/\sqrt{M}$ with the number of Markov steps M.
The fact that all simulations operate with finite system sizes leads to another issue. Once the correlation length ξ (compare Sec. 2.4) in the system approaches the system size L^d, it is possible that pseudo-order is observed. In this case, the critical points of phase transitions are depending on the system size [1]. This can be counteracted to a certain degree with finite-size scaling (Sec. 2.7). However, even for finite-size scaling, it is necessary to perform simulations at system lengths which deliver a good estimate for the order parameters. An extrapolation for the relevant order parameters in 2d simulations can be seen in Fig. 7.1. The graph shows that a system-size of $L^2 = 196$ delivers good results for simulations in two dimensions.

7.5 Limitations and caveats

The variational Monte Carlo method is easy to perform, but the quality of the results is highly depended on the trial wave function. The outcome is entirely predetermined by the physical arguments that build the foundation of the trial wave function [133]. In the case of the Jastrow wave function used in this work, translational symmetry is assumed, which eliminates a large number of states that all could affect the physics of the quantum system. The variational Monte Carlo prefers simpler phases in general. This will become especially clear when the spatially complex Haldane insulator phase, which was introduced in Chap. 5, is investigated.
When discussing the limitations during the computation, it is important to properly distinguish between issues in the course of the wave function optimization and issues during the Monte Carlo

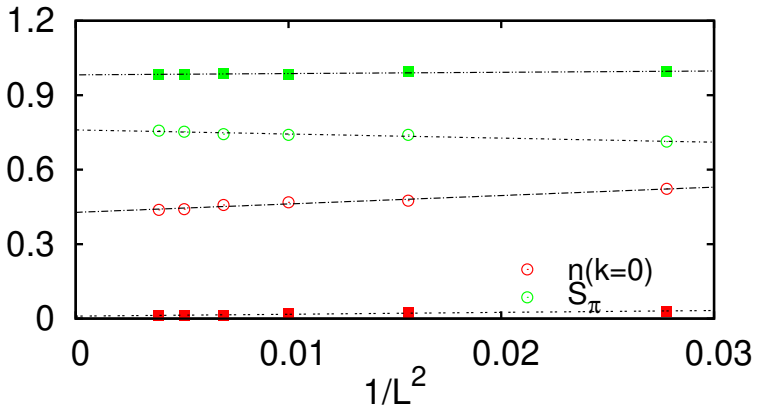

Figure 7.1: Example for a thermodynamic limit extrapolation in order to determine the reliability of simulations. The data was obtained in two-dimensional variational Monte Carlo simulations at $\rho = 1$, $t = 1$ and $U_l/U_s = 0.8$. Filled squares represent configurations in the density wave phase ($U_s = 11$) and empty circles are configurations in the supersolid phase ($U_s = 7$). Black lines are linear fit. This figure was also published in Ref. [1]. Reprinted with permission.

sampling. The most general problems of the wave function optimization were already pointed out in Ref. [132] and workarounds were provided.
The most common issue with the wave function optimization is associated with the assumption of a small $\boldsymbol{\gamma}$. Whenever $\boldsymbol{\alpha}$ is too different from the optimized solution, this results in a large correction $\boldsymbol{\gamma}$ and the approximation from Eq. 7.34 does not hold anymore. Higher Taylor corrections become important and more terms in the expansion are necessary for a reliable description. Another problem is the possibility that B might be not positive definite and the corrections $\boldsymbol{\gamma}$ may lead to a new wave function with a higher energy instead of a lower one. The simplest solution to avoid this problem is to check in every iteration if B is positive definite. If not, a correction of the form

$$B \to B + \mu S \tag{7.40}$$

should be made. The matrix S, introduced in Eq. 7.39 is a good choice in this case, as it is always positive definite. Its entries can be directly calculated from the operator $\hat{\mathcal{O}}_k$:

$$S^{k,k'} = \langle (\hat{\mathcal{O}}_k - \langle \hat{\mathcal{O}}_k \rangle)(\hat{\mathcal{O}}_{k'} - \langle \hat{\mathcal{O}}_{k'} \rangle) \rangle \,. \tag{7.41}$$

The positive prefactor μ is not predefined but should be fixed to a value that is appropriate for the respective problem.
In this sense, it can help to keep track of the change in the wave function:

$$\Delta\mathrm{WF} = \frac{|\Psi_T(\alpha + \gamma)\rangle - |\Psi_T(\alpha)\rangle}{|\Psi_T(\alpha)|} \,. \tag{7.42}$$

To check if the wave function is not altered too much during a single iteration, the constraint

$$|\Delta\mathrm{WF}|^2 \leq r^2 \tag{7.43}$$

is applied. r is again an appropriately chosen control parameter. This inequation can also easily be tested using the relation

$$|\Delta\mathrm{WF}|^2 = \sum_{k,k'} \gamma_k \gamma_{k'} S^{k,k'} \,. \tag{7.44}$$

If it is not fulfilled, the correction introduced in Eq. 7.40 is applied. It should be noted that this corrections will affect the convergence of the algorithm. In the sense of efficiency, the prefactor μ should be chosen as low as possible. Both parameters μ and r affect if and how fast the wave function converges.
If the system does not equilibrate well, this might not necessarily be associated with the wave function optimization and its parameters. Instead, the underlying Monte Carlo algorithm may be the problem. The Metropolis algorithm with local updates can get stuck in metastable states. An appropriate number of samples should be computed.
The initial state of the Monte Carlo algorithm becomes a valuable tool in this context. Generally, the outcome of the algorithm should not depend on the initial configuration of the system. There should be a large enough number of equilibration samples anyway. However, if the simulation is started with the system in a state far from its equilibrium configuration, it might run into a local minimum. This is especially dangerous near phase transitions. When the ground state is debatable, the Monte Carlo simulations should be performed with multiple initial configurations and the appoximated ground state energy compared, as described in Sec. 4.7.5.

Chapter 8

Discrete time world-line quantum Monte Carlo

To support and complement the results of the variational Monte Carlo method, an additional world-line quantum Monte Carlo algorithm was used in the investigation of the Bose Hubbard models. This finite temperature approach is based on Feynman's path integral formalism [97, 190, 191]. Although no exact zero temperature calculations can be carried out, it is possible to approach the absolute zero point at will. If simulation parameters are selected accordingly, the results of the method can be assumed to be approximate zero temperature results. The world-line quantum Monte Carlo algorithm was originally introduced to study the fermionic metal-insulator transition. However, it was soon adapted to many-body interacting boson problems. Meanwhile there are numerous different methods based on the path integral representation. Some methods use continuous imaginary time and are therefore exact. As mentioned, the algorithm used in this thesis works with a discretization of the imaginary time in sections of length $\Delta\tau$. The resulting limitations will be discussed later. The most modern methods, like worm algorithms, work with an extended Hilbert space to sample the system more efficiently. An overview of the different methods is provided in Sec. 6.3.
World-line based approaches of correlated quantum systems serve as a simple realization of the quantum-classical mapping. The world-lines provide a real space picture of the correlations in the original quantum system, as they describe the evolution in imaginary time of variables that are associated with the operators in the quantum Hamiltonian [192]. Path integrals are utilized to map the partition function of the d-dimensional quantum problem onto a $d+1$-dimensional classical model. The resulting classical problem is significantly easier to solve than the original quantum system. The eigenvalues of the quantum operators are represented by the classical degrees of freedom which are introduced through the mapping. These eigenvalues evolve in imaginary time, which represents the additional dimension of the new classical problem. The imaginary time τ corresponds to the inverse temperature β, which almost automatically results from the derivation. In short, the idea of the particular method used in this work is that a path integral representation of the state function is written by discretizing the inverse temperature and inserting complete sets of intermediate states at the junctions. Then classical Monte Carlo methods are utilized to sum stochastically over these states. This procedure converts the quantum problem into a classical problem with an additional dimension. A pictorial interpretation of this mapping might make the concept more understandable. The initial quantum system is characterized by the fact that it is not in a single specific state, but is much more in a superposition of all different possible states. The proportion of each state in the total system, classically speaking the probability of residence, corresponds exactly to its Boltzmann weight. Through the mapping, the quantum system is approximated as a sequence of linked classical systems. Classical Monte Carlo methods are then used to determine the proportion of individual states in the overall quantum state. It can also be seen as the evolution of the quantum system in the imaginary time direction.
The discrete-time world-line quantum Monte Carlo method used in this thesis is a standard technique. The following derivation in this chapter relies on Refs. [138, 139, 193]. As far as derivation is concerned, the simplest case to consider first is the standard Bose-Hubbard model in a canoni-

cal ensemble. The additional off-diagonal interaction terms contained in the extended models are treated separately. This method was used in the research for this thesis only for the simulation of one-dimensional systems.

8.1 Path integral representation of the quantum problem

The basis of the approach is the partition function, which is given by the trace of the state space:

$$\mathcal{Z} = \mathrm{Tr}\, e^{-\beta\hat{\mathcal{H}}}\,. \tag{8.1}$$

The dimension of $e^{-\beta\hat{\mathcal{H}}}$ is the number of energy eigenstates of $\hat{\mathcal{H}}$. $\beta = 1/(k_B T)$ is the inverse temperature. While the partition function of a classical system, presented in Eq. 6.4, is a mere sum of exponentials of the eigenenergies of the underlying Hamilton-function, the partition function of a quantum system is more complex. The exponential of the operators is defined through its expansion in a Taylor series:

$$e^{-\beta\hat{\mathcal{H}}} = \sum_{n=0}^{\infty} \frac{(-\beta\hat{\mathcal{H}})^n}{n!} \tag{8.2}$$

The partition function contains all information about the thermodynamic properties of the system. Therefore, the aim is to evaluate it as accurately as possible.
The many particle exponential operator from Eq. 8.2 is generally difficult to handle. It is better to divide the partition function into smaller problems that are easier to solve. The Hamilton operator should therefore be split in such a way that the resulting matrix elements are real, non-negative and easy to evaluate. An intuitive choice would be to divide the Hamilton operator into two terms that separate kinetic and potential energy. This would however not simplify the problem, as the off-diagonal matrix elements of the exponential of the entire kinetic energy operator are still cumbersome to evaluate [139].
Instead, the Hamiltonian is split into local Hamilton operators, such that it is written as a sum of pair Hamiltonians:

$$\mathcal{H}^{1d}_{\mathrm{BH}} = \sum_{i=0}^{L-1} \mathcal{H}_{i,i+1}\,. \tag{8.3}$$

The spatial length of the system is given by L, which is identical to the number of lattice sites in a one-dimensional system. In the case of the standard Bose-Hubbard model in one dimension, the local Hamilton operators are given by

$$\mathcal{H}_{i,i+1} = \frac{1}{4}U\left[\hat{n}_i\left(\hat{n}_i+1\right)+\hat{n}_{i+1}\left(\hat{n}_{i+1}+1\right)\right] - t\left(\hat{b}_i^\dagger\hat{b}_{i+1}+\hat{b}_{i+1}^\dagger\hat{b}_i\right)\,, \tag{8.4}$$

This maps the initial, complicated problem onto a series of connected two-site problems. These can then be combined into subtotals. The local Hamiltonians that start with an even site index and interact with their successive, odd neighbours, are summarized into a sub-Hamiltonian $\hat{\mathcal{H}}_e$, which is given by

$$\hat{\mathcal{H}}_e = \sum_{i=0}^{L/2-1} \hat{\mathcal{H}}_{2i,2i+1}\,. \tag{8.5}$$

The complementary sub-Hamiltonian $\hat{\mathcal{H}}_o$ contains the remaining terms [38]:

$$\hat{\mathcal{H}}_o = \sum_{i=0}^{L/2-1} \hat{\mathcal{H}}_{2i+1,2i+2}\,. \tag{8.6}$$

Note that both summations contain a series of two-site Hamiltonians, but each site only appears once per sum. The complete Hamiltonian is then given by

$$\hat{\mathcal{H}} = \hat{\mathcal{H}}_e + \hat{\mathcal{H}}_o \,. \tag{8.7}$$

The next step is to write down the entire partition function in a more manageable form. The individual terms in the Hamiltonian do not commute. Hence the exponential in Eq. 8.1 cannot be simply broken up into a product of exponentials.
Instead, the inverse temperature β is discretized into $\mathcal{L}$ subintervals of lenght $\Delta\tau$ [97], such that

$$\beta = \mathcal{L}\Delta\tau \,. \tag{8.8}$$

With this, the partition function from Eq. 8.1 can be rewritten as

$$\mathcal{Z} = \mathrm{Tr}\, e^{-\beta\hat{\mathcal{H}}} = \mathcal{Z} = \mathrm{Tr}\left[e^{-\Delta\tau\hat{\mathcal{H}}}\right]^{\mathcal{L}} = \mathrm{Tr}\left[e^{-\Delta\tau\left(\hat{\mathcal{H}}_e+\hat{\mathcal{H}}_o\right)}\right]^{\mathcal{L}} \,. \tag{8.9}$$

If the partition function is in this form, the Suzuki-Trotter formula [194–197] can be applied. This formula states that for $\Delta\tau \to 0$, or equivalently $\mathcal{L} \to \infty$, the exponential can be decomposited. This decomposition can also be employed for finite $\Delta\tau$ and $\mathcal{L}$, but is then referred to as "Suzuki-Trotter approximation":

$$\mathcal{Z} \approx \mathrm{Tr}\left[e^{-\Delta\tau\hat{\mathcal{H}}_e} e^{-\Delta\tau\hat{\mathcal{H}}_o}\right]^{\mathcal{L}} \,. \tag{8.10}$$

This involves an error of the order of $O(\Delta\tau^3)$. It is however a controlled approximation in the sense that the error can be reduced to any desired degree of accuracy by making $\Delta\tau$ increasingly small or $\mathcal{L}$ increasingly large. Concerning the approximative form, it is clear that systematic discretization errors are part of this procedure. It is however possible to obtain reliable results by performing calculations at different small values of $\Delta\tau$ and then to extrapolate to the limit $\Delta\tau = 0$.
The last step to obtain a world-line representation of the system is to insert $2\mathcal{L}$ sets of occupation number states $\{n^l\}$ between each exponential. This results in the effective 2D path integral representation of the system:

$$\mathcal{Z} \approx \sum_{\{n^l\}} \prod_{l=0}^{\mathcal{L}-1} \left\langle n^{2l+2}\right| e^{-\Delta\tau\hat{\mathcal{H}}_e} \left|n^{2l+1}\right\rangle \left\langle n^{2l+1}\right| e^{-\Delta\tau\hat{\mathcal{H}}_o} \left|n^{2l}\right\rangle \tag{8.11}$$

Note that the individual terms with operators in exponentials have the form of time-evolution

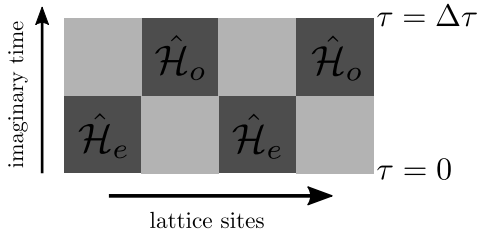

Figure 8.1: A single time slice of a one-dimensional system in the world-line representation. The horizontal direction is the spatial direction of the system, while the vertical direction represents the imaginary time direction and hereby the evolution of the system. Periodic boundary conditions apply to both directions. The dark squares depict the even and odd Hamiltonian terms from Eq. 8.5 and Eq. 8.6 and thereby represent the interactions on pairs of sites. The shifting between even and odd terms in imaginary time direction allows to treat the pairwise interactions with the adjacent sites individually.

operators. This is where the association of the inverse temperature with the imaginary time really takes place. For this reason, Eq. 8.11 is also known as the imaginary time path integral representation. The insertion of exactly $2\mathcal{L}$ complete sets of occupation number states was not arbitrary. Through Eq. 8.8, the imaginary time was split up into $\mathcal{L}$ timeslices of length $\Delta\tau$. However, since the Hamiltonian was also split up into even and odd terms in Eq. 8.7, each timeslice can also be divided into two parts. In the first part, only the even terms $\hat{\mathcal{H}}_e$ act on the system and in the second part only the odd terms $\hat{\mathcal{H}}_o$. This means that between the imaginary times $2l$ and $2l+1$, only the site-index-pairs $(1,2)$, $(3,4)$, $(5,6)$, and so on are coupled. Between the imaginary times $2l+1$ and $2l+2$ on the other hand, only the pairs $(N,1)$, $(2,3)$, $(4,5)$,... interact. A single time-slice is shown in Fig. 8.1.
This way, the bosons are described by world-lines in this formalism and the properties of the entire system are described by $2\mathcal{L}$ matrix elements. Each of these matrix elements consists of a two-site problem, which is easily calculated [38]. This form of a two-dimensional system with periodic boundary conditions describes the evolution of a one-dimensional Bose-Hubbard model through the imaginary time. Consequently, the particle paths (or world-lines) that describe the bosons need to obey periodic boundary conditions in spatial and temporal directions. Furthermore, the particle number must be conserved in each time slice. An example for the path integral representation of a one-dimensional Bose system is provided in Fig. 8.2.

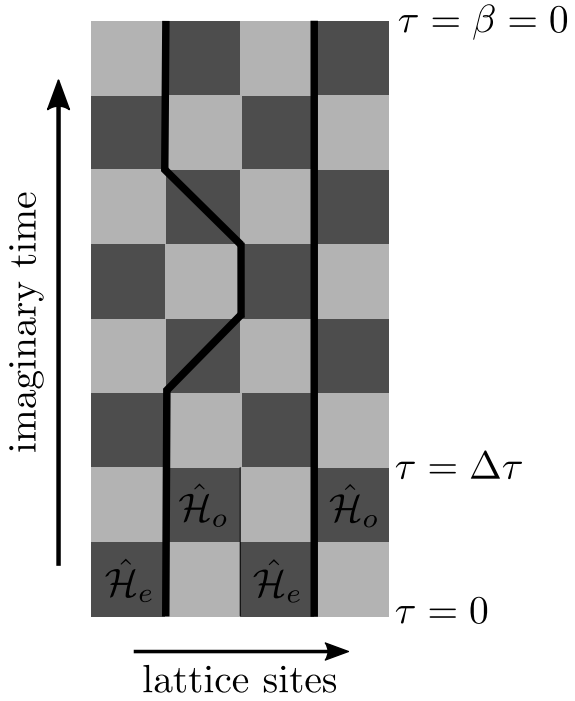

Figure 8.2: Path integral representation of a one dimensional system. The real space dimension of the system is represented by the horizontal dimension, while the vertical dimension depicts the evolution of the system in imaginary time. Both directions obey periodic boundary conditions. The dark grey squares represent the local Hamiltonian terms from Eq. 8.5 and Eq. 8.6.

This representation is also known as the "checkerboard decomposition". The dark grey plaquettes in Fig. 8.2 each represent a single matrix element. These matrix elements are especially simple. In fact, the energetic contributions can be seen directly in the figure. If a straight line is on the left or right of a grey square, the associated boson rests on that particular site for this (half) time slice and only contributes to the potential energy of the system. A diagonal line over a shaded plaquette however indicates that a boson has changed its location. This square consequently

represents a contribution to the kinetic energy. World-lines can only be parallel to the time directon or diagonal over shaded squares.
The path integral and world-line description is very helpful to visualize the difficult problem of correlated many-body quantum systems. The world-line in imaginary time of a single quantum degree of freedom is described by $2\mathcal{L}$ classical variables.

8.2 The Monte Carlo process

The initial quantum system was mapped to a two-dimensional classical system and the many-body problem with a rather large number of sites was split up into two-site problems which are easier to solve. The system is now in a form that can be treated with a classical Monte Carlo algorithm. There are two different types of updates in this algorithm. Local updates change the course of existing world-lines and conserve particle number. The mechanism of the local updates itself follows the Metropolis algorithm from Sec. 6.1.8. Global updates are only carried out when the grand-canonical ensemble is considered. Such an update either inserts or removes an entire world-line, which is associated with the addition or the removal of a particle.
The Monte Carlo algorithm used to sample the system in world-line representation is a Markov process, as introduced in Sec. 6.1.4. Therefore, the conditions ergodicity from Sec. 6.1.5 and detailed balance from Sec. 6.1.6 still need to be fulfilled. Starting point of the simulation are usually straight world-lines. After an appropriate number of updates, when the system has reached equilibrium, the measurements can commence.

8.2.1 Local updates

Coordinates in the world-line representation consist of a spatial coordinate and a point in imaginary time. The bosons are indistinguishable. If there are multiple world-lines stacked, it is not possible to assign them to certain particles. The same holds for intersections between world-lines. After two paths cross, it is not possible to differentiate the bosons.
The local update algorithm is a Metropolis algorithm and follows the outlines presented in Sec. 6.1.8. Starting points for local updates are only straight world-lines, as it only makes sense to change the location of a boson that in fact has a specific location. A straight line indicates that a boson rests at the particular site at the respective imaginary time slice. Diagonal lines over shaded squares however indicate hopping bosons. Each local update can be seen as a world-line being pulled over an empty square, to stay in the visualization of Fig. 8.2. Thus there are four energy terms, or shaded squares, involved with each update.
The outlines of the local updating mechanism are as follows. A time slice and a spatial coordinate are chosen randomly. All combinations of time slices and positions have equal probability. To see if updates at this coordinate are possible, it is checked if there exists at least one boson at the start and the end of each sub-time slice. In the case that hopping in both directions is possible, a direction is randomly chosen with equal probability. This step is not necessary if only an update in one direction is possible. Then the update is proposed. It is accepted with the acceptance ratio from the Metropolis algorithm, which was presented in Eq. 6.20. The acceptance ratio to change the local configuration from the current state μ to the new proposed state ν is given by

$$A(\mu \to \nu) = \begin{cases} e^{-\beta(E_\nu - E_\mu)} & \text{if } E_\nu - E_\mu > 0 \\ 1 & \text{otherwise.} \end{cases} \tag{8.12}$$

Consequently, the update is always accepted if the resulting local energy is lower. In the case that the new energy is higher, a random number q is drawn. If $q < e^{-\beta(E_\nu - E_\mu)}$, the update is also accepted. The world-line configuration is changed step-by-step by these local updates. An example for a local update is shown in Fig. 8.3.

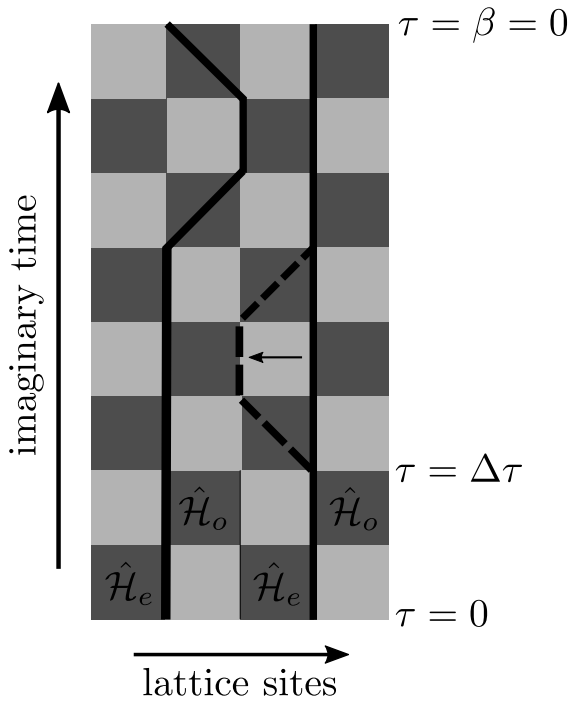

Figure 8.3: Local update of a world-line. The world-line is pulled over an empty square. This update affects the four interaction terms (represented by dark grey squares) which surround the empty square.

Calculation of local energy

To see if a local update is accepted, the difference in local energy has to be calculated. An update would pull the world-line over a empty square. Consequently, only the four grey plaquettes that surround this empty square are affected by the update. There are only five different geometries that a single world-line can have on the grey plaquettes. These possibilites are listed in Fig. 8.4. It should be emphasized that these are only the configurations for a single world-line. There can

Figure 8.4: Possible configurations of a single world-line on an interaction-square. The world-line can either not affect the square at all (boson passing the timeslice on a different site), go straight (boson resting at this site) or go diagonal over the square (boson changing the site).

be multiple world-lines on a single square, representing multiple bosons at the same site.
For a single world-line, there is a total of eight different kinds of changes that plaquettes can undergo. These changes are listed in Tab. 8.1. The cases 3, 4, 7 and 8 in Tab. 8.1 represent jumps. The changes in these plaquettes result in a change in kinetic energy. Also, there is a possible change in potential energy due to on-site repulsion. This is the case if other world-lines are involved. The cases 1, 2, 5 and 6 represent local parts of the Hamiltonian which only experience changes in potential energy. World-lines are either pulled away from or pulled onto these plaquettes. Consequently, there is only a small variety of very similar changes, which have to be evaluated very often during the sampling. It is most efficient to create a lookup table, which

allows to swiftly evaluate the affected parts of the Hamilton operator.

Case	Top left	Top right	Bottom left	Bottom right
1	0	+1	0	+1
2	0	−1	0	−1
3	+1	−1	0	0
4	−1	+1	0	0
5	−1	0	−1	0
6	+1	0	+1	0
7	0	0	+1	−1
8	0	0	−1	+1

Table 8.1: Alterations of plaquettes due to world-line updates.

8.2.2 Global updates

The manipulation of world-lines as described in the section before allows updates of the configuration in the canonical ensemble. The number of particles is conserved. However, there is also the possibility of grand-canonical updates. To realize this, entire world-lines are added to the system or removed from it. As all updates have to obey ergodicity, it is safest to only add or remove straight world-lines [138, 139]. The addition or the removal of a straight world-line only affects the potential energy, as it represents a boson that "rests" at a position i for the entire imaginary time. As there is a total of $2\mathcal{L}$ sub-timeslices, there are $2\mathcal{L}$ terms of the Hamiltonian affected by a global update. However, this can quickly be evaluated with a lookup table.
An important aspect is the rate at which global updates should be proposed. It is neither efficient nor effective to propose global updates as often as local updates. The natural approach to find a proper ratio between global and local updates is to compare both types. A global update takes the same time as $\mathcal{L}$ local updates. Consequently, the probability to propose a local update should be $\mathcal{L}$ times higher than the probability to propose a global update. In practice, a probability ratio is defined, based on parameters of the simulation. This ratio gives the probabilty to either propose one global update, or to propose a series of $\mathcal{L}$ local updates. Based on a random number, it is decided if either one global update is proposed or $\mathcal{L}$ local updates. All local sites of the chain have equal probability to be proposed for a global update. The acceptance ratio is the same as for the local updates, given by Eq. 8.12. The only difference is that more terms of the Hamiltonian are involved in the calculation of E_μ and E_ν. An example for a grand-canonical update is provided in Fig. 8.5.

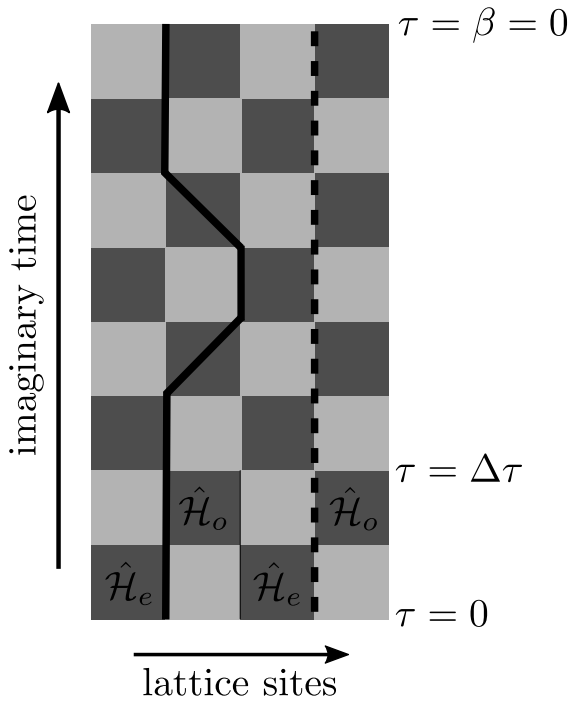

Figure 8.5: Grand canonical (or global) update in the world-line configuration through addition of a straight world-line. The update affects the energetic properties of the L adjacent interaction terms.

8.3 Nearest-neighbour interactions

To this point, only the standard Bose-Hubbard model was considered when the world-line formalism and the sampling were introduced. This was sufficient, as the involved interactions are rather simple to evaluate. For the standard Bose-Hubbard model, only two sites are involved in each update. Changes in the on-site interaction and chemical potential are reduced to the two sites that are involved in a boson-jump.
The Bose-Hubbard model with nearest-neighbour repulsion, introduced in Sec. 4.2, was also simulated with discrete world-line quantum Monte Carlo methods already [193]. It is not much more complicated to simulate than the standard Bose-Hubbard model. The off-site repulsion does not affect the partitioning of the Hamiltonian, as it can be evenly distributed to the even and odd parts.
The overall procedure is identical, except for the fact that more terms of the Hamiltonian are affected by local and global updates. This is of course due to the off-site interactions between bosons. In the case of global updates, the number of local terms involved doubles. Also, there are now six plaquettes associated with each local update, instead of only four. Both these types of updates can however be handled very easily with a lookup-table. Therefore the calculation is not much more complicated than for the standard Bose-Hubbard model.

8.4 Cavity-induced long-range interactions

The Bose-Hubbard model with cavity induced long-range interactions, presented in Sec. 4.3, is not as straightforward. It is helpful to consider the Trotter decomposition of the Hamiltonian. The following derivation was presented in Ref. [38].

In contrast to the standard Bose-Hubbard model, there is an additional long-range interaction

$$\hat{V}_{LR} = -\frac{U_l}{L}\left(\sum_{i\in e}\hat{n}_i - \sum_{i\in o}\hat{n}_i\right)^2 , \tag{8.13}$$

which does not decay with distance. This interaction is basically a potential. In the sense of the partition of the many-body Hamiltonian into even and odd parts, as seen in Eq. 8.4, Eq. 8.5 and Eq. 8.6, this term can be equally distributed to the even and odd terms. Then the sub-Hamiltonians are

$$\mathcal{H}_s = \hat{U}_s + \hat{T}_s + \hat{V}_{LR}/2 \tag{8.14}$$

with $s = \{e, o\}$. The matrix element of slice l in imaginary time can then be approximated with the symmetric Trotter decomposition:

$$\begin{aligned}\langle n^{l+1}|\, e^{-\Delta\tau\mathcal{H}_s}\,|n^l\rangle \approx \langle n^{l+1}|\, e^{-\frac{\Delta_\tau}{4}\hat{V}_{LR}} e^{-\frac{\Delta_\tau}{2}\hat{U}_s} \\ \times (1-\Delta\tau\hat{T}_s) e^{-\frac{\Delta_\tau}{2}\hat{U}_s} e^{-\frac{\Delta_\tau}{4}\hat{V}_{LR}}\,|n^l\rangle\ .\end{aligned} \tag{8.15}$$

The long-range interaction $\hat{V}_{LR}$ is diagonal when written in occupation-number basis. Because of this, the exponentials of these terms can be pulled out and the matrix element 8.15 can be re-written in the two-site representation of the standard Bose-Hubbard model with a prefactor:

$$\begin{aligned}\langle n^{l+1}|\, e^{-\Delta\tau\mathcal{H}_s}\,|n^l\rangle \approx & e^{-\frac{\Delta_\tau}{4}(V_{LR}(\{n^{l+1}\})+V_{LR}(\{n^l\}))} \\ & \times \prod_{\substack{i \text{ even} \\ (i \text{ odd})}} \langle n_i^{l+1} n_{i+1}^{l+1}|\, \mathcal{H}_{i,i+1}\,|n_i^l n_{i+1}^l\rangle\ .\end{aligned} \tag{8.16}$$

The prefactor represents the effect of the long-range interactions on the two sites that are affected by an update in the configuration. The evaluation of the matrix elements is therefore identical to the standard Bose-Hubbard model, with the exception of the $e^{-\frac{\Delta_\tau}{4}V_{LR}(\{n^l\})}$-terms.
The associated matrix elements

$$\langle n|\,\hat{V}_{LR}\,|n\rangle = V_{LR}(\{n\}) = f\left(\sum_i n_i\right) \tag{8.17}$$

are a function of only two quantities, the sums of the bosons on the even and odd sites of the lattice:

$$f = -\frac{U_l}{L}\left(\sum_{i\in e} n_i - \sum_{i\in o} n_i\right)^2 . \tag{8.18}$$

Keeping track of this sums is not complicated, as only hopping to nearest-neighbours is allowed and the updates are performed iteratively and not in parallel. Thus it is sufficient to update the sums at each update by ± 1 respectively.

8.5 Error estimation

The discrete time world-line method exhibits two different types of errors. On the one hand there is a statistical uncertainty because of the underlying Monte Carlo algorithm. This also affects the variational Monte Carlo method and was elaborated in Sec. 7.5.
On the other hand, there are also errors that are specifically associated with the discrete-time world-line Monte Carlo algorithm. One issue is the fact that the sampling is in fact executed at finite temperatures. The task is however the inverstigation of the ground states properties. For a quantum system, the true ground state is reached at $T = 0$, when all temperature fluctuations

are cancelled out and only quantum fluctuations prevail. It was furthermore addressed in Sec. 8.1 that the temperature is directly connected to the extent of the system. The inverse temperature β defines the length of the imaginary time dimension, together with the length $\Delta\tau$ of the time slices. The length $\mathcal{L}$ of the imaginary time direction is given by $\mathcal{L} = \beta/\Delta\tau$. The Trotter-discretization error occurs due to the decomposition of the imaginary time into finite intervals of length $\Delta\tau$. This discretization leads to an error of the order of $O(\Delta\tau^3)$. To obtain reliable results, the limit $\Delta\tau = 0$ should be extrapolated after performing the simulations at different finite values $\Delta\tau$.

8.6 Measurement of observables

The calculation of most quantities of interest is straightforward for the world-line algorithm, especially the observables that are diagonal in occupation number basis. The system was split up into smaller problems, and the properties of these sub-Hamiltonians are known. The evaluation of these Hamiltonians is mostly trivial. The lookup-tables which were built for the updating algrithm (Sec. 8.2.1) are useful for the evaluation. The energy can be obtained by summing over all local Hamiltonians, which are represented by shaded squares. The mean density $\bar{n}$ and the local density fluctuations κ_i can be estimated easily. First the occupation number has to be averaged over all l timeslices for all sites i.

$$\langle \hat{n}_i \rangle = \frac{1}{2\mathcal{L}} \sum_{l=0}^{2\mathcal{L}-1} \langle n(i,l) \rangle \ . \tag{8.19}$$

$n(i,l)$ denotes the number of bosons on the site i at timeslice l. Averaging the mean occupancy n_i over all sites i delivers the mean density,

$$\bar{n} = \frac{1}{L} \sum_{i=0}^{L-1} \langle \hat{n}_i \rangle \ , \tag{8.20}$$

where $\langle \ldots \rangle$ denotes the Monte Carlo average. The structure of the calculation holds for other quantities which are diagonal in occupation number basis. The structure factor Φ for example is calculated in the same way as the density, but the averages over even and odd sites are evaluated individually.

8.6.1 Superfluid density

Measuring whether the system is in a superfluid state is a little bit cumbersome with this method. The straightforward method of evaluating the phase coherence correlations function, which was presented in Sec. 4.7.1, is not efficient here. It is better to use the superfluid density that was introduced and defined in Sec. 4.7.3. This approach was already used in early works with the discrete-time world-line algorithm [97, 138, 139]. The derivation below is taken from Ref. [38].
The superfluid density scales with the mean square of the winding number $\langle W^2 \rangle$ and is defined as

$$\rho_s = \frac{\langle W^2 \rangle}{2\beta t} L \, , \tag{8.21}$$

with the hopping strength t. The winding number counts the world-lines that are wound around the system. In other words, it is the number of world-lines which overcome the periodic boundary conditions. In the algorithm presented in this chapter, the winding number is fixed to zero. There is no updating mechanism that is able to wind a world-line around the system. For this reason, the superfluid density is calculated with the help of a correlation function [97].
Some preliminary work must be done for this. The first step is to determine a function that evaluates the winding number for a given system. Thus the particles moving to the left side and

particles moving to the right side are counted individually and the difference is determined. In this sense, a function j is defined, which is evaluated for each time slice l. The function has the form

$$j(l) = \frac{1}{2} \sum_{i=0}^{L-1} [n(i,l) - n(i+1,l)] - [n(i,l+1) - n(i+1,l+1)] \; . \tag{8.22}$$

The computation of the mean-square winding number is in theory possible with this function:

$$\langle W^2 \rangle = \frac{1}{L^2} \sum_{l,l'=0}^{2\mathcal{L}-1} \langle j(l) j(l') \rangle \; . \tag{8.23}$$

As mentioned above, the update mechanism restricts the winding number to zero. Instead, a correlation function is introduced which allows the interpolation of the winding number. The correlator

$$J(l) = \langle j(l) j(0) \rangle \tag{8.24}$$

is determined and its Fourier transform is computed:

$$\tilde{J}(\omega_n) = \sum_l e^{il\omega_n} J(l) \, . \tag{8.25}$$

The value at $\omega = 0$ of this Fourier transform delivers a possibility to access the mean-square winding number

$$\tilde{J}(0) = \left\langle \sum_l j(l) j(0) \right\rangle = \frac{K^2}{2\mathcal{L}} \langle W^2 \rangle \; , \tag{8.26}$$

such that the superfluid density can be extrapolated with Eq. 8.21 and 8.26:

$$\rho_s = \lim_{\omega_n \to 0} \frac{\tilde{J}(\omega_n)}{t \Delta\tau L} \, . \tag{8.27}$$

Examples for such extrapolations are shown in Fig. 8.6.

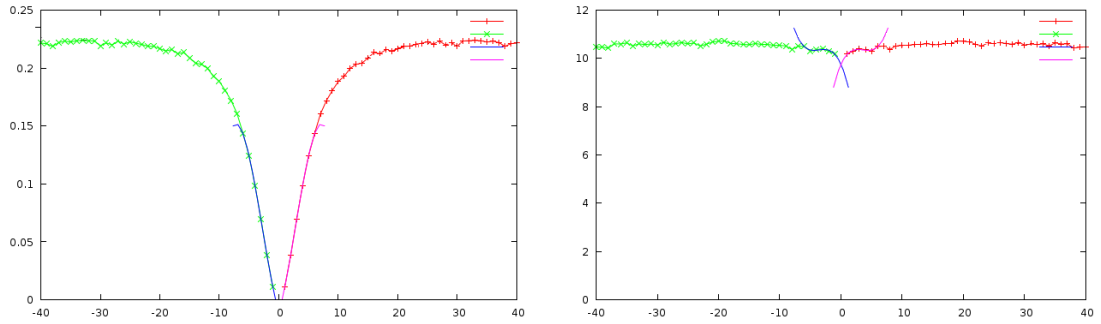

(a) $\rho_s = 0$ **(b)** $\rho_s > 0$

Figure 8.6: Fourier transform of the correlation function $\tilde{J}(\omega)$. The horizontal axis gives the frequencies ω associated with the boson modes. Superfluid bosons are in the $n(k = 0)$-mode. Thus the extrapolated value at $\omega = 0$ provides information about the superfluid density.
(a) $\rho_s = 0$ (b) $\rho_s > 0$

Chapter 9

One-dimensional phase analysis of the Bose-Hubbard models

The one-dimensional models are investigated with two different approaches: The variational Monte Carlo method (discussed in Chap. 7), which is restricted to the canonical ensemble by design, and the discrete-time world-line algorithm (presented in Chap. 8), which allows simulations in the canonical and the grand-canonical ensemble. This chapter presents ground state phase diagrams computed with the two methods. These diagrams were obtained by considering numerous "cuts" through the parameter space. This means that one of the parameters is varied while all others are fixed. The behaviour of the order parameters along these cuts reveals the phase configuration depending on the system parameters.
The standard Bose-Hubbard model is examined in Sec. 9.1 to verify the methods. The reproduction of known results serves to find suitable simulation parameters. In addition, this also offers a good opportunity to check the performance of the methods in areas that are difficult to reproduce. A grand-canonical phase diagram of the standard Bose-Hubbard model is presented and the phase transition from superfluid to Mott insulator phase is investigated with both methods.
The results for the Bose-Hubbard model with nearest-neighbour (Sec. 9.2) and long-range interactions (Sec. 9.3) each include a grand-canonical phase diagram and two canonical phase diagrams. The latter two show the same parameter range, but were generated with the two different algorithms.
One focus of the investigations in one dimension is the Haldane Bose insulator phase. Results from former publications are reproduced in order to show that the world-line quantum Monte Carlo method is capable of simulating the physics of this rare phase. Investigations of the Haldane insulator are also performed with the variational Monte Carlo method, but with non-conclusive results. In Sec. 9.5 simulations of models with nearest-neighbour interactions and long-range interactions are carried out, which indicate that the long-range interactions destroy the subtle order of the Haldane phase, even at very low U_l.

9.1 Standard Bose-Hubbard model

The standard Bose-Hubbard model was introduced in Sec. 4.1. It is described by the Hamiltonian given in Eq. 4.2. Boson hopping of the strength t and repulsion between particles with the strength U_s compete. The chemical potential μ is another parameter in grand-canonical

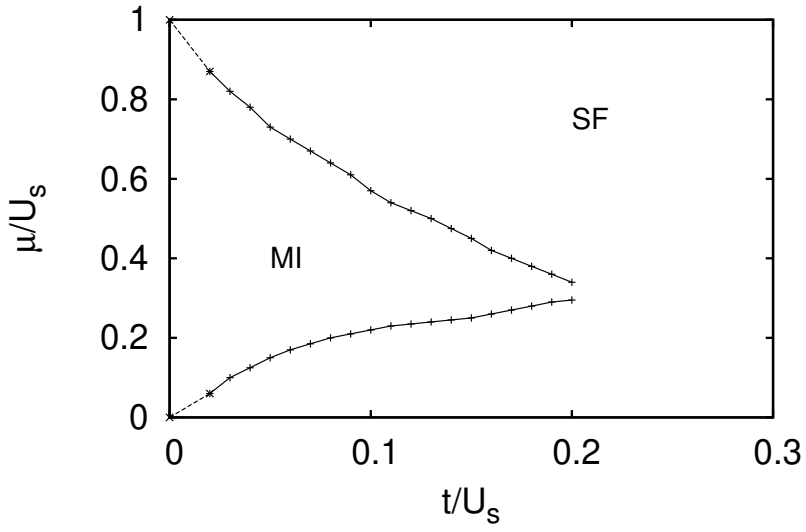

Figure 9.1: Grand-canonical phase diagram of the one-dimensional Bose-Hubbard model. Simulations were performed with a world-line quantum Monte Carlo algorithm at $\mathcal{L} = 64$, $\Delta\tau = 0.5$, $L = 64$ and $U_s = 1$. 250000 Monte Carlo updates were executed. The phase diagram comprises Mott insulator (MI) and superfluid (SF) phases. The results are in good agreement with former publications, like Ref. [84].

simulations. The standard Bose-Hubbard model only comprises two phases, the Mott insulator phase and the superfluid phase. Consequently, the order parameters S_π and Φ should be zero at all times. The phase transition between the superfluid and the Mott insulator phase is indicated by a vanishing superfluid density ρ_s. Another possibility to identify the phase transition is the parity order parameter $\mathcal{O}_p$, which is zero in the superfluid phase, and non-zero in the Mott insulator phase. The grand-canonical ground-state phase diagram of a system described by the one-dimensional Bose-Hubbard model can be seen in Fig. 9.1. The data for this graph was obtained with the discrete-time world-line algorithm at a fixed on-site repulsion strength $U_s = 1$. Solid lines indicate phase boundaries. The phase diagram is presented in the $(\mu/U_s, t/U_s)$-plane and comprises the incompressible Mott insulator phase (Sec. 4.6.1) and the superfluid phase (Sec. 4.6.2). Simulations below $t/U_s = 0.02$ were subject to severe critical slowing down and did not deliver reliable results. Therefore this was the lowest setting for which data points were acquired. The dotted lines connect these to the theoretically predicted $t = 0$-transitions.
The phase diagram is in good agreement with former works that used a similar algorithm [84,139]. The Mott insulator lobe has a fixed density $\rho = 1$ and is gapless. At low U_s/t, when the on-site repulsion is the dominant interaction, the system "prefers" the Mott insulator phase with localized particles. To minimize the energy, the chemical potential keeps the system at a constant density in the lobe. When the hopping strength t is increased, the width of the Mott insulator phase in the direction of the chemical potential becomes more narrow. The particles are delocalized in the superfluid phase, which surrounds the Mott insulator. The tip of the lobe is the only location where the transition between the two phases occurs at a constant density $\rho = 1$. This is a second

order phase transition. The rest of the phase transitions always comes along with a change in density. This can be seen in Fig. 9.2, where four density profiles are compared. These graphs are "cuts" of the phase diagram from Fig. 9.1 along the axis of the chemical potential. Above the Mott insulator phase, there are excess particles, making a commensurate filling impossible, which results in delocalization. Below the Mott lobe, the density is lower than $\rho = 1$, which also leads to delocalization of the bosons, as there are once more multiple states that are energetically equivalent. The phase transition between the superfluid and the Mott insulator phases are of

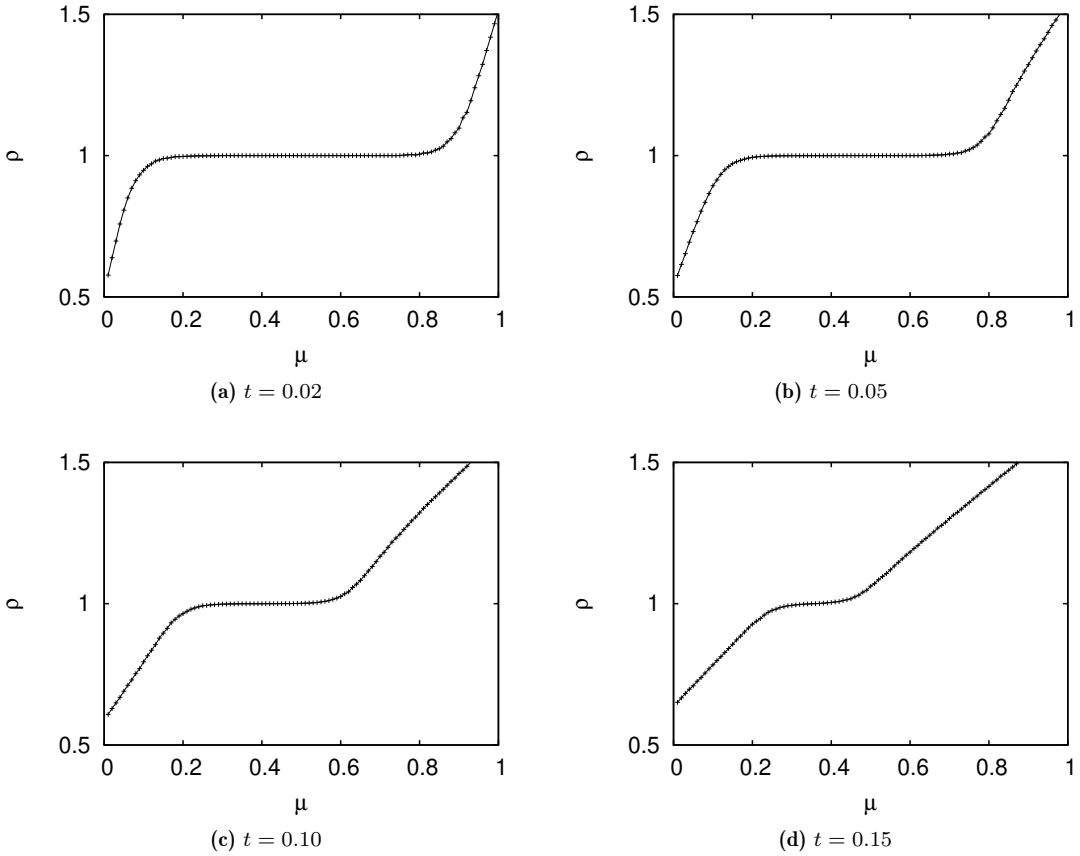

(a) $t = 0.02$ **(b)** $t = 0.05$

(c) $t = 0.10$ **(d)** $t = 0.15$

Figure 9.2: Density profiles ρ depending on the chemical potential for (a) $t = 0.02$, (b) $t = 0.05$, (c) $t = 0.10$, (d) $t = 0.15$ in the standard Bose-Hubbard model, obtained with world-line quantum Monte Carlo. The simulations were performed with $\mathcal{L} = 64$, $\Delta\tau = 0.5$, $L = 64$, $U_s = 1$, and 250000 Monte Carlo updates. Additional checking with the order parameter ρ_s shows that the areas of constant $\rho = 1$ belong exclusively to the Mott insulator phase. Areas of rising or declining density are superfluid.

second order. As mentioned, there is a difference between transitions that occur with or without a constant density. Transitions that are associated with a change in boson density are predicted to belong to the mean-field universality class, while the transition at constant density $\rho = 1$, at the tip of the lobe, is expected to belong to the 2D XY universality class [139]. More precisely, the latter was identified to be a Kosterlitz-Thouless transition [55].
The critical point of the transition which occurs at constant density was determined to be $(t/U_s)_c \approx 0.2$ with the world-line method. This transition is driven by phase fluctuations in the system. The parameters that indicate this phase transition are the superfluid density ρ_s and the parity order parameter $\mathcal{O}_p$. The superfluid density is zero in the Mott insulator phase and

non-zero in the superfluid phase. The parity order parameter behaves vice versa.
The superfluid density ρ_s was determined as explained in Sec. 8.6.1. The problem with this method is that it provides information whether the system is superfluid or not, but does not deliver an absolute value. In order to perform a finite-size scaling, the critical point at which the system starts to be superfluid was investigated for different system sizes L. The measured points are then plotted on a logarithmic scale against $1/L$. The zero-value of an exponential fit of this data delivers the critical t/U_s. This is presented in Fig. 9.3. The fit delivers the critcal

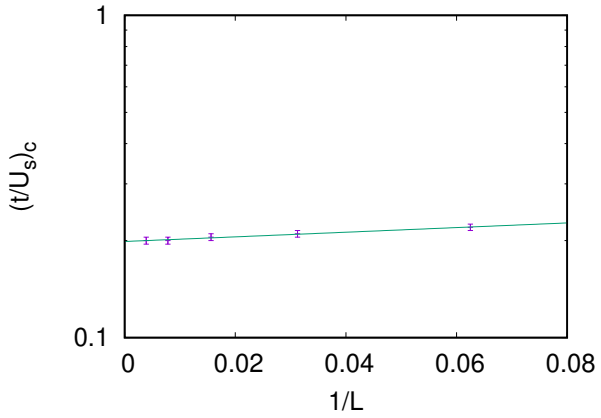

Figure 9.3: Finite-size scaling of the critical point of the Mott insulator to superfluid transition in the standard Bose-Hubbard model. The critical values of the different system sizes L are plotted on a logarithmic scale. The line denotes a fit which delivers the value $(t/U_s)_c = 0.199$ at the thermodynamic limit. Obtained with the world-line quantum Monte Carlo algorithm.

value $(t/U_s)_c = 0.199$ at the thermodynamic limit $L \to \infty$. To complement this result, the a finite-size scaling is also performed with the parity order parameter $\mathcal{O}_p$, which is non-zero in the Mott insulator phase and zero in the superfluid phase. Fig. 9.4 presents $\mathcal{O}_p$ during the Mott insulator to superfluid phase transition for various system sizes. Finite-size effects are visible.

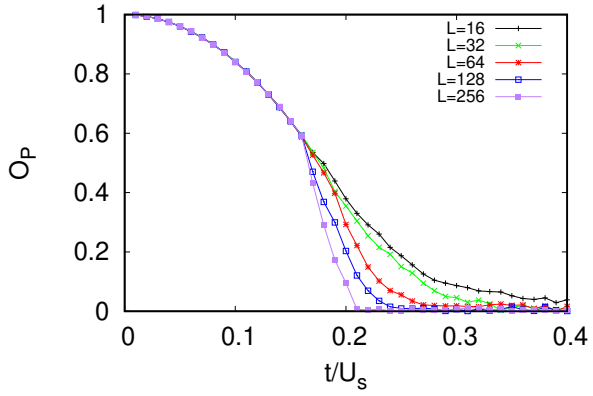

Figure 9.4: Parity order parameter during the transition from the Mott insulator to the superfluid phase in the standard Bose-Hubbard model for various system sizes L. The phase transition is characterized by a vanishing $\mathcal{O}_p$ at the critical point. Obtained with the world-line quantum Monte Carlo algorithm.

The values of $\mathcal{O}_p$ of the different system size at the critical point are plotted on logarithmic scale against the sytem sizes L. This is presented in Fig. 9.5. At the critical point, the order

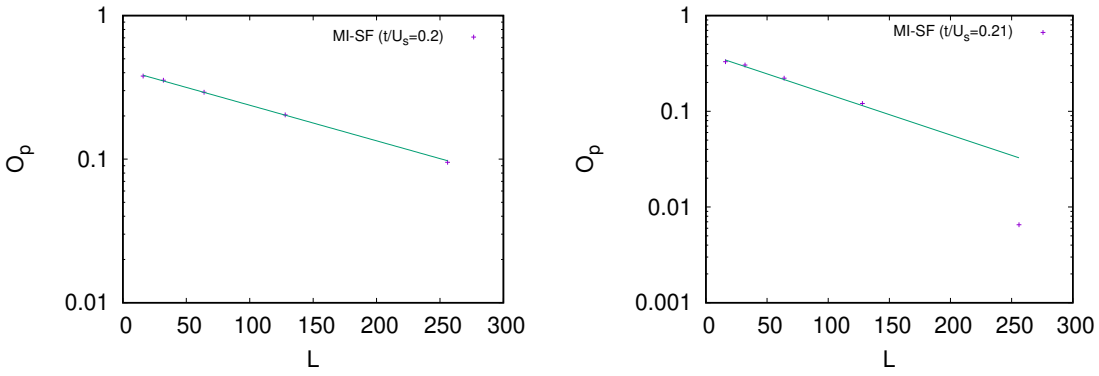

(a) $t/U_s = 0.2$ **(b)** $t/U_s = 0.21$

Figure 9.5: Finite-size scaling of the parity order parameter $\mathcal{O}_p$ for the transition from Mott insulator (MI) to superluid (SF) phase at (a) $t/U_s = 0.2$ (b) $t/U_s = 0.21$ in the standard Bose-Hubbard model. Straight lines show the best possible fits. Fig. (a) confirms the critical point at $t/U_s = 0.2$, as it shows that $\mathcal{O}_p$ goes exponentially to zero with the system size L. It was fitted with $\mathcal{O}_p = 0.42 \exp(-0.0057L)$. The point t/U_s lies already in the superfluid phase. Obtained with the world-line quantum Monte Carlo algorithm.

parameter should decay exponentially with the system size L. This is the case for the critical value $(t/U_s)_c = 0.2$, as Fig. 9.5a shows. The data was fitted with $\mathcal{O}_p = 0.42 \exp(-0.0057L)$. In the case of $(t/U_s)_c = 0.21$ in Fig. 9.5b such a fit is not possible, this point lies already in the superfluid phase.
The Mott insulator to superfluid phase transition in the standard Bose-Hubbard model was also investigated with the variational Monte Carlo method. A plot of ground state energies with error bars obtained with the variational Monte Carlo algorithm is presented in Fig. 9.6.

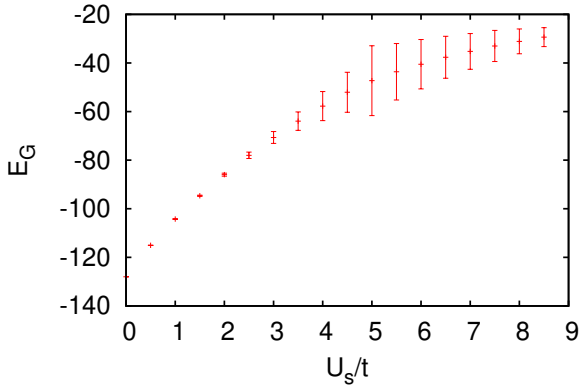

Figure 9.6: Ground state energy during the superfluid to Mott insulator in the standard Bose Hubbard model. Increasing of $U_s/$ leads to an increase in the ground state energy during the superfluid phase. The growing error bars indicate the critical region. Obtained with the variational Monte Carlo method.

Note that with this method, the phase transition was studied by varying the ratio U_s/t, in contrast to t/U_s with the world-line Monte Carlo method. The ground state energy rises with increasing U_s/t in the superfluid phase. As the particles are entirely delocalized, a higher on-site repulsion results in a higher energy of the system. The error bars in the superfluid phase are very small. This is expected, as the wave function of a superfluid state is the basis of the Jastrow ansatz (Sec. 7.2). The system reaches the critical region when U_s/t is increased further. This results in larger error bars. The largest error bar at $U_s/t = 5$ indicates the critical point. This corresponds well to the results from the world-line quantum Monte Carlo, which detected the critical point at $(t/U_s)_c = 0.2$. To support this, the phase coherence correlation function $G(R)$ was evaluated at $R = L/2$ for various L during the phase transition. This is presented in Fig. 9.7. A non-zero

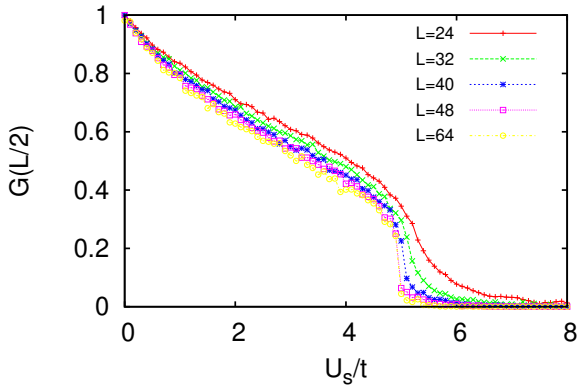

Figure 9.7: Correlation function $G(R)$ measured at the maximum distance in the system $R = L/2$ in the standard Bose-Hubbard model. A non-zero value indicates long-range phase coherence and thus superfluidity. For larger L, there is a spontaneous jump at $U_s/t = 5$, indicating a phase transition. Obtained with the variational Monte Carlo method.

phase coherence correlation function at the maximum distance in the system, which is $R = L/2$ in a one-dimensional chain, indicates superfluidity. Fig. 9.7 shows a spontaneous jump at $U_s/t = 5$ for larger system sizes L, which corresponds to a transition from a superfluid to an insulating phase. Both methods found the critical point between Mott insulator and superfluid phase in the one-dimensional Bose-Hubbard model at $(t/U_s)_c = 0.2$. This value is close to the results of former studies with a discrete-time world-line algorithm, which is very similar to the one used in this work. The critical point was found at $(t/U_s)_c = 0.215$. However these values deviate much from the results with other methods. The criticial point was found at $(t/U_s)_c = 0.277$ with DMRG [114], at $(t/U_s)_c = 0.275$ with exact diagonalization [198], at $(t/U_s)_c = 0.289$ with the Bethe-Ansatz solution [199] and at $(t/U_s)_c = 0.304$ with strong coupling expansion [200]. It was stated that *the range of these results demonstrates that determining the location of this transition is ill conditioned* [84].

9.2 Bose-Hubbard model with nearest-neighbour interactions

This section presents results for simulations of the one-dimensional Bose-Hubbard model with nearest-neighbour interactions, which was introduced in Sec 4.2. A grand-canonical phase dia-

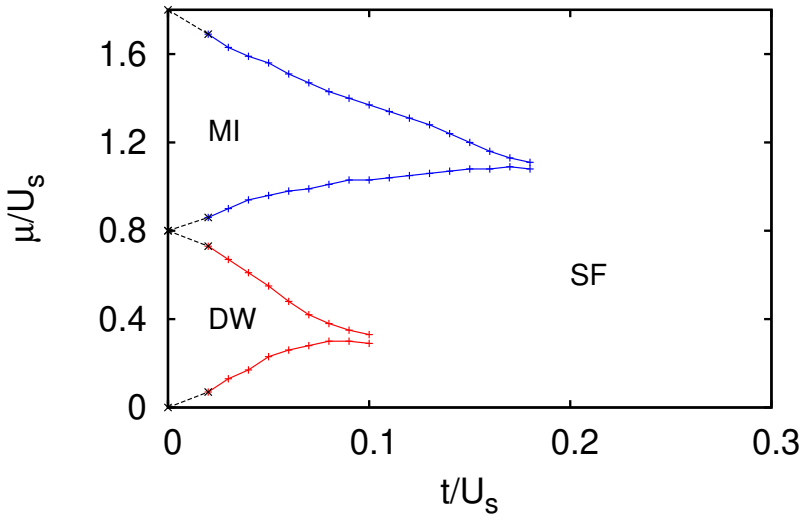

Figure 9.8: Grand-canonical phase diagram of the one-dimensional Bose-Hubbard model with nearest-neighbour interactions. Simulations were performed with a world-line quantum Monte Carlo algorithm at $\mathcal{L} = 64$, $\Delta\tau = 0.5$, $L = 64$, $N = 64$, $U_s = 1$ and $U_{nn} = 0.4$. The phase diagram comprises Mott insulator (MI), superfluid (SF) and density wave (DW) phases. The results are in good agreement with former publications, like Fig. 5 in Ref. [84].

gram with nearest-neighbour interactions at a fixed strength $U_{nn} = 0.4$ is presented in Fig. 9.8. The diagram is in good agreement with former results [84]. A comparison of this phase diagram to the corresponding phase diagram of the standard Bose-Hubbard model from Fig. 9.1 shows that the nearest-neighbour interactions give rise to an additional phase. Aside from the Mott insulator lobe, which is also present here, but smaller and vertically shifted, there is a density wave lobe at low chemical potential μ and low t/U_s. The density wave phase was introduced in Sec. 4.6.3. It is characterized by localized particles and a modulation in the spatial occupation of sites. The dotted lines in Fig. 9.8 connect the simulation data at $t/U_s = 0.02$ with the theoretically obtained $t = 0$-transitions.
The diagrams in Fig. 9.9 present cuts through the phase diagram along the chemical potential at various hopping strengths t. The subfigures show density profiles ρ and the order parameter Φ (Sec. 4.7.4), which measures the imbalance in the occupation of even and odd lattice sites. In comparison to the graphs in Fig. 9.2, which were measured at the same hopping strengths t but with $U_{nn} = 0$, the density profiles are significantly altered by the additional interaction between the bosons.
The density wave phase is a lobe of constant density $\rho = 0.5$. It has the spatial structure $DW(1, 0)$ which means that, on average, every other site is occupied by one boson. The phase transitions between the density wave phase and the other two phases are first order phase transitions.

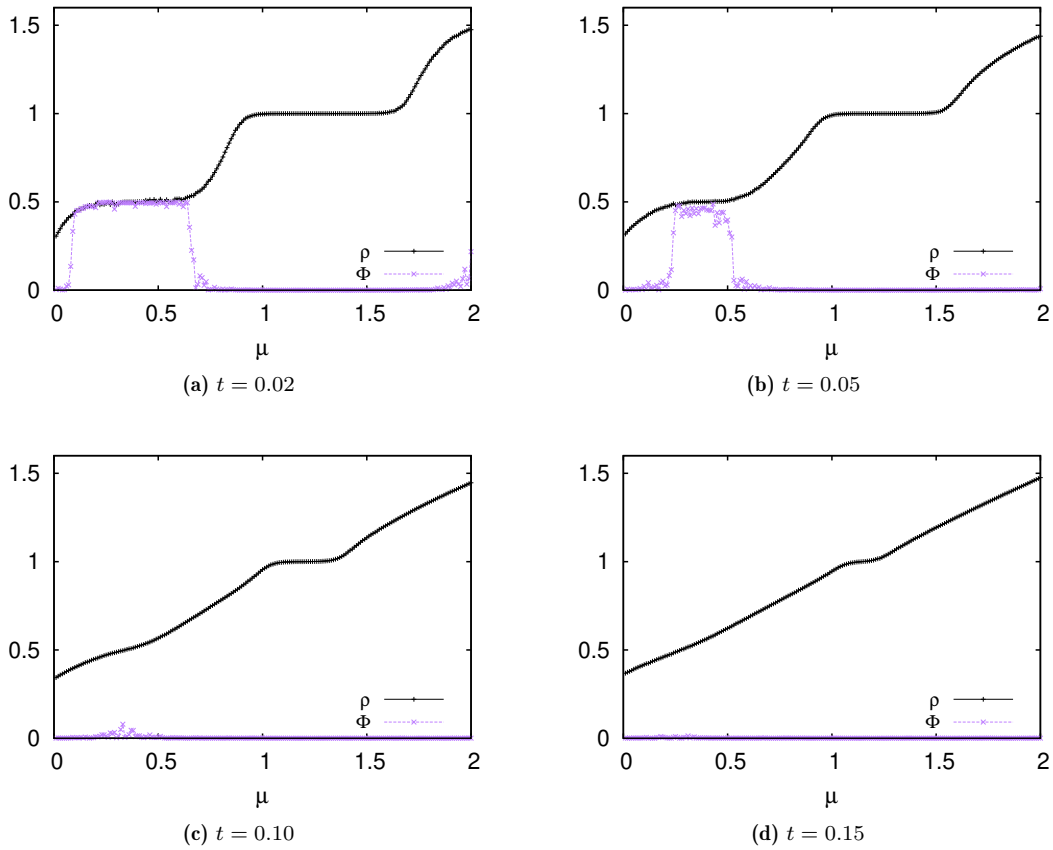

(a) $t = 0.02$ **(b)** $t = 0.05$

(c) $t = 0.10$ **(d)** $t = 0.15$

Figure 9.9: Density profiles ρ and the imbalance Φ in a Bose-Hubbard model with nearest-neighbour interactions depending on the chemical potential for (a) $t = 0.02$, (b) $t = 0.05$, (c) $t = 0.10$, (d) $t = 0.15$. The world-line quantum Monte Carlo simulations were performed with $\mathcal{L} = 64$, $\Delta\tau = 0.5$, $L = 64$, $N = 64$, $U_s = 1$ and $U_{nn} = 0.4$. In comparison to the corresponding graphs in Fig. 9.2, there is an additional density wave lobe with constant density $\rho = 0.5$.

Another grand-canonical phase diagram of the Bose-Hubbard model with nearest-neighbour interactions is presented in Fig. 9.10. The strength of the nearest-neighbour interactions has been raised to $U_{nn} = 0.75$ in this phase diagram. The higher strength of the nearest-neighbour interactions leads to a significantly different phase diagram compared to the system with $U_{nn} = 0.4$ (Fig. 9.8). The Mott insulator is suppressed in the parameter area covered by the diagram. Instead, there are multiple density wave lobes at low hopping strengths t. Each of this lobes has a half-integral or integral density. Starting from the bottom, the density rises from lobe to lobe in half-integral steps. The spatial structure of the density wave phases in these areas is characterized by an occupation that alters between zero and an integer value.
The strong nearest-neighbour interactions have also induced the formation of the supersolid phase. The supersolid phase was discussed in Sec. 4.6.4. Particles are delocalized in this phase, but the average density alters between neighbouring sites. There is a second order phase transition between the density wave phase and the supersolid phase, characterized by the emergence of the superfluid density, or condensate fraction.
A large part of the parameter range shown in the diagram is occupied by the superfluid phase. The transition from the supersolid to the superfluid phase is also of second order and is characterized by a declining structure factor. At low chemical potentials and low t/U_s, there is a

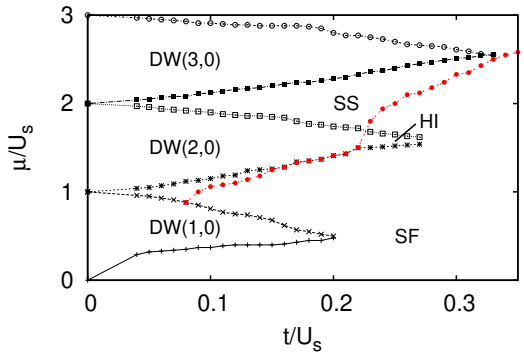

Figure 9.10: Grand-canonical phase diagram of the one-dimensional Bose-Hubbard model with nearest-neighbour interactions. Simulations were performed with a world-line quantum Monte Carlo algorithm at $\mathcal{L} = 64$, $\Delta\tau = 0.5$, $L = 32$, $N = 32$, $U_s = 1$ and $U_{nn} = 0.75$. The Mott insulator (MI) phase is not present in this phase diagram. Instead there are multiple density wave (DW) lobes, an intermediate supersolid (SS) region and a superfluid (SF) area. There is a small Haldane insulator phase at the tip of the lowest density wave lobe.

first order transition from the density wave phase to the superfluid phase. The second lobe has the density $\rho = 1$ and represents an area in which the ground state of the system is the density wave phase with the spatial structure $(2, 0)$. However, at the tip of this lobe there is a small Haldane insulator phase, which has also density $\rho = 1$ (Sec. 5). The Haldane insulator shows a non-zero string order paramter $\mathcal{O}_s$, while the remaining order parameters are zero. There is a small, intermediate supersolid area between the $\rho = 0.5$ and the $\rho = 1$ density wave phases. An imaginary connection-line between the highest end of this area and the start of the supersolid phase above the $\rho = 1$ lobe "cuts" right through the lobe and marks the beginning of the Haldane insulator phase. This was also observed in Ref. [110].
The phase diagram shown in Fig. 9.10 is in agreement with the results shown in Fig. 4 from Ref. [110].

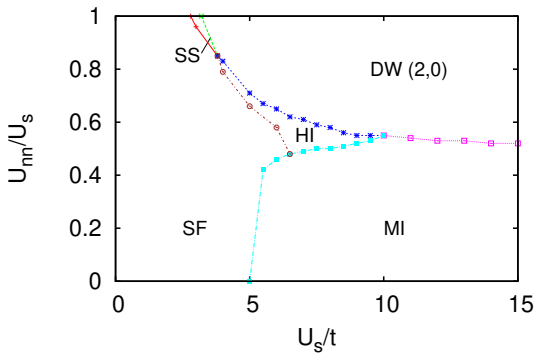

Figure 9.11: Phase diagram of the Bose-Hubbard model with nearest-neighbour interactions in one dimension. Simulations were performed with a world-line quantum Monte Carlo algorithm at $\mathcal{L} = 64$, $\Delta\tau = 0.5$, $L = 64$, $N = 64$ and $t = 1$. The phases which could be identified are Mott insulator (MI), superfluid (SF), density wave (DW), supersolid (SS) and Haldane insulator (HI).

A phase diagram in the $(U_{nn}/U_s), (U_s/t)$-plane at a fixed density $\rho = 1$ is presented in Fig. 9.11. This phase diagram was obtained with the world-line quantum Monte Carlo method. There are five different phases. The superfluid phase prevails at low U_s/t, independent of the strength U_{nn} of the nearest-neighbour interactions. At high U_s/t, the system is in the insulating Mott and density wave phases. Between the superfluid and the density wave phase, there is a small but stable supersolid phase. There is also a small Haldane insulator region in the center of the phase diagram. The transition line between Mott insulator and density wave is located at about $U_{nn}/U_s = 0.5$ for high U_s/t. The critical point between the superfluid and the Mott insulator phases lies at $(U_s/t)_c = 5$, which agrees with the measurement $(t/U_s)_c = 0.2$ from the grand-canonical simulation of the standard Bose-Hubbard model from Fig. 9.1. The transition line between superfluid and Mott insulator states depends on the strength of the nearest-neighbour interactions U_{nn}, which will be discussed later. Only a small area of the phase diagram is covered by the supersolid phase. It is located between the superfluid and the density wave phases. The

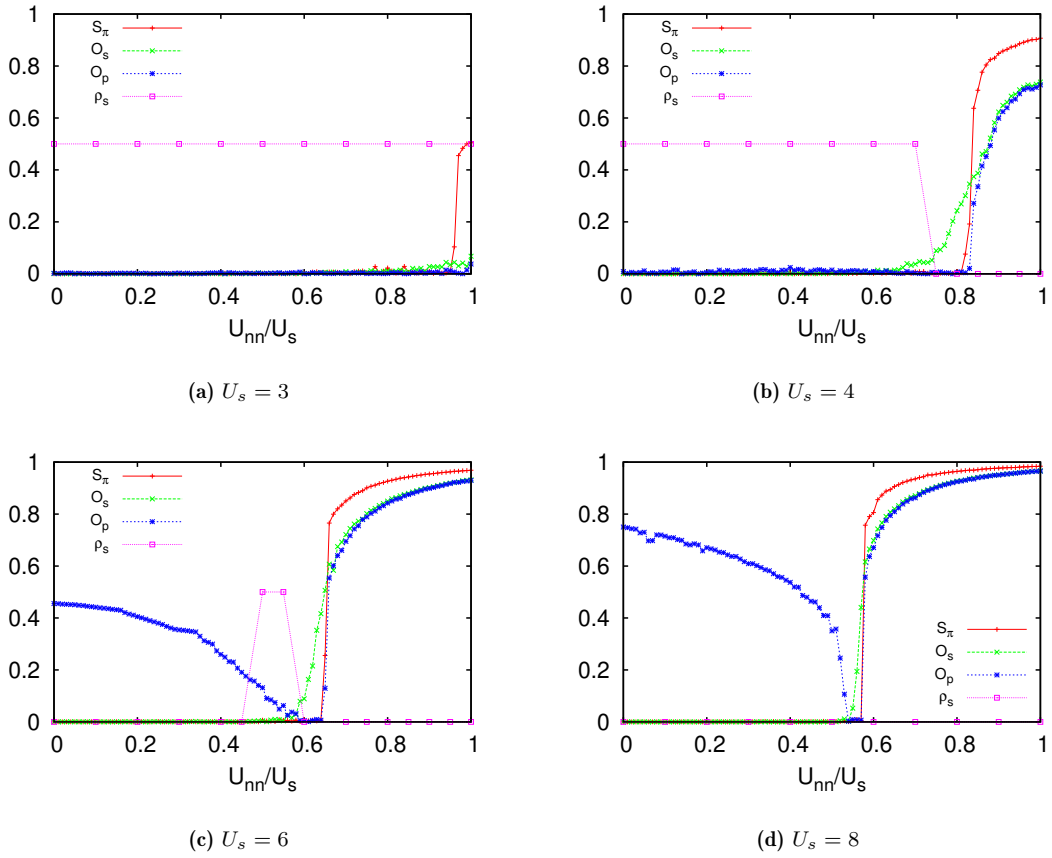

(a) $U_s = 3$ **(b)** $U_s = 4$

(c) $U_s = 6$ **(d)** $U_s = 8$

Figure 9.12: Order parameters in the Bose-Hubbard model with nearest-neighbour interactions in one dimension at (a) $U_s = 3$ (b) $U_s = 4$ (c) $U_s = 6$ (d) $U_s = 8$. Simulations were performed with a world-line quantum Monte Carlo algorithm at $\mathcal{L} = 64$, $\Delta\tau = 0.5$, $L = 64$, $N = 64$ and $t = 1$.

Haldane insulator phase lies between Mott insulator and density wave phase. The size and placement of the Haldane phase is in good agreement with the DMRG results presented in Fig. 1 in Ref. [81]. Both plots show a similar parameter range, but are scaled differently. The main difference lies in the size of the Haldane phase, which is smaller in Fig. 9.11 in comparison to the DMRG results. The DMRG results are most probably more precise, as the world-line Monte

Carlo also underestimates the size of the Haldane phase in Fig. 9.10 in comparison to Ref. [110], which uses an exact quantum Monte Carlo method. Cuts through the phase diagram from Fig. 9.11 which show the order parameters for varying U_{nn}/U_s are presented in Fig. 9.12. The order parameters indicate the existence of a stable Haldane insulator phase.
An additional phase diagram is provided in Fig. 9.13. It shows the same model and parameter range as Fig. 9.11, but the data was obtained with variational Monte Carlo simulations. A

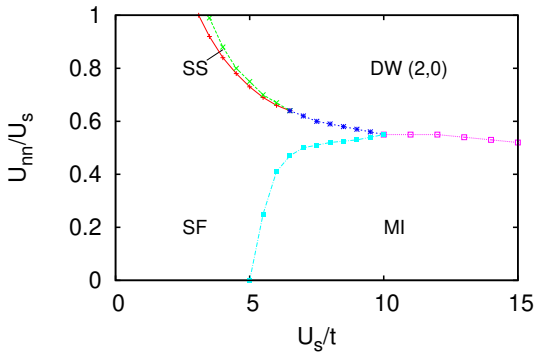

Figure 9.13: Phase diagram of the Bose-Hubbard model with nearest-neighbour interactions in one dimension. Simulations were performed with a variational Monte Carlo algorithm at 200 iterations, $L = 64$, $N = 64$ and $t = 1$. The Mott insulator (MI), superfluid (SF), density wave (DW) and supersolid (SS) phases could be identified, while this is not the case for the Haldane insulator with this method.

comparison of the phase diagrams in Fig. 9.11 and Fig. 9.13 shows that both methods deliver very similar results. The Haldane insulator phase could however not be identified with the variational Monte Carlo method. Cuts through the phase diagram in Fig. 9.13 are shown in Fig. 9.14. The cuts were taken at the positions in the parameter space as the ones in Fig. 9.12. Comparison between the subfigures in Figs. 9.12 and 9.14 shows that the results from the worldline algorithm show a Haldane insulator phase between Mott insulator and density wave phases, while this region is superfluid according to the variational Monte Carlo method. Aside from this, the results from both methods are in very good agreement.

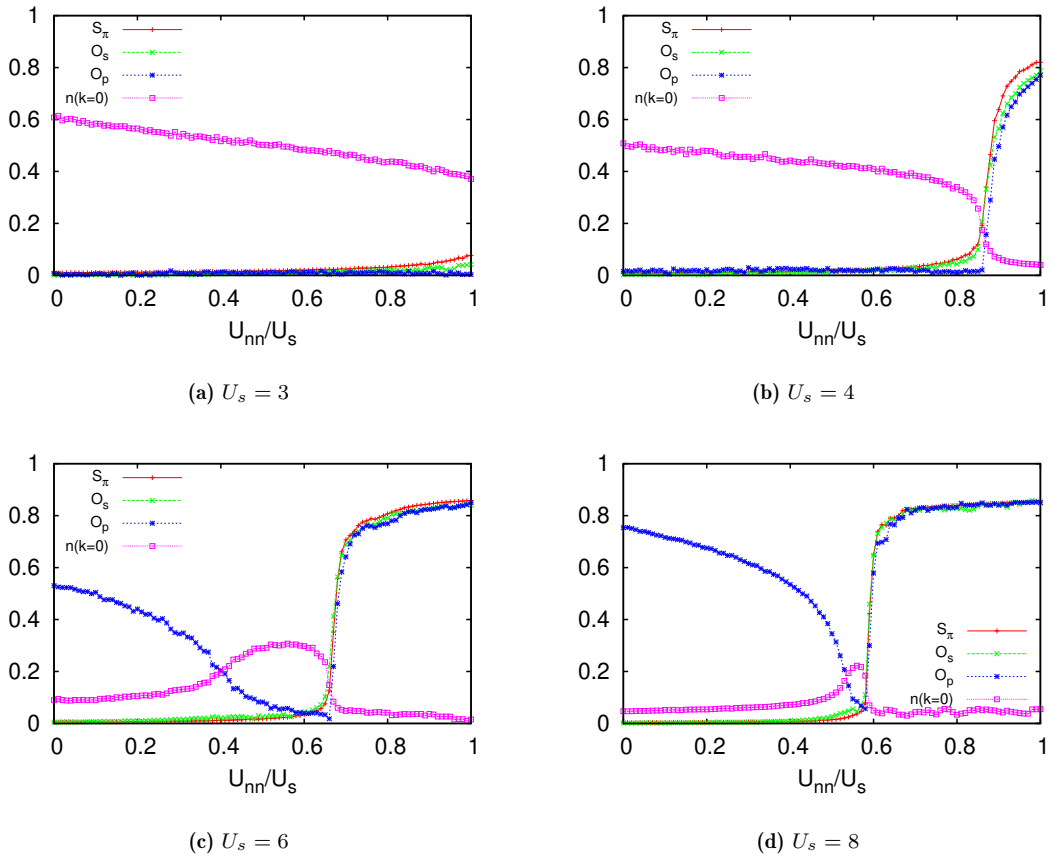

(a) $U_s = 3$ **(b)** $U_s = 4$

(c) $U_s = 6$ **(d)** $U_s = 8$

Figure 9.14: Order parameters in the Bose-Hubbard model with nearest-neighbour interactions in one dimension at (a) $U_s = 3$ (b) $U_s = 4$ (c) $U_s = 6$ (d) $U_s = 8$. Simulations were performed with a variational Monte Carlo algorithm at 200 iterations, $L = 64$, $N = 64$ and $t = 1$.

9.2.1 Haldane insulator phase

The Haldane Bose insulator state was introduced and discussed in Chap. 5. It is a rare insulating phase, characterized by a strongly non-local order. It can be identified using the string order parameter, a non-local string correlation function. The remaining order parameters are zero in this phase.
This Haldane insulator phase was detected in the phase diagrams in Figs. 9.10 and 9.11 in this chapter. The simulations were performed usind world-line quantum Monte Carlo methods in the canonical and the grand-canonical ensemble. Taking a closer look at the second lobe in the grand-canonical phase diagram in Fig. 9.10, there is a phase transition from density wave to the Haldane insulator state to the superfluid phase at $\rho = 1$. Fig. 9.15 shows the change of the order parameters during this double phase transition. The data for this figure was calculated with a

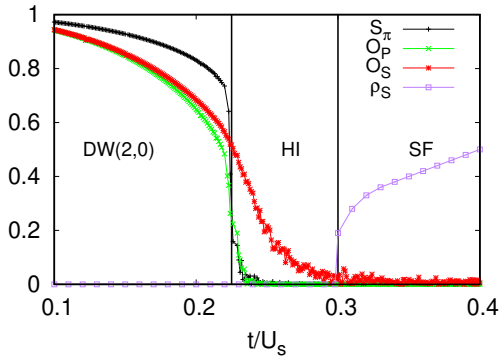

Figure 9.15: Order parameters during phase transitions from density wave (DW) to Haldane insulator (HI) to superfluid (SF) phase at constant density $\rho = 1$ in the Bose-Hubbard model with nearest-neighbour interactions. The data was obtained with world-line quantum Monte Carlo methods at $\mathcal{L} = 64$, $\Delta\tau = 0.5$, $L = 256$, $N = 256$ and $U_{nn} = 0.75$.

world-line Monte Carlo simulation with $\mathcal{L} = 64$, $\Delta\tau = 0.5$, $L = 256$, $N = 256$ at $U_{nn} = 0.75$. The phase transition between density wave and Haldane Bose insulator takes place at $t/U_s = 0.23$, where only the string order parameter $\mathcal{O}_s$ keeps a value that is significantly different from zero. The superfluid density ρ_s rises at $t/U_s = 0.3$. This is where the Haldane insulator ends and the superfluid density begins. These critical points are in good agreement with the data from Fig. 1 in Ref. [110]. The phase boundaries between the Haldane insulator and its neighbouring phases were determined with finite-size scaling. The order parameters and the finite-size scaling plot are shown in Fig. 9.16. The order parameters in Figs. 9.16c, 9.16a and 9.16b show finite-size effects. The transition from density wave phase to Haldane phase is characterized by a vanishing parity order $\mathcal{O}_p$, while a vanishing string order $\mathcal{O}_s$ indicates the transition from Haldane insulator to superfluid phase. The finite-size scaling is performed as explained in Sec. 9.1. The critical points are confirmed by the fits in Fig. 9.16d. The parity order decays exponentially at the critical point between density wave and Haldane phase. The fit $\mathcal{O}_p = 0.181 \exp(-0.0069L)$ determines the critical point at $(t/U_s)_c = 0.231$. The string order parameter at the critical point $(t/U_s)_c = 0.301$ is fitted with $\mathcal{O}_s = 0.468 \exp(-0.0072L)$.
The world-line Monte Carlo method delivers fairly good results for the Haldane insulator phase despite of being non-exact. The variational Monte Carlo method however does not deliver conclusive results for the Haldane insulator phase. Fig. 9.17 shows variational Monte Carlo measurements for the parameter range in which a Haldane insulator phase is expected. The Haldane insulator phase can not be detected with this data. The simulations indicate a direct transition from the density wave to the superfluid phase. A possible explanation for this is the fact that the variational Monte Carlo method only considers translational invariant states. States of Haldane

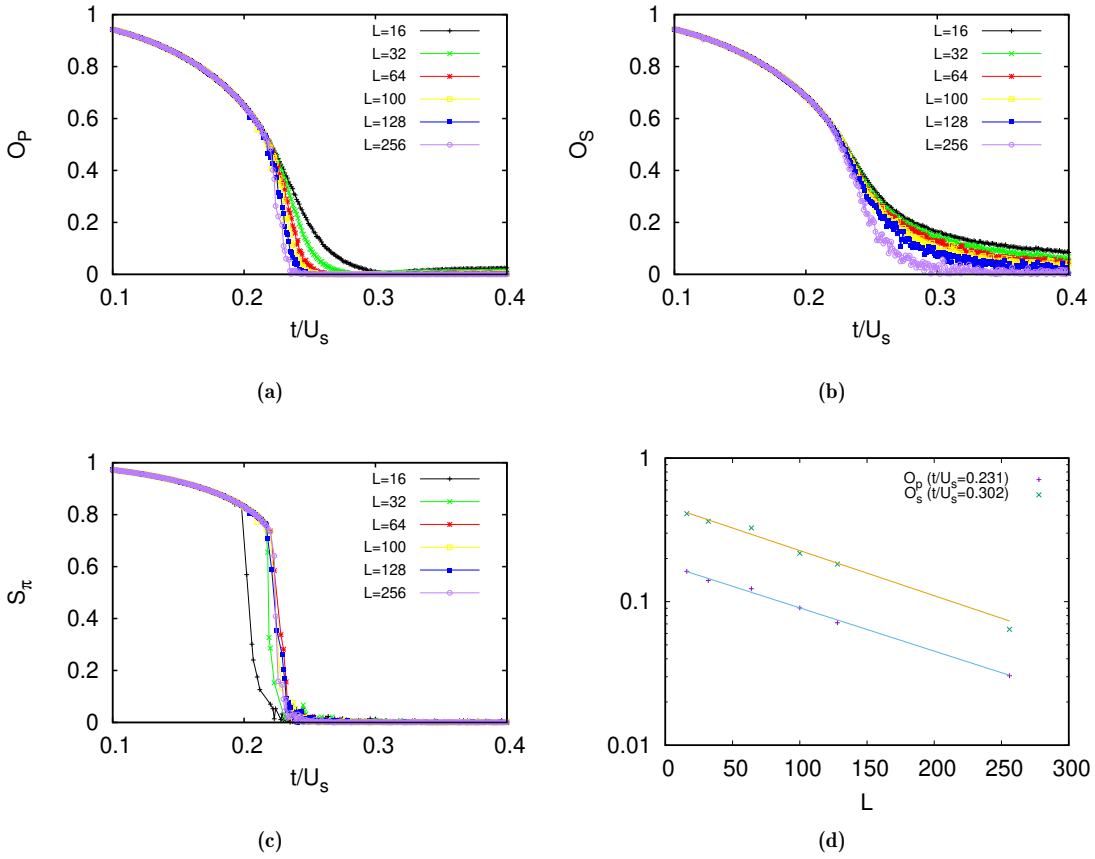

Figure 9.16: Order parameters (a) $\mathcal{O}_p$ (b) $\mathcal{O}_s$ (c) S_π during the the density wave to Haldane insulator transition in the Bose-Hubbard model with nearest-neighbour interactions at $\rho = 1$, $U_{nn} = 0.75$ for various system sizes. (d) shows finite-size scaling plots for the transitions from density wave to Haldane insulator phase ($\mathcal{O}_p \to 0$) and from Haldane insulator to superfluid phase ($\mathcal{O}_s \to 0$).

insulator are however generally not translational invariant. This restriction leads to meaningless values when measuring the string and parity order parameters. This assumption is supported by Fig. 9.17, in which Φ, $\mathcal{O}_s$ and $\mathcal{O}_p$ all have almost the same value. The phase coherence correlation function, measured with variational Monte Carlo simulations, is shown Fig. 9.18. While the investigations with world-line quantum Monte Carlo methods above indicate that the Haldane phase is located in a parameter range from $t/U_s = 0.23$ to $t/U_s = 0.3$ at $U_{nn} = 0.75$, these parameter configurations are identified as superfluid with the variational Monte Carlo.
The results above have shown that the variational Monte Carlo algorithm used in this work in principle delivers good results in simulations of the Bose-Hubbard model with next-neighbour interaction. The phase diagram in Fig. 9.13 is very similar to the respective results of the world-line quantum Monte Carlo in Fig. 9.11 and to phase diagrams obtained with DMRG [81]. It is however not capable of identifying the Haldane insulator phase. This is most likely caused by the fact that this particular variational Monte Carlo algorithm is based on a Jastrow wave function (Sec. 7.2), which can only represent translational invariant configurations. A many-body interaction term (Sec. 7.2.2) has been added to make the algorithm more precise regarding fluctuations. However, this may not be sufficient to allow the simulation of states with non-local, non-translational invariant order.

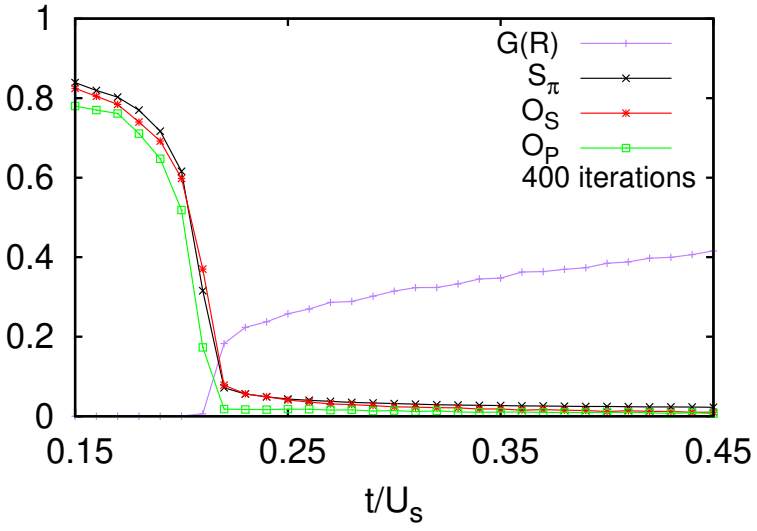

Figure 9.17: Order parameters during the expected phase transitions from density wave to Haldane insulator to superfluid phase in the Bose-Hubbard model with nearest-neighbour interactions at $U_{nn} = 0.75$. The Haldane insulator phase cannot be detected with this data. Instead, a direct phase transition from density wave to superfluid phase is indicated.

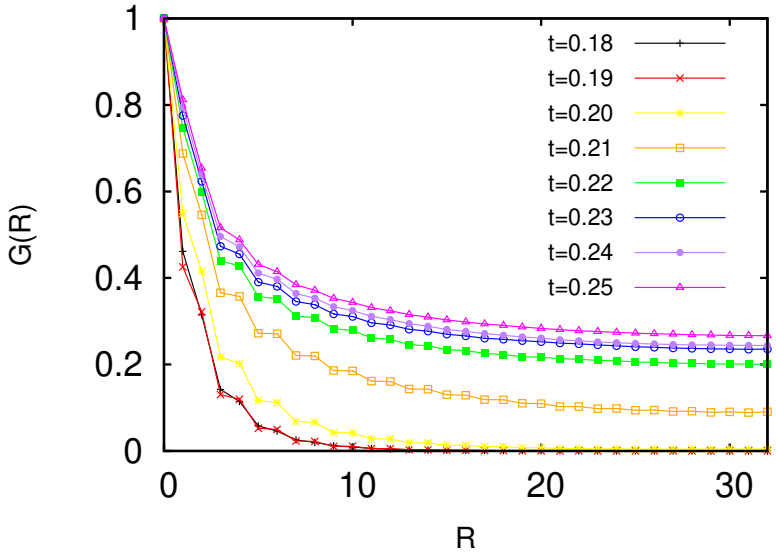

Figure 9.18: Phase coherence correlation function $G(R)$ at different hopping strengths t. A non-zero value at $R = L/2$ indicates superfluid behaviour. The data was obtained by variational Monte Carlo simulations with 200 optimization iterations at $L = 64$, $U_s = 1$ and $U_{nn} = 0.75$.

9.3 Bose-Hubbard model with long-range interactions

This section presents results for the one-dimensional Bose-Hubbard model with long-range interactions, which was introduced in Sec. 4.3.
A grand-canonical ground state phase diagram is shown in Fig. 9.19. The diagram was created using the world-line Quantum Monte Carlo algorithm, with the strength of the long-range interactions fixed to $U_l = 0.3$. This rich phase diagram comprises Mott insulator, density wave,

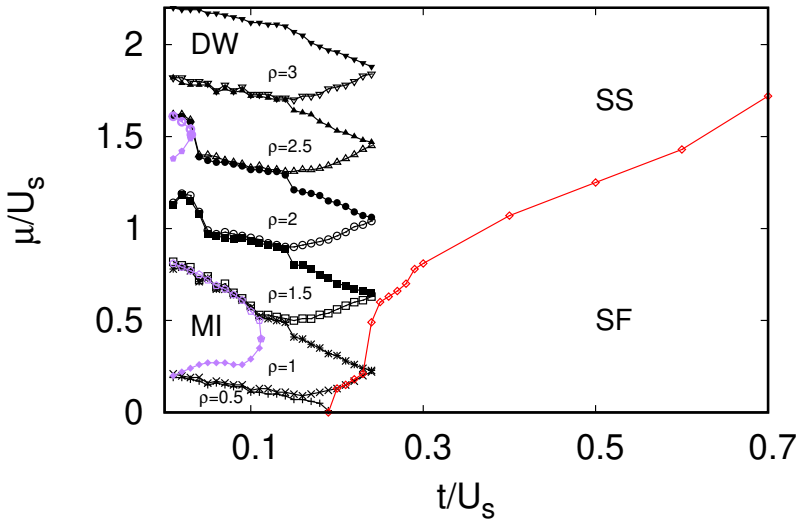

Figure 9.19: Grand-canonical phase diagram of the Bose-Hubbard model with long-range interactions in 1D at $U_l = 0.3$. Simulations were performed with a world-line quantum Monte Carlo algorithm at $\mathcal{L} = 64$, $\Delta\tau = 0.5$, $L = 32$, $N = 32$ and $U_s = 1$. The phase diagram comprises Mott insulator (MI), density wave (DW), supersolid (SS) and superfluid (SF) phases.

supersolid and superfluid phases. The insulating states prevail at low t/U_s. Stacked density wave lobes dominate the phase diagram in this region. The lobes, which all have half-integer oder integer particle densities, are of very similar size. The spatial structure in these density wave phases is always the same. Sites with (on average) zero particles alternate with sites that are (on average) occupied by the same integer number of particles. The lowest lobe has the particle density $\rho = 0.5$ an the occupation structure $(1, 0)$, the second lobe has density $\rho = 1$ and structure $(2, 0)$ and so on.
The areas with $\rho = 1$ and $\rho = 2$ area special, because there is a stable Mott insulator lobe inside of the density wave phase. These exist only for very low t/U_s, when the on-site repulsion dominates the energetic properties of the system. There is a first order phase transition which separates Mott insulator and density wave phases. Superfluid and supersolid phases emerge when the parameters are tuned and the hopping t becomes dominant. The transition from density wave to supersolid phase is of second order, the transition from density wave to superfluid phase is of first order.
Overall, this phase diagram is quite similar to the grand-canonical phase diagram which was shown in Fig. 9.10, with the exception that the Mott insulator phase is not entirely suppressed in the phase diagram of the system with long-range interactions. An imaginary line “cuts” through the second density wave lobe in both diagrams, when the supersolid phases below and above this lobe are connected. In the case of the system with nearest-neighbour interactions, this is the region of the Haldane insulator. In the model with long-range interactions, the tip of the lobe

behaves like an ordinary density wave phase and no Haldane insulator phase was detected.
Two canonical phase diagrams of the Bose-Hubbard model with long-range interactions are presented in Fig. 9.20 and Fig. 9.21. The phase diagram shown in Fig. 9.20 was created with

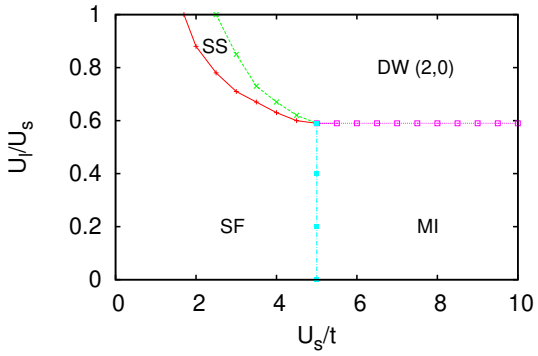

Figure 9.20: Phase diagram of the Bose-Hubbard model with long-range interactions in one dimension. It comprises Mott insulator (MI), superfluid (SF), density wave (DW) and supersolid (SS) phases. The data was obtained with the world-line quantum Monte Carlo method. The parameters of the simulation were $\mathcal{L} = 64$, $\Delta\tau = 0.5$, $L = 64$, $N = 64$ and $t = 1$.

the world-line quantum Monte Carlo method. Mott insulator, density wave, supersolid and superfluid phases appear. The Haldane insulator phase was not observed. The phase diagram with nearest-neighbour interactions, which was presented in Fig. 9.11, contained such a phase. The major difference between both phase diagrams are the missing Haldane phase in the model with long-range interactions and the transition line between superfluid and Mott insulator phase. While this transition depends on the strength U_{nn} of the nearest-neighbour interactions, it is independent of U_l in the model with long-range interactions. This can be explained by considering the first order perturbation of the off-site interactions in the superfluid and the Mott insulator phase.

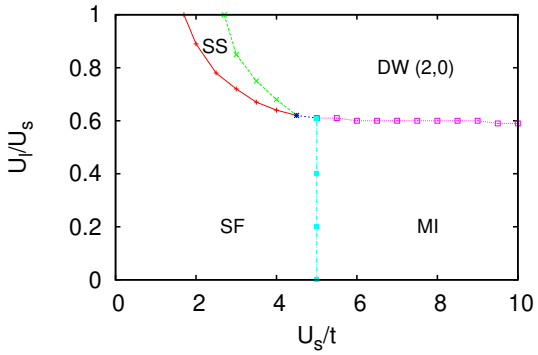

Figure 9.21: Phase diagram of the Bose-Hubbard model with long-range interactions in one dimension. The Mott insulator (MI), superfluid (SF), density wave (DW) and supersolid (SS) phases were identified. Simulations were performed with a variational Monte Carlo algorithm at 200 iterations, $L = 64$, $N = 64$ and $t = 1$.

The first order perturbations of the long-range interactions vanish in both phases. The nearest-neighbour interactions however have different perturbative effects on the supersolid and the Mott phase. The perturbation in the superfluid phase changes with U_{nn} as $(1 - 1/N)U_{nn}$, while it is linear in the Mott insulator phase, as $2NU_{nn}$. This explains the shift of the phase transition towards higher U_s/t. The same effect will be observed in the two-dimensional models. In the model with long-range interactions, there is no intermediate Haldane phase. Instead, the Mott insulator phase extends up to the density wave phase. The supersolid phase seems to be more stable in the long-range model, it exists for higher U_s/t, in comparison to the system with nearest-neighbour interactions. Because of this, there is a critical point at $U_s/t = 5$ at which supersolid, superfluid, density wave and Mott insulator phases meet. There is however no direct transition between supersolid and density wave, which was observed with nearest-neighbour interactions.
The phase diagram created with variational Monte Carlo methods, presented in Fig. 9.21 is in agreement with most of the results from the world-line algorithm. However a direct first order transition between the superfluid and the density wave phase is observed with the variational Monte Carlo algorithm.

9.4 Comparison of the $\rho = 1$ phase diagrams

In order to provide a better comparison, the $\rho = 1$ phase diagrams of the one dimensional models with nearest-neighbour and long-range interactions are plotted together in Fig. 9.22. This offers the possibility to directly compare the phase diagrams of the two different models, as well as the results of the two different algorithms. There is no new information, the subfigures are reprints of Figs. 9.11, 9.13, 9.20, 9.21 which have been presented before.
Subfigs. 9.22a and 9.22b show phase diagrams of the model with nearest-neighbour interactions, obtained with world-line quantum Monte Carlo and variational Monte Carlo. The variational Monte Carlo method is not able to identify the Haldane insulator phase.
The phase diagrams for the Bose-Hubbard model with long-range interactions are displayed in Subfigs. 9.22c (world-line quantum Monte Carlo) and 9.22d (variational Monte Carlo). Both look almost identical, except for the fact that a direct transition between the superfluid and the density wave phase was detected with the variational Monte Carlo method.

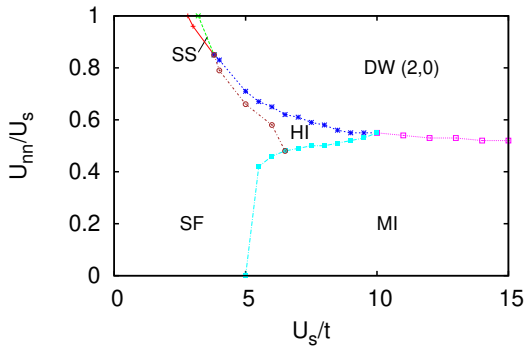

(a) BHM with nearest-neighbour interactions (world-line quantum Monte Carlo)

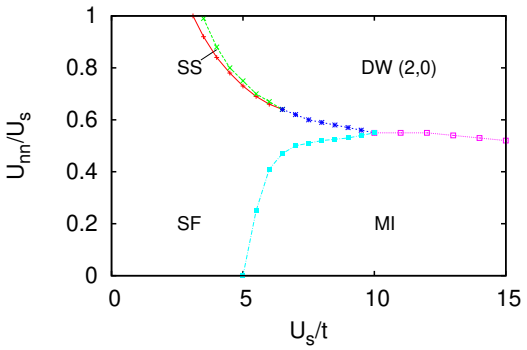

(b) BHM with nearest-neighbour interactions (variational Monte Carlo)

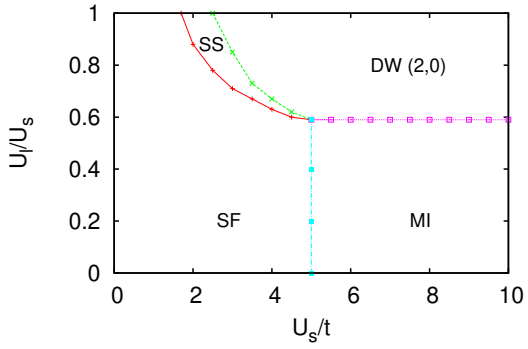

(c) BHM with long-range interactions (world-line quantum Monte Carlo)

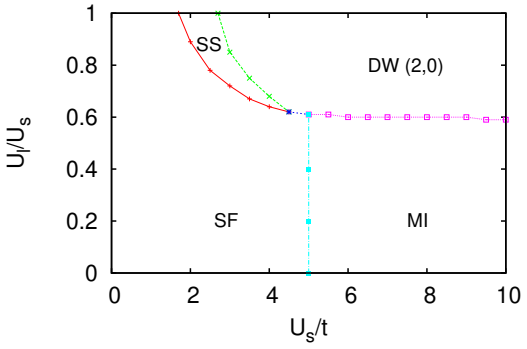

(d) BHM with long-range interactions (variational Monte Carlo)

Figure 9.22: Comparison of the $\rho = 1$ phase diagrams in one dimension.

Comparing the results of the two models with each other, the lack of the Haldane insulator in the long-range model is a difference. The supersolid and density wave phases appear for a lower ratio between off-site interactions and on-site repulsions in the nearest-neighbour model. While in that case the transition line between Mott insulator and density wave phases tends towards

$U_{nn}/U_s = 0.5$, the equivalent value in the model with long-range interactions is $U_l/U_s = 0.6$. Also, the superfluid to Mott transition is not depending on the ratio of the particle-particle interactions in the long-range model. Additionally, the model with nearest-neighbour interactions has a direct phase transition between superfluid and density wave phases.

9.5 Bose-Hubbard model with both nearest-neighbour and long-range interactions

The fact that the Haldane insulator phase can be observed in the model with nearest-neighbour interactions with the world-line quantum Monte Carlo method, but not in systems with long-range interactions raises the question whether the long-range interactions destroy the non-local string order. Similar regions at the tip of the $DW(2,0)$-lobe were identified in Fig. 9.10 and Fig. 9.19 and taken into consideration, but the Haldane insulator does not seem to exist in systems with long-range interactions.
At the end of this chapter the case described in Sec. 4.4 will be discussed, in which both interactions are included in the system. The region in which the Haldane insulator was observed is under consideration, and the long-range interactions are applied as a perturbation. The interaction strength U_l is chosen very low. Fig. 9.23 reprints the case with $U_l = 0$. The Haldane insulator phase exists between density wave and superfluid phases, at a range of $t/U_s = 0.23$ to $t/U_s = 0.3$. Fig. 9.24 shows the behaviour of the order parameters for different strengths

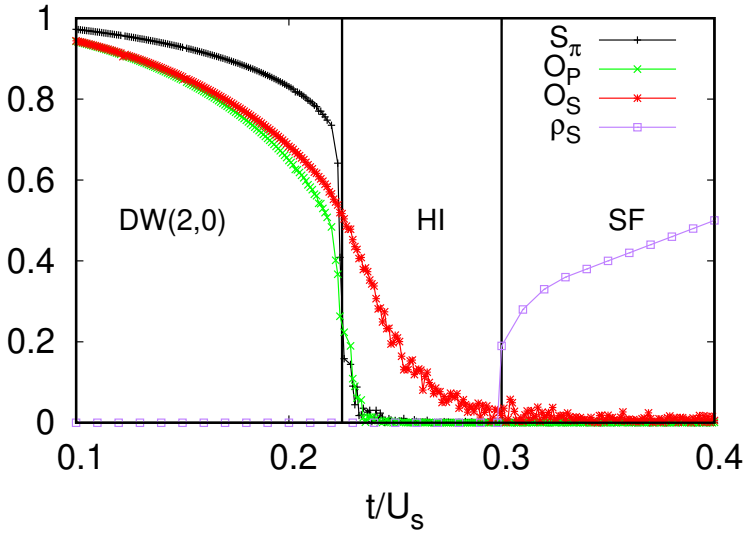

Figure 9.23: Order parameters during phase transitions from density wave (DW) to Haldane insulator (HI) to superfluid (SF) phase at constant density $\rho = 1$ in the Bose-Hubbard model with nearest-neighbour interactions and $U_l = 0$. The data was obtained with world-line quantum Monte Carlo methods at $\mathcal{L} = 64$, $\Delta\tau = 0.5$, $L = 256$, $N = 256$ and $U_{nn} = 0.75$.

of the long-range interactions. Aside from the different values of U_l, the remaining parameters are exactly the same as in Fig. 9.23 The subfigures indicate that the Haldane insulator phase is immediately suppressed by the long-range interactions. Even at the lowest value $U_l = 0.01$, there is no area where the string order $\mathcal{O}_s$ is significantly different from zero and all other order parameters are zero.

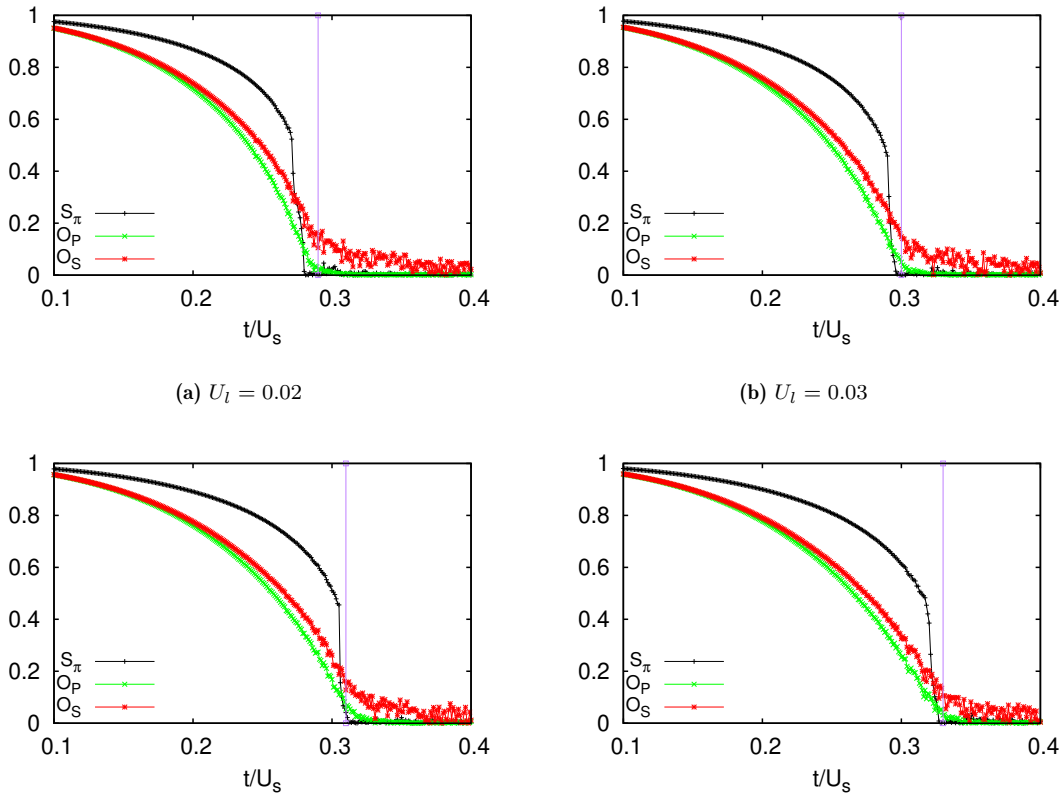

(a) $U_l = 0.02$

(b) $U_l = 0.03$

(c) $U_l = 0.04$

(d) $U_l = 0.05$

Figure 9.24: Order parameters in a system with both nearest-neighbour and long-range interactions. The interaction strength $U_{nn} = 0.75$ is fixed. The long-range interactions (a) $U_l = 0.02$ (b) $U_l = 0.03$ (c) $U_l = 0.04$ (d) $U_l = 0.05$ supress the Haldane insulator phase. The data was obtained with world-line quantum Monte Carlo methods at $\mathcal{L} = 64$, $\Delta\tau = 0.5$, $L = 256$ and $N = 256$.

Chapter 10

Two-dimensional phase analysis of the Bose-Hubbard models

This chapter presents the results for simulations of two-dimensional systems. All results in two dimensions were obtained with the variational Monte Carlo method introduced in Chap. 7. The system size in these simulations was chosen to be $L \times L = 196$ (if not stated otherwise), as the thermodynamic limit extrapolation in Sec. 7.4 showed that this is already a good estimate. The variational Monte Carlo simulations in 2D were performed with 500 optimization-iterations and 1 million Monte Carlo updates between each iteration and the final measurement.
This chapter is mainly concerned with comparing the phase diagrams of the models with nearest-neighbour and long-range interactions. The Haldane insulator phase, whose appearance in the Bose-Hubbard model with nearest-neighbour interactions was a major difference between the models in one dimension, does not exist in two dimensions. Instead, the phase behaviour in two dimensions is very similar, aside from an offset. The phase diagrams are however not identical, as predicted by mean-field theory [201]. The phase transition between Mott insulator and superfluid phases differs qualitatively in the model the nearest-neighbour interactions and the model with long-range interactions. This was also the case for the one-dimensional systems, as presented in Fig. 9.22. Furthermore, phase diagrams of the theoretical model described by Eq. 4.48, which comprises nearest-neighbour and long-range interactions, are presented. Phase diagrams in which both interactions are equally strong are shown, and phase diagrams in which one of the off-site interactions is constant. Finite-size scaling is performed in order to determine the universality classes of the second order phase transitions. Some of the results presented in this chapter were published in Ref. [1].

10.1 Standard Bose-Hubbard model

The standard Bose-Hubbard model in two dimensions, which is described by the Hamiltonian in Eq. 4.2, has only two different ground state phases. Similar to the one-dimensional case, which was discussed in Sec. 9.1, the ground state comprises the Mott insulator phase and the superfluid phase. The corresponding order parameter of the transition between these states is the condensate fraction $n(k = 0)$ (Sec. 4.7.1). This is a second order phase transition, as the order parameter changes continuously during the phase transition [43].
The critical point between these phases at fixed density $\rho = 1$ was determined via finite-size scaling, as introduced in Sec. 2.7. This finite-size scaling analysis can be seen in Fig. 10.1. As explained in Sec. 4.6.6, the $U(1)$ symmetry is broken during the phase transition from superfluid to Mott insulator phase. Consequently, in a system of constant density $\rho = 1$, this phase transtition should belong to the 3D XY universality class for two-dimensional systems [96]. The finite-size scaling with these theoretically expected 3D XY exponents $\beta = 0.348$ and $\nu = 0.671$ (Tab. 2.2) can be seen in Fig. 10.1. The inset graph shows the order parameter $n(k = 0)$ for different system sizes, rescaled with $L^{2\beta/\nu}$, against the ratio U_s/t between the strengths of the competing interactions on-site repulsion and hopping. The value at which the lines cross indicates the critical point. The crossing is in this case observed at $(U_s/t)_c = 18.4$ or $(t/U_s)_c = 0.0543$.

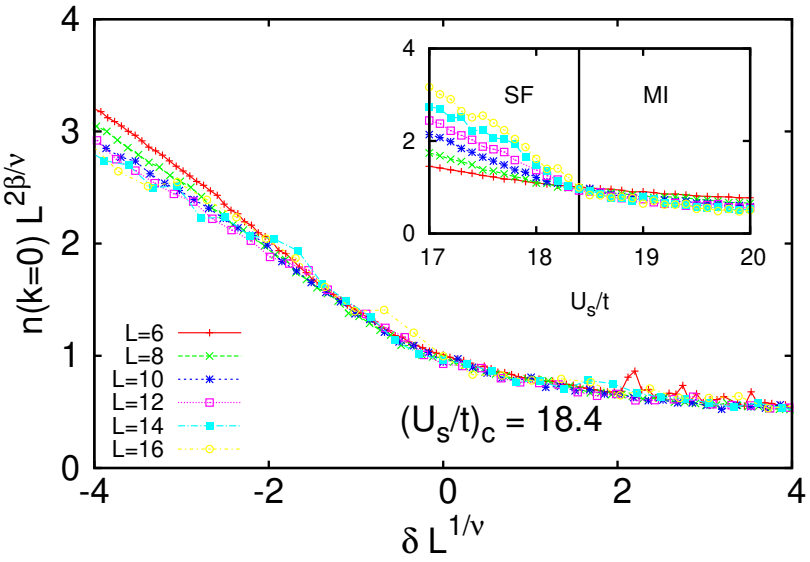

Figure 10.1: Finite-size scaling analysis of the superfluid (SF) to Mott insulator (MI) transition in the standard Bose-Hubbard model ($U_{nn} = U_l = 0$) in 2D at $\rho = 1$. The critical point $(U_s/t)_c = 18.4$ is indicated by the crossing of the curves in the inset plot. The main plot shows a scaling of the condensate fraction $n(k = 0)$ performed with exponents $\beta = 0.348$ and $\nu = 0.671$ of the 3D XY universality class. The data-collapse indicates that the critical point is correct. This figure was also published in Ref. [1]. Reprinted with permission.

This is close to the literature value, which is $U_s/t = 17$ [93] or $(t/U_s)_{BH} = 0.05974$ [153]. The main graph in Fig. 10.1 produces a data-collapse with a finite-size scaling. $\delta = (U_s - (U_s)_c)/(U_s)_c$ represents the normalized distance to the critical value $(U_s)_c$. The data-collapse is good and confirms the crossing at $(U_s/t)_c = 18.4$. The deviation from the literature value could be due to the fact that the variational Monte Carlo algorithm tends to overestimate the superfluid phase. As presented in Sec. 7.2, the basis of the trial wave function is a superfluid state, to which interactions between particles are introduced via Jastrow factors. This might lead to a small bias towards the superfluid state in critical regions. The same effect was also observed in one-dimensional systems with the variational Monte Carlo method.
The variational Monte Carlo method is not exact. Therefore the finite-size scaling was also performed with the mean-field exponents. However, no data-collapse could be realized. The fact that the finite-size scaling works better with the 3D XY exponents might indicate that the variational Monte Carlo method is capable of properly simulating the physics of this phase transitions.

10.2 Bose-Hubbard model with nearest-neighbour interactions

This section presents results for simulations of the Bose-Hubbard model in two dimensions with nearest-neighbour interactions, which was introduced in Sec. 4.2. A ground state phase diagram at density $\rho = 1$ in the U_{nn}/t-U_s/t-plane is shown in Fig. 10.2. The Mott insulator, density-wave, superfluid and supersolid phases are present. In contrast to the one-dimensional model, the Haldane insulator phase does not exist in two dimensions, because of the topological reasons explained in Chap. 5. The existing phases all cover large areas in the parameter space. The Mott insulator phase and the density wave phase are characterized by localized particles, while bosons are delocalized in the superfluid and supersolid phases. The density wave and supersolid phases show a modulation in the average occupancy between even and odd sites, which results in a non-zero structure factor.

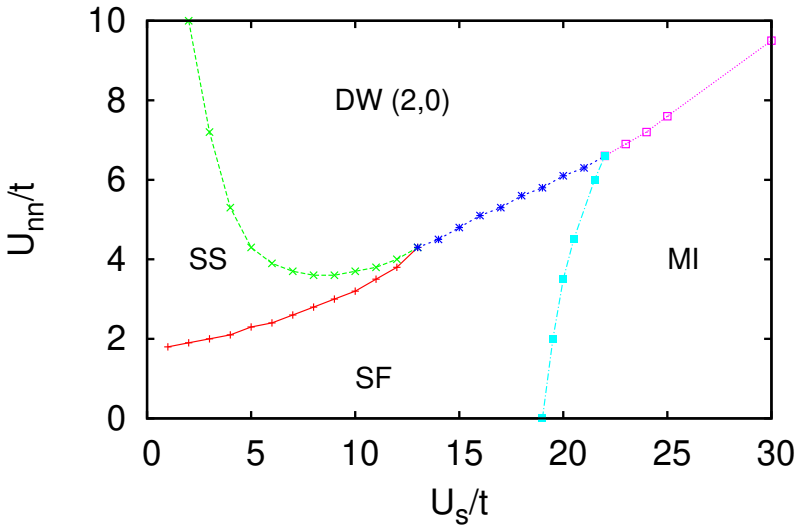

Figure 10.2: Ground state phase diagram of a Bose-Hubbard model with nearest-neighbour interactions at $\rho = 1$. The data was obtained with variational Monte Carlo simulations with system size $L^2 = 196$, tunneling strength $t = 1$ at 500 optimization-iterations. The observed phases are superfluid (SF), supersolid (SS), Mott insulator (MI) and density-wave (DW). This figure was also published in Ref. [1]. Reprinted with permission.

Phase diagrams at densities $\rho = 0.5$, $\rho = 1$, $\rho = 1.5$ and $\rho = 2$ are presented in Fig. 10.3. The vertical axis was rescaled to represent the ratio between nearest-neighbour interaction and on-site repulsion, in order to provide a better comparability between those interactions. A rescale of Fig. 10.2. is shown in Subfig. 10.3b. Four different phases are observed in these diagrams. There are five direct phase transitions. A first order phase transition takes place between the Mott insulator and the density wave, which is associated with an instantaneous breaking of the $\mathbb{Z}_2$ symmetry and thereby a change in the structure factor S_π. There is another first order phase transition between the superfluid and density wave states, which is associated with breaking in $U(1)$ and $\mathbb{Z}_2$ symmetries. The Mott insulator to superfluid and the supersolid to density wave transitions are second order phase transitions with a broken $U(1)$ symmetry due to the occurring superfluidity. The superfluid to supersolid transition is also a second order phase transition, in which the $\mathbb{Z}_2$ symmetry is broken.
With regards to the upcoming phase diagrams of the system with long-range interactions, the

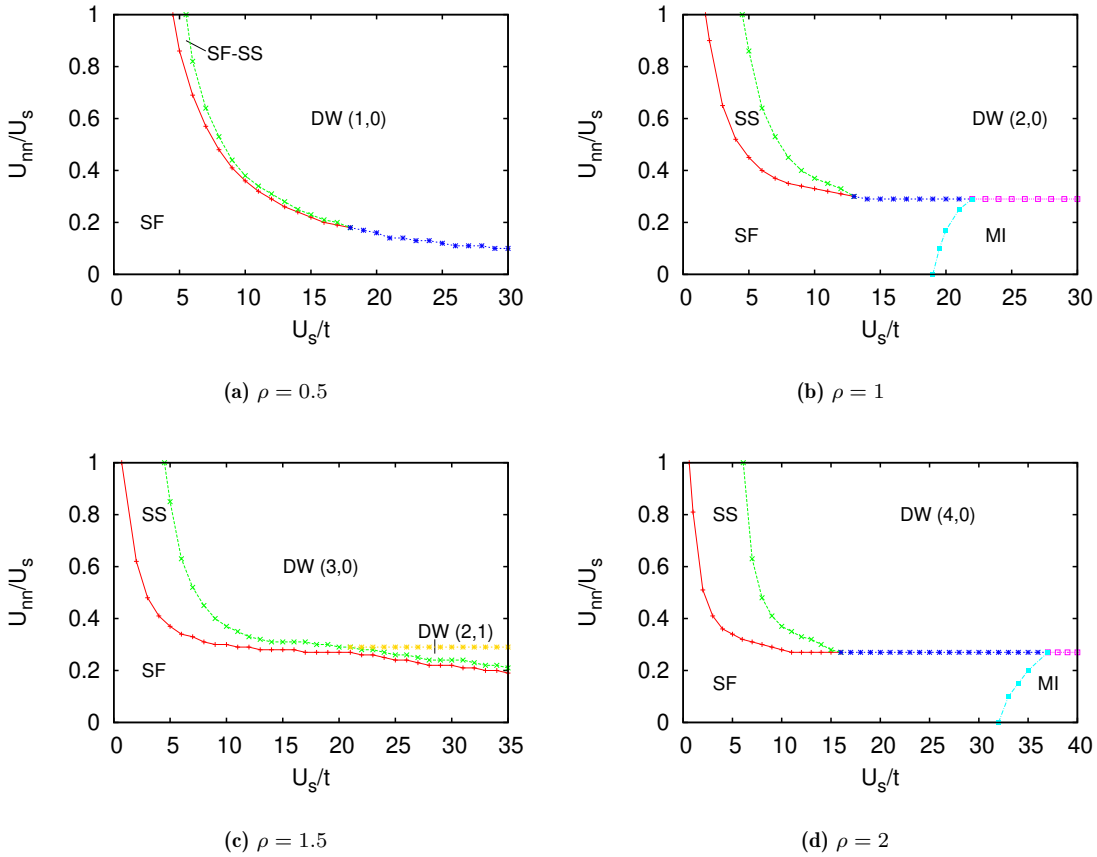

(a) $\rho = 0.5$ **(b)** $\rho = 1$

(c) $\rho = 1.5$ **(d)** $\rho = 2$

Figure 10.3: Ground state phase diagrams of the Bose-Hubbard model with nearest-neighbour interactions at various densities (a) $\rho = 0.5$ (b) $\rho = 1$ (c) $\rho = 1.5$ (d) $\rho = 2$. The data was obtained with variational Monte Carlo simulations with system size $L^2 = 196$, tunneling strength $t = 1$ at 500 optimization-iterations. The observed phases are superfluid (SF), supersolid (SS), Mott insulator (MI) and density wave (DW). At $\rho = 0.5$, there is no stable supersolid phase. Instead, it is a region of phase separation (SF-SS) between superfluid and supersolid. These figures were also published in Ref. [1]. Reprinted with permission.

attention should be drawn to the transition between the superfluid and Mott insulator phase in Figs. 10.2, 10.3b and 10.3d. In the system with nearest-neighbour interactions, this transition is dependent on U_{nn}. Finite-size scaling determines the critical point of this transition to be $(U_s/t)_c = 18.4$ at $U_{nn}/U_s = 0$ (Fig. 10.1), $(U_s/t)_c = 19.3$ at $U_{nn}/U_s = 0.1$ (Fig. 10.4a) and $(U_s/t)_c = 20.4$ at $U_{nn}/U_s = 0.2$ (Fig. 10.4b). The shift does not affect the universality class of the transition. Finite-size scaling plots of the condensate fraction are presented in Fig. 10.4. Like for the standard Bose-Hubbard model (Fig. 10.2), the exponents of the 3D XY universality class result in a good data-collapse. The shift of the phase transition depending on U_{nn} can be explaind by considering the perturbating effect that the nearest-neighbour interactions has on the superfluid and Mott insulator phases. The first order perturbation in the superfluid phase goes as $(1-1/N)U_{nn}$, while it is $2NU_{nn}$ in the Mott insulator phase. The shift due to the U_{nn} is therefore larger in the Mott insulator phase, and a shift of the critical point towards larger U_s/t is to be expected.

The phase diagram in Subfig. 10.3a shows a system at $\rho = 0.5$. The formation of the Mott insulator phase is impossible at half-integer densities. Consequently, this phase diagram depicts only

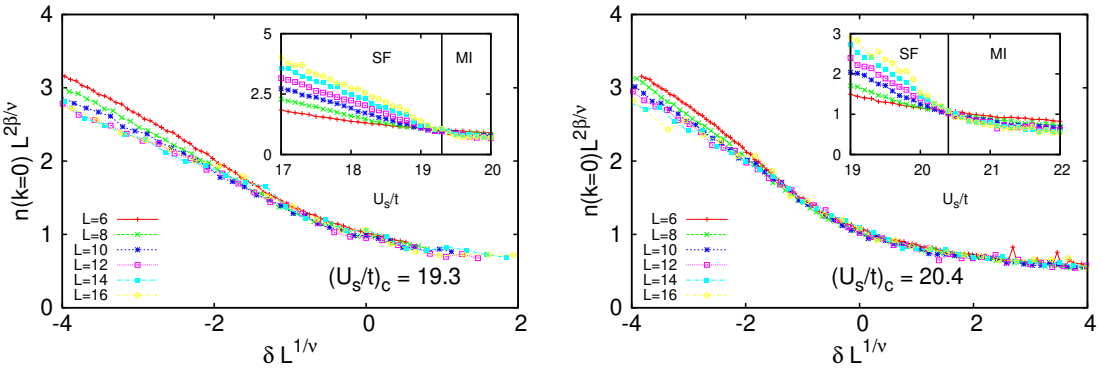

(a) $U_{nn}/U_s = 0.1$ **(b)** $U_{nn}/U_s = 0.2$

Figure 10.4: Finite-size scaling of the superfluid (SF) to Mott insulator (MI) transition in the Bose-Hubbard model with nearest-neighbour interactions at (a) $U_{nn}/U_s = 0.1$ (b) $U_{nn}/U_s = 0.2$ with the 3D XY scaling exponents $\beta = 0.348$ and $\nu = 0.671$. The crossing of the curves in the inset plots determines the critical points. These are confirmed by the good data-collapses in the main graphs. The nearest-neighbour interaction shifts the phase transition to higher values of U_s/t.

three different phases. The superfluid phase and the density wave phase with spatial structure $(1, 0)$ are straightforward. There is a small parameter region which seems to be covered by the supersolid phase. However quantum Monte Carlo studies have shown that the supersolid phase is unstable for $\rho = 0.5$ [93]. This area, denoted SF-SS in the graph, is in fact a phase separation between supersolid and superfluid phases. The supersolid phase is however stable at the other densities $\rho = 1$, $\rho = 1.5$ and $\rho = 2$. All three regions meet at $U_s/t = 18$.
For $\rho = 1.5$ in Fig. 10.3c, the phase diagram shows superfluid, supersolid and two density wave phases of different spatial structure. The density wave phase has the form $(2, 1)$ at lower ratios U_{nn}/U_s, which turns into $(3, 0)$ after a critical ratio. Both phases are stable and the transition was determined using an analysis of the ground states energy. The transition line seems to continue the phase boundary between supersolid and density wave $(3, 0)$. The phase transition between the density wave phases is the only first order transition in this phase diagram, all other phase transitions are of second order. In contrast to the integer densities $\rho = 1$ (Fig. 10.3b) and $\rho = 2$ (Fig. 10.3d), there is no direct transition between superfluid and density wave phases in the parameter area which is covered by the phase diagram. Instead, there is an intermediate, stable supersolid phase between superfluid and density wave states. It was shown above that the superfluid to Mott insulator transition can be identified as a phase transition which belongs to the 3D XY universality class. In the supersolid to density wave transition, there is also a $U(1)$ symmetry breaking. A finite-size scaling analysis of this phase transition is shown in Fig. 10.5. The finite-size scaling was performed at $U_{nn}/U_s = 0.7$ in a system with density $\rho = 1$. Using the 3D XY exponents, the critical point is found at $(U_s/t)_c = 5.91$. The inset plot shows that crossing of the lines at this point. A data-collapse is depicted in the main plot. When the finite-size scaling is performed with mean field exponents, no data-collapse can be obtained.
The remaining second order phase transition is the transition from superfluid to supersolid state. In contrast to the former examples, this transition is characterized by a breaking of the $\mathbb{Z}_2$ translational symmetry, indicated by a non-vanishing structure factor S_π in the supersolid phase. A finite-size scaling plot of this transition is presented in Fig. 10.6. The data was generated in a system with $\rho = 1$ at $U_{nn}/U_s = 0.7$. The finite-size scaling was performed with the critical exponents of the 3D Ising universality class $\beta = 0.326$ and $\nu = 0.630$. This should be the correct universality class in this case, as the structure factor is associated with the Ising magnetization.

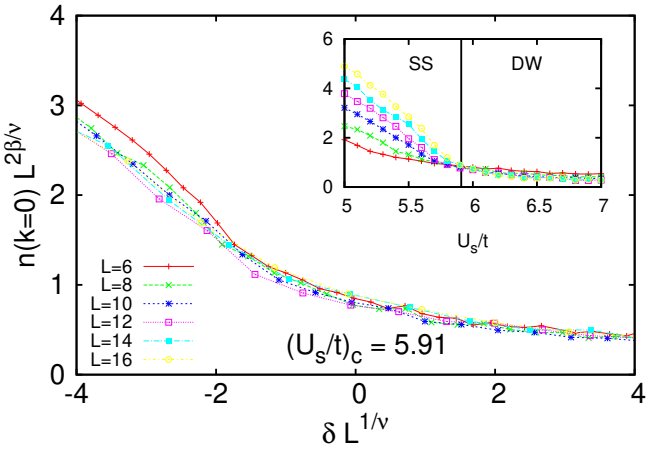

Figure 10.5: Finite-size scaling of the supersolid (SS) to density wave (DW) transition in Bose-Hubbard model with nearest-neighbour interactions at $U_{nn}/U_s = 0.7$ with the 3D XY exponents $\beta = 0.348$ and $\nu = 0.671$.

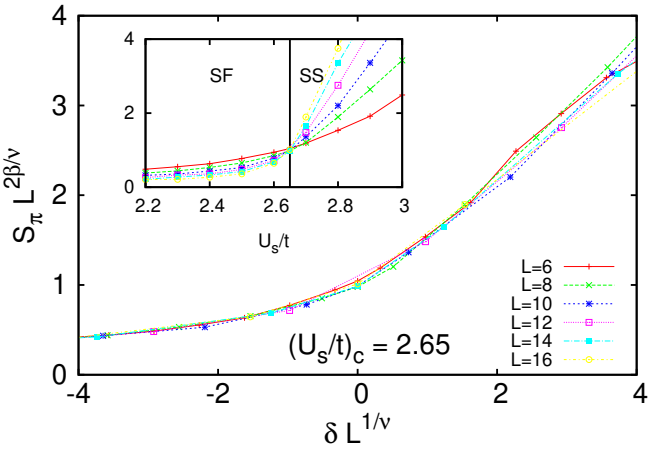

Figure 10.6: Finite-size scaling of the superfluid (SF) to supersolid (SS) transition in the Bose-Hubbard model with nearest-neighbour interactions at $U_{nn}/U_s = 0.7$ with the 3D Ising exponents $\beta = 0.326$ and $\nu = 0.630$.

The data-collapse confirms these exponents, the phase transition takes place at $(U_s/t)_c = 5.94$. In summary, the finite-size scaling plots in Fig. 10.4, 10.5 and 10.6 show that the variational Monte Carlo method is suitable for assigning the investigated phase transitions to the correct universality class in the Bose-Hubbard model with nearest-neighbour interactions.

10.3 Bose-Hubbard model with long-range interactions

The Bose-Hubbard model with long-range interactions was introduced in Sec. 4.3. A phase diagram in the $(U_s/t, U_l/t)$-plane of a system with particle density $\rho = 1$ is shown in Fig. 10.7. The scale is set by the tunneling, which is fixed to $t = 1$, while U_s and U_l are varied. The phase

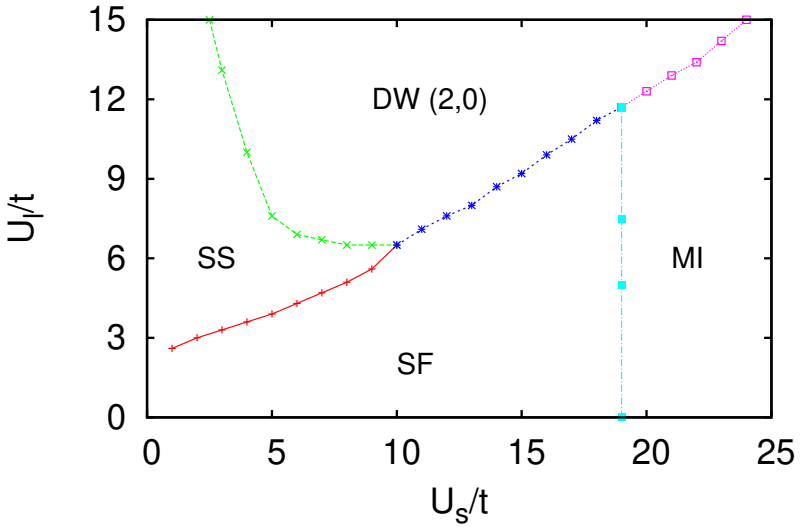

Figure 10.7: Ground state phase diagram of a Bose-Hubbard model with long-range interactions at $\rho = 1$. The data was obtained with variational Monte Carlo simulations with system size $L^2 = 196$, tunneling strength $t = 1$ at 500 optimization-iterations. The observed phases are superfluid (SF), supersolid (SS), Mott insulator (MI) and density-wave (DW). This figure was also published in Ref. [1]. Reprinted with permission.

diagram is very similar to the one of the Bose-Hubbard model with nearest-neighbour interactions, which was presented in Fig. 10.2. It comprises Mott insulator, density wave, superfluid and supersolid phases, with five different direct transitions between phases. The long-range interactions have no effect on the order of the phase transitions. Superfluid to density wave and Mott insulator to density wave are still first order transitions, while the remaining transitions are of second order.

The phase diagram in Fig. 10.7 can be compared to actual experimental data. Experimental data, which was obtained in the course of the realization of cavity-induced long-range interactions by Landig et al. [11], was rescaled to reflect the properties of the Hamiltonian from Eq. 4.37. The diagram can be found in the extended data section of Ref. [11] and is reprinted in Fig. 10.8. Comparing the experimental data with the results from the simulations with the variational Monte Carlo method reveals that both are in fair agreement when the shape and the location of the phases are considered. The transition between superfluid and Mott insulator phase is shiftet towards smaller U_s/t. The most signifant difference is the shape and the position of the supersolid phase, which stretches over a much larger area of parameter configurations in the experimental data.

As already mentioned, the phase diagrams in Fig. 10.2 and Fig. 10.7 are very similar. There is however an overall offset in such a way that U_l needs to be tuned higher in order to reach the supersolid and density wave phases. The most remarkable difference lies in the transition line between the supersolid and the Mott insulator phases. It was shown in Sec. 10.2 that the critical value $(U_s/t)_c$ of this transition depends on U_{nn} in the model with nearest-neighbour in-

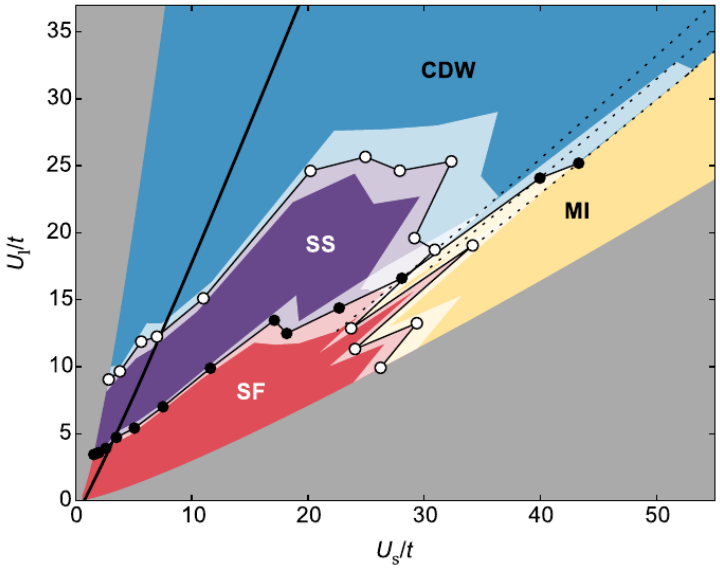

Figure 10.8: Experimentally obtained phase diagram of the model with long-range interactions. Originally published in Ref. [11]. Reprinted with permission.

teractions. The reason for this lies in the first order perturbations of the superfluid and Mott insulator phases, caused by the nearest-neighbour repulsions.
Finite-size scaling analysis in Fig. 10.10 shows that no such effect takes place in the model with long-range interactions. For $U_l/U_s = 0.1$ and $U_l/U_s = 0.2$, the critical point is at $(U_s/t)_c = 18.4$, the same value as in the standard Bose-Hubbard model with $U_l = 0$. This should be expected, as the first order perturbations of the long-range interactions vanish in the superfluid and Mott insulator phases.
Similar to the procedure in Sec. 10.2, Fig. 10.9 shows phase diagrams of the Bose-Hubbard model with long-range interactions at densities $\rho = 0.5$, $\rho = 1$, $\rho = 1.5$ and $\rho = 2$. The phase diagrams are presented in the $(U_s/t, U_l/U_s)$-plane. This representation is well suited to compare the phase diagrams in Fig. 10.9 to the quantum Monte Carlo and mean-field results from Ref. [93]. The results that are presented here are actually closer to the quantum Monte Carlo results than the mean-field results. Especially the superfluid to Mott insulator transition in the $\rho = 1$ domain is significantly better described by the variational Monte Carlo than by the mean-field results presented in Ref. [93].
Compared to the corresponding results for the model with nearest-neighbour interactions in Fig. 10.3, the phase diagrams are very similar. The same phases appear and the shape is comparable. There is an offset in the vertical direction. The phase diagrams $\rho = 1.5$ are remarkable, as the supersolid phase and the density wave $(2, 1)$ region are much broader in the case of long-range interactions.

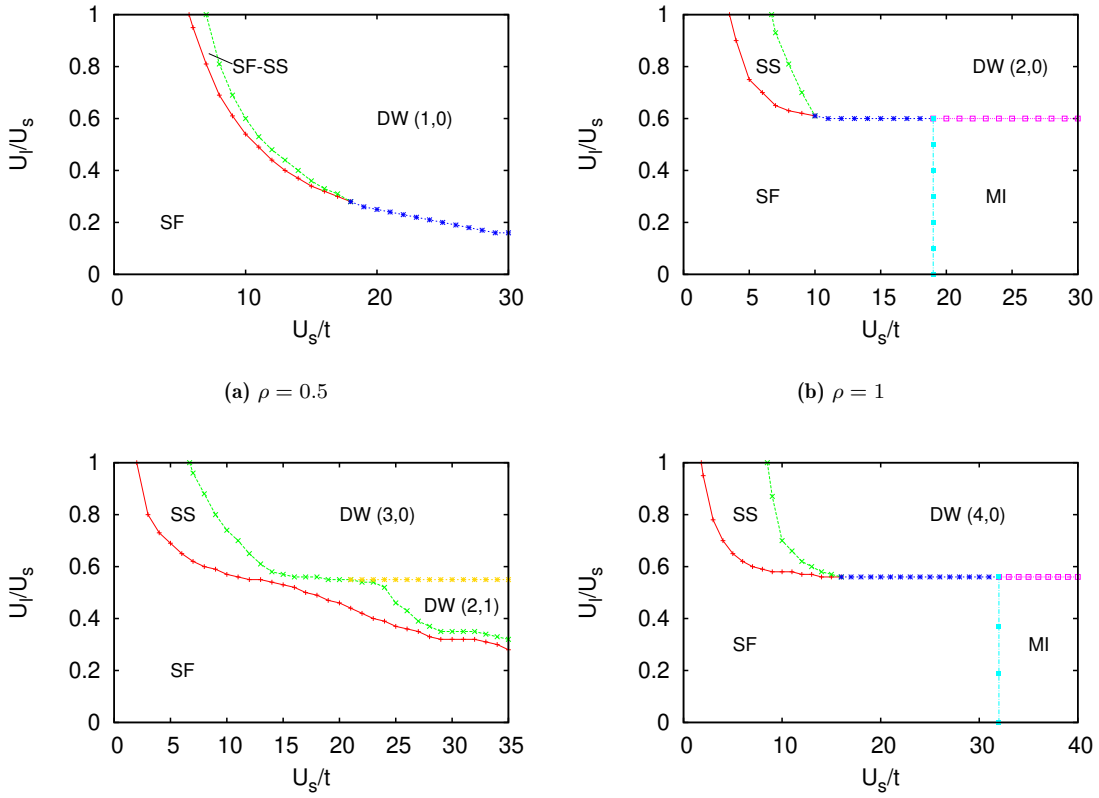

(a) $\rho = 0.5$ **(b)** $\rho = 1$

(c) $\rho = 1.5$ **(d)** $\rho = 2$

Figure 10.9: Ground state phase diagrams of the Bose-Hubbard model with long-range interactions at various densities (a) $\rho = 0.5$ (b) $\rho = 1$ (c) $\rho = 1.5$ (d) $\rho = 2$. The data was obtained with variational Monte Carlo simulations with system size $L^2 = 196$, tunneling strength $t = 1$ at 500 optimization-iterations. The observed phases are superfluid (SF), supersolid (SS), Mott insulator (MI) and density-wave (DW). At $\rho = 0.5$, there is no stable supersolid phase. There is however a region of phase separation between superfluid and supersolid (SF-SS). These figures were also published in Ref. [1]. Reprinted with permission.

Two finite-size scaling plots for the superfluid to Mott insulator phase are presented in Fig. 10.10. The finite-size scaling delivers good results with the exponents of the 3D XY universality class. As mentioned above, this phase transition is not shifted for $U_l \neq 0$. The finite-size scaling of the superfluid to supersolid transition, show in Fig. 10.11, is performed with the exponents of the 3D Ising universality class [45]. This universality class is theoretically expected, as this phase transition is associated with the breaking of the $\mathcal{Z}_2$-symmetry, the analogon of this system to the Ising magnetization [45]. The crossing of the curves in the inset plot indicates the critical point. The data-collapse confirms the correct choice of the critical exponents.

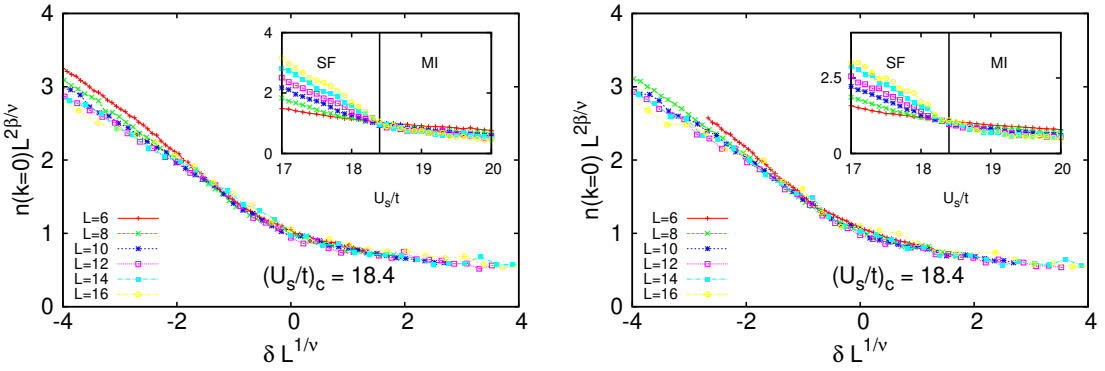

(a) $U_l/U_s = 0.1$ **(b)** $U_l/U_s = 0.2$

Figure 10.10: Finite-size scaling of the superfluid (SF) to Mott insulator (MI) transition in the Bose-Hubbard model with long-range interactions at (a) $U_l/U_s = 0.1$ and (b) $U_l/U_s = 0.2$ with the 3D XY exponents $\beta = 0.348$ and $\nu = 0.671$. The critical point is the same as in the standard Bose-Hubbard model (Fig. 10.1). The long-range interactions do not affect the transition.

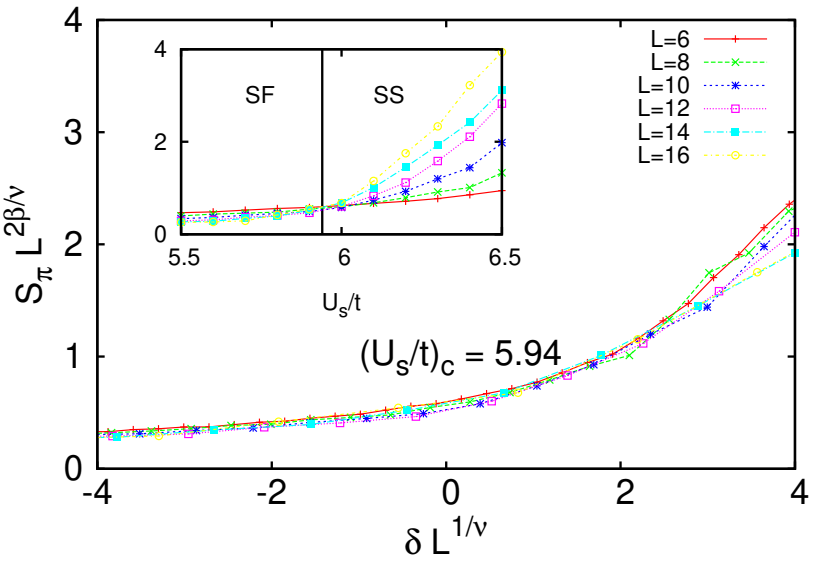

Figure 10.11: Finite-size scaling of the superfluid (SF) to supersolid (SS) transition in the Bose-Hubbard model with long-range interactions at $U_l/U_s = 0.7$ with the 3D Ising exponents $\beta = 0.326$ and $\nu = 0.630$.

10.4 Bose-Hubbard model with nearest-neighbour and long-range interactions

In this chapter systems which feature both nearest-neighbour and long-range interactions are studied. The corresponding Hamiltonian was introduced in Sec. 4.4. Such systems contain one long-range force term and multiple short-range interactions. The previous sections showed that nearest-neighbour and long-range interactions lead to the same order in the systems.

10.4.1 Nearest-neighbour and long-range interactions equally strong

The case that nearest-neighbour and long-range interactions have the same strength $U_{nn} = U_l$ might be unlikely from the perspective of an experimentalist. However, it is still worth looking into a configuration like this. A phase diagram of the model described by the Hamiltonian from Eq. 4.48 with $U_{nn} = U_l$ at $\rho = 1$ is depicted in Fig. 10.12. This phase diagram is similar to

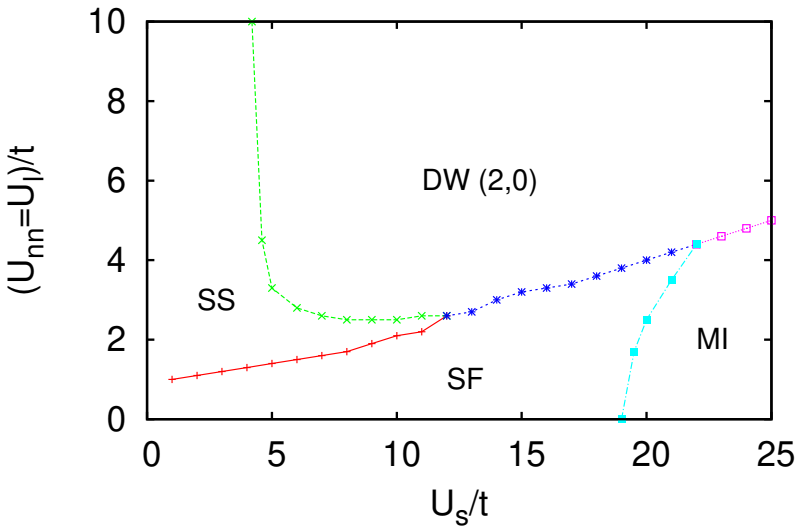

Figure 10.12: Ground state phase diagram of a Bose-Hubbard model with long-range interactions and nearest-neighbour interactions at $\rho = 1$. The data was obtained with variational Monte Carlo simulations with system size $L^2 = 196$, tunneling strength $t = 1$ at 500 optimization-iterations. The observed phases are superfluid (SF), supersolid (SS), Mott insulator (MI) and density-wave (DW). This figure was also published in Ref. [1]. Reprinted with permission.

those from the Bose-Hubbard models with nearest-neighbour interactions (Fig. 10.2) and long-range interactions (Fig. 10.7) only. The transition line from the superfluid to Mott insulator phase depends on the strength of U_{nn}, due to of the perturbating effect of the nearest-neighbour interactions that was elaborated in Sec. 10.2. The long-range interaction does not affect this. The critical point at which the superfluid, the supersolid and the density wave phases meet is located at $U_s/t = 12$. It lies between the equivalent values of the systems with only nearest-neighbour interactions ($U_s/t = 13$) and only long-range interactions ($U_s/t = 10$).
If both interactions are tuned simultaneously by the same factor, the combination of both acts like one effective interaction. In comparison to the individual interactions, the transition between superfluid and Mott insulator phase remains unaffected, but transition-lines involving phases with $S_\pi > 0$ are altered.

Further phase diagrams at particle densities $\rho = 0.5$, $\rho = 1$, $\rho = 1.5$ and $\rho = 2$ are provided in Fig. 10.13. Except for offsets, these phase diagrams are very similar to the phase diagrams with

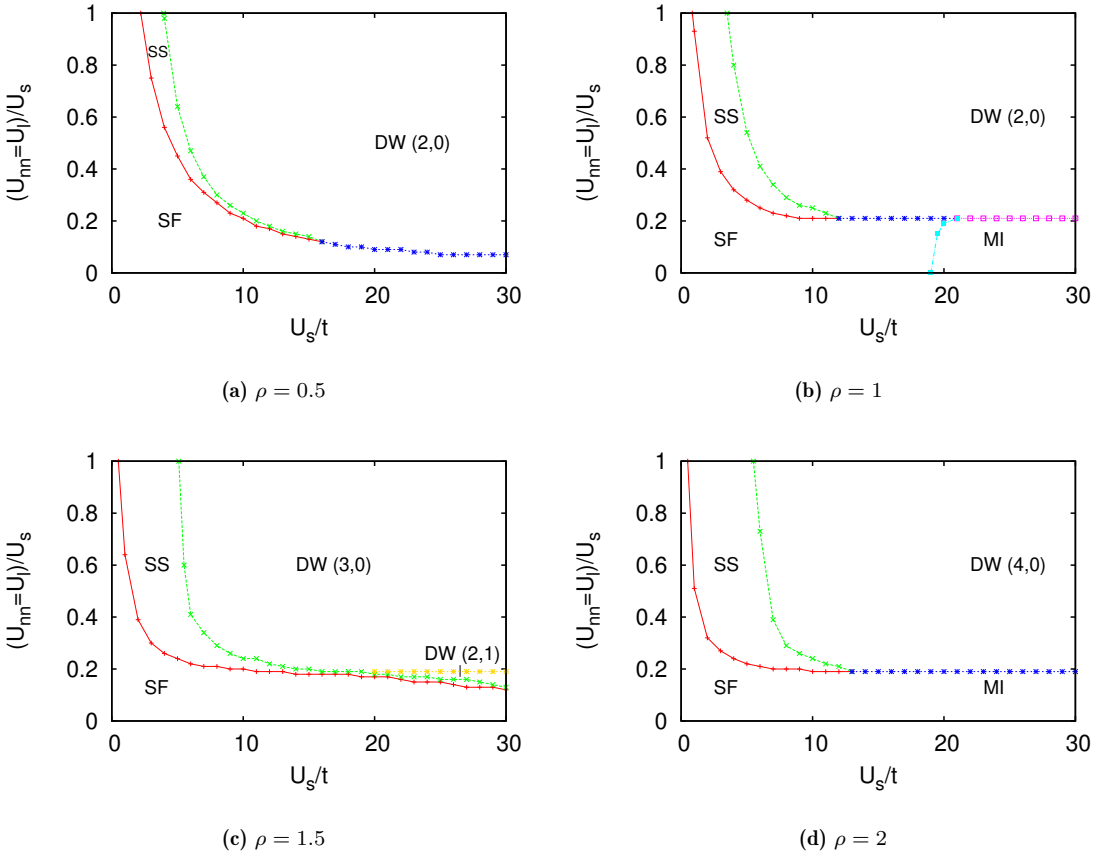

(a) $\rho = 0.5$

(b) $\rho = 1$

(c) $\rho = 1.5$

(d) $\rho = 2$

Figure 10.13: Ground state phase diagrams of the Bose-Hubbard model with nearest-neighbour and long-range interactions at various densities (a) $\rho = 0.5$ (b) $\rho = 1$ (c) $\rho = 1.5$ (d) $\rho = 2$. The data was obtained with variational Monte Carlo simulations with system size $L^2 = 196$, tunneling strength $t = 1$ at 500 optimization-iterations. The observed phases are superfluid (SF), supersolid (SS), Mott insulator (MI) and density wave (DW).
Subfig. (b) was also published in Ref. [1]. Reprinted with permission.

nearest-neighbour interactions and long-range interactions only, except that the whole diagram seems squeezed in the vertical direction. This is however to be expected, since the vertical axis now represents two equally strong interactions.

10.4.2 Nearest-neighbour interactions with fixed long-range interactions

Three phase diagrams in the $(U_{nn}/U_s, U_s/t)$-plane are shown in Fig. 10.14. The long-range interaction has a fixed strength U_l in each of these diagrams. The interaction U_l is zero in Subfig. 10.14a, while it is set to the values $U_l = 2$ in Subfig. 10.14b and $U_l = 5$ in Subfig. 10.14c. Comparison of the pictures shows that the long-range interactions act as an energetic offset. The shape of the phase diagrams is unchanged.

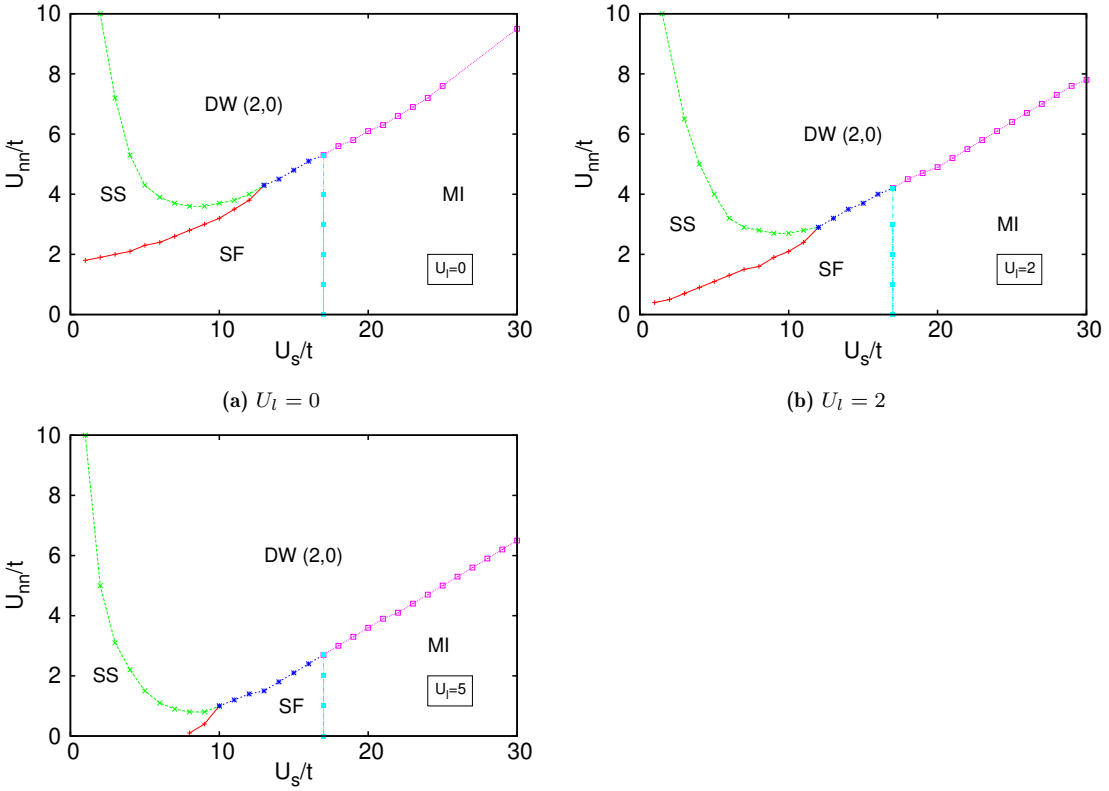

(a) $U_l = 0$

(b) $U_l = 2$

(c) $U_l = 5$

Figure 10.14: Ground state phase diagrams of the Bose-Hubbard model with nearest-neighbour interactions and long-range interactions at $\rho = 1$. The long-range interactions are fixed to constant values (a) $U_l = 0$ (b) $U_l = 2$ (c) $U_l = 5$. The shapes of the phase diagrams are not affected by this, the long-range interactions act as an energetic offset.

10.4.3 Long-range interactions with fixed nearest-neighbour interactions

In Fig. 10.15 phase diagrams with variable long-range interaction strengths U_l and constant nearest-neighbour interaction strengths U_{nn} are presented. This time the density was chosen to be $\rho = 1.5$ because of the richness of this phase diagram. However, the constant nearest-neighbour interactions do only act as an offset and do not affect the shape of the transition lines between the phases significantly. Even the transition between the two spatial configurations of the density wave phase is not affected.

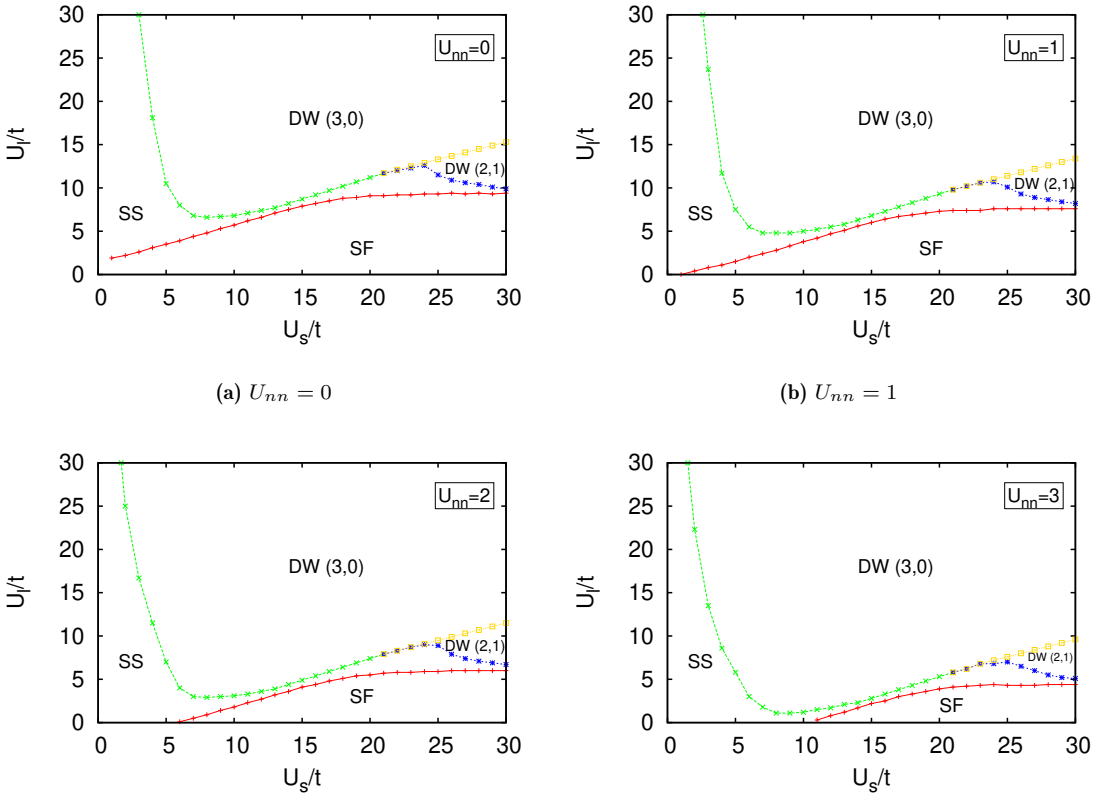

(a) $U_{nn} = 0$ **(b)** $U_{nn} = 1$

(c) $U_{nn} = 2$ **(d)** $U_{nn} = 3$

Figure 10.15: Ground state phase diagrams of the Bose-Hubbard model with nearest-neighbour interactions and long-range interactions at $\rho = 1.5$. The nearest-neighbour interactions are fixed to constant values (a) $U_{nn} = 0$ (b) $U_{nn} = 1$ (c) $U_{nn} = 2$ (d) $U_{nn} = 3$. The shape of the phase diagrams is not affected by this, the nearest-neighbour interactions act as an energetic offset.

10.5 Comparison of the resuls of the different models

To conclude this chapter, a short comparison of the results for the different models in two dimensions is provided in Fig. 10.16. The mean-field limit predicts the nearest-neighbour and

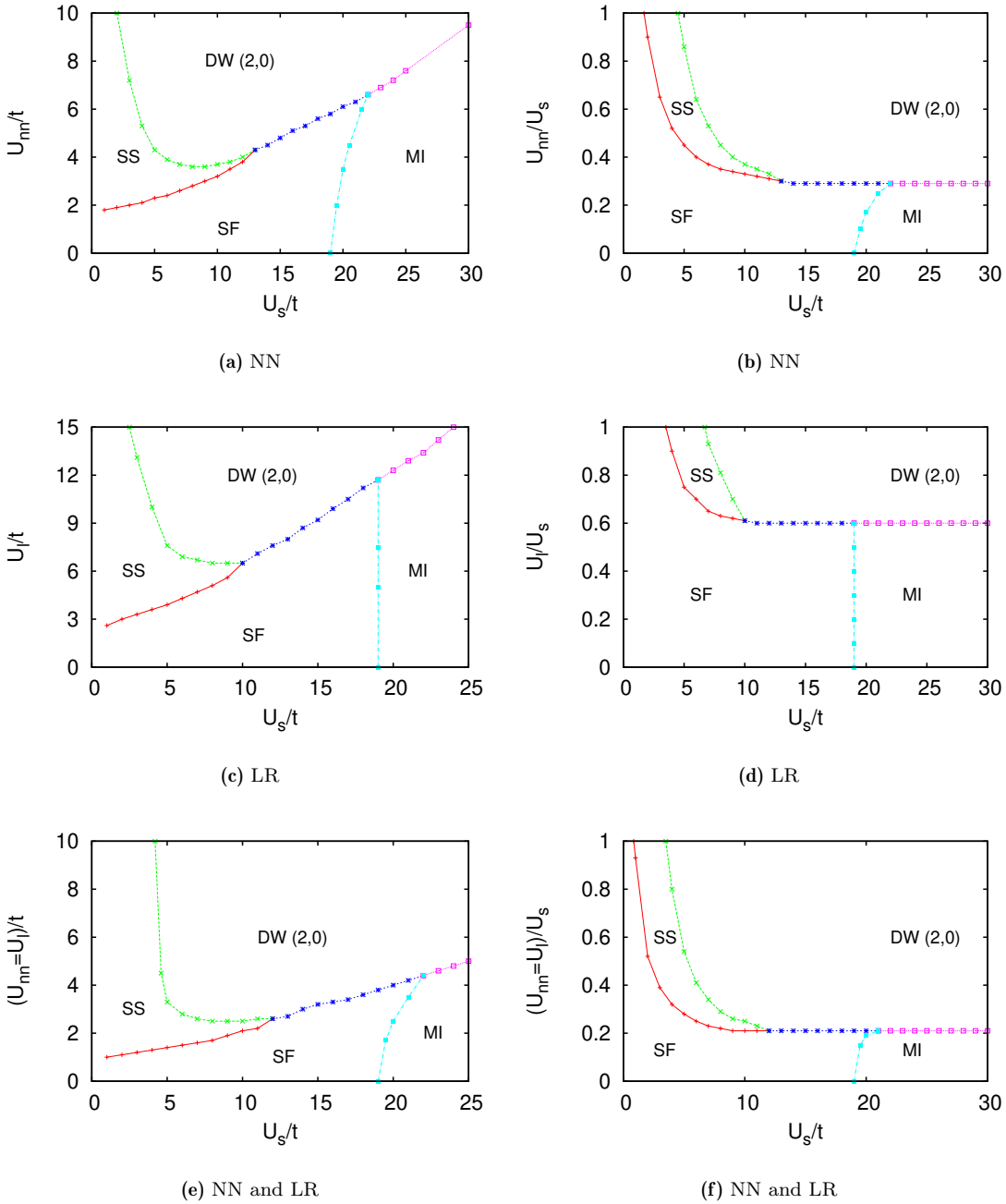

(a) NN **(b)** NN

(c) LR **(d)** LR

(e) NN and LR **(f)** NN and LR

Figure 10.16: Ground state phase diagrams at $\rho = 1$ for systems with (a),(b) nearest-neighbour (NN) interactions; (c),(d) long-range (LR) interactions; (e),(f) nearest-neighbour and long-range interactions equally strong.

the long-range interactions to be equivalent, aside from an offset [169]. In fact, the phase dia-

grams are fairly similar in this $\rho = 1$ case. Qualitative differences can be found in the supersolid phase, which exists up to $U_s/t = 13$ for the nearest-neighbour interactions and only up to $U_s/t = 10$ in the model with long-range interactions. Also, the transition line between superfluid to Mott insulator depends on the ratio between the particle-particle interactions for the model with nearest-neighbour interactions. The model with both interactions qualitatively resembles the nearest-neighbour case. The phase diagrams with both interactions look squeezed in comparison to the other ones. However, this should be the case, as a linear change in two different interactions is represented by the vertical axis in these pictures.
Overall, the results for two-dimensional systems are in good agreement with experimental data [11] as well as theoretic considerations [93, 96, 153, 169]

Chapter 11

Conclusion

This thesis investigated the phase behaviour and critical phenomena of extended Bose-Hubbard models, which are actually feasible in experiments. The standard Bose-Hubbard model, the Bose-Hubbard model with nearest-neighbour interactions and the Bose-Hubbard model with long-range interactions between particles were simulated in one and two dimensions. The phase behaviour was investigated with two different approaches, which both are quantum Monte Carlo methods. A world-line quantum Monte Carlo algorithm, which is capable of performing simulations of one-dimensional systems in the canonical and the grand-canonical ensemble, and a variational Monte Carlo algorithm, which operates in the grand-canonical ensemble and simulates systems in one and two dimensions. Both methods are not exact, since they cannot map the entire Hilbert space. However, this work showed that they are still relevant methods, although there are exact alternatives.

A grand-canonical phase diagram of the standard Bose-Hubbard model in one dimension was created with the world-line Monte Carlo algorithm. For large parts of the parameter area, it is in good agreement with former results. The phase transition between the Mott insulator and superfluid phases at $\rho = 1$ in the standard Bose-Hubbard model in one dimension was investigated. Finite-size scaling with both methods predicted the critical point at the same location at $(t/U_s)_c = 0.2$. The literature value is $(t/U_s)_c \approx 0.3$. However, former quantum Monte Carlo investigations located this critical point also at $(t/U_s)_c \approx 0.2$ [138, 139]. The determination of the exact location of this phase transition is known to be an ill-conditioned problem [84]. Results obtained with different methods are relatively widespread in a range between $t/U_s = 0.2$ to $t/U_s = 0.3$.

The world-line and the variational Monte Carlo both determined the critical point at the lower end of this range. This might be related to the fact that both methods tend to overestimate the superfluid phase. In the case of the variational Monte Carlo method, a possible reason for this might be the Jastrow wave function itself. The trial wave function is given by a superfluid wave function, to which interactions are applied through the Jastrow factors [185]. This could be an explanation for the fact that superfluid phases are slightly overrated in critical regions. Also, the quality of variational Monte Carlo simulations improves with increasing dimension. Variational methods work better if the there are more symmetries in a system [179]. In one-dimensional systems, particles are connected via variational parameters only in one direction, which might also affect the quality of the results.

The Bose-Hubbard model with nearest-neighbour interactions in one dimension was investigated with both methods. Grand-canonical phase diagrams were shown for two different strengths of the nearest-neighbour interactions. Both are in very good agreement with former results [84,110]. The canonical phase diagrams that were determined with the different algorithms are very similar. Mott insulator, density wave, superfluid and superfluid phases, and the transitions between them, are recognized by both methods, with little deviation between them. The world-line method is however capable of identifying the rare Haldane insulator phase through the non-local string order parameter [109]. Altough the Haldane phase was measured slightly smaller in comparison to other works, it can be clearly identified. This is remarkable for a non-exact method at relatively low system sizes. Critical points were determined using finite-size scaling. The critical

point between density wave and Haldane insulator phase is found at $t/U_s = 0.23$, which is the value that other works found with exact methods [110]. However the critical point between Haldane insulator and superfluid phase was determined at $t/U_s = 0.3$, which is slightly too low in comparison to the literature value [110]. This might be related to the fact that the superfluid phase is always a little overestimated. The variational Monte Carlo is not able to recognize the Haldane insulator phase at all. This is most probably due to the Jastrow ansatz, which only accounts translational invariant system [180]. While the configurations in Mott insulator, density wave, superfluid and supersolid phases are translational invariant, aside from defects, the Haldane insulator is a phase with a highly non-local order. The many-body term in the wave function was introduced to improve the algorithm near critical points by considering fluctuations. While the energetic properties of real systems are better reflected with this term, it is not capable of employing the long-range interactions between defects in the system. These are however the defining property of the Haldane phase.
Simulations of the Bose-Hubbard model with long-range interactions in one dimension were performed with both algorithms as well. The canonical phase diagrams that were created with the world-line and with the variational Monte Carlo are again very similar. A difference to note is that the results of the simulations with the variational Monte Carlo method indicate a direct transition between superfluid and density wave phases, while this direct transition does not exist in the results of the world-line algorithm. Instead, the supersolid phase separates the superfluid and density wave phases up to a critical point where all four phases meet. A grand-canonical phase diagram of the Bose-Hubbard model with long-range interactions was also presented, which structurally resembles the phase diagrams with nearest-neighbour interactions. However, no Haldane insulator phase was found in the model with long-range interactions. To investigate this further, a model with both nearest-neighbour and long-range interactions was constructed. The long-range interaction was set very low, while the rest of the parameters corresponded exactly to the range in which the Haldane phase was previously found. The Haldane phase was suppressed by the long-range interactions, even for very low U_l.
The significant differences between the canonical phase diagrams of the different models in one dimension are, aside from an energetic offset, the Haldane phase and the transition between the superfluid and Mott insulator phases. The results of the world-line algorithms indicate that the Haldane phase is suppressed by the long-range interactions. In the parameter areas displayed by the phase diagrams, this phase has been found for the model with nearest-neighbour interactions, but not for the model with long-range interactions. Results from both algorithms indicate that the phase transition between the superfluid phase and the Mott insulator phase is depending on the strength of the nearest-neighbour interaction, but not on the strength of the long-range interactions. Considering the off-site interactions as perturbations of these two phases supports this.
The two-dimensional models were simulated only with the variational Monte Carlo method. Most of the results presented for two-dimensional models were published in [1]. Phase diagrams of Bose-Hubbard models with nearest-neighbour interactions, long-range interactions and with both these interactions were produced at various densities. The phase diagrams for the different models are very similar, aside from offsets. The most significant difference is, similar to the one-dimensional models, the transition between superfluid and Mott insulator phase, which is depending on the strength of the nearest-neighbour interactions, but not on the long-range interactions. The results for the Bose-Hubbard model with long-range interactions in two dimensions agree well with results obtained with exact quantum Monte Carlo algorithms [93]. The $\rho = 1$ phase diagram of the model with long-range interactions is for large parameter areas in agreement with experimental results [11]. The shape and placement of the supersolid phase is however significantly different in experimental and theoretical observations. As expected, there is no indication for the existence of the Haldane insulator phase in two-dimensional systems.
The Bose-Hubbard models with both nearest-neighbour and long-range interactions were investigated for the case in which the interactions are equally strong and for cases in which one of the

interactions is constant. If one of the interactions is constant, it acts as an offset and shifts the phase diagram.
The second order phase transitions were analysed with finite-size scaling in order to determine the universality classes. The correct universality classes were confirmed by good data-collapses for all phase transitions. As predicted by theoretical considerations, the phase transitions associated with a break in $\mathcal{Z}_2$ symmetry belong to the 2D Ising universality class, while phase transitions where the $U(1)$ symmetry is broken belong to the 2D XY universality class [41].
This thesis demonstrated the capabilites of the variational Monte Carlo method for bosonic systems. Comparisons with previous results, both theoretical and experimental, confirmed the efficiency of the method in the two-dimensional case. The method can also be used to determine the correct universality classes of phase transitions. In one dimension, the variational Monte Carlo method is expected to be less precise, as there are fewer variational parameters and fewer symmetries between lattice sites. This makes an adequate description by Jastrow factors more complex. However, the comparison with a world-line Monte Carlo algorithm showed that the variational Monte Carlo method also gives good results in one dimension. Aside from the Haldane insulator phase, which is technically not obtainable with this method, the phase diagrams produced with the variational Monte Carlo algorithm are close to those produced with the world-line method.
The thesis also provided insight into the phase behaviour of extended Bose-Hubbard models in one and two dimensions. The phase diagrams of the Bose-Hubbard model with nearest-neighbour interactions and of the Bose-Hubbard model with long-range interactions are very similar. This holds for one- and two-dimensional systems. Phases have in general the same shape and phase transition lines are similar, aside from an offset. An exception from this is the rare Haldane phase, whose non-local string order seems to be stable only in the model with nearest-neigbour interactions. Also, the transition from superfluid to Mott insulator phase is shaped differently in the two models.
The variational Monte Carlo method presented in this thesis can be used to simulate and predict the phase behaviour of extended Bose-Hubbard models with good accuracy. Phase transitions are adequately simulated and reflect the correct universality classes. The computational effort is relatively low, especially compared to alternatives like DMRG or exact world-line algorithms. The variational Monte Carlo algorithm is able to calculate a point in the phase diagram within an average of 20 minutes. Another possible application is the treatment of higher-dimensional systems. It is possible to modify the algorithm to simulate three-dimensional systems.

Bibliography

[1] B. Bogner, C.D. Daniloff, H. Rieger, Eur. Phys. J. B **92**, 111 (2019)

[2] S. Chu, Rev. Mod. Phys. **70**, 685 (1998)

[3] C.N. Cohen-Tannoudji, Rev. Mod. Phys. **70**, 707 (1998)

[4] W.D. Phillips, Rev. Mod. Phys. **70**, 721 (1998)

[5] M. Greiner, O. Mandel, T. Esslinger, T.W. Hänsch, I. Bloch, Nature **415**, 39 (2002)

[6] B.T. Seaman, M. Krämer, D.Z. Anderson, M.J. Holland, Phys. Rev. A **75**, 023615 (2007)

[7] R.A. Pepino, J. Cooper, D.Z. Anderson, M.J. Holland, Phys. Rev. Lett. **103**, 140405 (2009)

[8] D. Jaksch, C. Bruder, J.I. Cirac, C.W. Gardiner, P. Zoller, Phys. Rev. Lett. **81**, 3108 (1998)

[9] B. Yan, S.A. Moses, B. Gadway, J.P. Covey, K.R.A. Hazzard, A.M. Rey, D.S. Jin, J. Ye, Nature **501**, 521 (2013)

[10] S. Baier, M.J. Mark, D. Petter, K. Aikawa, L. Chomaz, Z. Cai, M. Baranov, P. Zoller, F. Ferlaino, Science **352**, 201 (2016)

[11] R. Landig, L. Hruby, N. Dogra, M. Landini, R. Mottl, T. Donner, T. Esslinger, Nature **532**, 476 (2016)

[12] F.L. Claude Cohen-Tannoudji, Bernard Diu, *Mécanique Quantique Tome I* (Hermann Éditeurs des Sciences et des Arts, 1977)

[13] F. Kuypers, *Klassische Mechanik* (Wiley, 2003)

[14] J.D. Jackson, *Classical electrodynamics* (Wiley, 1962)

[15] J.P. Sethna, *Statistical Mechanics: Entropy, Order Parameters, and Complexity* (Oxford University Press, 2006)

[16] E. Schrödinger, Annalen der Physik **79**, 361 (1926)

[17] M. Born, Z. Phys **37**, 863 (1926)

[18] W. Heisenberg, Z. Phys. **43**, 172 (1927)

[19] E. Fermi, Rend. Lincei **3**, 145 (1926)

[20] P. Dirac, Proc. Royal Soc. A **112**, 661 (1926)

[21] S.N. Bose, Z. Phys **26**, 178 (1924)

[22] N. Metropolis, A.W. Rosenbluth, M.N. Rosenbluth, A.H. Teller, E. Teller, J. Chem. Phys. **21**, 1087 (1953)

[23] D. Ceperley, Rev. Min. Geochem. **71**, 129 (2010)

[24] J. Shang, Y.L. Seah, H.K. Ng, D.J. Nott, B.G. Englert, New J. Phys. **17**, 043017 (2015)

[25] R.P. Feynman, Int. J. Theor. Phys. **21**, 467 (1982)

[26] S. Lloyd, Science **273**, 1073 (1996)

[27] D.S. Abrams, S. Lloyd, Phys. Rev. Lett. **79**, 2586 (1997)

[28] I. Buluta, F. Nori, Science **326**, 108 (2009)

[29] T.D. Ladd, F. Jelezko, R. Laflamme, Y. Nakamura, C. Monroe, J.L. O'Brien, Nature **464**, 45 (2010)

[30] F. Arute, K. Arya, R. Babbush, D. Bacon, J.C. Bardin, R. Barends, R. Biswas, S. Boixo, F.G.S.L. Brandao, D.A. Buell et al., Nature **574**, 505 (2019)

[31] I. Bloch, Nature Physics **1**, 23 (2005)

[32] I. Bloch, J. Dalibard, W. Zwerger, Rev. Mod. Phys. **80**, 885 (2008)

[33] J.S. Douglas, K. Burnett, Phys. Rev. A **84**, 033637 (2011)

[34] S. Fernández-Vidal, G. De Chiara, J. Larson, G. Morigi, Phys. Rev. A **81**, 043407 (2010)

[35] A.M. Rey, P.B. Blakie, G. Pupillo, C.J. Williams, C.W. Clark, Phys. Rev. A **72**, 023407 (2005)

[36] S. Rist, C. Menotti, G. Morigi, Phys. Rev. A **81**, 013404 (2010)

[37] H. Habibian, A. Winter, S. Paganelli, H. Rieger, G. Morigi, Phys. Rev. Lett. **110**, 075304 (2013)

[38] H. Habibian, A. Winter, S. Paganelli, H. Rieger, G. Morigi, Phys. Rev. A **88**, 043618 (2013)

[39] R. Mottl, F. Brennecke, K. Baumann, R. Landig, T. Donner, T. Esslinger, Science **336**, 1570 (2012)

[40] J.A. Hertz, Phys. Rev. B **14**, 1165 (1976)

[41] S. Sachdev, *Quantum Phase Transitions - Second Edition* (Cambridge University Press, 2011)

[42] M. Vojta, Rep. Prog. Phys. **66**, 2069 (2003)

[43] J.M. Kosterlitz, D.J. Thouless, J. Phys. C **6**, 1181 (1973)

[44] G. Jaeger, Archive for History of Exact Sciences **53**, 51 (1998)

[45] M.E. Fisher, M.N. Barber, D. Jasnow, Phys. Rev. A **8**, 1111 (1973)

[46] K.G. Wilson, Phys. Rev. B **4**, 3174 (1971)

[47] A. Pelissetto, E. Vicari, Phys. Rep. **368**, 549 (2002)

[48] G.S. Rushbrooke, J. Chem. Phys **39**, 842 (1963)

[49] D.S. Fisher, Phys. Rev. Lett. **56**, 416 (1986)

[50] A.T. Ogielski, D.A. Huse, Phys. Rev. Lett. **56**, 1298 (1986)

[51] H. Rieger, Phys. Rev. B **52**, 6659 (1995)

[52] De Broglie, Annalen der Physik **10**, 22 (1925)

[53] M. Lewenstein, A. Sanpera, V. Ahufinger, B. Damski, A. Sen(de), U. Sen, Adv. Phys. **56**, 243 (2007)

[54] P.A. Crowell, J.D. Reppy, Phys. Rev. Lett. **70**, 3291 (1993)

[55] M.P.A. Fisher, P.B. Weichman, G. Grinstein, D.S. Fisher, Phys. Rev. B **40**, 546 (1989)

[56] G.T. Zimanyi, P.A. Crowell, R.T. Scalettar, G.G. Batrouni, Phys. Rev. B **50**, 6515 (1994)

[57] D. Jaksch, H.J. Briegel, J.I. Cirac, C.W. Gardiner, P. Zoller, Phys. Rev. Lett. **82**, 1975 (1999)

[58] T.J. Osborne, M.A. Nielsen, Phys. Rev. A **66**, 032110 (2002)

[59] A. Osterloh, L. Amico, G. Falci, R. Fazio, Nature **416**, 608 (2002)

[60] W.D. Phillips, P.L. Gould, P.D. Lett, Science **239**, 877 (1988)

[61] D.J. Wineland, R.E. Drullinger, F.L. Walls, Phys. Rev. Lett. **40**, 1639 (1978)

[62] R. Grimm, M. Weidemüller, Y.B. Ovchinnikov, **42**, 95 (2000)

[63] D. González-Cuadra, P.R. Grzybowski, A. Dauphin, M. Lewenstein, Phys. Rev. Lett. **121**, 090402 (2018)

[64] L. Amico, A. Osterloh, F. Cataliotti, Phys. Rev. Lett. **95**, 063201 (2005)

[65] S. Inouye, M.R. Andrews, J. Stenger, H.J. Miesner, D.M. Stamper-Kurn, W. Ketterle, Nature **392**, 151 (1998)

[66] K. Góral, L. Santos, M. Lewenstein, Phys. Rev. Lett. **88**, 170406 (2002)

[67] M. Köhl, H. Moritz, T. Stöferle, C. Schori, T. Esslinger, J. Low Temp. Phys. **138**, 635 (2005)

[68] W.S. Bakr, A. Peng, M.E. Tai, R. Ma, J. Simon, J.I. Gillen, S. Fölling, L. Pollet, M. Greiner, Science **329**, 547 (2010)

[69] J.F. Sherson, C. Weitenberg, M. Endres, M. Cheneau, I. Bloch, S. Kuhr, Nature **467**, 68 (2010)

[70] O. Dutta, M. Gajda, P. Hauke, M. Lewenstein, D.S. Lühmann, B.A. Malomed, T. Sowiński, J. Zakrzewski, Rep. Prog. Phys. **78**, 066001 (2015)

[71] K. Biedroń, M. Łącki, J. Zakrzewski, Phys. Rev. B **97**, 245102 (2018)

[72] A. Frisch, M. Mark, K. Aikawa, S. Baier, R. Grimm, A. Petrov, S. Kotochigova, G. Quéméner, M. Lepers, O. Dulieu et al., Phys. Rev. Lett. **115**, 203201 (2015)

[73] J. Larson, S. Fernández-Vidal, G. Morigi, M. Lewenstein, New J. Phys. **10**, 045002 (2008)

[74] J. Larson, B. Damski, G. Morigi, M. Lewenstein, Phys. Rev. Lett. **100**, 050401 (2008)

[75] H. Ritsch, P. Domokos, F. Brennecke, T. Esslinger, Rev. Mod. Phys. **85**, 553 (2013)

[76] Y. Li, L. He, W. Hofstetter, Phys. Rev. A **87**, 051604 (2013)

[77] J. Hubbard, Proc. Royal Soc. A **276**, 238 (1963)

[78] H.A. Gersch, G.C. Knollman, Phys. Rev. **129**, 959 (1963)

[79] W.L. McMillan, Phys. Rev. **138**, A442 (1965)

[80] T. Lahaye, C. Menotti, L. Santos, M. Lewenstein, T. Pfau, Rep. Prog. Phys. **72**, 126401 (2009)

[81] D. Rossini, R. Fazio, New J. Phys. **14**, 065012 (2012)

[82] C. Kittel, *Introduction to Solid State Physics* (Wiley, 1996)

[83] G.H. Wannier, Phys. Rev. **52**, 191 (1937)

[84] T.D. Kühner, H. Monien, Phys. Rev. B **58**, R14741 (1998)

[85] A.E. Niederle, G. Morigi, H. Rieger, Phys. Rev. A **94**, 033607 (2016)

[86] K. Baumann, C. Guerlin, F. Brennecke, T. Esslinger, Nature **464**, 1301 (2010)

[87] N.F. Mott, Proc. Phys. Soc. **62**, 416 (1949)

[88] M. Endres, Ph.D. thesis (2013)

[89] S.D. Huber, E. Altman, H.P. Büchler, G. Blatter, Phys. Rev. B **75**, 085106 (2007)

[90] G. Grüner, Rev. Mod. Phys. **60**, 1129 (1988)

[91] G.V. Chester, Phys. Rev. A **2**, 256 (1970)

[92] G.G. Batrouni, R.T. Scalettar, Phys. Rev. Lett. **84**, 1599 (2000)

[93] T. Flottat, L.d.F. de Parny, F. Hébert, V.G. Rousseau, G.G. Batrouni, Phys. Rev. B **95**, 144501 (2017)

[94] A.S. Moskvin, Phys. Rev. B **69**, 214505 (2004)

[95] P. Sengupta, L.P. Pryadko, F. Alet, M. Troyer, G. Schmid, Phys. Rev. Lett. **94**, 207202 (2005)

[96] M. Campostrini, M. Hasenbusch, A. Pelissetto, P. Rossi, E. Vicari, Phys. Rev. B **63**, 214503 (2001)

[97] E.L. Pollock, D.M. Ceperley, Phys. Rev. B **36**, 8343 (1987)

[98] G.G. Batrouni, V.G. Rousseau, R.T. Scalettar, B. Grémaud, Phys. Rev. B **90**, 205123 (2014)

[99] E.G. Dalla Torre, E. Berg, E. Altman, Phys. Rev. Lett. **97**, 260401 (2006)

[100] F. Haldane, Phys. Lett. A **93**, 464 (1983)

[101] F.D.M. Haldane, Phys. Rev. Lett. **50**, 1153 (1983)

[102] J. Sólyom, T.A.L. Ziman, Phys. Rev. B **30**, 3980 (1984)

[103] U. Glaus, T. Schneider, Phys. Rev. B **30**, 215 (1984)

[104] M.P. Nightingale, H.W.J. Blöte, Phys. Rev. B **33**, 659 (1986)

[105] H.J. Schulz, T. Ziman, Phys. Rev. B **33**, 6545 (1986)

[106] M. den Nijs, K. Rommelse, Phys. Rev. B **40**, 4709 (1989)

[107] T. Kennedy, H. Tasaki, Phys. Rev. B **45**, 304 (1992)

[108] J. Werner, A. Griesmaier, S. Hensler, J. Stuhler, T. Pfau, A. Simoni, E. Tiesinga, Phys. Rev. Lett. **94**, 183201 (2005)

[109] E. Berg, E.G. Dalla Torre, T. Giamarchi, E. Altman, Phys. Rev. B **77**, 245119 (2008)

[110] G.G. Batrouni, R.T. Scalettar, V.G. Rousseau, B. Grémaud, Phys. Rev. Lett. **110**, 265303 (2013)

[111] S. Ejima, H. Fehske, J. Phys. Conf. Ser. **592**, 012134 (2015)

[112] B. Grémaud, G.G. Batrouni, Phys. Rev. B **93**, 035108 (2016)

[113] J.P. Lv, J.S. Wang, EPL (Europhysics Letters) **123**, 10004 (2018)

[114] T.D. Kühner, S.R. White, H. Monien, Phys. Rev. B **61**, 12474 (2000)

[115] D.L. Kovrizhin, G.V. Pai, S. Sinha, EPL (Europhysics Letters) **72**, 162 (2005)

[116] R.V. Pai, R. Pandit, Phys. Rev. B **71**, 104508 (2005)

[117] G.G. Batrouni, V.G. Rousseau, R.T. Scalettar, B. Grémaud, J. Phys. Conf. Ser. **640**, 012042 (2015)

[118] K. Kawaki, Y. Kuno, I. Ichinose, Phys. Rev. B **95**, 195101 (2017)

[119] K.B. David P. Landau, *A Guide to Monte Carlo Simulation in Statistical Physics* (Cambridge University Press, 2000)

[120] J.M. Thijssen, *Computational Physics* (Cambridge University Press, 1999)

[121] G.T.B. M. E. Newman, *Monte Carlo Methods in Statistical Physics* (Oxford University Press, 1999)

[122] W. Krauth, *Statistical mechanics: Algorithms and Computations*, Vol. 13 (OUP Oxford, 2006)

[123] L. Devroye, *Non-uniform random variate generation* (Springer, 1986)

[124] M. Matsumoto, T. Nishimura, ACM Trans. Model. Comput. Simul. **8**, 3–30 (1998)

[125] L.D. Landau, E.M. Lifshitz, *Statistical Physics, Third Edition* (Butterworth-Heinemann, 1980)

[126] W.K. Hastings, Biometrika **57**, 97 (1970)

[127] J. Zhang, R. Dong, Eur. J. Phys. **31**, 591 (2010)

[128] R. Assaraf, M. Caffarel, Phys. Rev. Lett. **83**, 4682 (1999)

[129] L. Pollet, S.M.A. Rombouts, K. Van Houcke, K. Heyde, Phys. Rev. E **70**, 056705 (2004)

[130] A. Harju, B. Barbiellini, S. Siljamäki, R.M. Nieminen, G. Ortiz, Phys. Rev. Lett. **79**, 1173 (1997)

[131] C.J. Umrigar, C. Filippi, Phys. Rev. Lett. **94**, 150201 (2005)

[132] S. Sorella, Phys. Rev. B **71**, 241103 (2005)

[133] W. von der Linden, Phys. Rep. **220**, 53 (1992)

[134] V.A. Kashurnikov, B.V. Svistunov, Phys. Rev. B **53**, 11776 (1996)

[135] S.R. White, Phys. Rev. Lett. **69**, 2863 (1992)

[136] W. Krauth, M. Caffarel, J.P. Bouchaud, Phys. Rev. B **45**, 3137 (1992)

[137] N. Elstner, H. Monien, Phys. Rev. B **59**, 12184 (1999)

[138] G.G. Batrouni, R.T. Scalettar, G.T. Zimanyi, Phys. Rev. Lett. **65**, 1765 (1990)

[139] G.G. Batrouni, R.T. Scalettar, Phys. Rev. B **46**, 9051 (1992)

[140] W. Krauth, N. Trivedi, EPL (Europhysics Letters) **14**, 627 (1991)

[141] W. Krauth, N. Trivedi, D. Ceperley, Phys. Rev. Lett. **67**, 2307 (1991)

[142] D.M. Ceperley, Rev. Mod. Phys. **67**, 279 (1995)

[143] N. Prokof'ev, B. Svistunov, I. Tupitsyn, Phys. Lett. A **238**, 253 (1998)

[144] N. Prokof'ev, B. Svistunov, Phys. Rev. Lett. **87**, 160601 (2001)

[145] N. Prokof'ev, B. Svistunov, Phys. Rev. Lett. **92**, 015703 (2004)

[146] N. Kawashima, K. Harada, J. Phys. Soc. Jpn **73**, 1379 (2004)

[147] K. Van Houcke, S.M.A. Rombouts, L. Pollet, Phys. Rev. E **73**, 056703 (2006)

[148] M. Boninsegni, N.V. Prokof'ev, B.V. Svistunov, Phys. Rev. E **74**, 036701 (2006)

[149] V.G. Rousseau, Phys. Rev. E **77**, 056705 (2008)

[150] V.G. Rousseau, Phys. Rev. E **78**, 056707 (2008)

[151] F. Alet, E.S. Sørensen, Phys. Rev. B **70**, 024513 (2004)

[152] B. Capogrosso-Sansone, N.V. Prokof'ev, B.V. Svistunov, Phys. Rev. B **75**, 134302 (2007)

[153] B. Capogrosso-Sansone, S.G. Söyler, N. Prokof'ev, B. Svistunov, Phys. Rev. A **77**, 015602 (2008)

[154] T. Ohgoe, T. Suzuki, N. Kawashima, Phys. Rev. B **86**, 054520 (2012)

[155] E. Duchon, N. Trivedi, Annalen der Physik **525**, L35 (2013)

[156] P. Gunacker, M. Wallerberger, E. Gull, A. Hausoel, G. Sangiovanni, K. Held, Phys. Rev. B **92**, 155102 (2015)

[157] G.G. Batrouni, R.T. Scalettar, G.T. Zimanyi, A.P. Kampf, Phys. Rev. Lett. **74**, 2527 (1995)

[158] M. Boninsegni, N.V. Prokof'ev, Rev. Mod. Phys. **84**, 759 (2012)

[159] A.E. Niederle, H. Rieger, New J. Phys. **15**, 075029 (2013)

[160] T. Kimura, Phys. Rev. A **84**, 063630 (2011)

[161] G.G. Batrouni, F. Hébert, R.T. Scalettar, Phys. Rev. Lett. **97**, 087209 (2006)

[162] K.W. Mahmud, E.N. Duchon, Y. Kato, N. Kawashima, R.T. Scalettar, N. Trivedi, Phys. Rev. B **84**, 054302 (2011)

[163] A. van Otterlo, K.H. Wagenblast, R. Baltin, C. Bruder, R. Fazio, G. Schön, Phys. Rev. B **52**, 16176 (1995)

[164] K. Yamamoto, S. Todo, S. Miyashita, Phys. Rev. B **79**, 094503 (2009)

[165] B. Xi, F. Ye, W. Chen, F. Zhang, G. Su, Phys. Rev. B **84**, 054512 (2011)

[166] M. Iskin, Phys. Rev. A **83**, 051606 (2011)

[167] T. Keller, S.B. Jäger, G. Morigi, J. Stat. Mech. Theory Exp. **2017**, 064002 (2017)

[168] R. Liao, H.J. Chen, D.C. Zheng, Z.G. Huang, Phys. Rev. A **97**, 013624 (2018)

[169] N. Dogra, F. Brennecke, S.D. Huber, T. Donner, Phys. Rev. A **94**, 023632 (2016)

[170] Y. Chen, Z. Yu, H. Zhai, Phys. Rev. A **93**, 041601 (2016)

[171] B. Sundar, E.J. Mueller, Phys. Rev. A **94**, 033631 (2016)

[172] J. Panas, A. Kauch, K. Byczuk, Phys. Rev. B **95**, 115105 (2017)

[173] B. Blaß, H. Rieger, G.m.H. Roósz, F. Iglói, Phys. Rev. Lett. **121**, 095301 (2018)

[174] E.I. Rodríguez Chiacchio, A. Nunnenkamp, Phys. Rev. A **97**, 033618 (2018)

[175] F. Iglói, B. Blaß, G.m.H. Roósz, H. Rieger, Phys. Rev. B **98**, 184415 (2018)

[176] P.J. Reynolds, R.N. Barnett, B.L. Hammond, W.A. Lester, J. Stat. Phys. **43**, 1017 (1986)

[177] L. Pollet, Rep. Prog. Phys **75**, 094501 (2012)

[178] D. Ceperley, G.V. Chester, M.H. Kalos, Phys. Rev. B **16**, 3081 (1977)

[179] M. Capello, F. Becca, M. Fabrizio, S. Sorella, E. Tosatti, Phys. Rev. Lett. **94**, 026406 (2005)

[180] M. Capello, F. Becca, M. Fabrizio, S. Sorella, Phys. Rev. B **77**, 144517 (2008)

[181] L. Cevolani, G. Carleo, L. Sanchez-Palencia, Phys. Rev. A **92**, 041603 (2015)

[182] J.K.L. MacDonald, Phys. Rev. **43**, 830 (1933)

[183] J.C. Slater, Phys. Rev. **81**, 385 (1951)

[184] D.J. Griffiths, *Introduction to Quantum Mechanics, Second Edition* (Prentice Hall International, 1995)

[185] C. De Michelis, G. Masserini, L. Reatto, Phys. Rev. A **18**, 296 (1978)

[186] G. Dev, J.K. Jain, Phys. Rev. B **45**, 1223 (1992)

[187] F. Schautz, C. Filippi, J. Chem. Phys. **120**, 10931 (2004)

[188] H. Yokoyama, H. Shiba, J. Phys. Soc. Jpn **59**, 3669 (1990)

[189] M. Capello, Ph.D. thesis, Scuola Internazionale Superiore di Studi Avanzati Trieste (2006)

[190] E.L. Pollock, D.M. Ceperley, Phys. Rev. B **30**, 2555 (1984)

[191] D.M. Ceperley, E.L. Pollock, Phys. Rev. Lett. **56**, 351 (1986)

[192] J.E. Hirsch, R.L. Sugar, D.J. Scalapino, R. Blankenbecler, Phys. Rev. B **26**, 5033 (1982)

[193] P. Niyaz, R.T. Scalettar, C.Y. Fong, G.G. Batrouni, Phys. Rev. B **50**, 362 (1994)

[194] H.F. Trotter, Proc. Amer. Math. Soc. **10**, 545 (1959)

[195] M. Suzuki, Commun. Math. Phys. **51**, 183 (1976)

[196] M. Suzuki, Progr. Theor. Phys. **56**, 1454 (1976)

[197] H. De Raedt, B. De Raedt, Phys. Rev. A **28**, 3575 (1983)

[198] V.A. Kashurnikov, A.V. Krasavin, B.V. Svistunov, JETP Lett. **64**, 99 (1996)

[199] W. Krauth, Phys. Rev. B **44**, 9772 (1991)

[200] J.K. Freericks, H. Monien, Phys. Rev. B **53**, 2691 (1996)

[201] D. van Oosten, P. van der Straten, H.T.C. Stoof, Phys. Rev. A **63**, 053601 (2001)

Acknowledgments

An incredibly important, but often neglected aspect of research is that it needs to be talked about. In this sense many people contributed to this thesis, either indirectly or very directly. I would like to honor this in the following.
First of all, I would like to thank Professor Rieger for giving me the opportunity to work in this fascinating field. He allowed his staff great freedom in carrying out their research, not only in terms of how they worked, but also in the choice of priorities. Nevertheless, he always took the time for interesting discussions, was open to ideas and offered support when problems arose. His expertise, especially in the fields of critical phenomena and computational physics, was very helpful and at times nothing short of astonishing. He is understanding and very loyal to his employees, but he also encourages them to work independently. For me the work together was a very instructive and valuable time.
I also want to thank Professor Santen for financing several months of my research. This was crucial for the success of the whole project, as it gave me the opportunity to work full-time on my paper. I am very grateful for the funding, which he granted me without hesitation.
Furthermore, I would like to thank Mrs Balzert very much. Not many people are lucky enough to work with a secretary who is both competent and likeable. She always had an open ear for the problems and needs of the group members. In some cases she solved organizational problems even before you knew about them yourself. It was a pleasure to work with her.
To refer to the group members, I would like to mention André Winter, who has been very supportive during my work on the world-line algorithm. The discussions with him and his input on the topic were very helpful. Part of the research with the variational Monte Carlo algorithm was done together with Clément De Daniloff. I supervised him during his internship with us, which resulted in a successful collaboration and ultimately in a paper. Apart from the fact that he is very talented, it was a pleasure to work with him. Johannes Sicks also needs to be named and thanked. The joint reflection on the latest simulation results over a cup of coffee was more than once very enlightening.
I also thank Professor Morigi and her group for useful discussions concerning bosonic systems.
My special thanks go to Karsten Schwarz, Benjamin Blaß and Michael Brill, who proofread this work. In addition to their undisputed professional qualities, I especially appreciate their personal qualities. They are very dear friends of mine and had a considerable influence on this thesis. Not only by their feedback, but also by motivating me.
It must be emphasized that within the group I had the fortune to work with many very likeable people. I thank all of them for the good work together and the many nice little chats at the coffee machine. I would especially like to thank my office partners Thierry and Ivan for the pleasant time together.
The most important people who made all this possible should not go unnoticed. I would like to thank my parents very much for their continuous support over the whole time. The contribution of my girlfriend Malika to this work is invaluable. She put up with my grumpiness and gave me constant support without complaining once. Malika, je n'oublierai jamais cela.
I also want to thank Jonesy, whose noble spirit was more than inspiring.